Unraveling Efficiency-Limiting Processes in Organic Solar Cells by Ultrafast Spectroscopy – Impact of Chemical Structure and Morphology on Photophysics and Efficiency

Dissertation

zur Erlangung des Grades

“Doktor der Naturwissenschaften“

im Promotionsfach Chemie

am Fachbereich Chemie, Pharmazie und Geowissenschaften

der Johannes Gutenberg-Universität

in Mainz

Dominik Werner Gehrig

geb. in Karlstadt am Main

Mainz, den 30.06.2015

Tag der mündlichen Prüfung: 18.11.2015

I hereby declare that I wrote this dissertation submitted without any unauthorized external assistance and used only sources acknowledged in the work. All textual passages which are appropriated verbatim or paraphrased from published and unpublished texts as well as all information obtained from oral sources are duly indicated and listed in accordance with bibliographical rules. In carrying out this research, I complied with the rules of standard scientific practice as formulated in the statutes of the Johannes Gutenberg-University Mainz to insure standard scientific practice.

Dominik Gehrig

Summary

This work is dedicated to the investigation of the photophysical processes that occur in photovoltaic blends of electron-donating and -accepting materials. As electron donors the copolymer PBDTTT-C which consists of benzodithiophene and thienothiophene units and the small molecule p-DTS(FBTTh$_2$)$_2$ that contains silicon-bridged dithiophene, fluorinated benzothiadiazole and bithiophene are used. As electron-accepting material a planar 3,4:9,10-perylenetetracarboxylic acid diimide (PDI) derivative and different fullerene derivatives are employed. PDIs are regarded as a promising alternative to fullerenes due to the tunable structural, optical, and electronic properties with elaborated chemical synthesis. The most substantial argument for PDI derivatives is the pronounced absorption in the visible part of the sunlight which can potentially increase the photocurrent that can be extracted from photovoltaic devices of donor-PDI blends. However, fullerene-based blends significantly outperform PDI-based blends.

Therefore, thin films of the various donor-acceptor combinations are characterized with optical, electrical, and structural experiments to reveal the bottleneck in the less-performing PDI-based blends compared to the respective fullerene-based blends. Time-resolved spectroscopy, especially transient absorption (TA) spectroscopy, is employed to analyze the charge generation efficiency and the comparison of donor-PDI and donor-fullerene blends demonstrates that the formation of charge-transfer (CT) states at the donor-acceptor interface is one of the main loss channels in the investigated PDI-based blends. Furthermore, time-delayed collection field experiments prove field-assisted charge generation in blends of PBDTTT-C and the planar PDI derivative investigated in this thesis.

Moreover, blends of PBDTTT-C with the fullerene derivative [6,6]-phenyl C61 butyric acid methyl ester (PC$_{61}$BM) are investigated with TA spectroscopy in detail on the ps-μs timescale. It is demonstrated that the non-geminate recombination of free charges to the polymer's triplet state occurs on a sub-ns timescale and sophisticated data analysis including multivariate curve resolution (MCR) is applied to disentangle overlapping signal contributions. Additionally, the re-creation of charges on the ns-μs timescale is observed and assigned to triplet-triplet annihilation.

Furthermore, the positive influence of the solvent additive 1,8-diiodooctane (DIO) on the performance of p-DTS(FBTTh$_2$)$_2$:PDI solar cells is investigated. The findings of morphological and photophysical experiments are unified to relate the structural properties and photophysics to the relevant device characteristics. Time-resolved photoluminescence (TRPL) shows that DIO reduced PL quenching which is assigned to stronger phase separation in the optimized blend. Moreover, TA spectroscopy shows that DIO increases the crystallinity and thus the efficiency of the generation of free charges. For detailed analysis the decay dynamics are described with a two-pool model which takes the parallel recombination of bound CT

states and separated charges into account and in fact, optimized blends show a higher fraction of non-geminate recombination of spatially-separated charges.

In another case study, the influence of the fullerene derivative, namely IC$_{60}$BA and PC$_{71}$BM, in combination with the same small molecule donor on the performance and photophysics is addressed. A combination of structural analysis as well as TA spectroscopy reveals that blends using ICBA as electron acceptor show less efficient splitting of CT states and suffer from stronger geminate-recombination compared to PCBM-based blends. This is assigned to the lower energy offset and higher energetic disorder in ICBA-based blends which hinders charge separation in this blend.

Apart from non-fullerene acceptors, the influence of pure fullerene domains on the operation of a photovoltaic blend consisting of the thienothiophene-based polymer pBTTT-C14 and PC$_{61}$BM is investigated. For this reason, the photophysics of films with a donor-acceptor ratio of 1:1 and 1:4 are compared. While 1:1 blends show only a cocrystal phase in which the fullerene intercalates into the side chains of the polymer, the fourfold excess of fullerene results in the formation of pure fullerene domains in addition to the cocrystal phase. TA spectroscopy reveals that CT states generated in 1:1 blends decay mainly *via* geminate recombination, while in 1:4 blends a substantial fraction of CT states overcome their mutual Coulomb attraction and form spatially-separated charges that finally recombine non-geminately.

Zusammenfassung

Diese Arbeit widmet sich der Untersuchung der photophysikalischen Prozesse, die in Mischungen von Elektronendonoren in Kombination mit Elektronenakzeptoren zur Anwendung in organischen Solarzellen auftreten. Als Elektronendonoren werden das Copolymer PBDTTT-C, das aus Benzodithiophen- und Thienothiophene-Einheiten besteht, und das kleine Molekül p-DTS(FBTTh$_2$)$_2$, welches Silizium-überbrücktes Dithiophen, sowie fluoriertes Benzothiadiazol als auch Dithiophen beinhaltet, verwendet. Als elektronakzeptierende Komponente finden ein planares 3,4:9,10-Perylentetracarbonsäurediimid-(PDI)-Derivat und verschiedene Fullerenderivate Anwendung. PDI-Derivate gelten als vielversprechende Alternativen zu Fulleren-Derivaten aufgrund der durch vielfältige chemische Synthese abstimmbaren strukturellen, optischen und elektronischen Eigenschaften. Das gewichtigste Argument für PDI-Derivate ist deren ausgeprägte Absorption im sichtbaren Bereich des Sonnenspektrums was den extrahierbaren Photostrom grundsätzlich verbessern kann. Fulleren-basierte Mischungen übertreffen jedoch für gewöhnlich die Effizienz, die mit Donor-PDI-Mischungen erreicht werden kann.

Um den Nachteil der weniger effizienten PDI-basierten Mischungen im Vergleich zu den entsprechenden Fulleren-basierten Mischungen zu identifizieren, werden die verschiedenen Donor-Akzeptor-Kombinationen auf ihre optischen, elektronischen und strukturellen Eigenschaften untersucht. Zeitaufgelöste Spektroskopie, vor allem transiente Absorptionsspektroskopie (TA), wird zur Analyse der Ladungsgeneration angewendet und der Vergleich der Donor-PDI Mischfilme mit den entsprechenden Donor-Fulleren Mischfilmen zeigt, dass die Bildung von Ladungstransferzuständen an der Donor-Akzeptor-Grenzfläche einen der Hauptverlustkanäle in PDI-basierten Mischungen darstellt. Des Weiteren kann mit Hilfe von *time-delayed collection field* (TDCF) Experimenten eine feldabhängige Ladungsgeneration in Mischfilmen von PBDTTT-C und PDI nachgewiesen werden.

Weiterhin werden Mischungen aus PBDTTT-C und [6,6]-Phenyl-C61-buttersäuremethylesther (PC$_{61}$BM) mittels TA-Spektroskopie auf einer Zeitskala von ps bis µs untersucht und es kann gezeigt werden, dass der Triplettzustand des Polymers über die nicht-geminale Rekombination freier Ladungen auf einer sub-ns Zeitskala bevölkert wird. Hochentwickelte Methoden zur Datenanalyse, wie *multivariate curve resolution* (MCR), werden angewendet um überlagernde Datensignale zu trennen. Zusätzlich kann die Regeneration von Ladungsträgern durch Triplett-Triplett-Annihilation auf einer ns-µs Zeitskala gezeigt werden.

Darüber hinaus wird der Einfluss des Lösungsmitteladditivs 1,8-Diiodooctan (DIO) auf die Leistungsfähigkeit von p-DTS(FBTTh$_2$)$_2$:PDI Solarzellen untersucht. Die Erkenntnisse von morphologischen und photophysikalischen Experimenten werden kombiniert, um die strukturellen Eigenschaften und die Photophysik mit den relevanten Kenngrößen des Bauteils in Verbindung zu setzen. Zeitaufgelöste

Photolumineszenzmessungen (*time-resolved photoluminescence*, TRPL) zeigen, dass der Einsatz von DIO zu einer geringeren Reduzierung der Photolumineszenz führt, was auf eine größere Phasentrennung zurückgeführt werden kann. Außerdem kann mittels TA Spektroskopie gezeigt werden, dass die Verwendung von DIO zu einer verbesserten Kristallinität der aktiven Schicht führt und die Generation freier Ladungen fördert. Zur genauen Analyse des Signalzerfalls wird ein Modell angewendet, das den gleichzeitigen Zerfall gebundener CT-Zustände und freier Ladungen berücksichtigt und optimierte Donor-Akzeptor-Mischungen zeigen einen größeren Anteil an nicht-geminaler Rekombination freier Ladungsträger.

In einer weiteren Fallstudie wird der Einfluss des Fullerenderivats, namentlich $IC_{60}BA$ und $PC_{71}BM$, auf die Leistungsfähigkeit und Photophysik der Solarzellen untersucht. Eine Kombination aus einer Untersuchung der Struktur des Dünnfilms sowie zeitaufgelöster Spektroskopie ergibt, dass Mischungen, die ICBA als Elektronenakzeptor verwenden, eine schlechtere Trennung von Ladungstransferzuständen zeigen und unter einer stärkeren geminalen Rekombination im Vergleich zu PCBM-basierten Mischungen leiden. Dies kann auf die kleinere Triebkraft zur Ladungstrennung sowie auf die höhere Unordnung der ICBA-basierten Mischungen, die die Ladungstrennung hemmen, zurückgeführt werden.

Außerdem wird der Einfluss reiner Fullerendomänen auf die Funktionsfähigkeit organischer Solarzellen, die aus Mischungen des Thienothienophen-basierenden Polymers pBTTT-C14 und $PC_{61}BM$ bestehen, untersucht. Aus diesem Grund wird die Photophysik von Filmen mit einem Donor-Akzeptor-Mischungsverhältnis von 1:1 sowie 1:4 verglichen. Während 1:1-Mischungen lediglich eine *co*-kristalline Phase, in der Fullerene zwischen den Seitenketten von pBTTT interkalieren, zeigen, resultiert der Überschuss an Fulleren in den 1:4-Proben in der Ausbildung reiner Fullerendomänen zusätzlich zu der *co*-kristallinen Phase. Transiente Absorptionsspektroskopie verdeutlicht, dass Ladungstransferzustände in 1:1-Mischungen hauptsächlich über geminale Rekombination zerfallen, während in 1:4 Mischungen ein beträchtlicher Anteil an Ladungen ihre wechselseitige Coulombanziehung überwinden und freie Ladungsträger bilden kann, die schließlich nicht-geminal rekombinieren.

Contents

1 Introduction

If the question is asked "What is the motivation for the research efforts invested in the field of organic photovoltaics (OPV)?", the answer is often given by a triad composed of flexibility and light-weight of the devices, and low costs of the production which could enable new applications and open doors to new markets. This is related to the possibility of the implementation of established solution-based printing procedures like inkjet printing and the feasibility of roll-to-roll processes. Various studies have proven the potential of OPV in this respect.[1]

The need for non-fossil energy production is undoubted. Apart from global warming, the use of fossil energy sources, especially coal, is accompanied by massive air pollution, leading to smog which paralyzes whole regions of the world. Additionally, car traffic with conventional fuel technology contributes to air pollution and the limits of fine and ultra fine particles are regularly surpassed in urban areas and display a severe threat to health of people living in the affected areas. This leads to unusual measures; for instance, the mayor of Paris limited the car traffic in the city by not allowing cars with even-numbered license plates in March 2015. Furthermore, extreme weather events occur more often and more intense causing high costs. More than 90% of natural catastrophes are related to the weather, showing the threat which is emanating from changing climate conditions.[2]

However, OPV just as other renewable energy resources including classical photovoltaics or wind-based power generation have the disadvantage that the power is not available on a constant basis but exhibits strong fluctuations depending on the time of the day and year or the weather condition.

Yet, concepts for energy storage are available including physical storage of electric power with pumped storage hydro power stations or compressed air energy storage. Moreover, recent engagement in the development of battery technology with increased power density enables energy storage in large scale battery packs. For instance, a lithium-ion-battery was installed in Schwerin, Germany, with a capacity of 5 MWh and a power of 5 MW. The storage system consists of 25.600 lithium-manganese oxide-cells and has been connected to the power grid since September 2014. However, this concept is not designed for long-term storage but for compensating short-term fluctuations. Very recently, Tesla Motors introduced a battery into the market which is intended for household use and has a capacity of 7 kWh or 10 kWh and up to nine units can be connected in series to increase the capacity. Such an installation can equalize the higher energy consumption in the mornings and evenings while storing the energy generated during the day with photovoltaic installations.

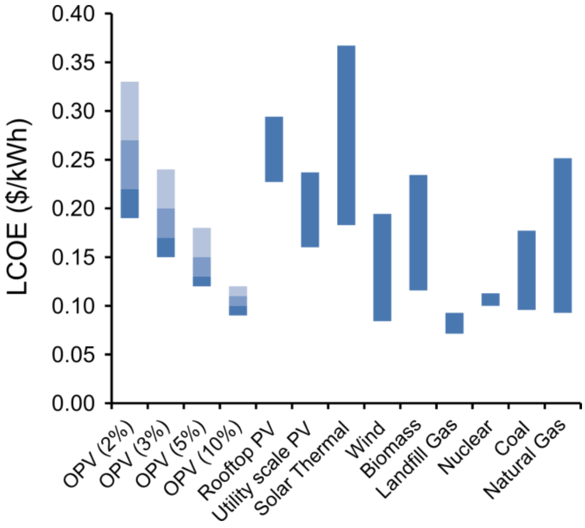

Figure 1. Levelized cost of electricity (LCOE) for different renewable and conventional technologies. Note the strong dependence of OPV on the power conversion efficiency of the module. LCOE takes into account factors like building, operating, and maintaining a power plant over the assumed lifetime cycle. The boundaries between shaded regions correspond to modeled lifetimes of 2, 3, 5, and 10 years. Reprinted with permission from reference [3]. Copyright (2015) Elsevier B.V.

Surely, photovoltaics in general and organic photovoltaics in particular can only contribute a piece in the puzzle that depicts the future energy mix providing renewable and CO_2-reduced energy, but still research efforts are important to enable the full potential and the optimum benefit from this technology.

Yet, new technologies will only be relevant and gain impact, if they can compete with classical energy sources like coal, oil, and gas not only as far as reliability is concerned as mentioned in the previous paragraph, but also if they can produce energy at competitive costs. And indeed, the technological improvements and the milestones which have been taken in the last decade are hopeful signs. Recent calculations by Mulligan *et al*.[3] showed that the costs of OPV can become competitive with fossil fuels if the efficiency of solar modules approaches 10% power conversion efficiency and a sufficiently high lifetime. And the limit of 10% has recently been surpassed even in a single junction BHJ on the lab scale which was demonstrated by Liu *et al*. in November 2014[4] as well as for homo-tandem solar cells.[5]

The improvement in organic photovoltaics is mainly driven by the development of new absorber materials. Researchers aim to harvest as much sunlight as possible by introducing materials that absorb a large fraction of the incident light. This is often done by improving the absorption properties of the donor-type component of the active layer of a solar cell but also the contribution of the electron acceptor to the absorption properties of solar cells can be beneficial. For instance, perylene diimides (PDIs) are a well-known class of electron-accepting material which can be utilized in OPV, however, their efficiency is often inferior to the ubiquitous fullerene acceptors despite their better absorption. This thesis deals with the investigation of a planar PDI used in photovoltaic applications and the efficiency-determining steps involved in the photon-to-electron conversion are analyzed with time-resolved optical spectroscopy. For this purpose, blends of PDI with a polymeric donor and a small molecule donor are investigated and compared to the respective fullerene-based devices. Furthermore, the influence of solvent additives and the role of microstructure, *i.e.* the interplay of intermixed and pure phases, are investigated. The structure of this thesis is as follows:

Chapter 2 sheds light on the basics and principles which are responsible for the semiconducting properties of organic molecules, the interaction of molecules with light and the processes triggered by photon uptake, the basic working principles of organic solar cells and the related figures of merit, and common strategies to improve the photovoltaic performance.

The third chapter is dedicated to the explanation of the experimental techniques and the material systems used for the case studies presented in Chapter 4. Note, that the results presented in the main chapter of this work were published in peer-reviewed journals and therefore will be given as a compilation of the respective articles and supporting informations.

The first case study (Section 4.1) highlights the efficiency-limiting processes in a photovoltaic blend using a low-bandgap polymer, namely PBDTTT-C, as the electron donor and a perylene diimide derivative as the electron acceptor. This work is continued by the investigation of the same polymer in combination with the fullerene derivative $PC_{61}BM$ as electron accepting material in Section 4.2. The behavior of this acceptor differs strongly from the perylene-based blend, as the formation of triplets and the re-creation of charges *via* triplet-triplet annihilation is observed. Section 4.3 involves the perylene diimide used in the first study in combination with the small molecule donor $p\text{-DTS(FBTTh}_2)_2$. The influence of the solvent additive 1,8-diiodooctane is studied in detail by time-resolved spectroscopic methods and by examination of the thin film crystallinity and morphology. In analogy to the donor polymer PBDTTT-C, the donor small molecule $p\text{-DTS(FBTTh}_2)_2$ is combined with fullerene derivatives, namely $PC_{71}BM$ and $IC_{60}BA$, and the influence of the fullerene derivative on the device performance and the related photophysics is presented in Section 4.4. The following Section 4.5 is a study dedicated to the influence of the nanomorphology of the active layer on charge generation and recombination. The nanomorphology is controlled by the donor acceptor blending ratio, where an access of fullerene leads to the formation of pure fullerene domains in addition to an omnipresent donor-acceptor cocrystal phase.

Chapter 5 summarizes and combines the findings of the aforementioned case studies. Section 5.1 contrasts perylene diimides with fullerenes with a focus on the polymer-based systems in Section 5.1.1 and the small molecule-based systems in Section 5.1.2. The point of view is changed to a comparison of polymers *vs.* small molecule donors in Section 5.2 with the perylene diimide combination highlighted in Section 5.2.1 and the fullerene combination in Section 5.2.2.

This thesis is wrapped up by concluding remarks in Chapter 6 and gives an outlook on further developments and perspectives for organic photovoltaic research which is driven recently by new material systems, especially the class of lead halide perovskites.

2 Background

2.1 Organic Semiconductors

2.1.1 Conjugated Molecules

The main structure of organic molecules consists of carbon atoms which have six electrons in their neutral state. According to Hund's rules these are distributed in $1s^2 2s^2 2p^2$-configuration so that four electrons are involved in covalent bonding. Depending on the type of bond a carbon atom forms, namely single, double or triple bond (as shown in Figure 2), it will form 4 sp^3 hybrid orbitals or 3 sp^2-hybrid orbitals and 1 remaining p-orbital or 2 sp-hybrid orbitals and 2 p-orbitals. The overlap of a sp^x-orbital with an s- or another sp^x-orbital will result in the formation of a σ-bond while the overlap of p-orbitals forms π-bonds.

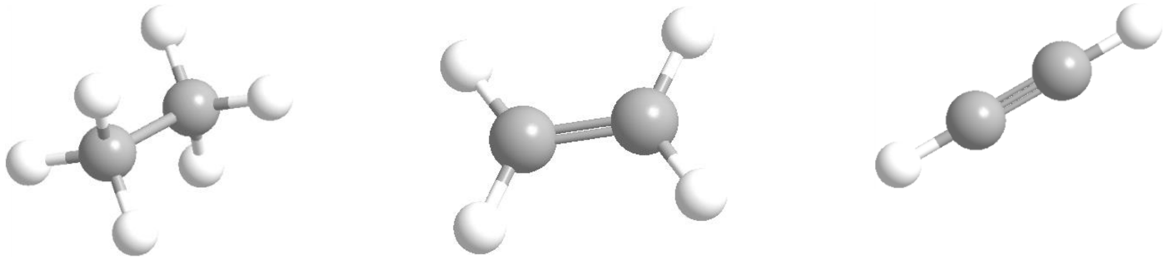

Figure 2. C_2H_x (x = 6, 4, 2) molecules with sp^3, sp^2, and sp hybridization, namely ethane, ethylene, and ethyne.

Carbon atoms with sp^2 hybridization will form σ- and π-bonds by overlap of their sp^2- and p-orbitals, respectively. The linear combination of atomic orbitals (LCAO) will result in bonding orbitals if the wave functions have the same sign while the combination of orbitals with opposite signs will form anti-bonding orbitals, denoted with a star (*). A schematic representation of the bond formation is illustrated in Figure 3. σ-bonds show their maximum electron density between the nuclei while π-bonds have a nodal plane with no contribution of the wave function along the axis while the maximum electron density is located diametrically opposed along the connection of the nuclei. Anti-bonding σ- and π-bonds show an additional nodal plane between the atoms. In C=C double bonds two electrons fill the bonding σ-orbital and two electrons occupy the π-orbital resulting in a bond order of 2.

By alternating single and double bonds a conjugated π-system is obtained. Synthetically, this can be achieved *e.g.* by Ziegler-Natta polymerization of ethyne to polyacetylene. Generally speaking, the extension of the π-system is accompanied by a gradual decrease of the HOMO–LUMO gap and thus leads to a bathochromic shift in absorption which is the promotion of an electron from the ground state to an excited

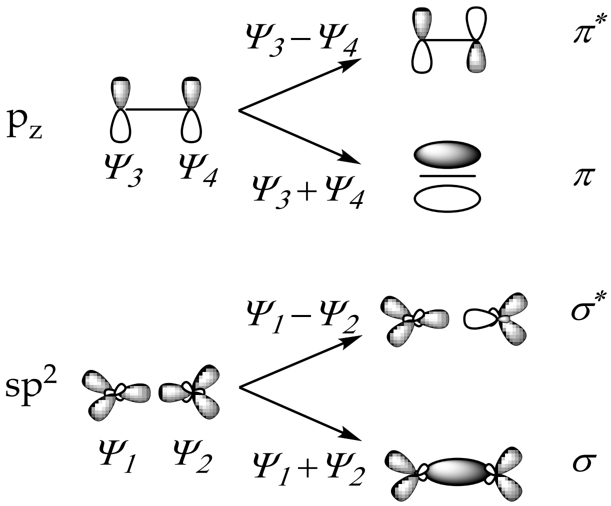

Figure 3. Schematic illustration of the formation of σ-bonds by linear combination of 2 $\mathrm{sp^2}$ hybrid orbitals and of π-bonds by linear combination of 2 p orbitals. Molecular orbitals denoted with a star (*) are anti-bonding.

state. Excited states and light-matter interactions will be discussed in more detail in the following section. The shift of the HOMO and LUMO levels originates from gradual mixing of the molecular orbitals according to molecular orbital (MO) theory which is shown in Figure 4 with the example of benzene and the related polyacenes which were investigated by Lipari *et al.*[6, 7] Further examples were given by Gierschner *et al.* who described the behavior of a series of oligophenylenvinylenes.[8] They showed by means of a combination of theoretical work as well as experimentally obtained emission and excitation spectra a systematic shift in the band position of fluorescence and absorption of a series of para-phenylene vinylenes. A method to estimate the absorption maximum was empirically developed by Woodward and is known as Woodward's rules.[9] These rules take into account the size of the π-system as well as the impact of electron donating groups and electron withdrawing groups.

However, the shift of the absorption by steadily increasing the π-system is limited by the so called Peierls distortion.[10, 11] This means that extended π-systems will show partially localized single and double bonds and consequently no infinite lowering of the bandgap is possible. This in turn also means that organic, conjugated molecules will always have a bandgap and consequently will not show metallic behavior but act as a semiconductor.

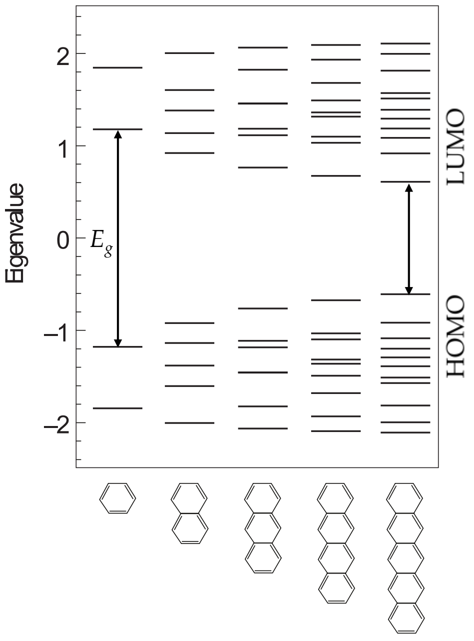

Molecule	Absorption maximum
Benzene	255 nm
Naphthalene	315 nm
Anthracene	380 nm
Tetracene	480 nm
Pentacene	580 nm

Figure 4. Eigenvalue calculations showing the reduced bandgap as well as increased density of states for a series of polyacenes ranging from benzene to pentacene. Values for absorption maxima are taken from reference [12]. Reprinted with permission from reference [7]. Copyright (2006) Nature Publishing Group.

In addition to Peierls distortion, the conjugation in extended polymers can be interrupted by so called 'defect cylinder' conformation, also known as static disorder, which was addressed in a review by Scholes *et al.*[7] This means that rotations, kinks, and twists along single bonds lead to the disruption of the π-system which hinders the unlimited delocalization of electrons in the system. As a consequence, polymers can be considered as a chain of oligomer-like subunits with a distribution of conjugation lengths. This distribution influences characteristics like absorption as well as electronic properties and charge transport.

2.1.2 Excited States in Conjugated Materials

Figure 5 depicts a Jablonski diagram which summarizes the photophysical cascade of processes that can occur in organic materials after photoexcitation.[13] If a molecule absorbs a photon with sufficient energy an electron is promoted from the ground state S_0 to an electronically excited singlet state S_n, where n = 1,2,… depending on the excitation energy. The probability for a transition is given by the Franck-Condon factors and depends on the overlap of the initial and final wave function ψ and ψ' as well as the dipole operator μ.[14, 15] A schematic representation of the Franck-Condon principle is depicted in Figure 6. As a prerequisite, the Born-Oppenheimer approximation is applied, meaning that electron und nuclear motion are treated separately and that the velocity of electrons exceeds nuclear motion.[16] Subsequent to photon absorption,

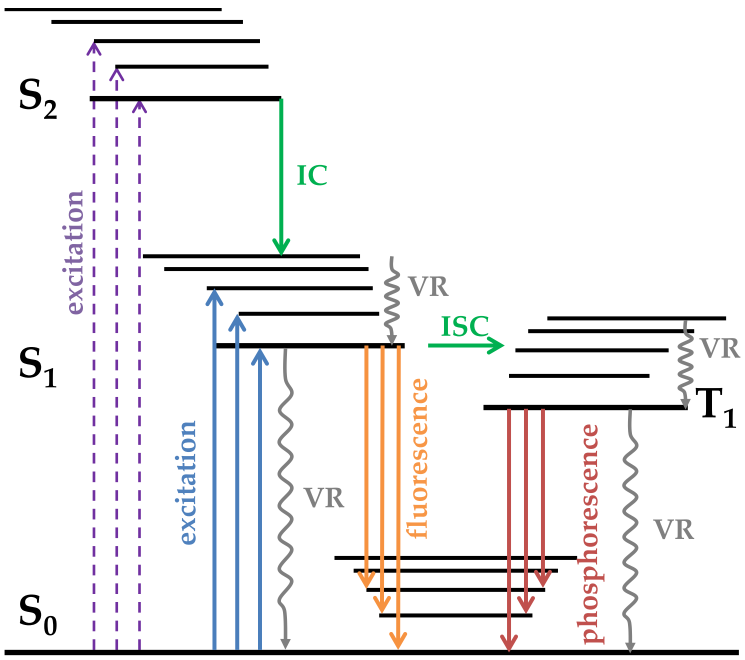

Figure 5. Jablonski diagram giving a summary of the photophysical processes triggered by the absorption (blue and violet arrows) of a photon. The transition probability depends on the overlap of the respective wave functions and can be calculated using the Franck-Condon factors. Excited higher singlet states can relax *via* internal conversion (IC) and return to the ground state (S_0) radiatively *via* fluorescence (orange arrows) or can be converted to triplet states *via* intersystem crossing (ISC) and return to the ground state *via* phosphorescence (red arrows). Additionally, excited states can relax non-radiatively and energy is distributed to the surrounding medium by vibrational relaxation.

higher excited states can be deactivated to the lowest excited state by internal conversion (IC) and vibrational cooling (VR) by dissipating the energy as heat to the environment on a timescale of 0.1–10 ps. Ultimately the lowest excited singlet state (S_1) can return to the ground state *via* fluorescence on a timescale of normally 0.1–10 ns. In accordance with Kasha's rule, this process occurs from the lowest vibronically, *i.e.* vibrational and electronic, excited S_1 state.[17] However, exceptions are possible among which azulene is a prominent example.[18]

Additionally, excited singlet states can be converted to triplet states by intersystem crossing (ISC). In general, the ISC rate is very low and ISC is an uncommon feature in most organic molecules. ISC is favored by a strong coupling between singlet and triplet states and can be promoted by heavy atoms like metals or halogens which lead to a strong spin-orbit-coupling. Triplet states T_n can be subsequently deactivated non-radiatively *via* vibrational relaxation (VR) or radiatively *via* phosphorescence which occurs on timescales of microseconds to seconds.

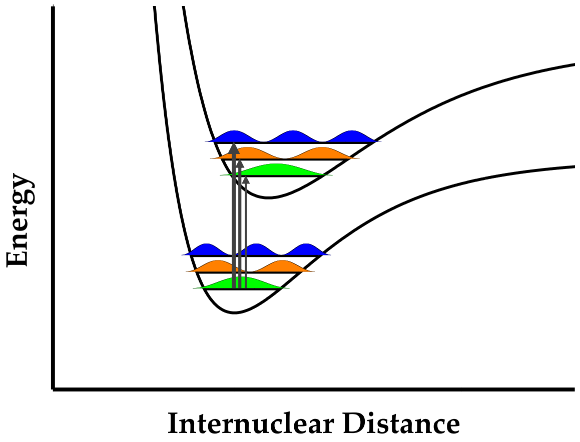

Figure 6. Franck-Condon principle depicted with the example of two anharmonic oscillators. Franck-Condon factors, which are related to the transition probability between S_n and S_{n+1} under the assumption of a vertical transition without nuclear motion and the application of Fermi's Golden Rule, are high if the wave function between the initial and final state exhibit good overlap.

Intensities P for the transition from one state to higher vibrationally and electronically excited states are calculated with the following equation according to Fermi's golden rule which is used to determine transition rates between two eigenstates of a system:

$$P = \overbrace{\langle\psi_v'|\psi_v\rangle}^{\text{Overlap integral = Franck-Condon factor}} \cdot \underbrace{\langle\psi_\varepsilon'|\mu_\varepsilon|\psi_\varepsilon\rangle}_{\text{Orbital selection rule}} + \overbrace{\langle\psi_\varepsilon'|\psi_\varepsilon\rangle\langle\psi_v'|\mu_K|\psi_v\rangle}^{=0} \qquad \text{Equation } \mathbf{1}$$

This equation takes into account the overlap integral of the initial and final wave function, the probability of the electronic transition according to the selection rules and the last term is zero as the electronic wavefunctions of different states are orthogonal with respect to each other.

In addition to ISC as shown before, triplets can be generated *via* singlet fission which was described first by Schneider and co-workers for anthracene.[19] Later, singlet fission was demonstrated by Merrifield *et al.* for tetracene[20] and by Jundt *et al.*[21] as well as Zimmerman *et al.* for pentacene.[22] Singlet fission is depicted schematically in Figure 7. It is a spin-allowed process in which the interaction of a molecule in an excited singlet state with a molecule in the ground state leads to the formation of a triplet pair. This process was also described for organic electronics and was successfully exploited in organic solar cells. For instance, Congreve *et al*. demonstrated internal quantum efficiency values, *i.e.* photon-to-electron-conversion, exceeding 100%.[23] The authors argue that *via* singlet fission the photocurrent can be doubled. However,

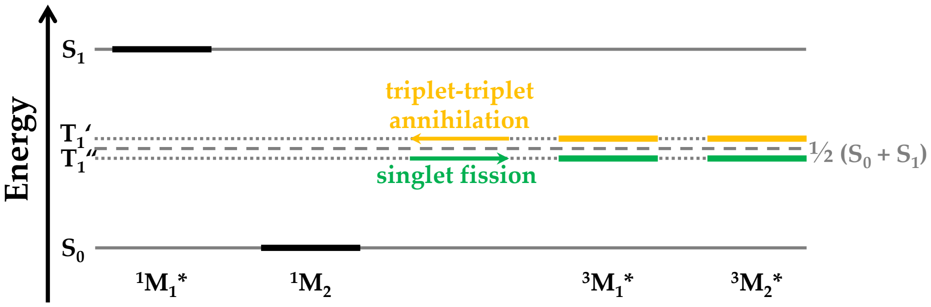

Figure 7. Schematic representation of singlet fission (green) which is possible if the triplet energy T_1'' is less than half of the singlet energy S_1 and of triplet-triplet annihilation which can occur if the triplet energy T_1' is higher than half of the S_1 energy.

triplet states are also less energetic than singlet states which means that the open-circuit voltage is smaller if charges are generated by the dissociation of triplets. Open-circuit voltage as well as internal quantum efficiency will be discussed in more detail in Section 2.2.3.

Furthermore, the reverse process of singlet fission is known which is the reaction of two triplets that leads to the population of an excited singlet state and the ground state. This process is called triplet-triplet annihilation (TTA). Delayed fluorescence, originating from regenerated singlet states *via* triplet-triplet annihilation was described *e.g.* by Sternlicht *et al*. for pure and mixed organic crystals.[24] Recently, TTA was demonstrated in a polymeric material which was sensitized by porphyrin-based molecules containing heavy-metals, namely Palladium-octaethylporphyrin.[25] Singlet state population enabled by TTA in conjunction with delayed charge separation has also been observed in blends of donor polymers with a fullerene derivative and is described in Section 4.2 of this thesis.

The transition probability according to the Franck-Condon principle as described above will determine the strength of the interaction of organic molecules with light and consequently how much light is absorbed when it passes through a medium. The Beer-Lambert law describes the reduction of the light intensity by absorption of light in a medium under a set of assumption, *i.e.* that no light is scattered by the material, non-linear processes do not occur and emission in the direction of transmission is negligible.[26, 27]

$$T(\lambda) = \frac{I(\lambda)}{I_0(\lambda)} = 10^{-\mathrm{OD}(\lambda)} = e^{-\varepsilon(\lambda)\cdot c\cdot d} \qquad \text{Equation } \mathbf{2}$$

The transmission T as a function of the wavelength λ is defined as the ratio of the light intensity after passing through the medium I and the initial light intensity I_0. This ratio equals the negative optical density OD with the base 10 or the exponential function of the extinction coefficient ε times the concentration c times the path length d.

A typical absorption and emission spectrum is depicted in Figure 8. Absorption spectra show usually a vibronic fine structure originating from excitations from the ground state to higher lying electronically excited states with progressing vibrational levels indicated by the solid lines in Figure 8. The probability of a single transition can be calculated by the Franck-Condon principle as described by Equation 1 shown earlier in this section. At the same time, the emission can show different peaks that can be assigned to transitions from the lowest excited state S_1 to different vibrationally excited levels of the ground state S_0. The energetic difference between the 0–0 transition of absorption and emission is known as Stokes shift. This is the result of two phenomena: Vibrational relaxation or dissipation and solvent reorganization. The latter originates from the change in the dipole of the molecular upon promotion from the ground to the excited state and the associated rearrangement of solvent molecules. Consequently, the Stokes shift depends strongly on the dipole moment of the surrounding medium.[28] Changes in absorption and emission induced by the solvent are known as solvatochromism.

Furthermore, the absorption of chromophores can be altered by aggregation determined by the relative orientation of the respective dipole moments of the chromophore units. Two extreme cases are distinguished, namely H- (for hypsochromic) and J-aggregates (for Jelly) which are defined by the slip angle θ between two chromophores as shown in Figure 9. If $\theta < 54.7°$ the dimer aggregate is denoted as J-aggregate while aggregates exhibiting a slip angle $\theta > 54.7°$ are H-aggregates. Excited states are stabilized by van der Waals interactions ΔE_{vdW} and therefore lowered in energy. Allowed transitions from the ground state to the excited state require a transition dipole moment $\mu \neq 0$. In J-aggregates, this is given for the electrostatically preferred combination of the transition dipole moments in which positive and negative dipoles are neighboring. As a result, the allowed transition for J-aggregates is lower in energy compared to the respective monomers and therefore the absorption is bathochromically shifted. In contrast, the allowed

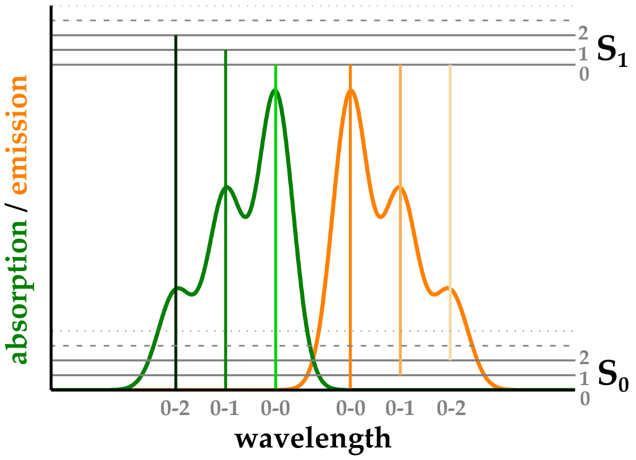

Figure 8. Typical absorption (green line) and emission (orange line) spectrum.

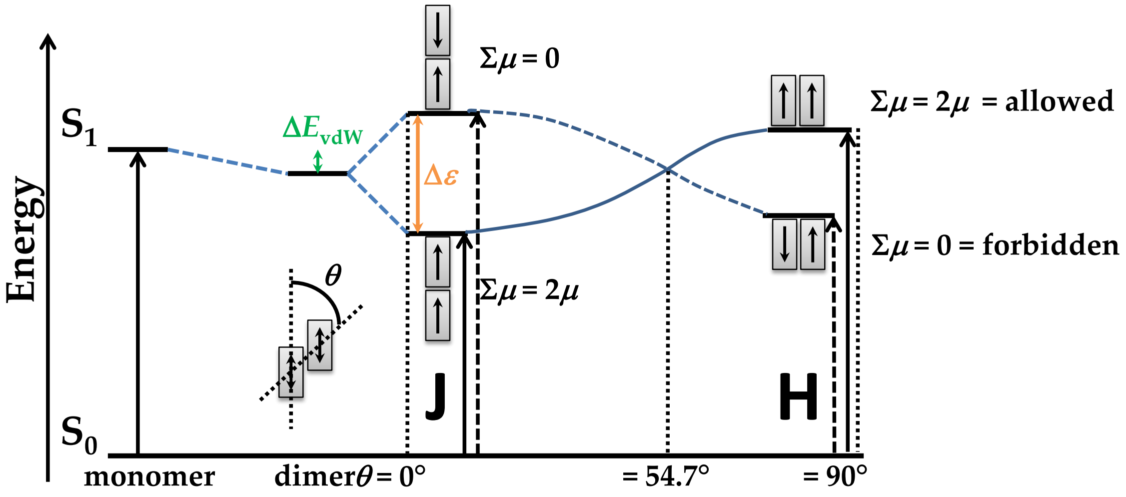

Figure 9. Schematic illustration of J- and H-aggregates based on a review article by Würther *et al.*[29]

transition in H-aggregates requires an energetically unfavorable arrangement of the dipole moments with respect to each other, resulting in a higher lying allowed transition and as a consequence a hypsochromic shift of the absorption.

Furthermore, aggregation does not only influence the absorption properties of molecule dimers, but also their emission. In J-aggregates, the transition of the lowest excited state to the ground state is allowed and consequently J-aggregates are strongly fluorescent. On the other hand, H-aggregates relax to the lowest excited state in which the dipole moments point in opposite directions and thus show a transition dipole moment $\mu = 0$. Therefore, fluorescence is suppressed in H-aggregates and excited states are depopulated *via* non-radiative processes.

2.2 Organic Solar Cells

2.2.1 Basic Working Principles

The following section is based on several review articles and summarizes the operation principles of organic solar cells.[30-33]

A typical organic solar cell consists of an active layer, composed of electron-donating and -accepting type materials, shortly denoted as donor (D) and acceptor (A), sandwiched between two electrodes, of which at least one has to be transparent. Often, transparent conductive oxides (TCO) like indium tin oxide (ITO) are used. Electrodes have to grant efficient charge extraction, thus their work function must match the HOMO level of the donor and LUMO level of the acceptor in the active layer to ensure Ohmic contacts. This is

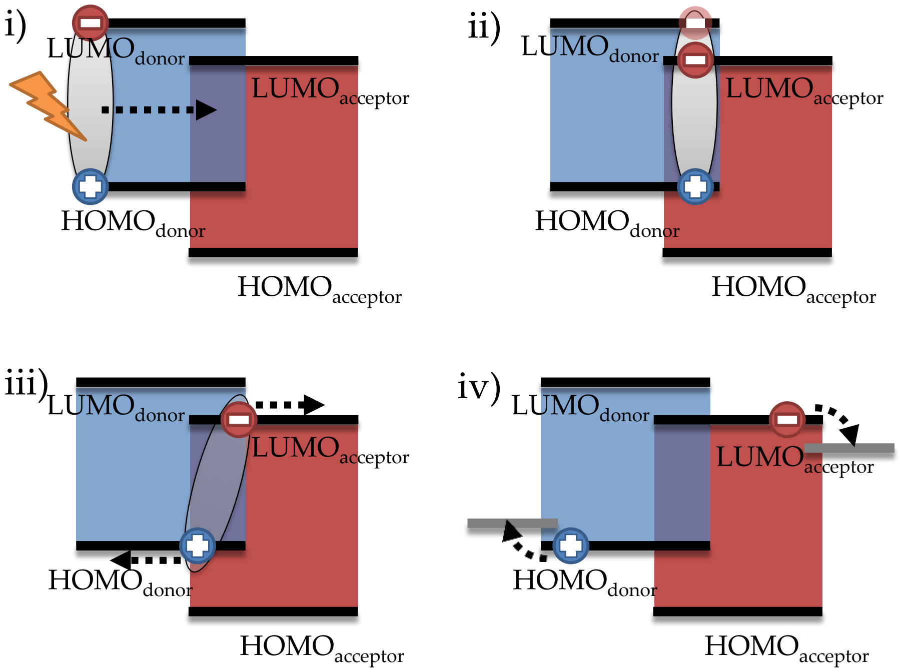

Figure 10. Charge generation mechanism in an organic solar cell including from top left to bottom right the processes of i) photon absorption/exciton creation, ii) exciton diffusion to and quenching at the interface, iii) charge separation, and iv) transport to and extraction of charges at the respective electrodes.

described in more detail in Section 2.2.2. The processes leading from photon absorption to charge generation are summarized in Figure 10. Incident photons may be absorbed by the active layer depending on the absorbance of the donor and acceptor and the energy/wavelength of the photon. Upon absorption of a photon, a Frenkel-type exciton is created, *i.e.* an exciton which is tightly bound by Coulombic interaction as a consequence of the low dielectric constant of the organic materials (ε_r = 2–4). Subsequently, excitons which are created at a donor-acceptor interface or diffuse to an interface can undergo charge transfer (CT), driven by the energy offset between the donor's and acceptor's LUMO or HOMO levels, depending on whether donor or acceptor have been excited. The process of charge transfer is described theoretically by Marcus theory (see Section 2.4.1). For efficient solar cells, CT states have to be separated into free charges, the detailed mechanism of charge separation, however, is still under debate and reviewed in greater detail in Section 2.4. After charge separation, the extraction of charge carriers is enabled *via* a bicontinuous network of percolation pathways that connects donor and acceptor domains to their respective electrodes. In conclusion, the overall efficiency is determined by several factors including[30]

i) Fraction of absorbed photons,
ii) Exciton quenching efficiency,
iii) Charge separation/dissociation efficiency,
iv) Charge transport and extraction efficiency.

To achieve an optimal photovoltaic performance, each of the above mentioned steps involved in the process of charge generation requires careful optimization and the basic strategies are addressed in the following sections after introduction of the most important characteristics of organic solar cells.

2.2.2 Metal-Semiconductor Interface – Schottky *versus* Ohmic Contact

The interface between the electrodes and the organic layer in an organic solar cell can be described by the metal-semiconductor-metal model. If brought in contact, the Fermi levels of the two electrodes align, causing band bending in the organic layer at the interface due to Fermi-level pinning. As a consequence, Ohmic and Schottky contacts are formed depending on the work function of the metal and the energy levels of the material in contact. Figure 11 shows the four possible combinations of p- and n-type semiconductors with electrodes of high and low work function metals. If not in contact, electrode and organic material do not interact. This case is shown on the left-hand side of each panel. However, if the materials are brought into contact, Fermi levels will align. The LUMO and HOMO of the organic material are "pinned" at the metal

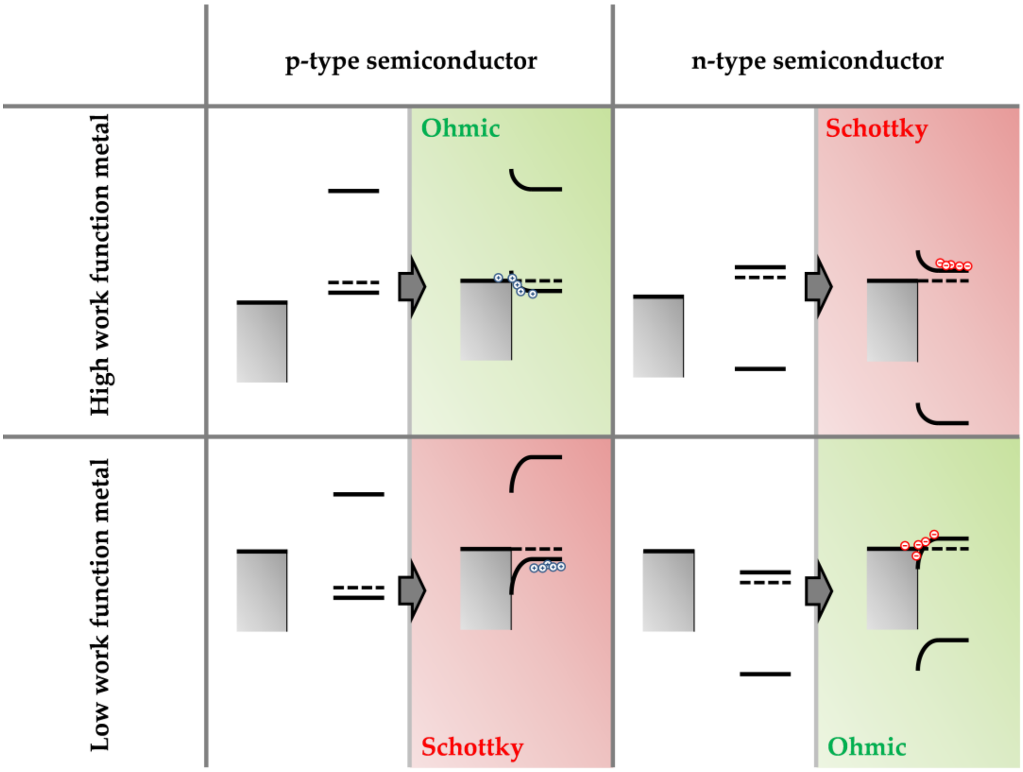

Figure 11. Metal semiconductor interface for high (upper row) and low (bottom row) work function metals in combination with p-type (left column) and n-type (right column) semiconductor. The energetics are shown without and with contact for each combination. Solid lines represent the HOMO and LUMO of the organic component, dashed lines the Fermi level. Grey bars depict the metal electrode. Red circles with minus sign stand for electrons, blue circles with plus signs for holes.

interface and band bending occurs. As a consequence, a Schottky contact is formed if a low work function metal is brought into contact with a p-type semiconductor which hinders the efficient extraction of charges. In analogy, barriers for electrons are formed if a high work function metal is brought into contact with an n-type semiconductor. Therefore, the choice of suitable electrode materials and electrode interlayers is of great importance. As holes are transported in the HOMO of the donor-type material, high work-function electrodes are used as anode material to form barrier-less, Ohmic contacts. Typically, this is indium-tin oxide (ITO) covered glass. Electrons on the other hand are located in the LUMO of the acceptor-type material and successful charge extraction at the cathode requires low-work function metals like Ca or Al to form an Ohmic contact. Additional interlayers are reported to reduce barriers for extraction as well as increase the selectivity of contacts by reducing the injection of counter-charges for recombination. For instance, the ITO contact is often covered by poly(3,4-ethylenedioxythiophene) polystyrene sulfonate (PEDOT:PSS) to improve hole extraction. For more detailed information about interfacial layers and the impact on device parameters the review by Servaites, Ratner and Marks is recommended.[34]

2.2.3 Figures of Merit

The ability of an organic solar cell to convert light to electrical energy is reflected in the current density *J* as a function of the voltage *V* und illumination conditions. The resulting graph is called *J*-*V* characteristic or *J*-*V* curve, a typical graph is depicted in Figure 12.

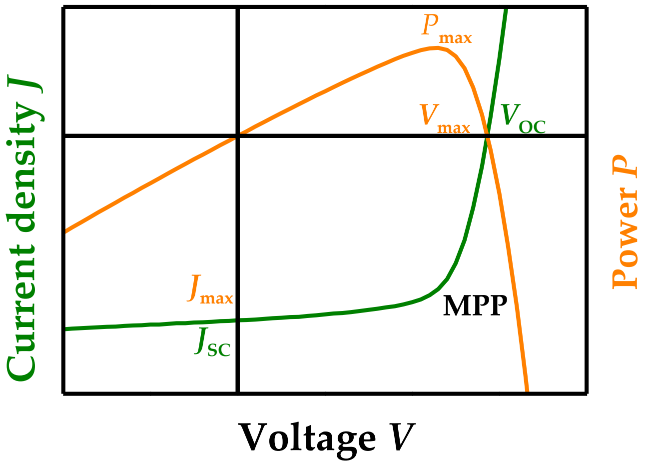

Figure 12. Typical *J*-*V* curve (green line) together with the power at each voltage (orange line) calculated from the product of current density and voltage. J_{max} is the current density and V_{max} the voltage at the maximum power point (MPP). The short-circuit current density J_{SC} is the current density at zero voltage and the open-circuit voltage V_{OC} is the voltage at zero current density. The fill factor FF corresponds to the ratio of the orange square to the green square.

The power conversion efficiency, abbreviated as PCE or η, depends on all the aforementioned processes (i–iv, Section 2.2.1, page 13) and is defined as the fraction of the electric power output P_{out} over the power of the incident light P_{in}.

$$\eta = \frac{P_{\mathrm{out}}}{P_{\mathrm{in}}} = \frac{V_{\mathrm{OC}} \times J_{\mathrm{SC}} \times \mathrm{FF}}{P_{\mathrm{in}}} \qquad \text{Equation } \mathbf{3}$$

The power output of a solar cell, P_{out}, is determined by three factors, namely the open-circuit voltage V_{OC}, the short-circuit current density J_{SC}, which gives the number of generated electrons, and the fill factor FF. The values can be found in a *J*-*V* curve as shown in Figure 12. V_{OC} is the voltage where no net current flows in the external circuit and corresponds to the maximum voltage obtainable from the device. J_{SC} is the current when the applied voltage is 0 and is the maximum current extractable from the device. The fill factor is defined as the ratio of the maximum power obtainable to the product of open circuit voltage and short circuit current.

$$\mathrm{FF} = \frac{P_{\mathrm{mpp}}}{V_{\mathrm{OC}} \times J_{SC}} = \frac{V_{\mathrm{mpp}} \times J_{\mathrm{mpp}}}{V_{\mathrm{OC}} \times J_{\mathrm{SC}}} \qquad \text{Equation } \mathbf{4}$$

The FF is limited *e.g.* by the field dependence of charge generation or extraction. If there is no field-dependence in the organic solar cell the FF might approach a value of 1. However, the FF is often limited to about 0.4 by effects like unbalanced charge transport,[35] *i.e.* very different hole and electron mobility values. Unbalanced charge transport results in a space charge limited photocurrent in turn limiting the FF. The space charge limited regime can be identified by a square-root dependence of the current on the applied voltage.[36, 37]

The short-circuit current is the current density measured at an applied bias of 0 V (where cathode and anode are directly connected) and limited by the number of absorbed photons. The open-circuit voltage is mainly determined by the energy difference between LUMO of the acceptor[38] and HOMO of the donor.[39] V_{OC} can be estimated from the HOMO–LUMO gap by taking into account the empirically found reduction of ~0.3 V which is needed to overcome the Coulombic attraction between electron and hole to form spatially separated charges.[39]

$$V_{\mathrm{OC}} = (1/\mathrm{e})(|E^{Donor}HOMO| - |E^{Acceptor}LUMO|) - 0.3\,V \qquad \text{Equation } \mathbf{5}$$

Here, e is the elementary charge. Furthermore, V_{OC} depends on radiationless losses, temperature, and the size of the interfacial area between donor and acceptor domains[40] and more recent, refined concepts take the energy of the interfacial CT state rather than the HOMO–LUMO gap into account:[41]

$$V_{\mathrm{OC}} = \frac{E_{\mathrm{CT}}}{\mathrm{q}} - \Delta V_{rad} - \Delta V_{nonrad} \qquad \text{Equation } \mathbf{6}$$

$$\Delta V_{rad} = -\frac{\mathrm{k_B}T}{\mathrm{q}} ln\left(\frac{J_{\mathrm{SC}}\mathrm{h}^3\mathrm{c}^2}{f\mathrm{q}2\pi(E_{\mathrm{CT}} - \lambda)}\right) \qquad \text{Equation } \mathbf{7}$$

$$\Delta V_{nonrad} = -\mathrm{k_B}Tln(EQE_{EL}) \qquad \text{Equation } \mathbf{8}$$

Vandewal *et al.*[41] correlate V_{OC} with the energy of the CT state E_{CT} which is determined from a fit to the CT band in the $\mathrm{EQE_{PV}}$ spectrum. Equation 6–Equation 8 show that V_{OC} depends linearly on the temperature T and logarithmically on the illumination intensity which has been confirmed in experiments. Hereby q is the elementary charge, $\mathrm{k_B}$ is Boltzmann's constant, h is Planck's constant, λ is the reorganization energy, f is a prefactor taking into account the photovoltaic $\mathrm{EQE_{PV}}$ spectrum, and c is the speed of light in vacuum. V_{OC} losses originate from radiative as well as non-radiative losses that account for ~0.25 eV and ~0.35 eV, respectively, which reduces the obtainable V_{OC} by ~0.6 eV in total with respect to the energy of the CT state. The reduction of the open-circuit voltage by a high degree of energetic disorder and a high amount of trap states has also been discussed on the basis of a Gaussian disorder model by Blakesley and Neher.[43] Very recently, Burke *et al*. presented a study in which they combined statistical mechanics as well as temperature dependent CT state absorption measurements to unravel the contributions to V_{OC} losses.[42] Figure 13 shows the losses reducing the V_{OC} emanating from electron transfer/exciton splitting, the CT binding energy, disorder, and recombination. A loss of 75–225 mV originates from interfacial disorder while recombination effects contribute with 500–700 mV to V_{OC} losses which is on a similar order as given by Vandewal *et al.*

The external quantum efficiency (EQE) is defined as the number of extracted electrons in relation to the number of incident photons at short-circuit condition as a function of the wavelength. The internal quantum

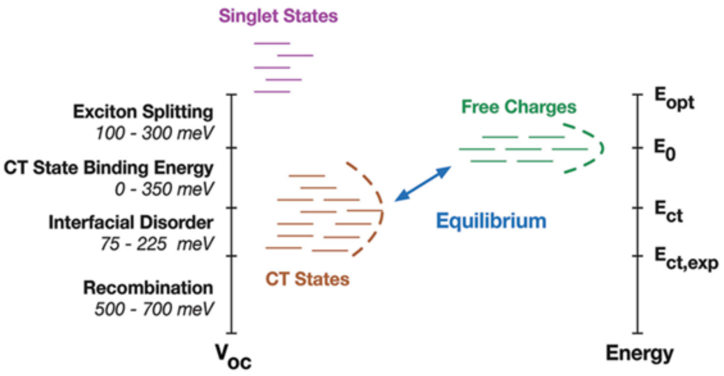

Figure 13. Contributions to losses in V_{OC} according to Burke *et al.* determined by statistical mechanics as well as temperature dependent CT state absorption measurements. Reprinted with permission from reference [42]. Copyright (2015) WILEY-VCH Verlag & Co. KGaA, Weinheim.

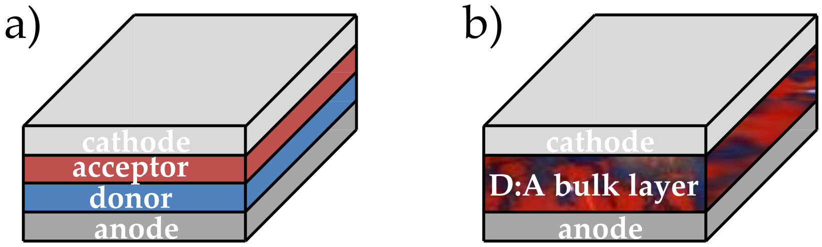

Figure 14. Schematic representation of a) bilayer and b) bulk heterojunction device architecture. Electrons are extracted at the cathode and holes at the anode.

efficiency (IQE) is the EQE under consideration of the absorption of the active layer of the solar cell. The absorption is corrected for effects like parasitic absorption, scattering effects as well as reflection of incident light at the electrodes. These effects can be taken into account *e.g.* by the application of a transfer matrix approach.[44] The IQE gives the photon-to-charge conversion efficiency and is always larger than the EQE.

$$\mathrm{EQE} = \frac{electrons_{out}}{photons_{in}} \qquad \text{Equation } \mathbf{9}$$

$$\mathrm{IQE} = \frac{electrons_{out}}{photons_{absorbed}} = \frac{electrons_{out}}{photons_{in}(\lambda) \times abs(\lambda)} \qquad \text{Equation } \mathbf{10}$$

The IQE is important with respect to two questions. Firstly, if donor and acceptor molecules show complementary absorption profiles, the IQE gives information to which extent both components of the blend contribute to the efficiency of an organic solar cell. Secondly, the wavelength/photon energy dependence of the IQE measurements can help to answer the question whether higher excited states contribute stronger to the device efficiency than relaxed charge-transfer states. The question of excess energy and the correlation with CT state dissociation is discussed in more detail in Section 2.4.4.5.

2.2.4 Development of the Efficiency

The first organic solar cell published by Tang and co-workers in 1986 was a bilayer structure consisting of a 30 nm layer of copper phthalocyanine as electron donor and a 50 nm layer of a perylene tetracarboxylic derivative as electron acceptor.[45] A total power conversion efficiency of about 1% was achieved and consequently drew immense attention to the emerging technology of organic photovoltaics.

Later, Sariciftci *et al.* were the first to demonstrate the suitability of fullerenes, namely C_{60}, as electron accepting materials in OPV in 1993.[46] Fullerenes offer a variety of beneficial properties like isotropic electron transport, a multiple degeneration of the LUMO level as well as advantageous molecular packing.

A major breakthrough in the field of organic photovoltaics was achieved with the invention of the bulk heterojunction device architecture by Yu *et al.* and Halls *et al.* in 1995. [47, 48] In this approach the donor and acceptor phases are not stacked on top of each other, but are intimately mixed which in turn increases the donor-acceptor interface. In the first devices [6,6]-Phenyl C61 butyric acid methyl ester, shortly $PC_{61}BM$, which is a soluble derivate of C_{60} developed by Hummelen *et al.* in the same year,[49] functioned as the electron acceptor.

Since then, the development of novel electron donating polymers and small molecules has determined the development of OPV in combination with the ubiquitous electron acceptors $PC_{61}BM$ and $PC_{71}BM$. Important milestone in the development of donor polymers include thiophene derivatives, especially regioregular poly(3-hexylthiophen-2,5-diyl), abbreviated as P3HT,[50] the carbazol-*co*-thiophenediyl-2,1,3-benzothiadiazole polymer PCDTBT[51] and low-bandgap polymers like polythieno[3,4-*b*]-thiophene-*co*-benzodithiophene, known as PTB7,[52] which lead to a steady increase in PCE. Molecular structures are shown in Figure 15.

Figure 16 is a graph supplied by the National Renewable Energy Laboratory (NREL) that shows the relevant development of different OPV technologies. The PCE values have been improved in ongoing research efforts and very recently the benchmark of 10% was overcome by a combination of the low-bandgap donor polymer PffBT4T-2OD and different fullerene derivatives, namely $PC_{61}BM$, $PC_{71}BM$, and $TC_{71}BM$, yielding PCE values of 10.4%, 10.5% and 10.8%, respectively.[4] The chemical structures are shown in Figure 17.

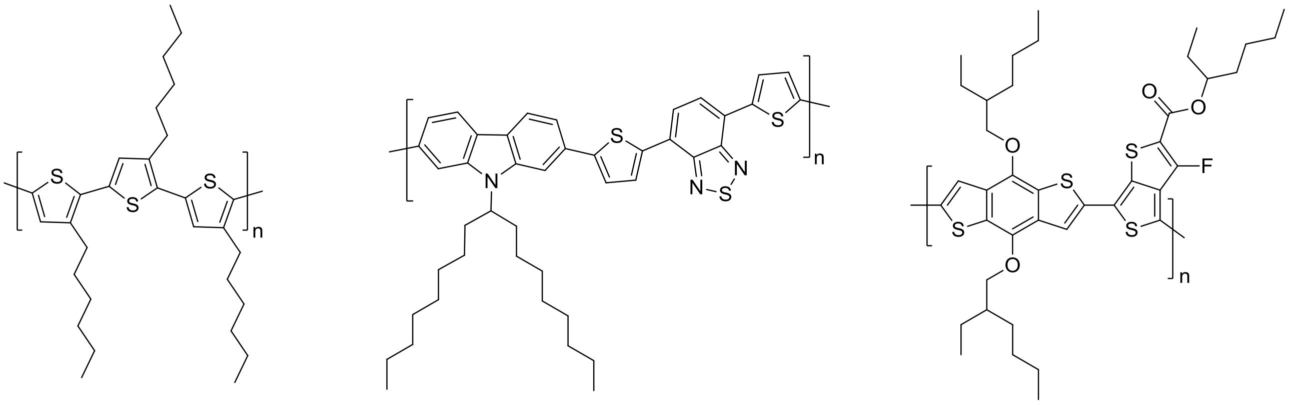

1 (P3HT) **2** (PCDTBT) **3** (PTB7)

Figure 15. Chemical structures of P3HT, PCDTBT, and PTB7 important steps in the development of donor polymers.

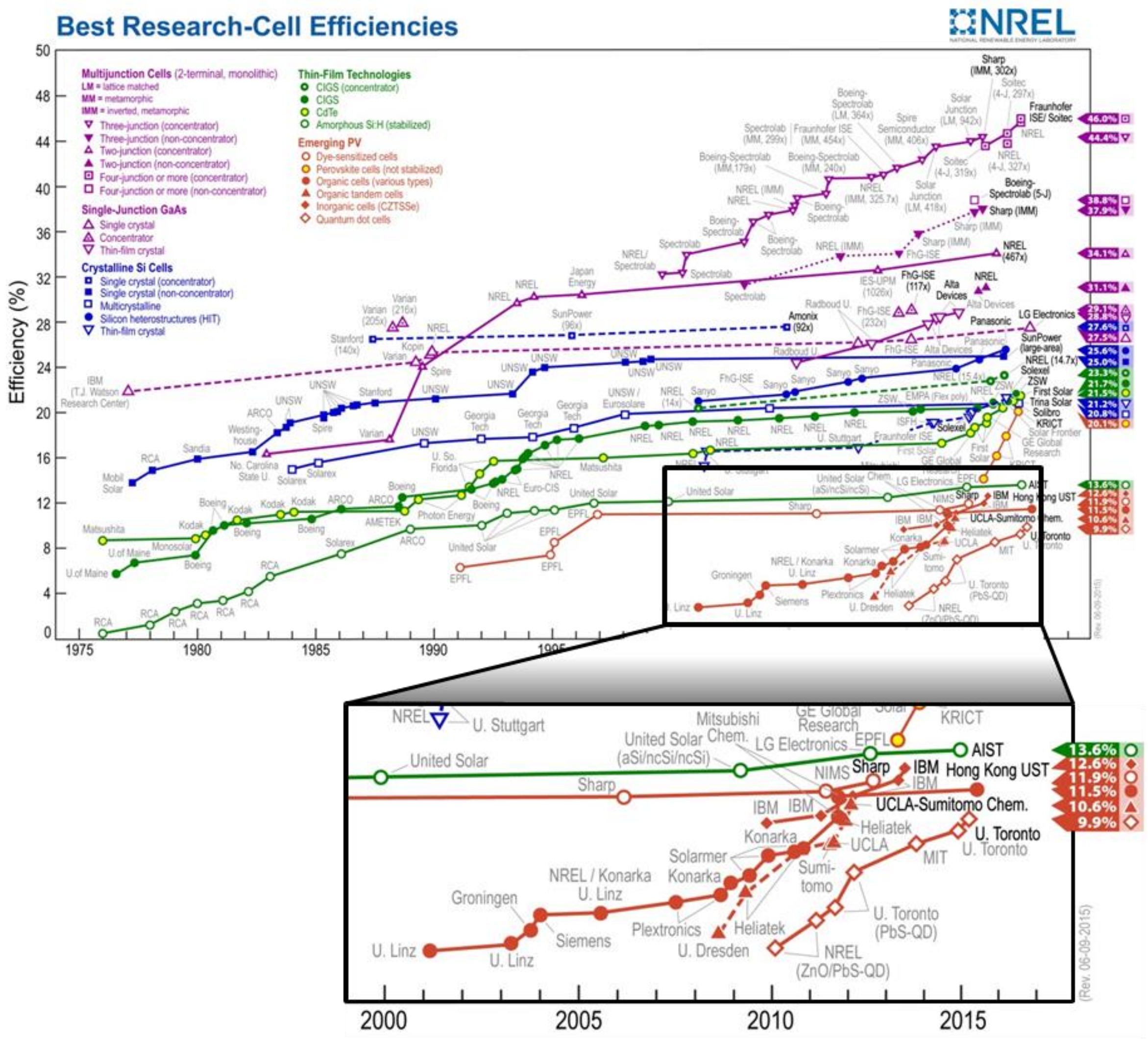

Figure 16. National Renewable Energy Laboratory (NREL) efficiency table summarizing the recent development of solar cells. Filled orange circles show the development of organic cells.[53]

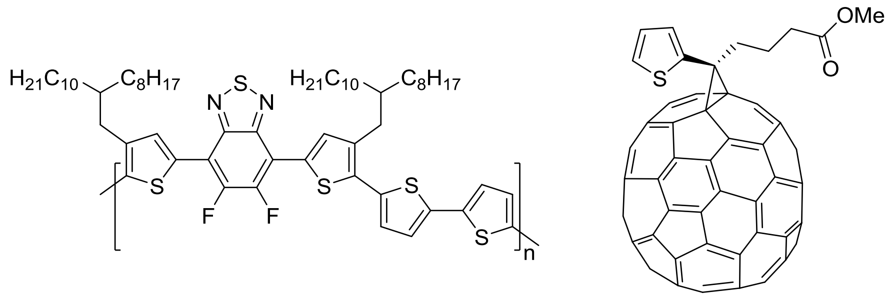

4 (PffBT4T-2OD)

5 ($TC_{71}BM$)

Figure 17. Record single junction device utilizing PffBT4T-2OD as donor polymer and $TC_{71}BM$ as electron acceptor resulting in an optimum PCE of 10.8%.[4]

2.3 Loss Mechanisms

The figures of merit, which were discussed in the previous section, are limited by a series of factors in the cascade of processes which lead from photon absorption to charge extraction. The different loss channels are presented in the following sections.

2.3.1 Exciton Decay

For efficient charge generation, photogenerated excitons have to reach a donor-acceptor interface by diffusion where they undergo charge transfer. However, excitons might decay before reaching a heterojunction which is governed by two factors: Firstly, the size of pure D and A domains is crucial, as exciton quenching is limited to the D-A interface. Secondly, an important measure is the exciton diffusion length L_D which gives the length an exciton can migrate before it decays to the ground state and this in turn determines the maximal donor or acceptor domain size. L_D depends strongly on the material systems and their trap density. Typical values for L_D are reported to be in the range of a few nanometers (3 nm) up to 20 nm.[32, 54-56] Often, L_D is determined with photoluminescence quenching experiments (PL intensity as well as PL lifetime) which are modeled by application of the Stern-Vollmer equation but also time-resolved microwave conductivity measurements can be utilized to determine the diffusion coefficient and hence the exciton diffusion length.[54] For example, values reported for the ubiquitous donor polymer P3HT range from 4 nm,[54] 2.6–5.3 nm[55] to 8.5 nm.[56]

2.3.2 Geminate Recombination

The exciton quenching at the donor-acceptor interface and the subsequent electron transfer from the donor to the acceptor results in the formation of a CT state as described earlier in Section 2.2.1 (see step ii in Figure 10) and in more detail later in Section 2.4.1. The question if and how this CT state can be dissociated is still under debate and will be the focus of Section 2.4. The recombination of CT states that do not manage to overcome their mutual Coulomb attraction and decay back to the ground state (GS) follows a monoexponential decay behavior as shown in Equation 11.

$$CT(t) = N_0 \exp(-k_{\mathrm{CT}\to\mathrm{GS}} t) \qquad \text{Equation } \mathbf{11}$$

The amount of CT states as a function of time t, depends on the amount of initially generated CT states N_0 and the rate of geminate recombination $k_{\mathrm{CT}\to\mathrm{GS}}$. The process of geminate recombination involves exclusively CT pairs which were not separated and consequently their decay behavior does not depend on the excitation intensity which translates into the excited-states density. A high fraction of geminate recombination will result in a reduced short-circuit current density[57] and is also detrimental for the open-circuit voltage.[42]

2.3.3 Non-geminate Recombination

The recombination of free charge carriers at the donor-acceptor interface is called non-geminate recombination. This type of recombination follows ideally a Langevin-type, bimolecular recombination behavior and the decay of spatially separated charges (SSC) as a function of time can be described by Equation 12.[57]

$$SSC(t) = \left(\lambda\gamma t + (N_0)^{-\lambda}\right)^{-1/\lambda} \qquad \text{Equation } \mathbf{12}$$

Where λ gives the order of recombination, γ is the bimolecular recombination rate, and N_0 is the charge carrier density. A simulation of bimolecular recombination for excitation density values which are typical for spectroscopic experiments is shown in Figure 18.

Classic Langevin-type recombination is bimolecular, meaning that $\lambda+1$ equals 2. However, this value often deviates and shows higher values in experiments. Deibel and co-workers assigned this observation to 'dynamic trapping of charges in the tail states of the Gaussian density of states'.[58] Additionally, the high recombination order was found to originate from charge-carrier density dependent mobility.[59] Also Kirchartz *et al*. identified the recombination *via* traps and a localized tail in the density of states (DOS) as reason for recombination on the order exceeding 2.[60]

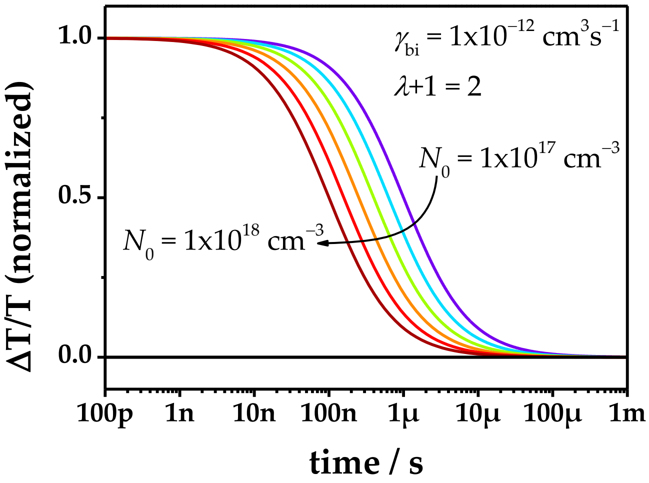

Figure 18. Simulated bimolecular recombination ($\lambda + 1 = 2$) shown at an excited-state density ranging from 10^{17}–10^{18} cm^{-3} with a bimolecular recombination rate of 10^{-12} cm^3 s^{-1}.

2.4 Concepts for Charge Transfer and Charge Separation

2.4.1 Marcus Theory for the Description of Charge Transfer

A theoretical description of charge separation was presented by Marcus in 1956[61] and a comprehensive review was given by Clarke and Durrant.[32] Marcus chose a semiclassical approach in which the motion of nuclei is considered to be slow and is therefore treated classically. On the other hand, the fast movement of electrons is assumed to be decoupled from the nuclear motion as postulated by Born-Oppenheimer approximation and treated quantum mechanically. Marcus theory describes the states which are involved in charge transfer, namely the ground state D-A, the excited state D*-A, and the charge-transfer state D^+-A^- as harmonic oscillators (parabolas). To avoid confusion with terminology, it should be stated clearly that the product outcome of electron transfer which is described by Marcus theory is not (necessarily) a charge-separated state in the sense that charges have overcome their mutual Coulomb attraction but may still be

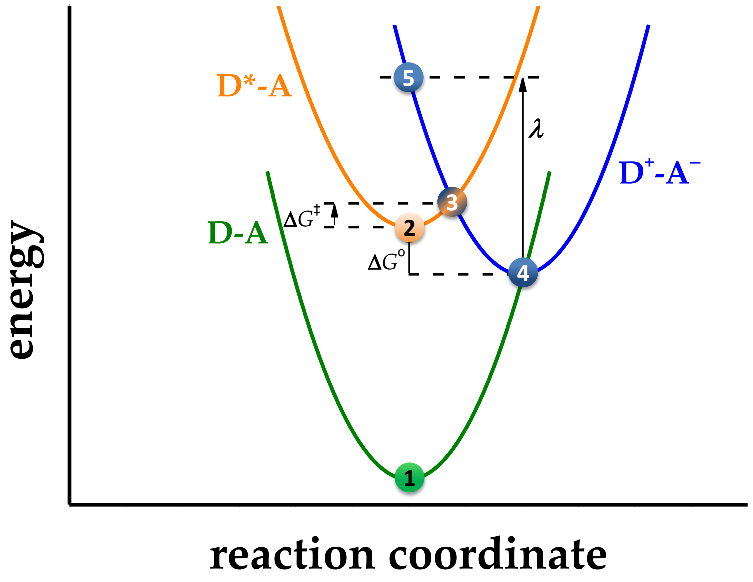

Figure 19. Schematic description of Marcus theory with energy potential surfaces for the ground state in which donor and acceptor are in their neutral states (green parabola), excited donor state (orange parabola) and charge-transfer state in which an electron was transferred from the donor to the acceptor (blue parabola). Upon photon absorption by the donor the system is excited from the ground state (D-A) to the excited state (D*-A). The activation energy $\Delta G^‡$ for charge transfer corresponds to the energy difference between the minimum of the excited state (2) and the crossing point with the potential surface of the excited and the charge-separated (3) state. The reorganization energy λ is the energy difference between the minimum of the charge-transfer state (4) and the energy of the charge-transfer state at the reaction coordinate corresponding to the minimum of the excited state (5).

confined to the donor-acceptor interface. The process of charge transfer is considered to be non-adiabatic, so that the potential surfaces intersect and thus show isoenergetic points as a function of the reaction coordinate. A schematic illustration is shown in Figure 19.

The absorption of a photon excites the donor-acceptor system from the ground state D-A to the excited state D*-A according to the Franck-Condon principle discussed earlier in Section 2.1.2. Charge transfer can be understood as the reaction of the reactant D*-A to the product D^+-A^- and is only feasible if a vertical transition is possible which is given at point 3 in Figure 19. At this nuclear configuration, the energy of the reactant equals the energy of the product. The energy difference between the reactant state's minimum (2) and the energy of the reactant-product transition (3) is the activation energy $\Delta G^{\ddagger}$, which can be described as a function of the free enthalpy, *i.e.* Gibbs free energy ΔG^0, and the reorganization energy λ which corresponds to the energy difference between the product's minimum (4) and the product's energy after electron transfer (5) from the reactant's minimum (2) without nuclear motion:

$$\Delta G^{\ddagger} = \frac{(\lambda + \Delta G^0)^2}{4\,\lambda}$$

Equation **13**

The Gibbs free energy is the energy difference between the minima of the parabolas representing reactant and product (positions 2 and 4 in Figure 19). The reorganization energy consists of two contributions, namely inner and outer reorganization energy, which refers to nuclear motion of the system (which is, again, much slower than the electronic events) and the reorganization of solvent dipoles which become necessary due to changes in polarization between the reactant and product state.

Furthermore, the rate constant for electron transfer k_{ET} can be obtained from Marcus theory by the following equation:

$$k_{\mathrm{ET}} = \frac{2\pi}{\hbar\sqrt{4\pi\lambda \mathrm{k_B} T}} V^2 exp\left(-\frac{(\lambda + \Delta G^0)^2}{4\lambda \mathrm{k_B} T}\right)$$

Equation **14**

The electron transfer rate depends on the electronic coupling between reactant and product state which is described with the matrix element term V. Moreover, k_{ET} is a function of the reorganization energy λ, the Gibbs free energy ΔG^0 and the temperature T. Note that the exponential expression is a Gaussian normal distribution and is maximal if the argument of the exponent is zero, which is when λ equals $-\Delta G^0$. As a consequence, k_{ET} becomes slower for ΔG^0 that surpass λ. This regime, which might be counterintuitive at first, is known as Marcus inverted region and was verified for different material systems and also shown to be valid for certain photovoltaic systems. Very recently, Ward *et al.* have shown with time-resolved fluorescence experiments that electron transfer occurs within less than 2 ps for Gibbs free energy between 0.2 eV and 0.6 eV and with slower electron transfer rates outside of this range for combinations of the donor polymer PTB7 with a set of different acceptors. From their experiments a reorganization λ of ~0.4 eV was deduced which is the driving force where the highest electron transfer rate was observed as shown in Figure 20.[62]

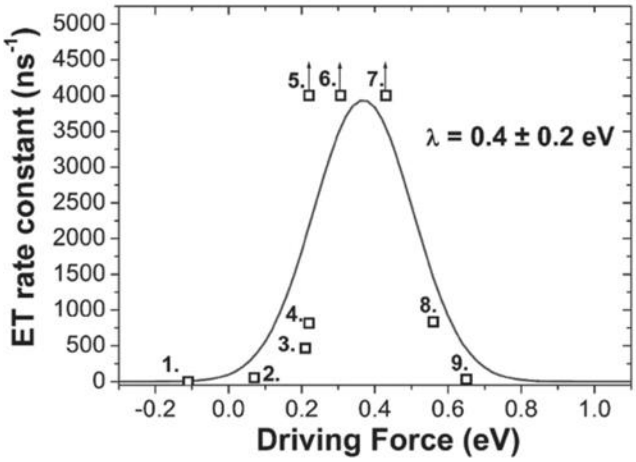

Figure 20. Electron transfer rate k_{ET} as a function of the driving force with a set of nine different acceptors (open squares) and a fit with a reorganization energy of 0.4 eV. Reprinted with permission (open access) from reference [62]. Copyright (2015) the authors.

2.4.2 Coulomb Binding Energy and Charge Separation

The previous section described the process of charge transfer, which is the quenching of the initially formed exciton located on donor or acceptor sites, at the donor-acceptor interface. However, CT states might still feel their mutual Coulomb attraction and are therefore confined to the site at the D-A interface where they were generated. A variety of theories exists to explain how the mutual Coulomb attraction between electron and hole that captures the photogenerated charge pair at the donor-acceptor interface is overcome. The Coulomb attraction E_{CB} is calculated according to the following equation:[32]

$$E_{\mathrm{CB}} = \frac{\mathrm{e}^2}{4\pi\varepsilon_{\mathrm{r}}\varepsilon_0 r} \qquad \text{Equation } \mathbf{15}$$

The magnitude of the Coulomb attraction depends on the elementary charge e, vacuum permittivity ε_0 and is influenced by the relative dielectric constant of the surrounding medium ε_r as well as the electron-hole distance r and typically ranges from 100 to 500 meV. A surface plot of the Coulomb binding energy E_{CB} as a function of the electron-hole distance and the relative dielectric constant is shown in Figure 21. However, the thermal energy at room temperature is only 25.7 meV.

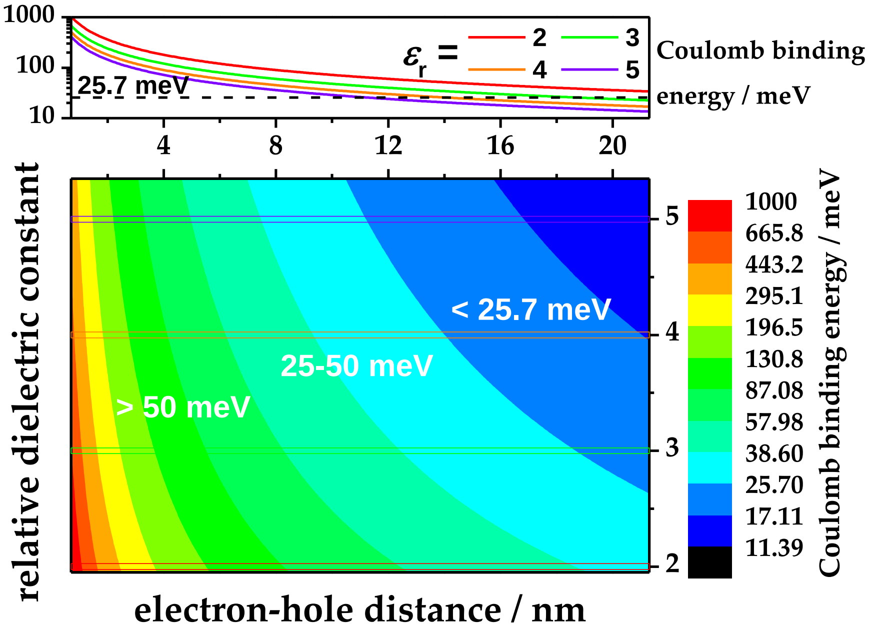

Figure 21. Coulomb binding energy of an electron-hole pair as a function of the electron-hole distance and the relative dielectric constant of the medium. Only electron-hole pairs of the blue areas possess a Coulomb binding energy which is smaller than the thermal energy at room temperature (= 25.7 meV; dashed line in the upper panel). Electron-hole pairs in the region with cyan to red color show binding energy values exceeding thermal energy at room temperature.

As a consequence, thermal energy at room temperature is not sufficient to overcome the mutual Coulomb attraction unless the electron-hole distance is sufficiently large which is *e.g.* 14 nm at $\varepsilon_r = 4$ and 18.6 nm at $\varepsilon_r = 3$. Different concepts which have been developed to explain charge separation and how the Coulomb attraction is overcome are discussed in the following sections.

2.4.3 The Onsager-Braun Model *vs.* Ultrafast Charge Separation

The Onsager-Braun model, developed in the 1980s by Braun[63], is often used to describe the dissociation of charge transfer states in organic thin films. The model is based on the description of the separation and recombination of ions in solution by Onsager dating back to 1938.[64] A major drawback of the Onsager-Braun model is the unrealistic morphology of the films, *i.e.* the assumption of having equally distributed donor and acceptor molecules instead of a phase-separated nanomorphology. A schematic illustration of the Onsager-Braun model and the alternative concept of ultrafast charge generation is depicted in Figure 22.

The Onsager-Braun model explains the cascade of photophysical processes triggered by photon absorption as follows: Firstly, a tightly bound exciton is created. Secondly, excitons are quenched at the donor-acceptor interface to form 'hot' CT states with a certain electron-hole distance depending on the excess energy, which then relax within ~100 fs to 'cold' CT states. Thirdly, electrons and holes diffuse *via* a hopping mechanism within the organic material which results in either a) their encounter and subsequent instant, geminate recombination or b) the diffusion of oppositely charged charge carriers away from each other so that they finally overcome their mutual Coulomb attraction and are regarded as spatially separated. This process depends on the electric field F and the temperature T and is limited by the lifetime of the CT state, *i.e.* a longer CT state lifetime increases the chances to separate CT states. This is expressed in Equation 16–Equation 19. Finally, spatially separated charges (SSC) can be collected at the respective electrodes or recombine non-geminately *via* CT states back to the ground state. Recombination and separation events can be described by their respective rate constants k_r and k_{dis}, respectively. As these two processes compete with each other, the fraction of charge separation P can be expressed by the following equation:

$$P(F,T) = \frac{k_{\mathrm{dis}}(F,T)}{k_{\mathrm{dis}}(F,T) + k_r}$$ Equation **16**

The dissociation rate k_{dis} depends on field and temperature as shown in the following equation:

$$k_{dis}(F,T) = \nu \exp\left(\frac{-\Delta E}{\mathrm{k_B}T}\right)\left(1 + b + \frac{b^2}{3} + \frac{b^3}{18} + \cdots\right)$$ Equation **17**

Where, $$\nu = \frac{3\langle\mu\rangle\mathrm{e}}{4\pi\langle\varepsilon_r\rangle/\varepsilon_0 a^3}$$ Equation **18**

and $$b = \frac{\mathrm{e}^3 F}{8\pi\langle\varepsilon_r\rangle\varepsilon_0 \mathrm{k_B^2} T^2}$$ Equation **19**

Here, ΔE is the Coulomb energy, which is the barrier for CT dissociation. The summation is an approximation based on a so-called Bessel function, which is a cylinder function and used to solve diffusion problems on a lattice. The parameter a describes the thermalization length, which is the distance between electron and hole after dissociation. As mentioned above, the organic thin film is treated as a homogeneous medium and as a consequence, $\langle\mu\rangle$ and $\langle\varepsilon_r\rangle$ represent spatially averaged values for the charge carrier mobility and the relative dielectric constant.

The limitation of the Onsager-Braun model is that it does not account for ultrafast charge generation, which is, however, often observed in organic solar cells. Furthermore, charge separation occurs on a timescale dictated by the hopping rate, *i.e.* in the range of nanoseconds, *via* the electronically and vibrationally lowest excited state. It is often debated whether or not excess energy of CT states (not to be confused with excess energy of the initially generated exciton) is necessary for efficient charge separation and addressed in more detail in Section 2.4.4.5.

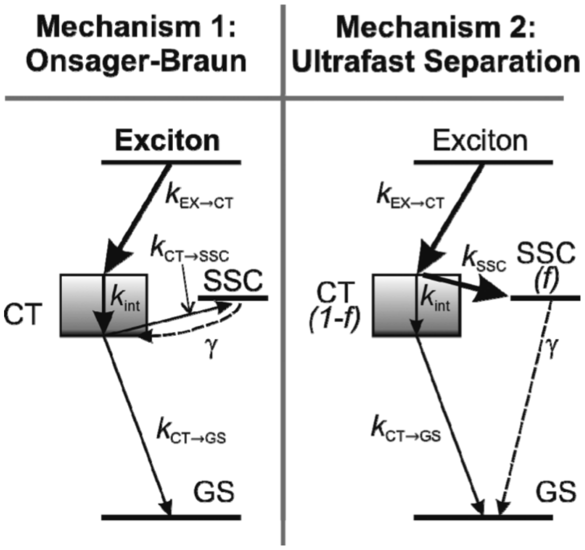

Figure 22. Models for charge separation: *Mechanism 1* depicts the Onsager-Braun model, where excitons located on the donor or acceptor form charge-transfer (CT) states at the donor-acceptor interface and relax to the vibrationally and electronically lowest CT state. Subsequently, CT states might recombine geminately to the ground state (GS) or dissociate to form spatially separated charges (SSC) which recombine non-geminately to the GS *via* CT states. *Mechanism 2* describes the concept of ultrafast charge separation. In this theory, excitons form CT states at the interface which are labeled as 'hot' due to excess energy. Hot CT states might either relax to 'cold' CT states or directly generate SSC. CT states and SSC then recombine geminately or non-geminately, respectively, to the GS. The fraction *f* of SSC is determined on a sub-100 fs timescale. Reprinted with permission from reference [57]. Copyright (2010) American Chemical Society.

If the process of charge separation is assessed as an ultrafast process and occurs prior to thermal relaxation of excited CT states, the formation of separated charges originates from hot CT states. The model itself does not comment on the origin of ultrafast charge separation. Concepts under debate include larger electron hole distances in the wave function of higher excited CT states[65], and the direct conversion of excess energy in kinetic energy of the electron and hole.[66]

2.4.4 Influences on Charge Generation

2.4.4.1 Conjugation

Many factors have been analyzed and turned out to influence charge separation. Among these factors, an improved conjugation of the donor polymer was identified to improve charge separation.[67] For this purpose, a series of poly-(paraphenylene)s (see structures **6–8** in Figure 23) was investigated by electronic measurements. A strong field was applied to the investigated solar cells which was sufficiently high to

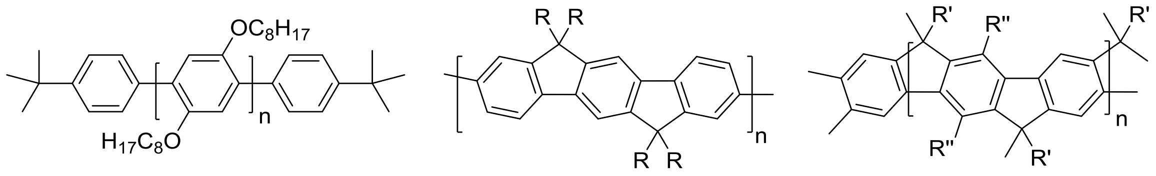

6 (DOOPPP) **7** (PIF) **8** (MeLPPP)

Figure 23. Poly-(paraphenylene)s with increasing conjugation from DOOPPP to PIF to MeLPPP. (R = 2-ethylhexyl, R′ = 1,4-C_6H_4-*n*-$C_{10}H_{21}$, R′′ = *n*-C_6H_{13})

collect all charge carriers. The required field to obtain saturated currents decreased with the conjugation of the system. Additionally, this effect was observed for different electron acceptors.

The authors argued that charges in a pointlike picture require a distance of around 10 nm for spatial separation. Furthermore, a more rigid backbone will reduce scattering by conformational disorder and hence increase the coherence length and coherent motion of the carrier. Also, a larger coherent length results in a larger oscillation of the hole on the polymer chain segments and therefore enhances the electron-hole separation. Consequently, the critical spatial separation might be achieved more easily.

However, more rigid structures could also improve other factors which govern the spatial separation of CT states. For example, more rigid structures tend to show a higher degree of crystallinity which in turn results in both higher charge carrier mobility and changed energetic levels that could drive charges away from the donor acceptor interface by the formation of so-called ‘energetic sinks’.[68] Both factors, mobility and the altered energy landscape, are reported to improve charge separation and are discussed in the sections 2.4.4.3 and 2.4.4.4.

2.4.4.2 Coherent Processes

Heeger and co-workers presented results from transient absorption spectroscopy of different material combinations and showed ultrafast charge generation within the temporal resolution of their setup.[69] The explanation for this ultrafast charge generation is that the initial exciton which is formed upon absorption of a photon has a spatial extension of ~20 nm and is delocalized over a large number of chromophoric units. This rather high value originates from the treatment of the photon according to Heisenberg’s uncertainty principle stating that the more precisely the momentum of a particle is determined, the less precisely its position can be known. Moreover, the photo-excited state which is created is also uncertain and therefore the position is not unique but a delocalized, spatially extended wave function. The delocalization on the basis of coherence is seen as key driver for efficient charge separation on an ultrafast timescale.

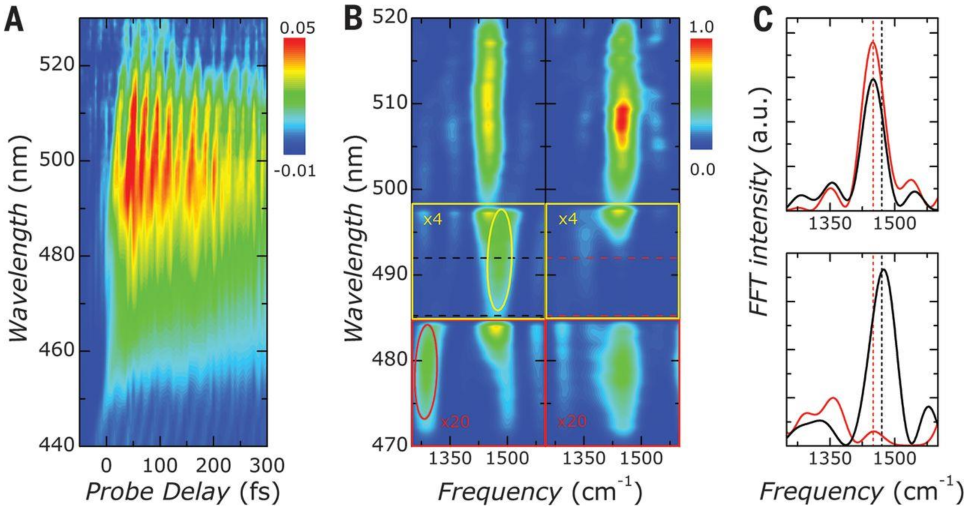

Figure 24. A) "Experimental differential transmission ΔT/T map of the P3HT:PCBM blend as a function of probe delay and probe wavelength. The pronounced oscillations in the ΔT/T signal reflect coherent vibrational wave-packet motion initiated by the short pump pulse. B) Fourier transform spectra of the ΔT/T dynamics of the blend (left) and pristine P3HT (right). The spectral intensity is amplified by a factor of 4 for $\lambda = 498$ to 485 nm and by a factor of 20 for $\lambda = 485$ to 470 nm. C) Integrated Fourier transform spectra for $\lambda = 520$ to 498 nm (top) and $\lambda = 492$ to 485 nm [bottom, dashed lines in (B)] of the blend (black) and pristine P3HT (red). The dashed vertical lines indicate the frequency of the P3HT C=C stretch mode (red) at 1450 cm^{-1} and pentagonal-pinch mode of the fullerene (black) at 1470 cm^{-1}."[71] Reprinted with permission from reference [71]. Copyright (2014) American Association for the Advancement of Science.

The effect of delocalization was also considered by Gagorik *et al.*[70] who chose a kinetic Monte Carlo (KMC) approach to explain charge separation. The authors propose that energetic barriers, namely Coulomb interactions, are reduced and thus charge separation is enhanced. Moreover, the authors argue that the probability to escape interface traps is increased.

Lienau and co-workers understand the process of ultrafast charge separation within 50–70 fs as a coherent vibrational motion of the fullerene after excitation of the polymeric donor.[71] They investigated the prototypic P3HT:PCBM system by ultrafast, time-resolved pump-probe spectroscopy and performed time-dependent density functional theory (TDDFT) calculations. Figure 24 A) shows the experimental data on the timescale of hundreds of femtoseconds. For the analysis, the observed oscillations on the sub-100 fs timescale were Fourier transformed and frequencies with 1450 cm^{-1} and 1470 cm^{-1} were identified. These frequencies were assigned to the C=C stretching of P3HT and the so-called pentagonal-pinch mode of PCBM, respectively, proving the ultrafast coherent charge transfer.

2.4.4.3 Mobility

High charge mobility is frequently discussed as key driver for the spatial separation of CT states. To understand the charge transport in disordered organic materials, it is advisable to have a look at classical semiconductors first. The density of states (DOS) of a semiconductor is described best with band structures of parabolic shape as shown in Figure 25 a. The lower, occupied energetic state is named valence band, the higher, unoccupied state is called conduction band. Semiconductors possess a defined bandgap E_g which corresponds to the energy difference between the energy of the valence band E_v and the energy of the conduction band E_c. If E_g is sufficiently small, a certain amount of charges is promoted from the valence band to the conduction band at room temperature. Electrons in the conduction band are delocalized, highly mobile and as a consequence the semiconductor shows electrical conductivity. Additional factors like doping and electric fields affect the behavior of charges in semiconductors.

On the contrary, the behavior and thus the model used for organic semiconductors differ. A theoretical description is given by the Gaussian Disorder Model (GDM) which describes the organic material with a certain density of states ρ (DOS) as a function of the energy E. The DOS depends on the energy at the center of the DOS E_c and the standard deviation of the Gaussian profile σ.[72] σ itself depends on the molecular properties, the arrangement of the molecules in the solid state which in turn also determines the surrounding environment and can be regarded as a measure for the disorder of the polymer.

$$\rho(E) = \frac{1}{\sqrt{2\pi\sigma^2}} exp\left[-\frac{(E-E_c)^2}{2\sigma^2}\right] \qquad \text{Equation } \mathbf{20}$$

The charge transport is understood as incoherent hopping of electrons from occupied to unoccupied

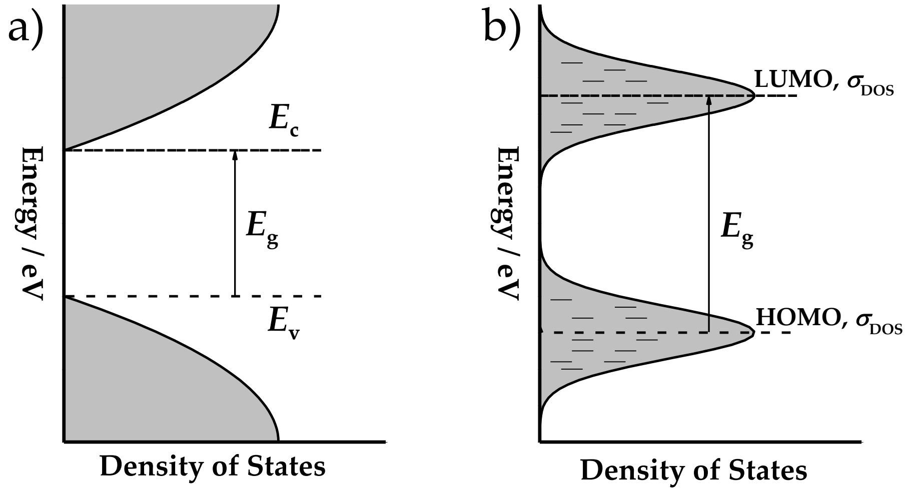

Figure 25. a) Parabolic density of states as observed in semiconductors and single crystals and b) Gaussian density of states according to the Gaussian disorder model.

localized sites and the hopping rate can be calculated according to Miller-Abrahams (Equation 21):[73]

$$v_{i,f} = v_0 exp\left(-\alpha\Delta r_{i,f}\right)\begin{cases} exp\left(-\frac{E_f - E_i}{\mathrm{k_B}T}\right) & , E_i < E_f \\ 1 & , E_i \geq E_f \end{cases}$$

Equation **21**

Here $\nu_{i,f}$ is the hopping rate from the initial site i to the final site f. ν_0 is the frequency of hopping attempts, α the inverse localization radius and $\Delta r_{i,f}$ the distance between the initial and final site. If the hop is upwards in energy, *i.e.* if the initial site energy is lower than the final site energy ($E_i < E_f$), the hopping rate is additionally altered by a Boltzmann factor, wherein E_i and E_f are the energies of the respective sites, $\mathrm{k_B}$ is the Boltzmann constant and T the temperature. If the jump is downhill, the factor is set to 1. This model takes into account the dependence of the hopping rate on the distance between two sites which results in a slower rate at higher distance. A consequence of the model for the hopping rate according to Miller-Abrahams is the trapping of charge carriers in low energetic sites as charge carriers easily access sites which are low in energy, their escape, however, is limited by thermal activation. Trapping of charge carriers is pinpointed as a possible loss channel in organic solar cells and so-called multiple trapping and release models have been developed, originally applied to hydrogenated amorphous silicon (a-Si:H),[74] and later applied to organic materials to explain charge transport in field-effect transistor devices.[75]

With Monte Carlo simulations Equation 22 can be deduced from the GDM and the trapping and release model to describe the mobility for macroscopic charge transport as a function of the temperature T and the electric field F. Important parameters in this equation are the mobility at zero-field and infinite temperature μ_0, the width of the Gaussian profile σ, the distribution of jump distances Σ, and the empirically determined constant $C_0 = 2.9 \times 10^{-4}$ (cm V^{-1})$^{0.5}$.

$$\mu(T,F) = \mu_0 \times exp\left[-\left(\frac{2\sigma}{3\mathrm{k_B}T}\right)^2\right] \times exp\left[C_0\sqrt{F}\left(\left(\frac{\sigma}{\mathrm{k_B}T}\right)^2 - \Sigma^2\right)\right]$$

Equation **22**

Mobility is also a parameter present in the Onsager-Braun model (see Equation 18, Section 2.4.3) where a higher average mobility increases the dissociation rate due to an increase in the attempt frequency ν. To further determine the influence of the mobility, Burke *et al.* employed kinetic Monte Carlo (KMC) simulations to investigate the process of charge separation at the donor acceptor interface under the assumption of initially high local charge carrier mobility.[76] An important advantage of the KMC simulation compared to the Onsager-Braun model is that the investigated morphology is more realistic, *i.e.* not a homogeneous, one-phase system but a phase-separated thin film morphology that serves as the basis of the calculations. The assumption of initially higher mobility is backed up by time resolved terahertz conductivity measurements that suggest high charge-carrier mobility exceeding 1 cm^2 (Vs)$^{-1}$.[77] This is in contrast to mobility values determined by other methods like the time-of-flight (TOF) technique or space-charge limited current (SCLC) which are limited by the macroscopic transport of charge carriers which are relaxed within the density of states through devices with hundreds of nanometers or even micrometer thick layers. Consequently, mobility values extracted from these equilibrated systems do not reflect the situation of in-situ generated charges at the donor-acceptor interface and therefore may not be relevant for the initial process of CT state dissociation. The simulation by Burke *et al.* considers that a CT state at the donor-acceptor interface undergoes several attempts to overcome its Coulomb attraction of which each attempt has a certain probability to be successful. On the basis of the high local mobility, the number of attempts is considerably increased and thus the overall charge-separation probability is improved. KMC simulations resulted in a separation efficiency of more than 40% considering a hole mobility of 4 cm^2 (Vs)$^{-1}$, an electron mobility of 4×10^{-5} cm^2 (Vs)$^{-1}$ and a lifetime of the CT state of 5 ns. In addition to the high charge carrier mobility, energetic offsets originating from the coexistence of pure and intermixed donor and acceptor phases were taken into account. Given the set of parameters mentioned before, a realistic energetic offset of 200 meV results in a splitting efficiency of more than 90% which is in perfect agreement with the high IQE values often observed in OPV devices.

Also Blom and co-workers identified a higher mobility in P3HT:PCBM devices after thermal annealing as the main explanation for increased efficiency of annealed devices.[36] Importantly, the increase in power conversion efficiency is strongly related to an increase in dissociation efficiency. However, a higher mobility will also improve charge transport through the sample and thus charge extraction. A more balanced charge transport reduces the chance of space-charge limit which is observed when electron and hole mobility differ by more than two orders of magnitude.

2.4.4.4 The Role of Intermixed Phases

Intermixed phases and the energetic offset between intermixed and pure domains has been shown to provide the driving force for efficient charge generation. It is reported that a higher degree of crystallinity in semiconducting materials will alter the energetic landscape. For instance, studies about P3HT report a shift of the ionization potential or HOMO by 50 meV,[78] 150 meV,[79, 80] and 300 meV[81] for amorphous to crystalline P3HT. The shifts were determined by cyclic voltammetry[78, 80], computational models based on classical and quantum simulation methods,[79] and ultraviolet and x-ray photoelectron spectroscopy in combination with absorption and emission spectroscopy. In addition to the changes in the energetic landscape of the donor, a higher molecular order in fullerene phases has been reported to increase the electron affinity by 100 meV compared to finely intermixed PCBM.[68] Moreover, donor-acceptor interactions

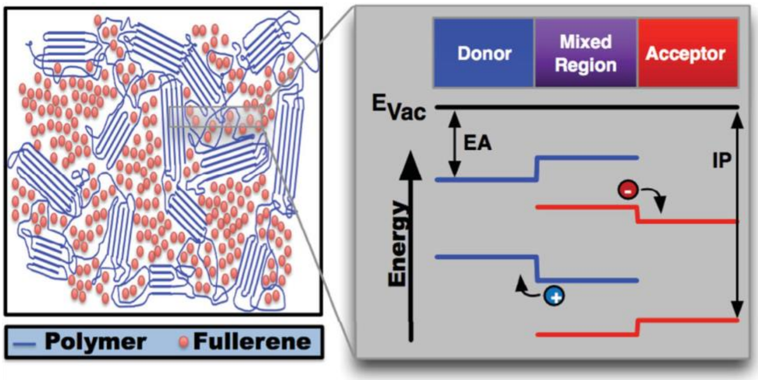

Figure 26. Proposed nanoscale morphology including pure donor (blue) and fullerene (red) domains together with intermixed phases (purple). Energy levels show the change in the energetic landscape affected by the aggregation behavior. Reprinted with permission from reference [76]. Copyright (2013) WILEY-VCH Verlag GmbH & Co. KGaA, Weinheim.

have been reported that yield an additional energetic offset of about 100 meV.[80] From this it is concluded, that intermixed phases can increase the fraction of separated charges[80, 82] as well as decrease charge recombination.[80, 83]

The role of intermixed phases is furthermore studied frequently on the archetypal system of pBTTT:PCBM in which the microstructure can be controlled *via* the donor-acceptor ratio,[84-87] the length of the alkyl side chains,[88] the size of the fullerene[80, 89, 90] and non-volatile additives.[91, 92] A study about charge generation and recombination in blends of pBTTT:PCBM is presented in Section 4.5. Burke *et al*. considered the energetic offset which is determined experimentally in KMC simulations.[76] In the framework of this publication, the role of high initial charge-carrier mobility is highlighted (see Section 2.4.4.3). An energetic offset of 200 meV provides the driving force for charge carriers to diffuse away from the donor-acceptor interface and thus increases the probability of CT dissociation. The role of cascaded energy heterojunctions was also addressed by Groves by implementation of a KMC model.[83] Groves argued, that a cascaded heterojunction that mimicks photosynthesis is an efficient way to enhance charge separation. The cascaded structure is realized *via* disordered regions at the donor-acceptor interface that are higher in energy compared to the more ordered bulk material in the case of P3HT.

2.4.4.5 Excess Energy - Hot *versus* Cold Charge Transfer States

The influence of CT state excess energy on charge separation is still under debate und not finally resolved. Examples in the literature span the range from no benefits at all to the excess energy being crucial for charge separation.

Bakulin *et al*. showed by pump-push-probe spectroscopic experiments that an infrared push pulse increased the yield of spatially separated charges.[93] The additional excitation with a push pulse is thought to repopulate higher-lying band states which are the primary products after exciton quenching at the donor-acceptor interface. These excited states exhibit increased electron-hole distance and thus facilitated CT state dissociation.

Also Grancini *et al*. employed spectroscopic techniques to investigate charge separation. They used TA spectroscopy to investigate the influence of the pump pulse wavelength.[94] The excitation wavelength was chosen to selectively excite S_1, S_2, and S_4 states of PCPDTBT:PCBM blends which translates into excitation wavelengths of 710 nm, 640 nm, and 510 nm, respectively. Inverse rates for the formation of a photo-induced absorption signal of 48 fs, 38 fs, and 22 fs, respectively, were found and interpreted as a faster formation of spatially-separated charges at shorter wavelength excitation. The increase in charge separation efficiency is also explained by a resonant coupling of excited singlet and hot CT states. Furthermore, the authors argue that hot CT states show delocalization which in turn supports ultrafast charge separation. It was shown that the IQE value at the optical bandgap is lower than for absorption at higher energy.

However, Scharber commented on the findings of Grancini *et al*. in a separate correspondence especially addressing the finding of the wavelength dependent IQE.[95] In contrast to Grancini *et al*., Scharber determined a constant IQE independent of the wavelength for the same blend of PCPDTBT:PCBM and thus postulated that another interpretation as given by Grancini *et al*. is necessary to describe their findings. Furthermore, it is questioned how universal the findings of Bakulin *et al.* and Grancini *et al*. are or if their findings could be material specific. Furthermore, the question was raised how relevant spectroscopic experiments, usually performed with higher excitation densities, are in comparison to solar standard conditions.[96]

On the contrary, the dissociation of relaxed, 'cold' charge-transfer states was reported by Vandewal *et al.* for different material systems including donor polymers and small molecule donors as well as fullerene-based electron acceptors and CN-ether-PPV as electron accepting polymer.[96] Using a combination of highly sensitive absorption measurements, namely photothermal deflection spectroscopy (PDS), electroluminescence measurements and exact external quantum efficiency measurements, the internal quantum efficiency from singlet absorption as well as CT state absorption could be determined. Interestingly, the IQE turned out to be constant over the whole spectral range including the absorption directly into the relaxed CT states. From this finding the authors concluded that no additional assistance, *e.g.* by excess energy of the CT state, is necessary to dissociate CT states into free charges.

2.5 Materials

One of the most important factors that determine the potential efficiency of organic solar cells is the absorption of incident photons by the active layer. Therefore, strategies aim at maximizing photon harvesting by employing materials with high extinction coefficients as well as a broad absorption spectrum that maximize the overlap of the absorptivity of the photoactive layer with the solar spectrum. Consequently, donor materials with absorption extending into the near-infrared (NIR) spectrum and acceptor-type molecules that contribute to the absorption of the active layer have been developed. These materials are described in detail in Sections 2.5.1–2.5.3. Shockley and Queisser calculated the maximum efficiency obtainable from *p*-*n* junction solar cells with the bandgap E_g and the fraction of radiative decay f_c as parameters and found an optimum efficiency of 30% for E_g values of 1.1 eV and f_c values equal 1.[97] This approach was later extended to organic solar cells under the assumption of different FF and bandgaps resulting in theoretical PCE values exceeding 15% for E_g values in the range from 1.35 eV to 1.65 eV.[33, 39]

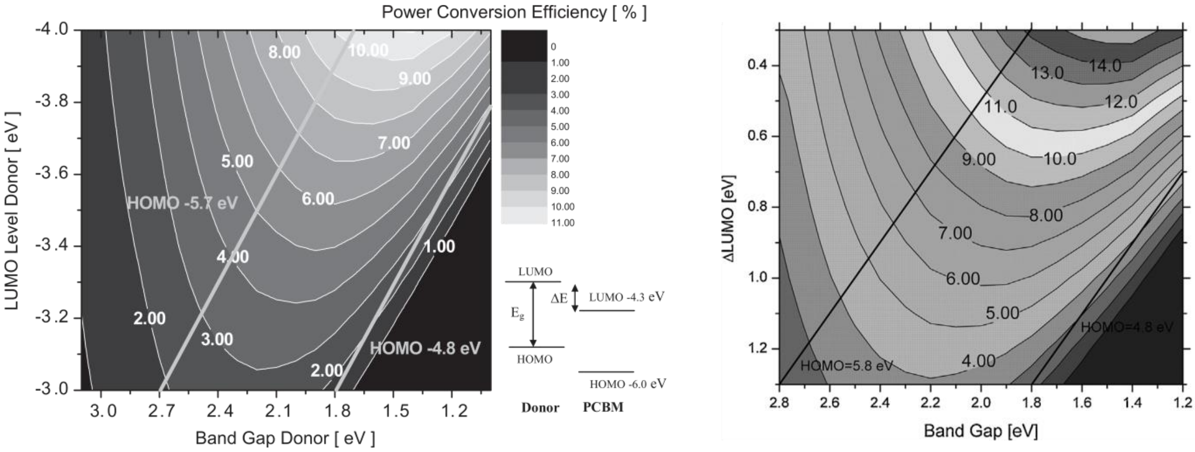

Figure 27. Simulations of the theoretical PCE of organic solar cells performed by Scharber *et al.* in 2006[39] (left) and 2013[33] (right). FF and EQE are assumed to be 65% in the first calculation allowing theoretical efficiency values up to 11%, and were raised to 80% and 75%, respectively, due to the progress in organic photovoltaic research allowing theoretical PCE exceeding 15%. Reprinted with permission from references [39] and [33]. Copyright (2006) WILEY-VCH Verlag GmbH & Co. KGaA, Weinheim and open access funded by Austrian Science Fund (FWF).

The following sections address the question how the loss mechanisms discussed in the previous section can be overcome and how the single steps leading to charge generation and thus the factors determining the PCE can be improved.

2.5.1 Perylene Diimides in Organic Solar Cells

In addition to the absorption of the donor the contribution of the electron acceptor to light harvesting is important to maximize photon harvesting of the active layer. The additional absorption can potentially increase the current which can be extracted from an organic solar cell.

The majority of solar cells work with fullerene as acceptor. For instance, a search in the 'web of science' (13.04.2015) with the search terms "fullerene" + "solar cell" (as topic) results in 11,525 publications, while "perylene" + "solar cell" (as topic) shows only 1,156 results. It becomes evident that fullerene and its derivatives are ubiquitous in the field of OPV and are key drivers for the efficiencies obtained in the past decades. Yet, the search for alternative, non-fullerene acceptors remained of interest. Despite the advantages that fullerene offers like the isotropic charge transport with good electron mobility values, favorable electron affinity and nanoscale morphology, some disadvantages arise like the negligible absorption in the visible especially for $PC_{61}BM$ (see Figure 28) or the high costs of $PC_{71}BM$.[98] Furthermore, synthesis and purification of fullerenes is very challenging and the energy levels show low variability. These factors motivate the commitment to search for alternative acceptors. Among the possible candidates perylene is the most popular for several reasons. Perylene derivatives exhibit complementary absorption to many low-bandgap polymers which allows for a broad amount of coverage and hence an optimal photon harvesting. Additionally, perylene derivatives show a superior light- and heat-stability with sublimation temperatures as high as 550 °C.[99] Furthermore perylene diimides can be modified at many positions – namely bay, *ortho* and imide position (see Figure 29) – with flexible, manifold synthetic approaches which allows to control electronic properties, aggregation behavior and absorption properties.

Perylene derivatives have been known as potential acceptors which absorb in the visible part of the solar

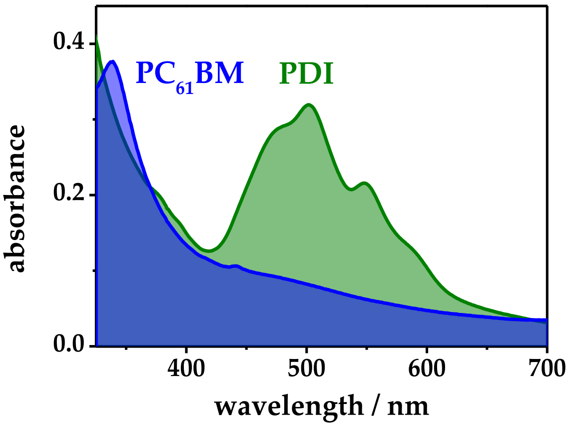

Figure 28. UV/Vis absorption spectra of $PC_{61}BM$ (blue solid line) and PDI **13** (as shown in Figure 30 on page 39; green solid line) in thin film.

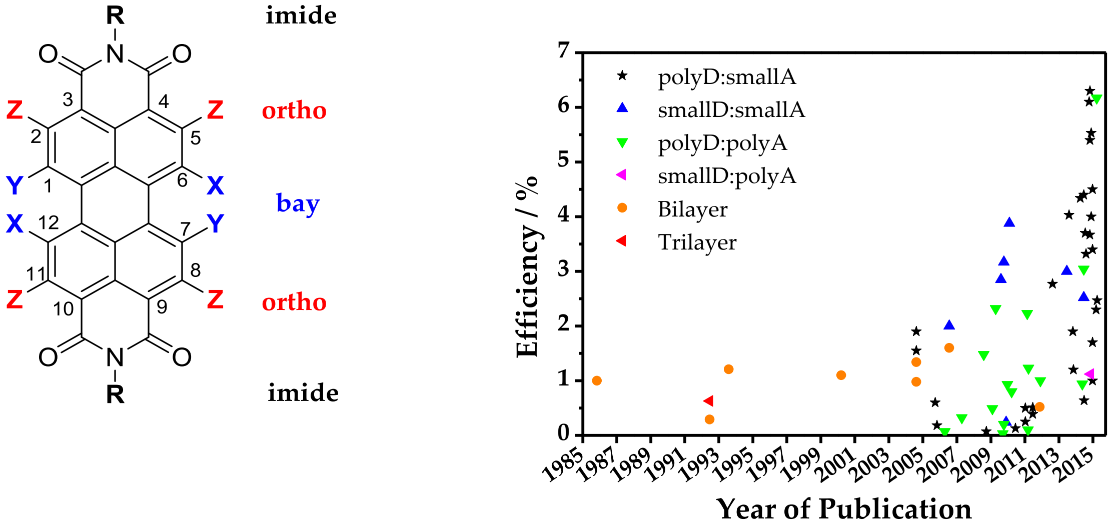

Figure 29. Development of organic solar cells which utilize perylene derivatives as electron acceptor.

spectrum since the earliest development of the organic solar cell technology. Tang utilized a perylene tetracarboxylic derivative, named PV (molecule **9** shown in Figure 30), as acceptor in combination with copper phthalocyanine CuPc yielding an at that time remarkable power conversion efficiency of 1%.[45] However, these molecules exhibited virtually no solubility in common organic solvents and therefore were processed *via* evaporation. Therefore, the device architecture realized by Tang and his co-workers was a bilayer device in which the donor acceptor interface is severely limited and therefore only marginal exciton quenching is observed if the layer thickness exceeds the exciton diffusion length.

Perylene diimides, a derivative of perylene, were developed as early as 1973[100] and have been applied as colorant pigments. For example, Pigment Red 179 (see **10** in Figure 30,) is a well-known representative of PDI pigments which finds its application in car finish. However, these pigments were tremendously lacking solubility due to the strong π-π-interaction of the planar aromatic core and the resulting pronounced aggregation behavior.

To avoid the problems with solubility, Seybold *et al.* developed new PDI derivatives for the use as fluorescent collectors. These were altered at the imide position by utilizing longer alkyl chains like heptyl or *ortho*-alkyl-substituted aromatics which have a perpendicular orientation with respect to the perylene core and consequently strongly reduce π-π-interaction of the perylene core.[101] Moreover, optimized conditions enabled the controlled synthesis of 1,6,7,12-tetrachloroperylen-3,4:9,10-tetracarboxylic acid diimides **11** using sulphuryl chloride in nitrobenzene[102] as chlorination agent. The substitution of hydrogen at the so called bay-position (see Figure 29 for the labeling of positions) by the more bulky chlorine resulted in a twist of the two naphthalene subunits of the backbone by 36.7° as shown by x-ray structure analysis of the molecules.[103]

Consequently, π-π-interactions are further reduced and concomitantly the solubility is enhanced without changing the spectral properties remarkably. The synthesis of perylene diimides is described in detail by Langhals.[104]

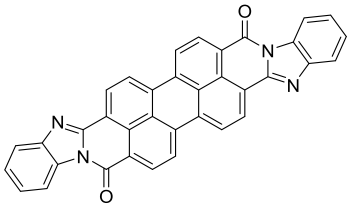

9 (PV)

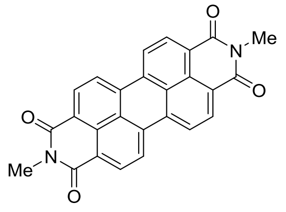

10 (Pigment Red 179)

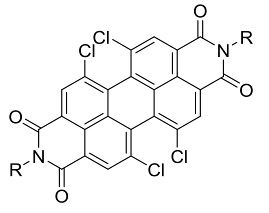

11 (PDI-Cl$_4$) R = 4-(n-$C_{12}H_{25}$)C_6H_4

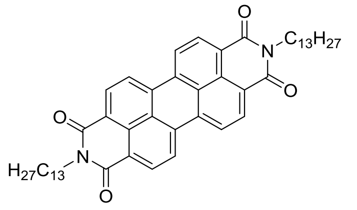

12 (PTCDP-C$_{13}$)

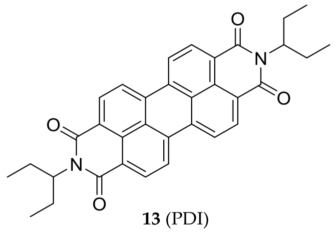

13 (PDI)

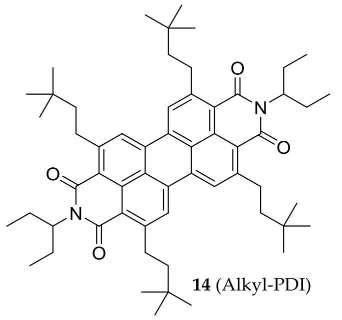

14 (Alkyl-PDI)

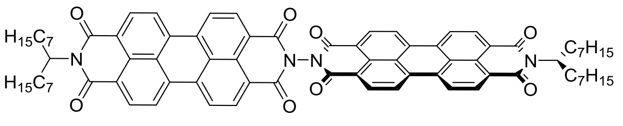

15 (PDI-Dimer)

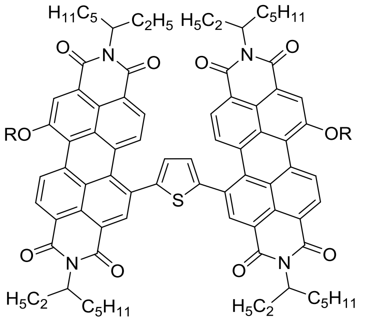

16 (Bis-PDI-T-EG) R =

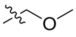

17 (Bis-PDI-T-MO) R = Me

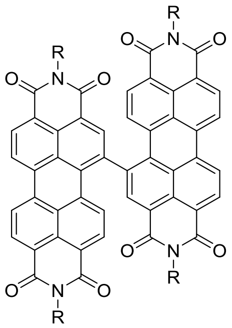

18 (s-diPBI)R =

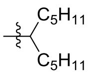

26 (diPDI) R =

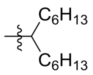

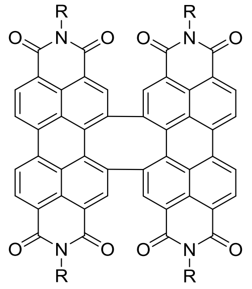

R =

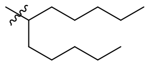

19 (d-diPBI)

Figure 30. Various perylene derivatives used as electron acceptors in organic photovoltaic devices. References for the structures are given in the text.

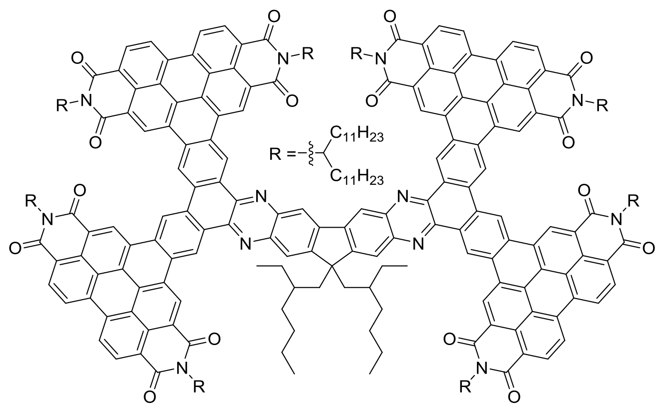

20 (TetraPDI-PF)

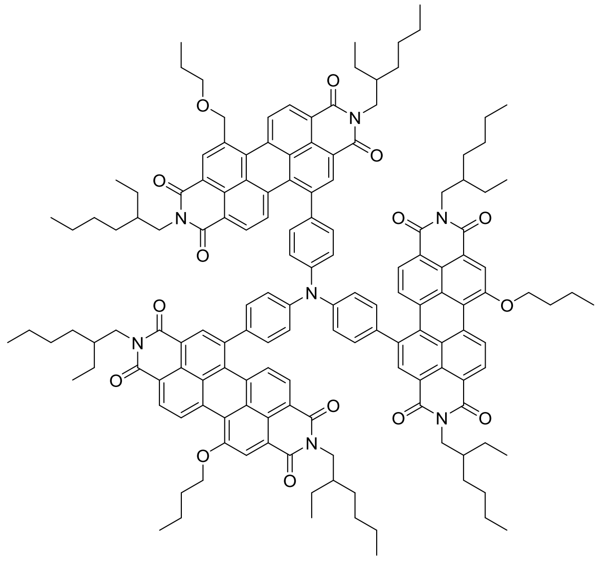

21 (S(TPA-PDI))

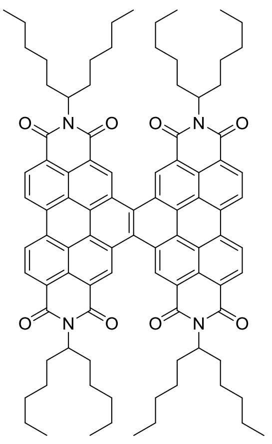

22 (Helical PDI)

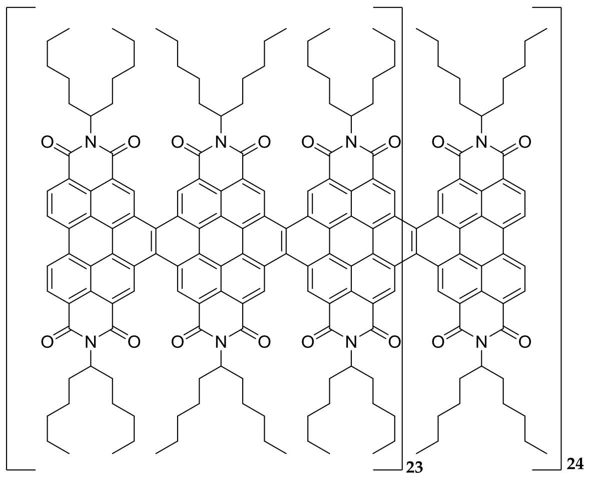

23 (PDI trimer) **24 (**PDI tetramer)

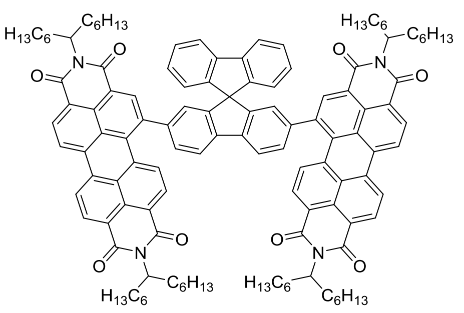

25 (SF-PDI$_2$)

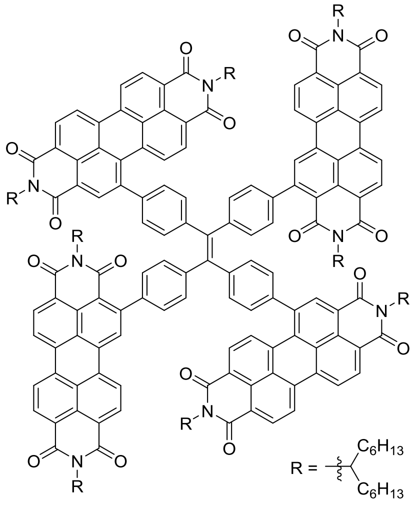

27 (TPE-PDI$_4$)

Figure 31. Continuation of perylene diimide based acceptor-type materials presented in Figure 30.

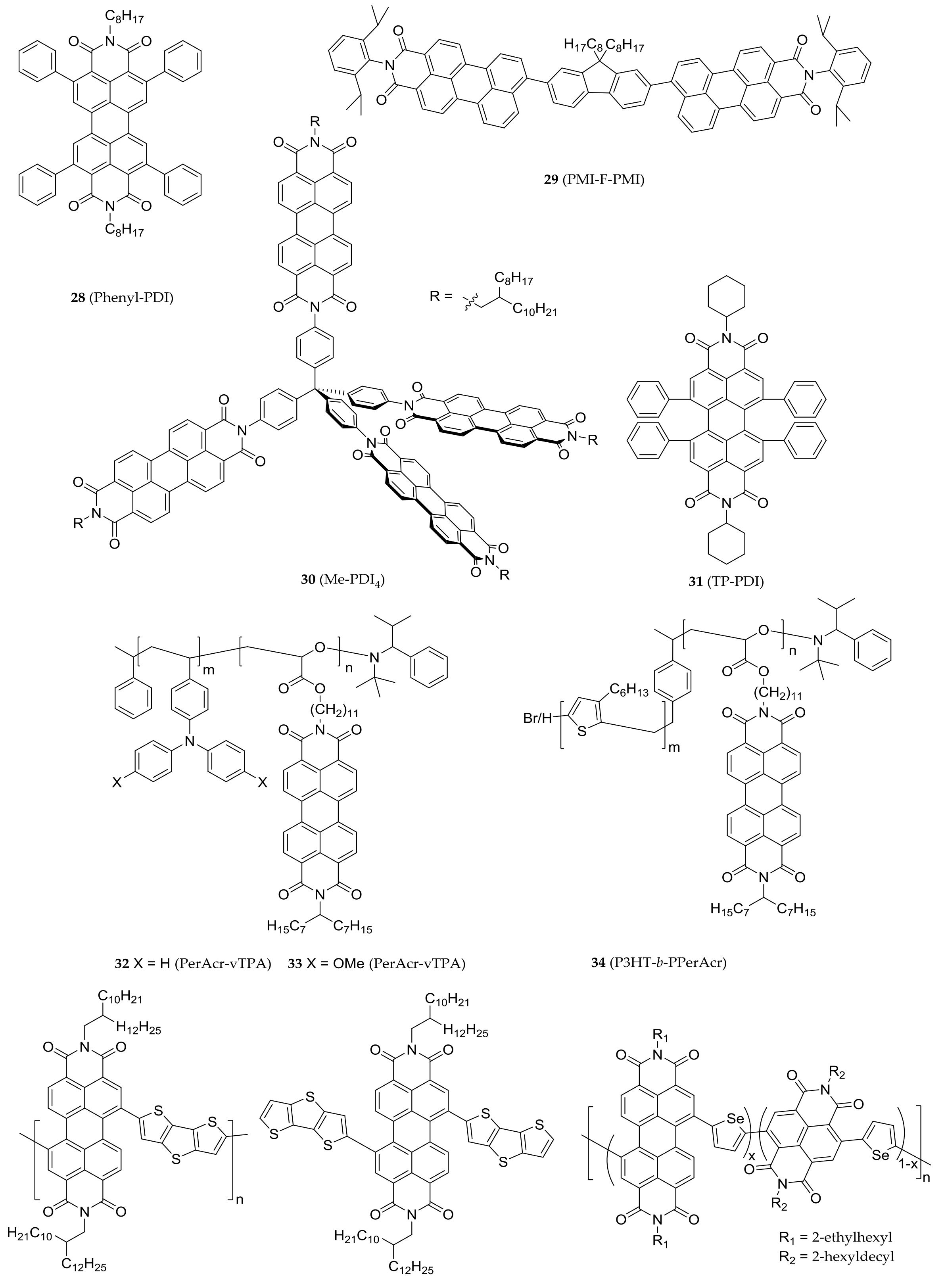

28 (Phenyl-PDI)

29 (PMI-F-PMI)

30 (Me-PDI$_4$)

31 (TP-PDI)

32 X = H (PerAcr-vTPA) **33** X = OMe (PerAcr-vTPA)

34 (P3HT-*b*-PPerAcr)

35 (PPDIDTT)

36 (PDI-2DTT)

37 (TP-PDI)

R_1 = 2-ethylhexyl
R_2 = 2-hexyldecyl

Figure 32. Continuation of perylene diimide based acceptor-type materials presented in Figure 30.

The performance of organic solar cells utilizing planar perylene diimides as electron acceptors is always dictated by the propensity to form up to micrometer sized crystals that both result in inefficient exciton quenching due to a small D-A interface and the formation of perylene excimer states that might not contribute to charge generation.[105] Some strategies have been developed to control the aggregation behavior, *e.g.*

i) Bulky substituents at the imide position
ii) Twisted core structure by inserting bigger substituents at the bay-position
iii) Alkyl-substitution at the *ortho*-position
iv) Dimer and higher oligomers of perylene diimides bridged *via* the imide or bay-position.

Hiramoto *et al.* published in 1992 a bilayer consisting of Pigment Red 179 (**10**) and phthalocyanine, H_2Pc, showing 0.29% efficiency. Inserting an intermixed, co-deposited layer of both components resulted in an improved performance with a PCE of 0.63%.[106] This can be explained by a higher interfacial area that improves exciton quenching. In 1993 Whitlock *et al.* presented a bilayer using the same PDI derivative as acceptor and chloroaluminum phthalocyanine as donor, resulting in an increased efficiency of 1.21%.[107]

Peumans *et al.* demonstrated an unprecedented PCE of 2.4% in 2000 using an electron-blocking layer making again use of copper phthalocyanine as donor and 3,4:9,10-perylenetetracarboxylic-bis-benzimidazole (PTCBI, **9**) as acceptor.[108] However, this efficiency was achieved using a sophisticated light-trapping mechanism and the efficiency of a normal device was limited to 1.1%.

One of the first examples for bulk heterojunction solar cells using PDI as electron acceptor was shown by Nakamura *et al.* in 2004, where Tang's PV **9** was combined with the donor polymer MEH-PPV yielding an efficiency of 0.98% and 1.55% in bilayer and BHJ device, respectively, and even higher PCE values of 1.34% and 1.90%, were achieved when PPAV-HH-PPV was used as donor for flat and bulk heterojunction, respectively.[109]

Pandey *et al.* published in 2006 work on $C_{13}H_{27}$-PTCDI (**12**) that showed efficiencies of 1.6% and 2.0% in a bilayer or BHJ device geometry in combination with pentacene as electron donor, respectively.[110] One advantage of this specific material system is the balanced charge transport in PTCDI and pentacene measured in OFET devices which reduces space-charge effects in the sample.[111] PDI **12** shows an improved solubility due to the long alkyl chain at the imide position which allows for efficient solution processing of the molecule.

Perylene derivative **13** was used by Howard *et al.* in a bulk heterojunction device architecture in combination with the polymeric donor F8BT.[105] This in depth study revealed by using several spectroscopic techniques that excitons on PDI aggregates relax within 100 ps into intermolecular states, referred to as excimers. These intermolecular states are immobile and low in energy, so that they are not capable of contributing to charge generation. Therefore, a fine intermixing of donor and acceptor is desired to efficiently quench excitons located on PDI molecules and to prevent the formation of PDI excimers which are identified as a terminal loss channel. This underlines the importance of sufficient solubility to achieve a favorable domain size. However, the authors also argue that a too fine intermixing is accompanied by pronounced bimolecular recombination opening a new loss channel.

Kamm *et al.* showed in 2011 that by substitution of hydrogen with bulky alkyl chains at the *ortho*-position (**14**) the aggregation of perylene derivatives can be reduced. By this approach the power conversion efficiency in combination with P3HT could be enhanced to 0.5%. This corresponded to a doubling in efficiency compared to the analogue PDI with an unsubstituted perylene core (See structure **13** in Figure 30) and proves the validity of Howard's results.[112] Photoluminescence lifetime measurements in solution and solid state revealed that the packing behavior of *ortho*-substituted PDI is drastically changed in comparison to PDI structures which are substituted exclusively at the imide positions. The emission of **14** is shifted by 160 meV to higher energy with respect to **13**, indicating that exciton trapping *via* excimer formation is less problematic in organic solar cells utilizing **14**. XRD experiments further suggested that PDI **14** strongly reduces crystallization of the donor polymer, namely P3HT, upon thermal annealing which might originate from the bulky side chains at the *ortho*-position.

Also, Keivanidis and co-workers utilized PDI **13** as acceptor, however, not in combination with F8BT or P3HT as shown previously, but with the low-bandgap polymer PBDTTT-E-O.[113] The authors showed that thermal treatment of the active layer resulted in a PCE value improvement from 0.47% to 1.37% after annealing at 100 °C. Higher temperatures lead again to a lower PCE. Keivanidis and co-workers showed by a thorough investigation of the blend morphology, including PL intensity measurements, wide-angle x-ray scattering (WAXS), AFM, and fluorescence optical microscopy that the flat PDI used in this system formed columnar structures and that the interconnection of the columns, which was achieved by thermal treatment of the donor-acceptor blend, improved charge transport of photogenerated charges.

PDI **13** was also combined with the small molecular donor p-DTS(FBTTh$_2$)$_2$ by Sharenko *et al*. and the PCE was increased to 3% by the use of chlorobenzene with the solvent additive 1,8-diiodooctane (DIO) from 0.1% for the blend processed from chlorobenzene without the solvent additive.[114] This was explained by a higher structural order, improved nanoscale morphology of the active layer and thus an improvement of the charge-generation efficiency. The influence on the photophysics was addressed in a follow-up study and is presented as Section 4.3 in this thesis.[115]

At this point, there is consensus that efficient bulk heterojunctions based on PDI derivatives require a better control of packing behavior and consequently active layer morphology which is crucial to enable the fabrication of efficient devices. Ongoing research focuses on the development of new concepts to suppress aggregation. New drive for the improvement of PDI acceptors was given by Rajaram *et al.* in 2012.[116] They presented a novel approach to overcome *π-π*-stacking in PDI-based solar cells by linking two PDI *via* the imide position using hydrazine as linking unit (see structure **15** in Figure 30). As a consequence of the electrostatic repulsion of adjacent imide-oxygen atoms, the two perylene cores are twisted by 90° with respect to each other, in turn lowering the propensity to aggregate. In combination with the low bandgap polymer PBDTTT-CT a PCE of 2.77% was achieved. This material combination was studied in greater detail with transient absorption (TA) spectroscopy in a follow-up study by Shivanna *et al.*[117] The authors demonstrated efficient exciton quenching as they observed strong photoluminescence quenching. The prerequisite for exciton quenching in both donor and acceptor domains is a favorable microstructure that shows a sufficiently fine intermixing, which could be proved by atomic force microscopy. Furthermore, the charge yield in PBDTTT-CT:twisted perylene **15** (TP) blends was comparable to the respective polymer:$PC_{71}BM$ blends as shown by TA spectroscopy. Moreover, both blends showed similar power-law decay on a few μs timescale which is consistent with recombination of dissociated charges. Additionally, the timescale of picoseconds to nanoseconds, when charge generation occurs, was investigated after excitation with 470 nm and 700 nm where mainly PDI and only PBDTTT-CT are excited, respectively. It was found that after excitation with 700 nm the polymer exciton was quenched at the D-A interface within 1.6 ± 0.4 ps which is about one order of magnitude faster than the 'half-time' observed in the pristine polymer, which was 10 ± 2 ps. If the blend was excited with 470 nm, only a weak photo-induced absorption (PIA, see Section 3.4 for detailed information about TA spectroscopy and the explanation of TA signals) of the polymer exciton was observed, however, the PBDTTT-CT polaron evolved with a rate of 1.8 ± 0.4 ps which was nearly identical to the timescale of PBDTTT-CT exciton quenching. In addition to spectroscopic experiments, the authors investigated the charge transport properties of the materials to evaluate the charge extraction behavior. For this reason, the model of space-charge limited current (SCLC) was applied to the *J-V* characteristics of devices with selective contacts. Balanced mobility values for electrons and holes in the range of $1–4 \times 10^{-4}$ cm^2 $(Vs)^{-1}$ were obtained with electron mobility values being slightly higher. Finally, AFM images showed an average domain size of about 10 nm which is in stark contrast to planar perylene derivatives that exhibit domains on a length scale up to micrometers. The intimate intermixing explained the efficient PL quenching as well as the rather fast rise of the charge signal in ps–ns TA experiments. However, the performance of the PBDTTT-CT:TP blends still lacks behind their PBDTTT-CT:$PC_{71}BM$ counterpart, which is not caused by inefficient exciton quenching or charge generation, but explained by reduced extraction efficiency as argued by Durrant and co-workers.[117]

A similar concept, *i.e.* the use of a dimeric structure to reduce aggregation tendency, was pursued by Zhang *et al.*[118] Two perylene cores are linked *via* a thiophene unit at the bay position (see structure **16**, Bis-PDI-T-EG). A careful choice of the processing conditions was necessary to guarantee an optimal device operation. A PCE of 4.03% in combination with PBDTTT-CT was achieved if the active layer was spin-coated with 5 vol% diiodooctane (DIO) as solvent additive. This is traced back to a reduced aggregation which resulted in favorable domain sizes and orientation of donor and acceptor. In fact, the comparison with the respective PDI monomer showed a 300-fold improvement of the PCE.

The efficiency of the similar PDI derivative **17** could be increased to 4.34% by Lu *et al.*[119] The side chain is shorter, namely methoxy groups are used instead of methoxyethoxy, and an inverted device structure was used which offers more favorable contacts contributing to the improved PCE.

The previous record was topped not much later in 2014 by Ye *et al.* when they presented a PCE of 4.4% for an acceptor molecule combining two directly linked perylene cores (**18**) in combination with the low bandgap donor polymer PBDTBDD[119] confirming the importance of the control over the aggregation properties inherent in planar perylene derivatives. Jiang *et al.* presented PDI **19** (d-diPDI) together with PDI **18** yielding a PCE of 1.54% and 3.63%, respectively, in combination with PBDTTT-CT with chloronaphthalene (CN) and DIO or only DIO as solvent additive.[120] Again, this study underlined the importance of flexible structures as the more flexible PDI **18** outperformed PDI **19**.

Ye *et al.*[121] presented a study about s-diPBI (**18**) in which they combined the acceptor with a series of polymers, namely PDPP3T, PSBTBT, PBDTTPD, and PBDTTT-EFT, which resulted in 1.0%, 1.7%, 3.4% and 4.5%, respectively. They authors argued that the interplay of donor and acceptor as well as the crystalline properties of the donor polymer determined factors like morphology, donor-acceptor phase separation and consequently resulted in different efficiencies. The high crystallinity of PDPP3T is responsible for the rather poor performance, while the high efficiency of PBDTTT-EFT:s-diPDI blends was attributed to the moderate crystallinity exhibited by the donor polymer which in turns allows for favorable molecular interactions and enables efficient current generation.

The concept of using more than one PDI core was even further extended in the work of Zhang *et al.*[122] In combination with P3HT, TetraPDI **20** yielded a power conversion efficiency of 0.64% which was by a factor of 64 higher compared to the single PDI acceptor according to this publication.

Lin *et al.*[123] presented a PCE of 3.22% (3.32% maximum) in combination with PBDTTT-CT with the star-shaped PDI **21**. This attempt included a tri-chromophore in which three PDI units are linked *via* a central triarylamine unit. As shown before with other PDI systems in combination with low-bandgap polymers a proper choice of solvent additives is important and the optimum performance was achieved when a fraction of 5 vol% DIO was added to *ortho*-dichlorobenzene. The solvent additive lead to partial demixing of the otherwise too finely intermixed donor-acceptor system. Although the combination of PBDTTT-CT:**21** was rather efficient for a non-fullerene acceptor, the current density still exhibited a pronounced dependence on the applied voltage and thus the FF stayed very moderate with ~33%.

A solar cell device with outstanding performance was presented by Zhong *et al.* with a combination of the donor polymer PBDTT-TT in combination with the helical PDI **22** with an average PCE of 5.94% and a top-efficiency of 6.05% when processed with DIO and CN solvent additive and 5.14% (5.21%) in combination with PTB7.[124] DFT calculations showed that the perylene subunits are twisted strongly and as a consequence aggregation is reduced. TA spectroscopy revealed that charge generation was very fast in blends of PTB7 and **22** and occurred with inverse rates of 0.2 ps and 1.2 ps that accounted for 62% and 38%, respectively, when the sample was excited with a wavelength of 390 nm. The former was assigned to ultrafast charge generation while the latter component was assigned to exciton-diffusion limited charge generation. The design principle applied for **22** can be further extended to the PDI trimer **23** and tetramer **24**.[125] These molecules show desirable properties as n-type semiconducting material in OFET devices yielding electron mobility values of 0.04 $cm^2\ (Vs)^{-1}$ and 0.05 $cm^2\ (Vs)^{-1}$, respectively, which is even higher than the mobility value of **22** which was determined to 0.02 $cm^2\ (Vs)^{-1}$.

The recent record efficiency for PDI-based acceptors is 6.3% which was realized by Zhao *et al.* when combining SF-PDI$_2$ (**25**) with a fluorinated polymer, namely PffBT4T-2DT.[126] Furthermore, the same publication contained the dimeric PDI **26** which gave a PCE of 5.4% in combination with the same polymer. It should be noted that **26** is identical to **18** except for a slightly longer alkyl substituent at the imide position. Remarkably, the efficiency of **25** was obtained without using any solvent additive. The authors showed that blends of PffBT4T-2DT with **25** exhibit efficient PL quenching which was assigned to favorable donor-acceptor domain sizes in agreement with AFM images. Furthermore, from the dependence of J_{SC} on the light intensity P, which showed a correlation of $J_{SC} \propto P^{0.95}$, the authors inferred that the bimolecular recombination is weak in the investigated devices.

The series of PDI-based acceptors with a PCE exceeding 5% was continued by Liu *et al.* with a PDI having a propeller-like and hence 3D structure (**27**) resulting in a 5.53% efficient solar cell device in combination with PBDTT-F-TT.[127] Liu *et al.* highlighted the importance of the reduced aggregation tendency resulting in homogeneous film formation with small domain size. Moreover, the 3D-like structure facilitated omni-directional charge transport. It should also be noted, that the four PDI subunits in PDI **27** show only minor conjugation which maintains the favorable electronic properties of single PDI.

Hartnett *et al.* presented the highly efficient small mono-PDI **28** yielding a 3.67% efficient solar cell in combination with PBTI3T.[128] This perylene diimide is substituted at the *ortho*-position with phenyl groups and consequently crystallizes in a slip-stacked manner. Therefore, crystallite sizes remain moderate allowing for efficient exciton harvesting as shown by transient absorption spectroscopy. These measurements showed that geminate recombination on the sub-ns timescale is reduced by the specific substitution pattern.

Also, new dimeric perylenes were developed which showed rather good efficiencies with the prototypic donor polymer P3HT. Very recently, Zhang *et al.* published structure **29** composed of two perylene monoimides (PMI) bridged with a fluorene unit.[129] Although the FF was moderate with values around 0.41, a PCE of 2.14% (2.30% maximum) was reported, partly enabled due to the high V_{OC} of 0.97 V. The low fill factor probably originates from imbalanced charge transport with mobilities of 1.29×10^{-3} cm^2 (Vs)$^{-1}$ and 9.85×10^{-5} cm^2 (Vs)$^{-1}$ for P3HT and PMI-F-PMI, respectively.

A similar approach, *i.e.* the introduction of 3-dimensionality mediated by the bridging unit in the center of the molecule was chosen by Chen *et al.* who connected four PDI chromophores *via* a tetrakis(4-aminophenyl)methane unit which gives the tetrahedral acceptor structure **30**.[130] Blends of this acceptor and the low-bandgap donor polymer PBDTTT-CT result in a PCE of 2.47% (maximum 2.73%) enabled by a rather high photocurrent of 7.83 mA cm^{-2}.

TP-PDI **31** is structurally closely related to PDI **16**, however, the four phenyl groups are connected to the perylene core *via* the bay and not the *ortho*-position. The combination with PTB7-Th results in a high V_{OC} of 0.87 V, J_{SC} of 9.74 mA cm^{-2} and moderate FF of 0.46 yielding an overall PCE of 3.8% (maximum 4.1%) which is comparable to dimeric PDI structures.[131] The bulky phenyl rings attached to the bay-positions cause a twist of the two naphthalene subunits of 15°. Furthermore, the phenyl rings are arranged above and below the perylene plane so that aggregation of PDI **31** is reduced compared to unsubstituted PDIs.

In addition to small molecule PDI-based acceptors, polymers containing PDI emerged. Early examples were shown by Thelakkat and co-workers with block copolymeric structures that contained PDI in a pendent-like fashion (structures **32-34**). However, device efficiency in blends with P3HT:**32** and P3HT:**33** as well as copolymers containing oligomers of 3-hexylthiophene (**34**) showed low PCE values below 0.33% limited by a very low short-circuit current density.[132-134] More recently, n-type polymers that incorporate PDI in the backbone (**35**) were developed. Cheng *et al.* compared **35** with the monomeric PDI structure **36** and combined both acceptors with the small molecule donor p-DTS(FBTTh$_2$)$_2$ and the low-bandgap donor polymer PBDTTT-CT.[135] Their work showed good performance for the polymer-polymer and the small molecule-small molecule combination with PCE values of 2.92% and 2.33%, respectively. On the contrary, PBDTTT-CT:**36** (polymer:small molecule) and p-DTS(FBTTh$_2$)$_2$:**35** (small molecule:polymer) exhibited moderate efficiency of 0.26% each. Very recently, the polymeric acceptor structure **37** showed very high efficiency with the donor polymer PBDTTT-CT with PCE values of 6.17%.[136] **37** is a n-type polymer consisting of PDI as well as naphthalene diimide (NDI) subunits. The PCE depends strongly on the ratio of PDI and NDI and the optimum performance was found for a PDI content of 30%. The authors showed a reduced crystallinity with increasing PDI content with an optimum mean crystalline domain size of ~5 nm for a PDI fraction of 30%. The top-device is still limited by a moderate FF of 0.43 showing the potential of polymeric PDI-based acceptor structures.

2.5.2 Other Non-fullerene and Non-perylene Acceptors

Apart from the perylene diimide motif, which was reviewed in the previous Section, other structures were successfully tested for their applicability as electron acceptors in organic solar cells. Molecular structures of electron accepting molecules are summarized in Figure 33–Figure 35.

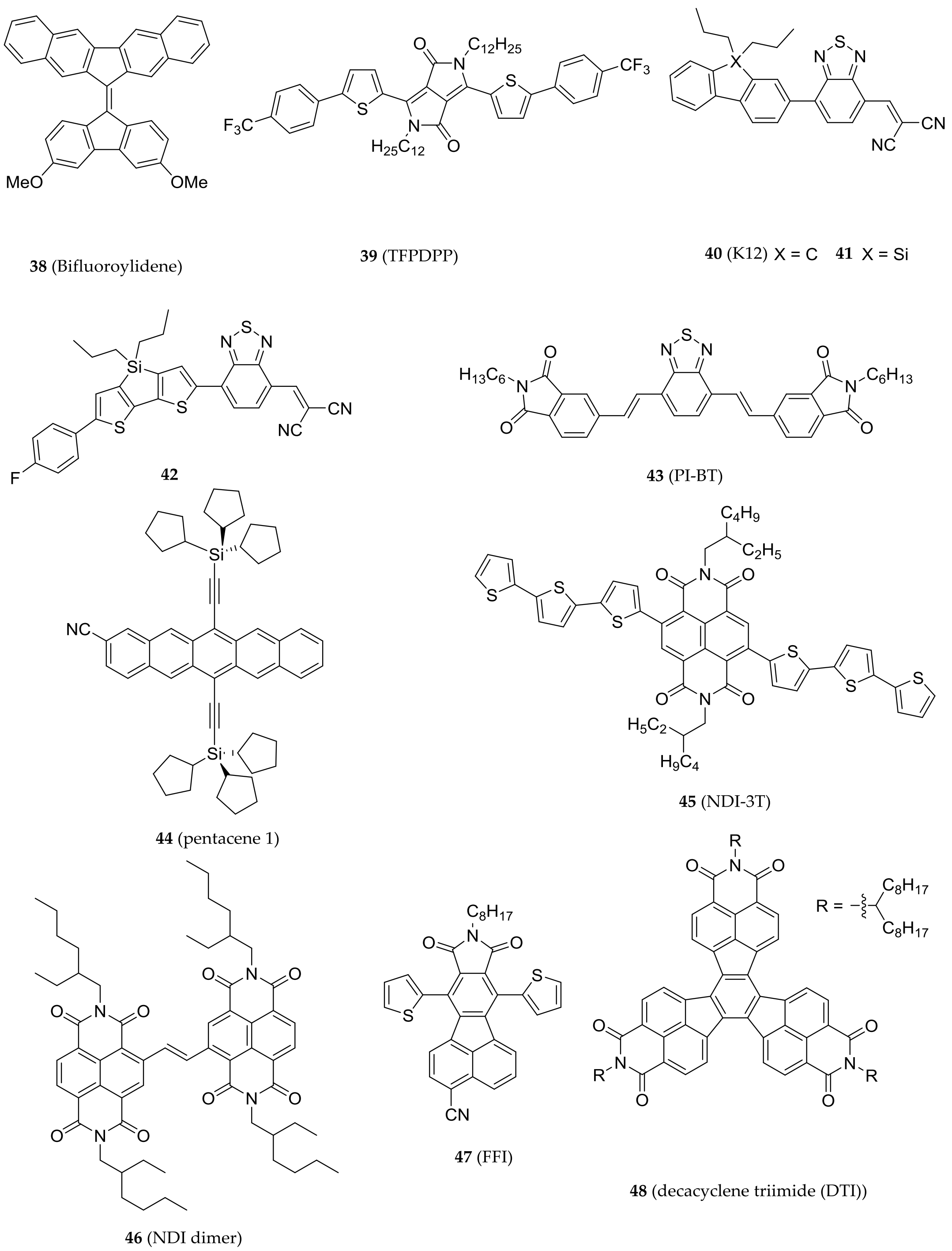

38 (Bifluoroylidene)

39 (TFPDPP)

40 (K12) X = C **41** X = Si

42

43 (PI-BT)

44 (pentacene 1)

45 (NDI-3T)

46 (NDI dimer)

47 (FFI)

48 (decacyclene triimide (DTI))

Figure 33. Different non-fullerene electron acceptors that do not use a perylene core as accepting unit.

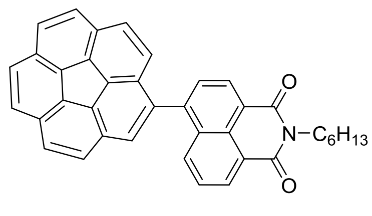

49 (Cor-NI)

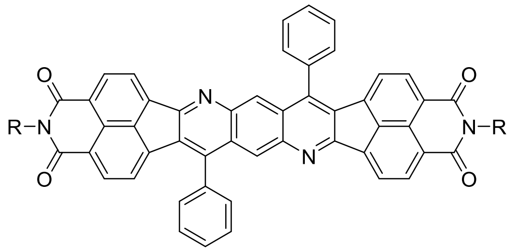

50 BNIDPA-BO , R =

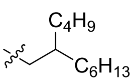

51 BNIDPA-DT , R =

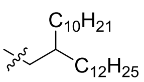

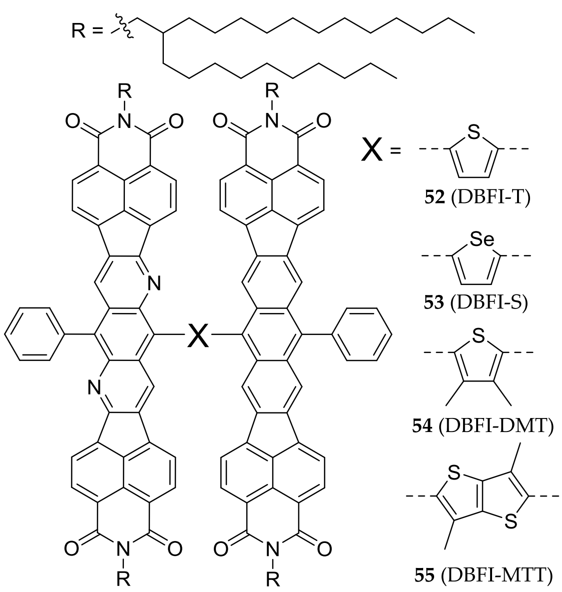

52 (DBFI-T)

53 (DBFI-S)

54 (DBFI-DMT)

55 (DBFI-MTT)

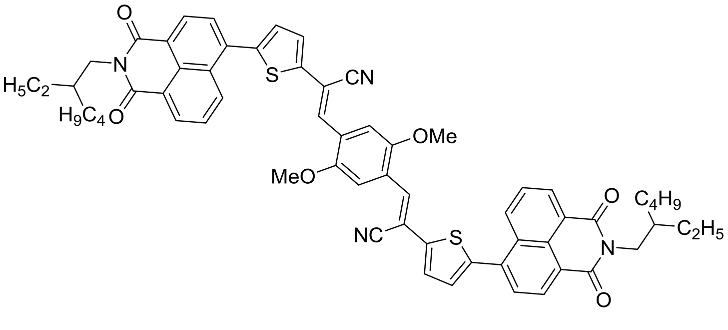

56 (NIDCS-MO)

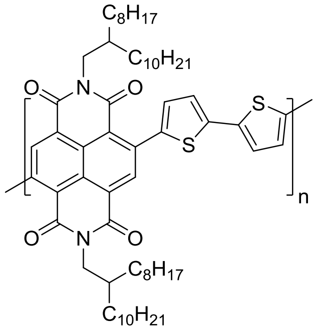

57 (NDI2OD-T2)

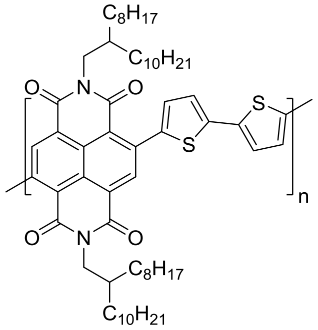

58 (NDI2OD-2FT)

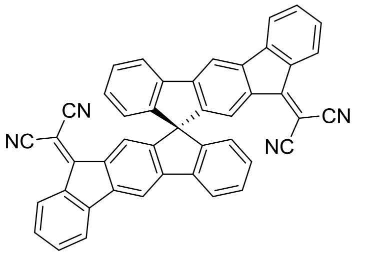

59 (4CN-spiro)

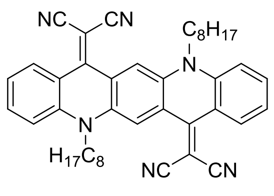

60 (DCN-8CQA)

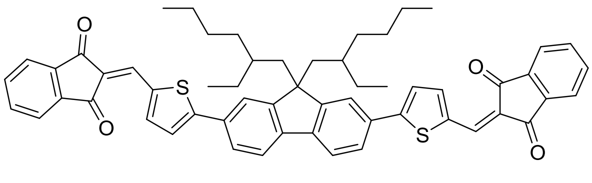

61 (FEHIDT)

Figure 34. Continuation of fullerene free acceptor-type materials.

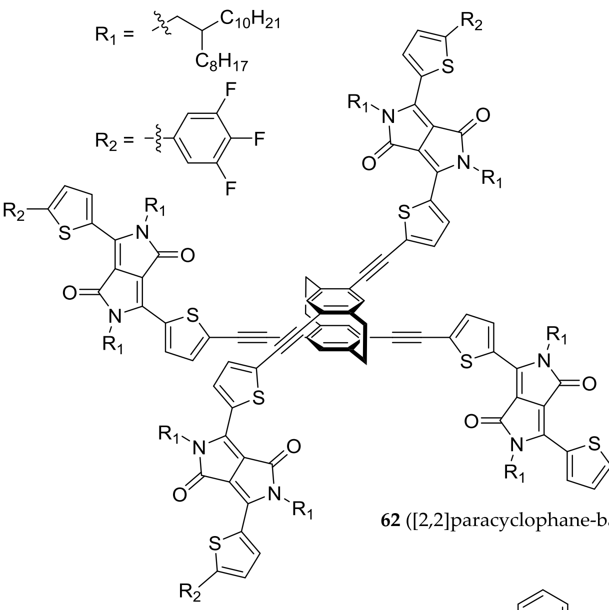

62 ([2,2]paracyclophane-based acceptor)

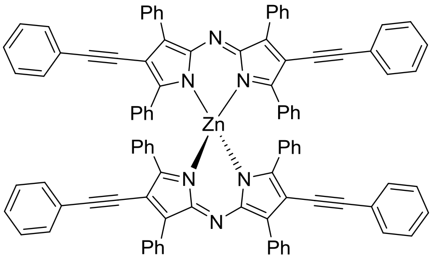

63 (Zn(WS3)$_2$)

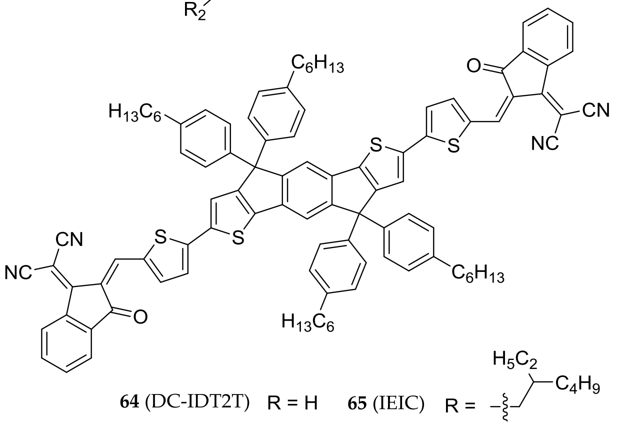

64 (DC-IDT2T) R = H **65** (IEIC) R =

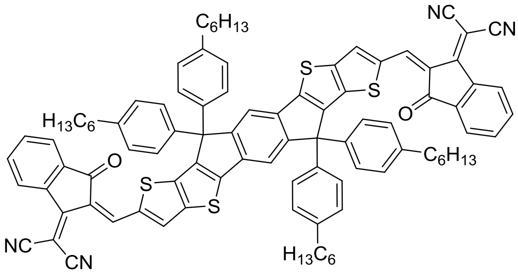

66 (ITIC)

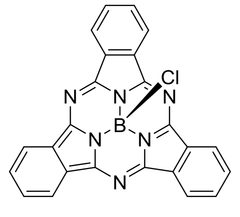

67 (SubPc)

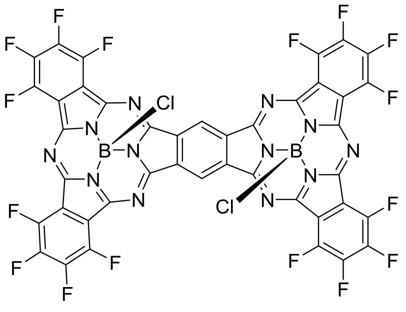

68 (FSubPcDimer)

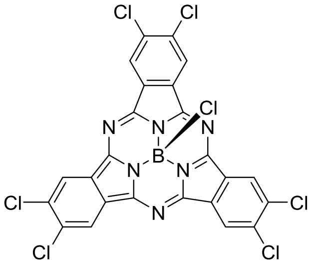

69 (Cl$_6$-SubPc)

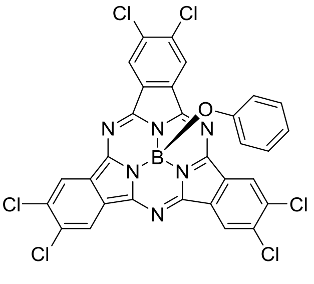

70 (Cl$_6$-SubPc)

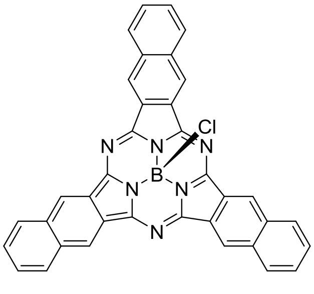

71 (SubNc)

Figure 35. Continuation of fullerene free acceptor-type materials.

For example, Brunetti *et al*. presented an acceptor based on bifluoroylidene **38** in 2010.[137] A PCE of 1.7% was reached in combination with P3HT. The electron-accepting character of these types of molecules originates from the possibility to reach an aromatic character if one or two electrons are accepted. Furthermore, repulsive forces between the two subunits cause a twist along the double-bond which gives the molecule a 3D-like, non-planar structure. Consequently, aggregation is suppressed and a more favorable nanoscale morphology is enabled.

In addition to perylene and bifluoroylidene derivatives, other structures have proven their suitability for organic solar cells. The well-know diketopyrrolopyrrole (DPP), which is the main building block in a variety of electron donating materials,[138-147] can be used in non-fullerene acceptors. This approach was chosen *e.g.* by Sonar *et al*. with the synthesis of **39**.[148] They reported a PCE of 1.0% in combination with P3HT in 2010. Important for the functionality are the electron-accepting end-capping groups, namely trifluoromethylphenyl. Interestingly, the PCE is strongly decreased to 0.05% if a di-trisfluoromethylphenyl is used instead of mono-trisfluorobenzene.

Just as the previously mentioned DPP, benzothiadiazole (BT) is a typical building block in organic electron donating molecules which are based on push-pull systems. Schwenn *et al*. use BT as part of an electron-accepting small molecule that furthermore contains fluorene and the strongly electron withdrawing dicyanovinyl resulting in structure **40**.[149] In combination with P3HT a PCE of 0.73% was demonstrated. Exchanging the bridgehead atom of the fluorene unit with silicon (see structure **41** in Figure 33) yielded an improved efficiency of 1.43%.[150] The substitution of carbon with its homologue silicon is an approach known to improve the solar cell performance for other types of molecules. A well-known example is the pair of the low-bandgap polymer donor PCPDTBT and Si-PCPDTBT, also known as PSBTBT.[151] The further derivatization of the molecule included the extension of the π-system by adding a fluorobenzene unit (**42**) and replacing fluorene by dithiophene bridged with silicon which resulted in a further improvement of the PCE to 1.5%.[152]

Also Bloking *et al*. presented non-fullerene acceptors which are based on BT accepting units. PI-BT, a BT derivative including two phthalimide units linked to BT (**43**), gave a respectable PCE of 2.54% in combination with P3HT.[153] In a follow-up study, this acceptor was revisited and the PCE further improved to 3.7%.[154] The authors noted, that the IQE of 56% still lacks behind those of the respective $PC_{61}BM$ devices with 75%. This is traced back to a lack of miscibility of PI-BT with the used polymers. Consequently, PI-BT is missing an energy offset of which comparable fullerene devices can profit.

Shu *et al.* showed the applicability of triisopropyl-silylethynyl-(TIPS)-modified pentacene as electron-acceptor in OPVs (see structure **44** in Figure 33). Also in this case, a cyano-substitution pattern is used to improve the electron accepting character of the molecule which gives 1.27% efficient solar cells in combination with P3HT.[155]

Another class showing sufficient electron accepting behavior is the class of various types of imides. For example, phthalimides as well as the huge variety of perylene diimides are suitable electron acceptors as shown before. Furthermore, naphthalene diimides were realized, which yielded efficiencies as high as 1.5% for **45** in combination with P3HT as demonstrated by Ahmed *et al*.[156] Recently, Russell and co-workers presented the NDI-dimer **46** which exhibited a PCE of 2.41% in combination with the low-bandgap polymer PTB7.[157] 0.5 vol% of DIO as solvent additive to DCB reduced the domain size and resulted in a favorable crystallinity of the blend. The NDI-dimer **46** is a planar molecule and DFT calculations showed that the HOMO and LUMO orbitals are delocalized over both naphthalene subunits.

Among the class of imides fluoranthene-fused imides (FFI, **47**) are found. A PCE of 1.86% could be obtained in combination with the ubiquitously used P3HT.[158] Another example of a novel imide was given by Pho *et al.* who synthesized a decacyclene triimide (DTI, **48**).[159] 1.6% efficient devices were fabricated in blends of **48** and P3HT. Furthermore, molecule **49**, in which naphthalene monoimide (NMI) is combined with corannulene was demonstrated to achieve efficiency values of 1.03% in combination with the donor P3HT.[160] The PCE of devices based on the NMI derivative **50** exceeded 3% in combination with low-bandgap polymers, namely PBDTT-FTTE and PTB7, as demonstrated by Jenekhe and co-workers.[161] Longer alkyl chains, however, resulted in less efficient devices exhibiting moderate PCE values of 1.71% and 1.42% in combination with PBDTT-FTTE and PTB7, respectively. The authors argued that the reduction in efficiency is due to smaller absorption as well as reduced mobility and less crystallinity of the acceptor. Based on the structures **50**/**51** the same group derived the dimeric structures **52–55**.[162] This approach was also demonstrated for PDI derivatives as an effective route towards high efficiency non-fullerene solar cells. The performance of the solar cells based on **52–55** depended strongly on the bridging unit as this influences the intramolecular orientation of the two chromophore subunits with respect to each other as shown by optimized geometries obtained from DFT calculations (B3LYP/6-31G(d)). In combination with the donor polymer PSEHTT efficiency values up to 6.37% were achieved for the acceptor structure **54** which used a dimethyl-thiophene linker.

In addition to the many polymer:non-fullerene based BHJ systems, combinations of two small molecules have been utilized. In a recent publication, Kwon *et al.* combined the NMI-based electron acceptor **56** with the small molecule donor p-DTS(FBTTh$_2$)$_2$ and achieved a PCE of 5.30%.[163]

On the other hand, fullerene-free polymer-polymer systems have been introduced. For instance, NDI2OD-T2 (**57**) is a n-type semiconductor that was first introduced by Facchetti and co-workers.[164] **57** showed high n-type charge transport with mobility values of 0.45-0.85 cm^2 (Vs)$^{-1}$. Schubert *et al.* combined NDI2OD-T2 (**57**) with P3HT and obtained a PCE of 1%.[165] The authors stressed the importance of the molecular orientation of donor and acceptor with respect to each other and found the best performance for face-to-face orientation. Recently, PCE values approached 6% for **57** in combination with the donor polymer PTB7-Th demonstrating the important choice of the best matching donor for each acceptor.[166] Very recently, Jung *et al*. presented a fluorinated derivative of NDI2OD-T2, namely NDI2OD-FT2 (**58**), which outperforms its non-fluorinated precessor with PCE values of 6.58% (maximum 6.71%) in combination with PBDTT-TT-F compared to 4.75% (maximum 4.93%) achieved with the non-fluorinated version.[167] The authors argue that the improvements introduced by fluorine originate from better electron affinity as well as improved intermolecular order due to hydrogen bonding between C-H and C-F units. Additionally, **58** shows higher electron mobility than **57** resulting in a more balanced electron and hole mobility in the devices.

The combination of the NDI-acceptor polymer **57** with an electron donating DPP-based small molecule, namely DTD, was presented recently by Tang *et al.* and gave a PCE of 3.74% if chloronaphthalene (CN) was used as solvent additive.[168] Solar cells prepared without CN resulted in a PCE of 0.52%. The authors showed that the use of CN lead to a stronger PL quenching and thus related the increase in PCE to a more efficient exciton quenching. The authors proposed a finer intermixing of donor and acceptor as explanation for the increase in exciton quenching.

Xia *et al.* implemented a 3D-like structure by the synthesis of the spiro-derivative **59**. Blends of PTB7 and **59** resulted in a PCE value of 0.8%. TA spectroscopy showed a pronounced signal decay on the sub-ns timescale pointing towards a high fraction of geminate recombination.[169]

More electron accepting structures where introduced and tested for their suitability in BHJ solar cells in combination with the donor polymer P3HT including the quinacridone based acceptor **60** by Zhou *et al.* yielding a PCE of 1.57%[170] and an indan-1,3-dione electron acceptor (FEHIDT, **61**) that generated a PCE of 2.12% by Winzenberg *et al.*[171]

Moreover, 3D-like structures included the paracyclophane derivative **62** which resulted in PCE values of 2.69% with P3HT as shown by Yang *et al.*[172] The two subunits of **62** which are connected to the paracyclophane core contain DPP units as well as thienophene and thus show a good absorption extending up to 700 nm in thin films. A very recent example for a non-fullerene acceptor is the class of azadipyrromethene-based Zn(II) complexes (see structure **63**) presented by Mao *et al.* which yielded PCE values as high as 4.1% in combination with P3HT which is even higher than the efficiency obtained from P3HT:PCBM devices fabricated for this study.[173] The authors assigned the high efficiency to the non-planar structure of the molecule and the favorable nanoscale morphology.

3.73% PCE were achieved by Bai *et al.* using **64** which is a 1,1-dicyanomethylene-3-indanone derivative in combination with PBDTTT-CT.[174] The same group published the related molecule **65** at the same time yielding up to 6.31% PCE with PTB7-Th.[175] **64** and **65** showed an absorption profile that extended beyond 800 nm guaranteeing a favorable photon harvesting. The improvement of the PCE for PTB7-Th:**65** blend resulted from increased V_{OC} as well as J_{SC}. The FF, however, is lower than that obtained from PBDTTT-CT:**64** blends. Further molecular engineering resulted in the development of **66**, which increased the PCE to values of 6.80% (6.58% on average) with higher J_{SC} and FF than previously obtained.[176] V_{OC}, however, was reduced from 0.97 V (for **65**) to 0.81 V (for **66**) although both acceptor structures show nearly identical LUMO levels. This performance was very close compared to the respective device of PTB7-Th in combination with PC$_{71}$BM which gave a PCE of 7.52% (7.29%) and higher than that of PTB7-Th blended with PC$_{61}$BM with PCE values of 6.05% (5.97% on average).

Another example of electron accepting molecules was given by Verreet *et al.* in 2011.[177] The device architecture used in this attempt was not a bulk heterojunction but a trilayer device consisting of a subphthalocyanine (SubPc, **67**) as electron donor, fluorinated subphthalocyanine-dimer (FSubPcDimer, **68**) as first accepting layer and C$_{60}$ as a third layer. A PCE of 4% could be achieved which is remarkably high for flat heterojunction devices.[177] If SubPc was combined only with FSubPcDimer or C$_{60}$, a smaller PCE of 1.2% and 3.3%, respectively, could be realized which supported the usefulness of the cascaded heterojunction.

Similar to the molecules used by Verreet *et al.* (**68**) which were presented earlier, Sullivan *et al.* introduced a combination of SubPc **67** and chloro-substituted SubPc **69**.[178] A PCE of 2.68% was demonstrated. SubPc was later combined with tetracene as electron donor, where 2.9% PCE were realized.[179] SubPc **69** was further modified, namely the chlorine attached to boron was substituted by phenol to yield the subphthalocyanine derivative **70**.[180] The combination with the donor polymers MEH-PPV, P3HT, and PTB7 in BHJ solar cells resulted in PCE values of 0.4%, 1.1%, and 3.5%, respectively. However, a simple comparison to the previously mentioned solar cells is not simple, as the latter were vacuum processed and used flat heterojunctions.

The most efficient fullerene-free organic solar cell was realized by Cnops *et al.*[181] They used a sophisticated energy cascade by stacking three layers of small molecules with complementary absorption and consequently covering the absorption from 350 to 750 nm. The electron donor in this study is α-sexithiophene (see Figure 41 on page 60 for the molecular structure), SubPc **67** is used as an interlayer and boron subnaphthalocyanine chloride (SubNc, **71**) as top layer. The device architecture, energy levels, absorption spectra, and EQE spectra are shown in Figure 36. Additionally, the cascaded structure resulted in a decrease of charge recombination. This was beneficial for a high internal quantum efficiency resulting in a power conversion efficiency of 8.4%.

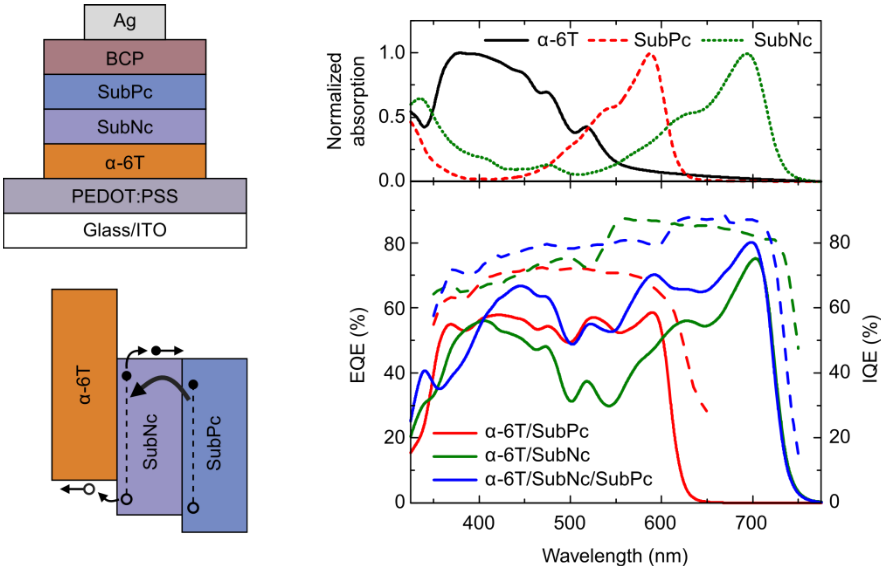

Figure 36. Device layout and energy cascade used in the study by Cnops *et al*. The graph shows the absorption profiles of the single components in the upper panel together with EQE and IQE in the lower panel. Reprinted with permission from reference [181]. Copyright (2014) Nature Publishing Group.

2.5.3 Strategies for Extending Absorption towards Lower Energy

2.5.3.1 Quinoid Structure

Extending the aromatic π-system to a heterocycle as shown in Figure 37 will favor the quinoid resonance structure (right side). These polymers were developed for high electrical conductivity but also show a low bandgap. For example, Wudl *et al*. synthesized a poly(isothianaphthene) (PITN) showing a favorable quinoid structure by annulation of benzene to thiophene.[182] The structure and the resonant electronic distributions are shown in Figure 37. The aromaticity of benzene, which is fused to the thiophene unit, favors the quinoid structure which affords to overcome the aromaticity of thiophene. The bandgap is reported to be 1.1 eV.[182] Later, Heeger and co-workers published a derivative of PITN by adding a dioxymethylene unit in the 5,6-position of benzene exhibiting a bandgap even as small as 1 eV.[183]

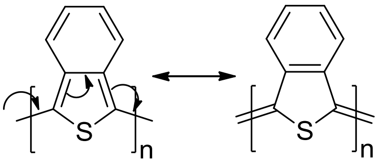

Figure 37. Basic chemical structure used by Heeger and co-workers to realize low-bandgap polymers.[182, 183]

A theoretical framework was set by Brédas in 1987 who did calculations on polymers with very low bandgaps and he inferred that low bandgap polymers could possess intrinsically high conductivity.[184] Brédas calculated the bandgap energy as a function of the difference in the carbon-carbon distance between the aromatic and quinoid structure (Δr) and found a linear dependence up to values for Δr of 0.06 Å where HOMO und LUMO might be degenerated in the case of high symmetry as shown in Figure 38.

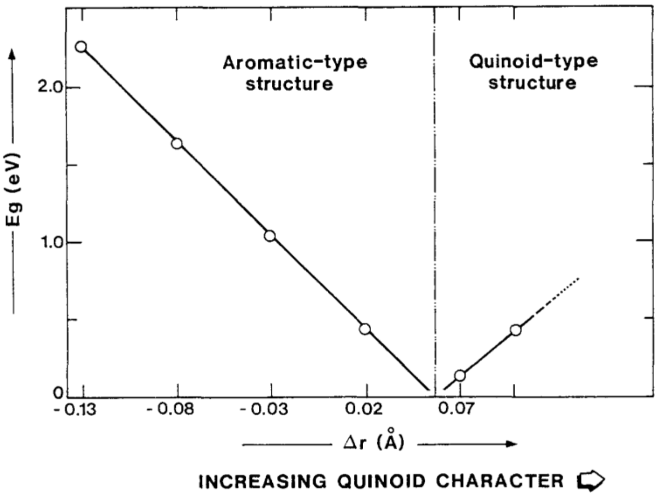

Figure 38. Calculation performed by Brédas showing the dependence of the bandgap E_g as a function of the carbon-carbon bond length difference Δr between quinoid and aromatic resonance structure.[184] Reprinted with permission from reference [184]. Copyright (1987) Elsevier B.V.

2.5.3.2 Donor-Acceptor Type Polymers

The development of low-bandgap polymers advanced greatly by the implementation of donor-acceptor design rules, *i.e.* the combination of electron-withdrawing and electron-donating subunits in the polymer backbone. This extends the absorption of the active layer of an organic solar cell considerably to longer wavelength and enables a better overlap of the absorption profile with the solar emission to facilitate more efficient harvesting of photons. Due to the interaction of the different moieties, the bandgap is narrowed which results in a bathochromically shifted absorption as illustrated schematically in Figure 39. The earliest low-bandgap polymers were published by Havinga *et al.*[185] in 1993 and they were explained theoretically three years later with MO theory by Brocks and Tol.[186]

Today, the vast majority of newly developed polymers profit from this concept to narrow the bandgap and recent PCE record holders originate from the family of low-bandgap, donor-acceptor type polymers. Typical donor and acceptor structures have been reviewed by Zhang *et al.* and most of the recent polymers are constituted of the structures presented in this review and are shown in Figure 40.[187] Recent record power

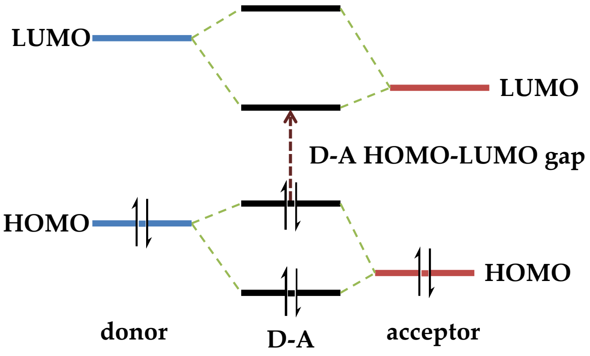

Figure 39. Energy level diagram of a donor-acceptor copolymer according to MO theory.

conversion efficiencies which exceeded 10% were achieved with polymers consisting of thiophenes and fluorinated benzothiadiazole in which the absorption extends up to 750 nm.[4] Very small bandgaps of ~1 eV have been demonstrated by Janssen and co-workers who combined the acceptor moieties diketopyrrolopyrrole and benzothiadiazole with electron donating thiophene units.[188]

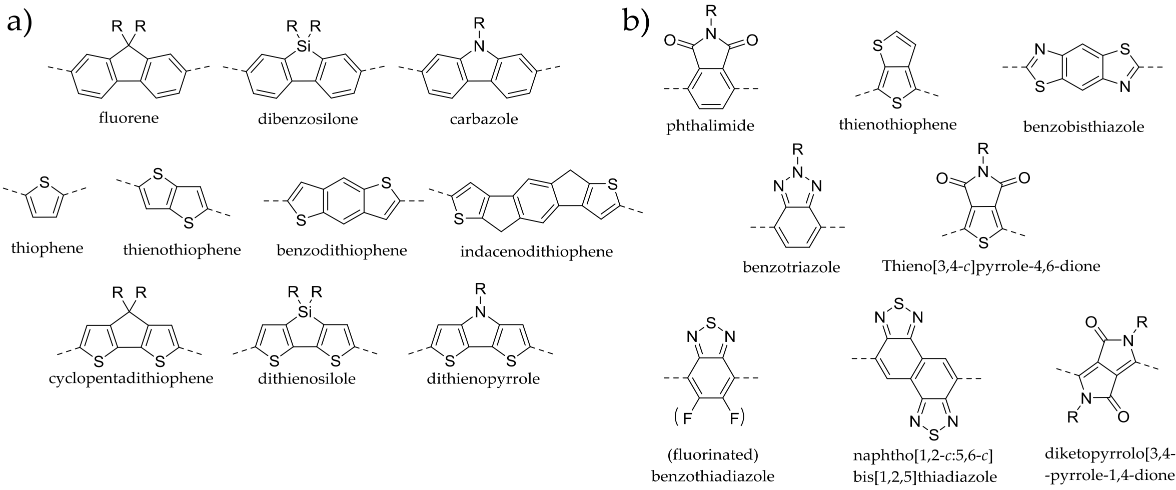

Figure 40. a) Typical donor and b) acceptor motifs used in donor-acceptor type low-bandgap polymers.

2.5.4 Donor Materials – Polymers *versus* Small Molecules

Most BHJ organic solar cells consist of polymer structures as donor-type material and fullerene derivatives as acceptor-type material although the earliest realization of an organic solar cell by Tang contained two small molecules as stated before.[45] Apart from the search for fullerene alternatives, which were shown in Sections 2.5.1 and 2.5.2, alternatives for donor *polymers* have been developed, namely small molecule donors.

Small molecule donors make use of the donor-acceptor concept introduced in Section 2.5.3.2 and accordingly their absorption profile can extent to the NIR part of the spectrum. The most important advantage inherent to small molecule donors is the well-defined structure in contrast to polymer structures that show a certain size distribution, which is manifested in the polydispersity index (PDI) of polymers. Consequently, small molecule donors will show less or even no batch-to-batch variation and hence better control of the properties. Moreover, another advantage is the possibility to evaporate small molecules and a better control of the morphology.

For instance, the small molecule donor molecule **72** (see Figure 41) was synthesized by Bürckstümmer *et al.* who combined this merocyanine-based small molecule donor with $PC_{61}BM$ as electron acceptor which resulted in a PCE of 2.59%.[189] The PCE was increased to 4.9% for vacuum processed solar cells based on HB194 and C_{60} showing the advantage inherent to thermally stable small molecules.[190]

Furthermore, a huge variety of small molecule donors is based on thiophene of which α-sexithiophene (see **73** in Figure 41) is one of the simplest representatives. Different side-chain patterns as well as electron-accepting end groups were demonstrated[191-197] to refine structures based on thiophene and the donor molecule DRCN7T (**74**) resulted in a PCE of 9.30% (9.05% on average) in combination with $PC_{71}BM$.[198]

A prominent representative of small molecule donor molecules studied in great detail is 7,7′-(4,4-bis(2-ethylhexyl)-4H-silolo[3,2-*b*:4,5-*b*′]dithiophene-2,6-diyl)bis(6-fluoro-4-(5′-hexyl-[2,2′-bithiophen]-5-yl)benzo[*c*][1,2,5]thia-diazole), known as (p-DTS(FBTTh$_2$)$_2$) or T1 shown in Figure 41. It was presented the first time by van der Poll *et al.*[199] and several other investigations were conducted which deal with this molecule.[114, 115, 200-206] Sections 4.3 and 4.4 of this thesis will show case studies based on this donor molecule in combination with a perylene diimide derivative and different fullerene derivatives, respectively.

The best performing small molecule donor so far, denoted as SMPV1 (see Figure 41), was introduced by Liu *et al.* and yielded a PCE of 8.02% in a single junction device when utilizing $PC_{71}BM$ as electron acceptor.[5] A tandem solar cell, *i.e.* a stack of two photovoltaic subcells to one solar cell, using two layers of SMPV1:$PC_{71}BM$ exhibited a PCE value as high as 10.1%.

For more information and a detailed overview of small molecule donor structures the reader is referred to a recent review article by Ni *et al.*[207]

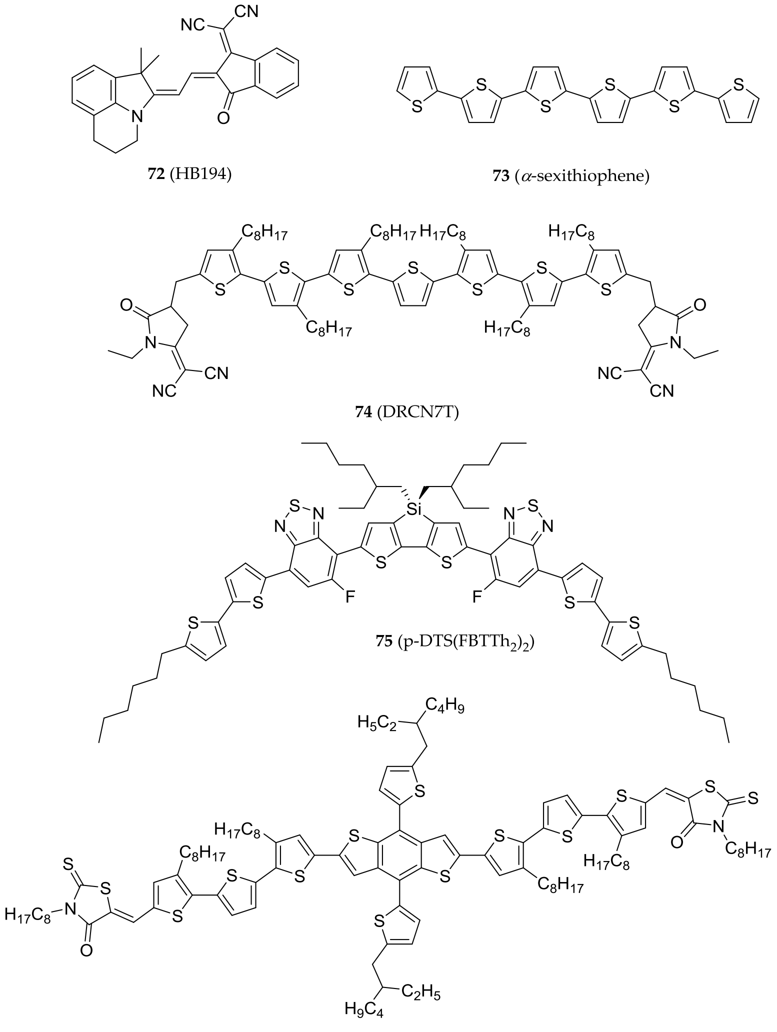

72 (HB194)

73 (α-sexithiophene)

74 (DRCN7T)

75 (p-DTS(FBTTh$_2$)$_2$)

76 (SMPV1)

Figure 41. Structures of small molecule donor structures including the recent record holder for small donor molecule SMPV1 as shown by Liu *et al*. which shows PCE values of 8.02% in single junction solar cells and 10.1% in homo-tandem solar cells with PC$_{71}$BM as electron acceptor.[5]

3 Experimental Section and Materials

3.1 Device Measurements

The current-voltage (*J-V*) characteristic of an organic solar cell is measured under illumination with light that corresponds to solar illumination. The international standard condition for illumination for solar cell testing is the AM1.5G spectrum defined by the American Society for Testing and Materials. AM stands for *air mass* which includes a set of conditions like a total column water vapor of 1.42 cm and a total column ozone equivalent of 0.34 cm.[208] *1.5* describes the distance l that light travels through the atmosphere before reaching the ground G with respect to the shortest distance l_0 which is at perpendicular incidence angle. A factor of l/l_0 of 1.5 corresponds to an incidence angle of 48.2° (= $\arccos(1.5^{-1})$) relating to the normal. The intensity is 100 mW cm^{-2}.

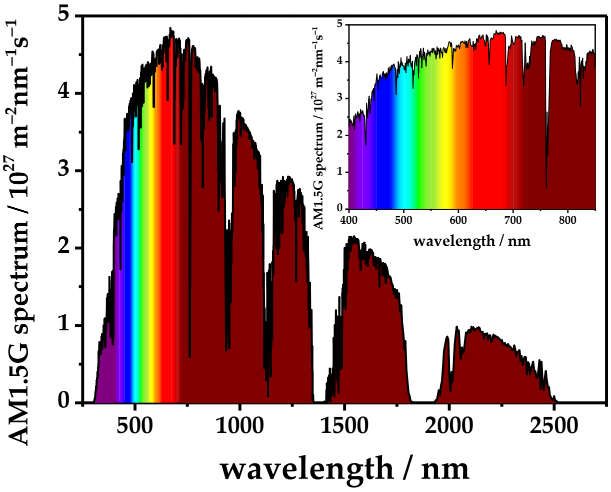

Figure 42. AM1.5G spectrum at an intensity of 100 mW cm^{-2} which corresponds to solar illumination at an incidence angle of 48.2°.[53]

For external quantum efficiency (EQE) measurements the solar cell is illuminated with monochromatic light which is realized experimentally by using a tungsten lamp in combination with a monochromator. EQE measurements are performed at short circuit conditions and the extracted current is measured in relation to the extracted current of a silicon detector which is used as a reference. Experimental details for *J-V* characteristics as well as EQE measurements are given in more detail in the experimental sections of the publications given in Chapter 4.

3.2 UV/Vis Absorption Spectroscopy

As explained in Equation 2 in Section 2.1.2 the Beer-Lambert law describes the reduction in light intensity when light passes through a material. The change of light intensity is measured experimentally with an UV/Vis absorption spectrometer which is depicted schematically in Figure 43. Light is emitted from a tungsten lamp and dispersed by a monochromator using a grating or a prism in combination with a slit. The monochromatic beam is then split in two equal parts by a beamsplitter. The reference beam is guided through the pure solvent (or blank substrate in case of a thin film) and then to a detector to give the light intensity I_0, the path of the second beam leads through the sample and the light intensity I is measured. By application of Equation 2 the optical density can be calculated with I and I_0.

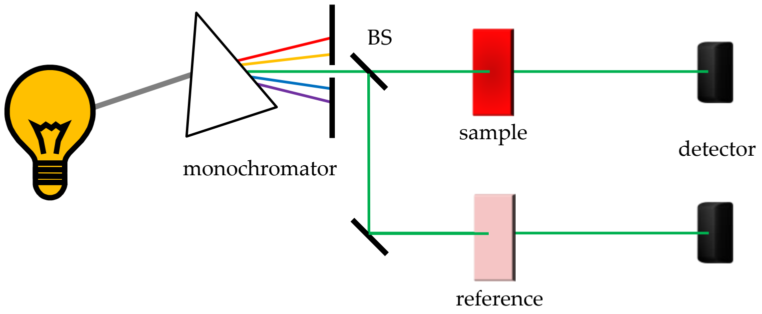

Figure 43. Schematic illustration of a UV/Vis spectrometer; BS = beam splitter.

3.3 Time-resolved Photoluminescence

Time-resolved photoluminescence (TRPL) can be measured with a streak camera setup which is shown

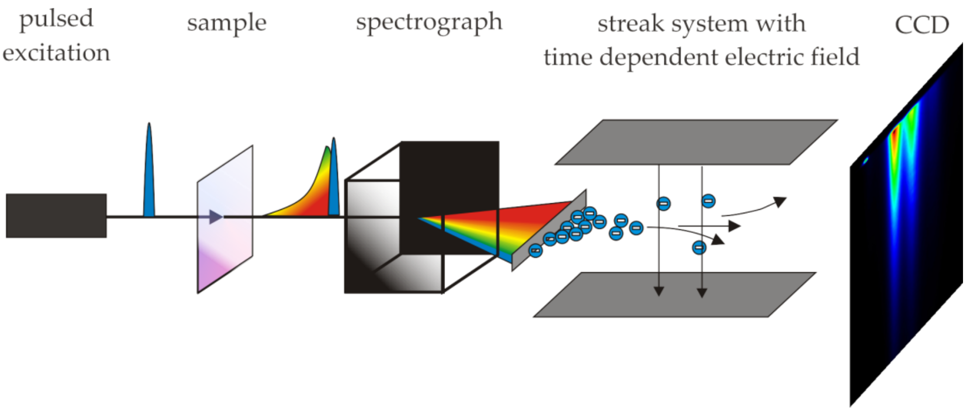

Figure 44. Schematic illustration of the operation principle of a streak camera. Adapted from reference with personal permission of the author.[209]

schematically in Figure 44. In TRPL measurement the sample is excited with a short laser pulses. The emitted light is then collected with a telescope consisting of two convex lenses and guided into the slit of the streak camera. The incident light is split into its different wavelengths by means of a grating or prism and lead to a photodiode. The photo-generated electrons are guided through metal plates on which a time-dependent electric field is applied, hence resulting in a time-dependent, spatial deviation of the electrons in the direction of the electric field. The electrons hit a charge-coupled device (CCD) where a streak image is detected depending on the wavelength (x-axis) and the time of emission (y-axis).

3.4 Transient Absorption Spectroscopy

Transient absorption spectroscopy is a pump-probe experiment that enables the time-resolved observation of the change in transmission related to photo-excited species. The change in transmission $\frac{\Delta T}{T}$ is defined with the following equation:

$$\frac{\Delta T}{T} = \frac{T_{on} - T_{off}}{T_{off}}$$ Equation **23**

where T_{on} is the transmission after the excitation of the sample while T_{off} corresponds to the transmission of light through the sample in the ground state.

When an organic material absorbs a photon, an electron is promoted from the HOMO to the LUMO, or in other words, an excited state is populated while the ground-state is depleted. This in turn will change the absorption/transmission behavior of the sample. On the one hand, the transmission of photons which would be absorbed by molecules in the ground state is increased, while on the other hand excited states contribute additional absorption in turn decreasing the transmission. The former process will result in a positive change in the transmission and is named ground-state bleach (GSB) the latter will be accompanied by a negative change in transmission and is denoted as photo-induced absorption (PIA). Additionally, stimulated emission (SE) of excited singlet states can be observed. Typical features observed in TA experiments are shown in Figure 46.

The signal height depends on the number of excited states N_i and their temporal evolution as well as their cross-section σ as a function of the wavelength λ, and the thickness of the sample d:

$$\frac{\Delta T}{T}(\lambda, t) = \sum_{i,f} \sigma_{i,f}(\lambda) \Delta N_i(t) d$$ Equation **24**

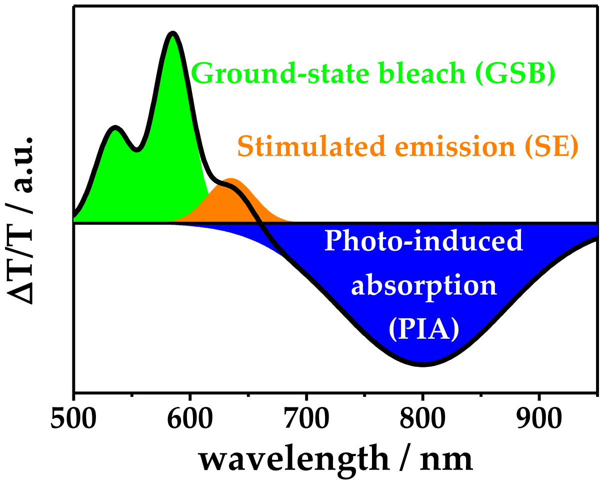

Figure 46. Constructed TA spectrum consisting of ground-state bleach (GSB, green), stimulated emission (SE, orange) and photo-induced absorption (PIA, blue). The black line represents the TA signal which is the sum of all contributions.

Often, different signal contributions overlap and consequently a direct extraction of dynamic information is not trivial. Therefore, sophisticated methods for data analysis have been developed among which multivariate curve resolution (MCR) is a powerful tool and will be the focus of the following section (see Section 3.5).

Experimentally, TA spectroscopy is realized as shown schematically in Figure 45 and described in literature as follows: "Transient absorption (TA) measurements were performed with a home-built pump-probe setup. To measure in the time range of 1–4 ns with a resolution of ~100 fs, the output of a commercial titanium:sapphire amplifier (Coherent LIBRA-HE, 3.5 mJ, 1 kHz, 100 fs) was split into two beams that

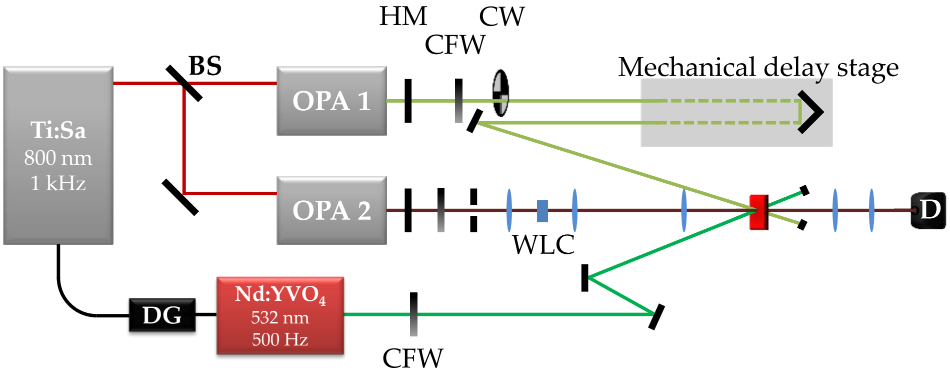

Figure 45. TA setup used for the measurements presented in the main part of this thesis. BS = beam splitter; D = detector; DG = delay generator; CFW = continuous filter wheel; CW = chopper wheel; HM = hot mirror; OPA = optical parametric amplifier; WLC = white light crystal.

pumped two independent commercial optical parametric amplifiers (Coherent OPerA Solo). One optical parametric amplifier (OPA) was used to generate the tunable excitation pulses in the visible, while the second OPA was used to generate the seed beam for white-light generation. For measurements in the spectral range between 550–1100 nm a 1300 nm seed of a few µJ was focused into a c-cut 3 mm thick sapphire window for white-light generation. The variable delay of up to 4 ns between pump and probe was introduced by a broadband retroreflector mounted on a mechanical delay stage. Mostly reflective elements were used to guide the probe beam to the sample to minimize chirp. The excitation pulse was chopped at 500 Hz, while the white-light pulses were dispersed onto a linear silicon photodiode array, which was read out at 1 kHz by home-built electronics. Adjacent diode readings corresponding to the transmission of the sample after an excitation pulse and without an excitation pulse were used to calculate $\Delta T/T$.

For measurements in the time range between 1 ns to 1 ms with a resolution of 600 ps, the excitation pulse was provided by an actively Q-switched $Nd{:}YVO_4$ laser (AOT Ltd. MOPA) at 532 nm. In this case the delay between pump and probe was controlled by an electronic delay generator (Stanford Research Systems DG535). TA measurements were performed at room temperature under a dynamic vacuum of $<10^{-5}$ mbar.

For TA measurements in the NIR spectral range covering 1100–2000 nm a 2100 nm seed was used to generate white-light in an yttrium vanadate window. Furthermore, a dichroic mirror was used to separate the residual seed beam (idler of the OPA at 2100 nm) from the broadband NIR supercontinuum. The NIR pulses were dispersed onto a Peltier-cooled 512 pixel long linear extended InGaAs array (Entwicklungsbüro Stresing) and read out as described above."[210]

3.5 Multi-Variate Curve Resolution

Multi-variate curve resolution alternating least squares (MCR-ALS) is a soft-modelling approach for the analysis of TA data which renders the spectra S as well as the concentration profiles C of the single species which contribute to the data surface D.

$$D = CS + E \qquad \text{Equation } \mathbf{25}$$

where E is the residual error matrix. The algorithm used herein is based on the work of Tauler *et al.*[211-213] who designed the algorithm for the analysis of systems consisting of many components, *e.g.* the deconvolution of absorption spectra in high performance liquid chromatography. It should be noted, that solutions obtained by MCR are not unique, but can be altered by a matrix and the respective transposed matrix. The initial conditions for the optimization are obtained by an evolving factor analysis (EFA) based on a singular value decomposition (SVD) which is used to determine the number of involved species and also allows for the identification of the time when a species evolves and/or decays. The advantage of MCR analysis is that a priori no input of physical knowlegde is necessary for the decomposition. However, additional information allows to select the physically most meaningful solution of the manifold of mathematically equivalent solutions. Moreover, physical constraints increase the accuracy of the analysis and reduce the ambiguity of the result. Constraints could be for example, that concentration profiles should not have negative values or spectra in the NIR region, where no GSB or SE occurs, should not be positive. However, the solution rendered by MCR is at first only a mathematical one and its validity has to be supported by independent measurements that enable the identification of single species. Spectra of excited or charged states can be used to support the analysis. In the case of the donor-acceptor blends which are in the focus of this thesis, this might be the exciton spectrum of the donor obtained by TA measurements of the pristine materials or the charge spectrum obtained by oxidation experiments using Iron(III)-chloride or Iodine vapor as oxidation agent. Triplet spectra can be obtained by TA measurements of blend films consisting of the material under investigation and a triplet sensitizer, typically metal-organic compounds in which the heavy-atom effect of the metal part allows for efficient intersystem crossing. MCR analysis and its applicability for the analysis of TA data has recently been reported and reviewed by us in a separate publication[214] and was successfully applied to a range of material systems.[205, 210, 215-218] Examples for the application are presented in Chapter 4 of this thesis.

3.6 Materials

3.6.1 Electron-donating Materials

Two parts of the main chapter of this thesis focus on the optoelectronic and photophysical properties of perylene diimide derivatives used as electron acceptors in photovoltaic devices in combination with different low-bandgap donors, namely the polymer PBDTTT-C as well as the small molecule p-DTS(FBTTh$_2$)$_2$. The findings of these studies are presented in Sections 4.1 and 4.3, respectively. To fully understand the suitability of the PDI derivatives and to evaluate their performance in comparison to the widely applied fullerene derivatives, the aforementioned donors were also combined with fullerene derivatives. The results are shown in Sections 4.2 and 4.4.

Poly[(4,8-bis-(2-ethylhexyloxy)-benzo[1,2-b:4,5-b′]dithiophene)-2,6-diyl-alt-(4-(2-ethylhexanoyl)-thieno[3,4-*b*]thiophene))-2,6-diyl], abbreviated as PBDTTT-C, is used as donor polymer in Sections 4.1 and 4.2. Its family of related polymers encompasses for example the widely used polymers PTB7 and PBDTTT-CT.[52, 219] PBDTTT-C is an alternating D-A structure with benzodithiophene and thienothiophene units as shown in

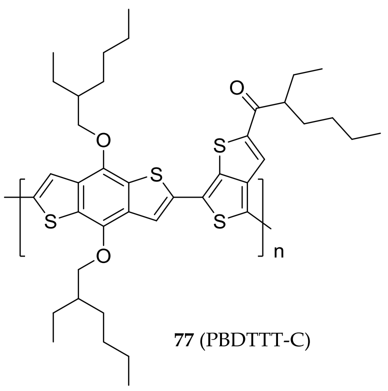

77 (PBDTTT-C)

Figure 47. PBDTTT-C is the low-bandgap donor polymer which is used in the case studies presented in Sections 4.1 and 4.2.

Figure 47. PBDTTT-C has a bandgap E_g of 1.77 eV or 700 nm and favorable energy levels with −3.35 eV for the LUMO and −5.12 eV for the HOMO energy.

7,7′-(4,4-bis(2-ethylhexyl)-4H-silolo[3,2-*b*:4,5-*b*′]dithiophene-2,6-diyl)bis(6-fluoro-4-(5′-hexyl-[2,2′-bithiophen]-5-yl)benzo[*c*][1,2,5]thiadiazole), shortly p-DTS(FBTTh$_2$)$_2$, is a small molecule consisting of typical donor and acceptor moieties which were introduced earlier in Figure 40 in Section 2.5.3.2. The molecule has a central donor-type dithienosilole unit, which is surrounded by the acceptor-type mono-fluorinated benzothiadiazole which are furthermore winged by two thiophene units each as shown in Figure 48. HOMO and LUMO levels are reported to be −5.12 eV and −3.34 eV, respectively.[199] The absorption maximum in thin film is located at 678 nm, the onset of absorption at 800 nm.

In addition to the investigation of PDI and the comparison with the respective fullerene blends, the influence of the nanomorphology is discussed in Section 4.5. Here, the donor polymer poly[2,5-bis(3-tetradecylthiophen-2-yl)thieno[3,2-*b*]thiophene] (pBTTT-C14) is used as a model system to elucidate the

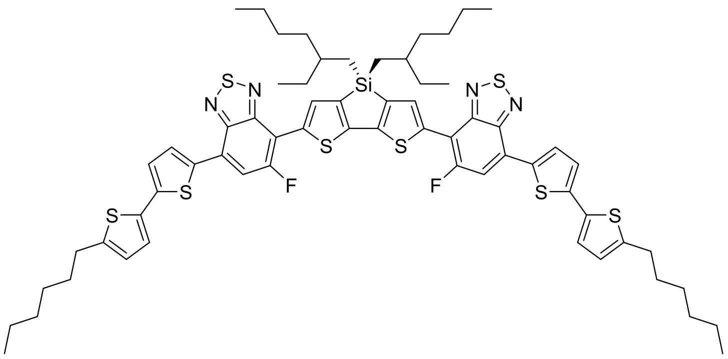

78 (p-DTS(FBTTh$_2$)$_2$)

Figure 48. Chemical structure of the small molecule donor p-DTS(FBTTh$_2$)$_2$ used in the case studies presented in Sections 4.3 and 4.4.

impact of phase separation in bulk heterojunction solar cells. Figure 49 shows the structure of pBTTT which offers the advantage that active layers with a well-defined nanomorphology can be achieved. For example, fullerene mono-adducts form cocrystals with pBTTT in which the fullerene intercalates between the sidechains of pBTTT while fullerene bis-adducts form separated domains as they are too large for intercalation.[89] Moreover, non-volatile additives, namely aliphatic acid methyl esters, can be used to direct the morphology.[91] The material system investigated in this thesis is controlled *via* the donor-acceptor ratio which is also known to influence the nanoscale morphology.[85] For low fullerene content only cocrystals are obtained while an increasing fullerene fraction triggers the formation of pure fullerene phases in addition to the cocrystal phase.

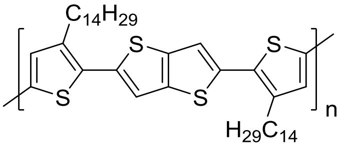

79 (pBTTT-C14)

Figure 49. Chemical structure of pBTTT-C14, used to study the influence of nanomorphology on the photophysics in blends used for organic solar cells in Section 4.5.

3.6.2 Electron-accepting Materials

The acceptor structures which are used in the framework of this thesis are displayed in Figure 50. Perylene diimide is in the focus of investigations for the reasons given in Section 2.5.1, including high extinction coefficients in the visible part of the spectrum, favorable electronic levels, and good thermal and photo stability. The PDI used in this study is substituted with a branched alkyl chain at the imide-position. It was shown in Section 2.5.1 as PDI **13** and is known as electron acceptor from several publications.[105, 112-114] The results of blends with the low-bandgap donor polymer PBDTTT-C and the small molecule donor p-DTS(FBTTh$_2$)$_2$ are presented in Sections 4.1 and 4.3.

To fully understand the performance of the perylene diimide based acceptors, their photophysics are compared with the widely-used and often well-performing fullerene derivatives. The fullerenes used herein include three different derivatives, namely Phenyl-C61-butyric acid methyl ester (PC$_{61}$BM), Indene-C60-bisadducct (IC$_{60}$BA), and Phenyl-C71-butyric acid methyl ester PC$_{71}$BM, each with its own advantages and disadvantages. PC$_{61}$BM and IC$_{60}$BA are cheaper compared to PC$_{71}$BM, while the absorption of PC$_{71}$BM extends further in the visible part of the spectrum.[220] IC$_{60}$BA exhibits a higher LUMO level of −3.74 eV[205] compared to PC$_{61}$BM (−3.91 eV[205]) and PC$_{71}$BM (−4.3 eV[201]) which enables higher V_{OC} values potentially improving the device efficiency.[221]

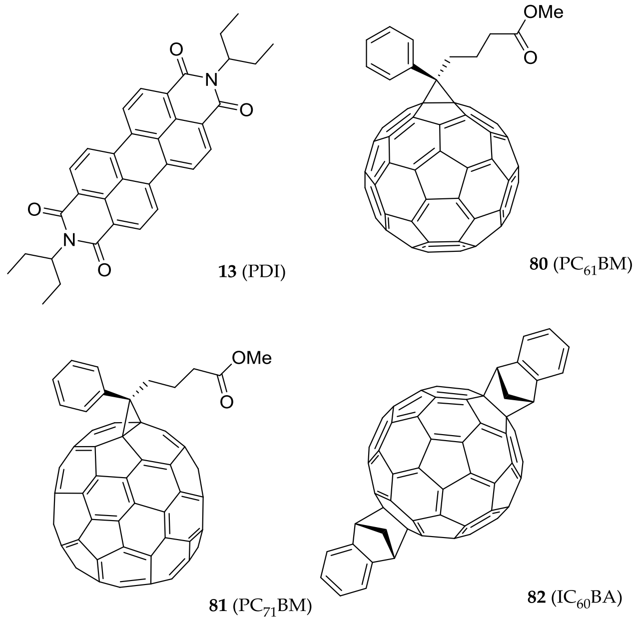

13 (PDI)

80 (PC$_{61}$BM)

81 (PC$_{71}$BM)

82 (IC$_{60}$BA)

Figure 50. Chemical structures used as electron acceptors in Chapter 4 of this thesis.

4 Results

In this chapter studies on different material systems are presented.

Section 4.1 is a case study of a low-bandgap polymer, namely PBDTTT-C, in combination with an imide-substituted perylene diimide derivative introduced in the previous Section 3.6.2. Transient absorption spectroscopy, time-resolved photoluminescence (TRPL), as well as time-delayed collection field (TDCF) experiments were applied to elucidate the limiting factors in devices using this material combination. For a full understanding of the system, PBDTTT-C was blended with $PC_{61}BM$ and the charge generation efficiency in both acceptors was compared.

The following Section 4.2 is a detailed study of the processes occurring in blends of the same polymer, PBDTTT-C, used in the previous Section 4.1, in combination with the fullerene derivative $PC_{61}BM$. Quantitative triplet generation on a sub-ns timescale was observed while the respective films showed a decent efficiency in a device. Moreover, charges were regenerated *via* triplet-triplet annihilation on a timescale of 200 ns and decaying subsequently *via* non-geminate recombination.

In Section 4.3 the PDI of the first case study comes again into play, now in combination with a small molecule donor, namely p-DTS$(FBTTh_2)_2$. This material combination was amongst the best performing PDI based solar cell with a PCE of 3% at the time of its publication. A series of techniques, namely TA spectroscopy, TRPL, grazing incidence x-ray scattering (GIWAXS), and atomic force microscopy (AFM) were applied to fully understand the processes governing the efficiency of the device. Especially, the important

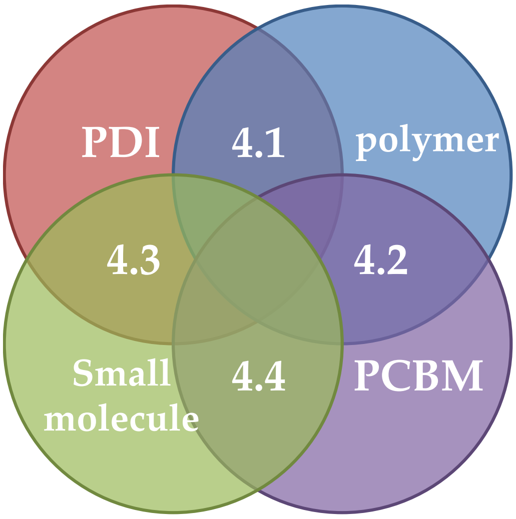

Figure 51. Graphical summary of Sections 4.1-4.4.

role of the solvent additive DIO which is necessary to achieve the optimal performance is investigated and the photophysical experiments could show the origin of the improvements associated with the solvent additive.

Furthermore, the small molecule p-DTS(FBTTh$_2$)$_2$ was combined with the fullerene derivatives PC$_{71}$BM as well as IC$_{60}$BA and the results are presented in Section 4.4. ICBA yielded a higher open-circuit voltage compared to PCBM due to its higher LUMO level, however, a reduced short circuit current was obtained, so that in summary an inferior performance was achieved for ICBA as compared to PCBM. A photophysical investigation by TA spectroscopy in combination with morphological experiments including AFM and GIWAXS measurements revealed a reduced generation of spatially separated charges in donor:ICBA blends in comparison to the donor:PCBM blends which could explain the lower efficiency of the respective photovoltaic devices.

Chapter 4 is completed by Sections 4.5 which deals with the influence of the nanomorphology on the performance of organic solar cells. The influence of the microstructural order on the process of charge generation and recombination introduced by the donor-acceptor ratio in the archetypical pBTTT:PCBM system was investigated by TA spectroscopy and it was found that extended pure fullerene domains aid the generation of SSC. This is in line with the finding that the coexistence of intermixed and aggregated phases results in a driving force for charge separation as the electron affinity of aggregated acceptor domains is larger than for less-ordered regions.[76]

4.1 PBDTTT-C:Perylene Diimide Solar Cells

The article “Efficiency-Limiting Processes in Low-bandgap Polymer:Perylene Diimide Photovoltaic Blends" was published in the Journal of Physical Chemistry C and is available online since August 8th, 2014. A previous study of the material system entitled "Charge generation in polymer:perylene diimide blends probed by Vis–NIR broadband transient absorption pump-probe spectroscopy" has been presented at the 12th Conference on Physical Chemistry of Interfaces and Nanomaterials and was published in the proceedings of the conference September 11th, 2013. The articles are reprinted with permission from references [210] and [215]. Copyright (2014) American Chemical Society and (2013) Society of Photo Optical Instrumentation Engineers.

THE JOURNAL OF
PHYSICAL CHEMISTRY C

Article

pubs.acs.org/JPCC

Efficiency-Limiting Processes in Low-Bandgap Polymer:Perylene Diimide Photovoltaic Blends

Dominik W. Gehrig,[†] Steffen Roland,[‡] Ian A. Howard,[†,§] Valentin Kamm,[†] Hannah Mangold,[†] Dieter Neher,[‡] and Frédéric Laquai*,[†]

[†]Max Planck Research Group for Organic Optoelectronics, Max Planck Institute for Polymer Research, Ackermannweg 10, D-55128 Mainz, Germany

[‡]Institut für Physik und Astronomie, Physik weicher Materie, University of Potsdam, Karl-Liebknecht-Straße 24–25, 14476 Potsdam-Golm, Germany

Ⓢ *Supporting Information*

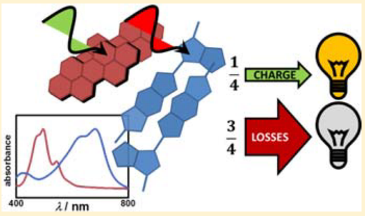

ABSTRACT: The charge generation and recombination processes following photoexcitation of a low-bandgap polymer:perylene diimide photovoltaic blend are investigated by transient absorption pump–probe spectroscopy covering a dynamic range from femto- to microseconds to get insight into the efficiency-limiting photophysical processes. The photoinduced electron transfer from the polymer to the perylene acceptor takes up to several tens of picoseconds, and its efficiency is only half of that in a polymer:fullerene blend. This reduces the short-circuit current. Time-delayed collection field experiments reveal that the subsequent charge separation is strongly field-dependent, limiting the fill factor and lowering the short-circuit current in polymer:PDI devices. Upon excitation of the acceptor in the low-bandgap polymer blend, the PDI exciton undergoes charge transfer on a time scale of several tens of picoseconds. However, a significant fraction of the charges generated at the interface are quickly lost because of fast geminate recombination. This reduces the short-circuit current even further, leading to a scenario in which only around 25% of the initial photoexcitations generate free charges that can potentially contribute to the photocurrent. In summary, the key photophysical limitations of perylene diimide as an acceptor in low-bandgap polymer blends appear at the interface between the materials, with the kinetics of both charge generation and separation inhibited as compared to that of fullerenes.

1. INTRODUCTION

The maximum power conversion efficiency of polymer:fullerene organic solar cells is restricted by the absorbance of the rather thin organic layer and limited absorption range of the blend's components; consequently, photon harvesting at the thin photoactive layer is incomplete. The low absorbance of fullerene acceptors exacerbates this problem, especially when low-bandgap polymers are used that often perform best if a higher fullerene loading, up to four times as much acceptor as donor, is used.[1] Recent theoretical work forecasts that optimum performance of single-layered solar cells using optimized polymer:fullerene blends is limited to roughly 12%,[2] and state-of-the-art polymer:fullerene solar cells are already close to this limit.[3] Thus, alternative acceptor materials, such as nonfullerene acceptors, must be designed to cope with these limitations. Typical requirements to be met by nonfullerene acceptor molecules are not only a high absorption but also a sufficient electron mobility, as well as a desirable donor–acceptor interaction to facilitate charge separation, while simultaneously avoiding charge recombination. The properties of fullerene derivatives which contribute to their high performance in organic solar cells likely include isotropic charge transport properties with reasonable mobility, a lowest unoccupied molecular orbital (LUMO) energy compatible with many different donor polymers, and the tendency to crystallize which assists in creating a desirable mesostructure in many blends.[4] To replace fullerenes, a detailed understanding of charge generation and separation at (mesoscale structured) organic interfaces is necessary and is hotly pursued from experimental and theoretical perspectives.

A variety of different organic as well as inorganic candidate fullerene replacements have been synthesized. Several have reached device efficiencies close to only 1%.[5−10] Some higher efficiencies have also been reported; for instance, Sellinger and co-workers recently claimed a power conversion efficiency (PCE) of 2.54% for an acceptor based on benzothiadiazole in combination with poly(3-hexylthiophene) (P3HT) as donor[5] and Zhou et al. showed a power conversion efficiency of inorganic CdSe quantum dots in combination with PCPDTBT as high as 4.7%.[11] Furthermore, an increase in PCE to 4.34% was achieved for a system consisting of a twisted perylene diimide (PDI) bichromophore in combination with the low-bandgap polymer PBDTTT-CT as recently reported by Lu et al.[12] A power conversion of 4.4% efficiency was achieved by Ye et al. following a similar stategy.[13] They related the appreciable performance observed for these material systems to the improved intermixing of the donor and acceptor compared to that of planar PDI derivatives and consequently a better exciton

Received: April 5, 2014
Revised: July 30, 2014
Published: August 8, 2014

dx.doi.org/10.1021/jp503366m | *J. Phys. Chem. C* 2014, 118, 20077−20085

quenching at the interface. Generally, PDI derivatives have received significant attention as novel acceptors in organic solar cells owing to their significant absorbance, photochemical stability, preferable electron transport properties, and scalability as well as low-cost synthesis.[14−16] They have also been implemented as accepting building block in donor−acceptor type block copolymers for photovoltaic applications.[17−20]

However, the photophysical processes that determine the performance of PDI as an acceptor have not yet been fully understood. In previous work we found that excimer (aggregate) formation could limit the flow of PDI excitons to the interface,[21,22] but that this could be addressed by core-alkylation of PDIs which increased their efficiency when mixed with higher bandgap polymers such as polythiophenes.[14] Durrant and co-workers demonstrated that, in contrast to fullerene blends, charge generation did not depend on the excess driving energy for PDI used as an acceptor in a sequence of polythiophene polymers with varying LUMOs.[23] On the other hand, Pensack et al. have recently reported that charge generation in a polythiophene:PDI blend is temperature-activated (in contrast to temperature-independent charge separation often found with fullerene acceptors).[24]

The full potential of PDI in terms of optimizing solar absorption lies in blends with low-bandgap polymers, so it is the photophysics in such blends that are most important. Very recent work on the photophysics of a twisted perylene bichromophore mixed with the low bandgap polymer PBDTTT-CT has revealed critical insights into the physical processes that lead to a 3.2% power conversion efficiency (in a 1:1 blend of these materials) and demonstrated that similar efficiencies of charge generation and separation could be obtained when either twisted-PDI dimers or fullerene was used as an acceptor. The success of this twisted-PDI dimer was hypothesized to arise from its increased dimensionality and its formation of more favorable morphologies (with respect to PDI monomers).

In this work we present a high time-resolution, high-dynamic range, photophysical study of a low-bandgap polymer:PDI blend that has distinct polymer as well as PDI ground-state absorption (GSA) and excited-state absorption (ESA) spectra that allow for selective PDI or polymer excitation and also minimize spectral overlap of the photogenerated species, which in turn facilitates the data interpretation and enables unexampled insights into the photophysics of polymer:PDI blends. The donor polymer selected was PBDTTT-C, and the processes including charge generation and recombination were monitored by transient absorption (TA) pump−probe spectroscopy capturing a spectral range from 500−1600 nm and a time range from 100 fs to microseconds. Importantly, we also performed time-delayed collection field (TDCF) experiments to study the field dependence of free-charge generation. As we will show below, the combination of these complementary techniques allows us to unravel the processes limiting the efficiency of these blends. Specifically, we identified slow charge transfer and inefficient charge separation at the interface in combination with substantial geminate recombination to be the main processes restraining the device performance. The TDCF experiments showed that charge separation in the device was also field-activated. This is consistent with observation of poor charge separation in transient absorption and also reduces the device's fill factor and short-circuit current. Finally, we found that even if free charges are created they do not necessarily contribute to the extractable photocurrent as nongeminate recombination competes with extraction, further limiting the performance of polymer:PDI solar cells. This gives a clear account of the losses faced by PDI monomers as acceptors in low-bandgap polymer matrices and clearly supports the motivation for the search of higher dimensionality small molecule acceptors which better support charge generation and separation.

2. RESULTS

2.1. Materials and Steady-State Absorption Spectra.

Scheme 1 shows the chemical structures of the low-bandgap donor polymer poly[(4,8-bis(2-ethylhexyloxy)-benzo[1,2-b:4,5-b’]dithiophene)-2,6-diyl-*alt*-(4-(2-ethylhexanoyl)-thieno[3,4−b]thiophene)-2,6-diyl], termed PBDTTT-C, and the PDI derivative used as electron acceptor in the present study. Figure 1 depicts the absorption spectra (lower panel) as reported earlier.[25] The spectra correspond to a polymer film and a blend of the PDI derivative and the electronically inactive polymer polystyrene as well as the spectrum corresponding to a PBDTTT-C:PDI (1:3) blend used as photoactive layer in the solar cells, for optical spectroscopy and electro-optical characterization. Figure 1 also compares the absorption spectra to the spectrum of the solar photon flux (upper panel). The absorption spectra of PDI and PBDTTT-C are complementary

Scheme 1. Chemical Structures of the Low-Bandgap Polymer, Namely PBDTTT-C, and the PDI Derivative Used in This Study

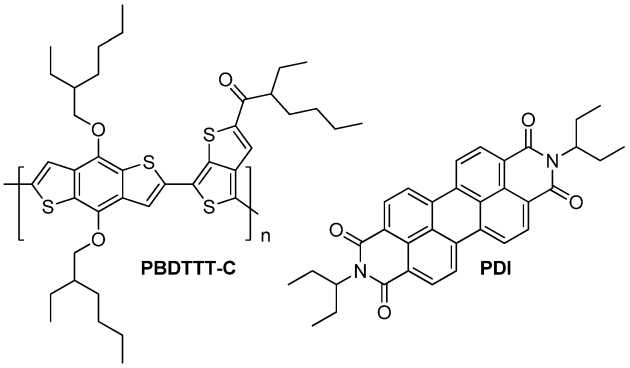

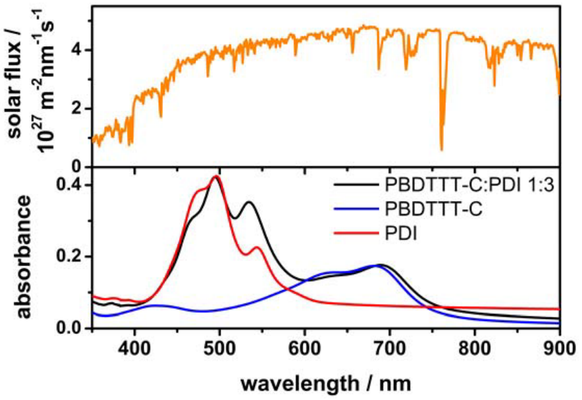

Figure 1. Solar irradiation spectrum (Terrestrial Global 37° South Facing Tilt; upper panel) and absorption spectra of a pristine PBDTTT-C thin film ($d \sim 100$ nm), a blend of PDI with polystyrene (50 wt %), and the PBDTTT-C:PDI photovoltaic blend (1:3 wt %) (lower panel).

in large parts as PDI covers the spectral region between 450 and 550 nm and PBDTTT-C the range from 550 to 750 nm. The PDI absorption exhibits features typical for H-aggregate formation, i.e., a reduced oscillator strength of the 0−0 transition relative to the 0−1 transition, as reported earlier for this class of materials.[14,26−28] The absorbance of the PDI was significantly larger than the absorbance of the polymer in the photoactive layer because of the relatively high content of PDI in relation to the polymer used in the best performing devices (see also Figure S1 of Supporting Information).

We note that the clear separation of the absorption features of PDI and PBDTTT-C allows for the selective excitation of PBDTTT-C at wavelengths exceeding 650 nm, where PDI does not absorb at all because of its larger optical bandgap. Furthermore, PDI excitation is favored at around 500 nm, as the polymer absorption is comparably weak, consequently enabling us to investigate the photophysical cascade triggered by the exclusive excitation of one or the other component.

2.2. Photovoltaic Performance. Figure 2a depicts the *JV*-curves of PBDTTT-C:PDI (1:3) solar cells before and after annealing together with the dark currents of the respective cells. The as-cast solar cell exhibited an open-circuit voltage (V_{OC}) of 0.59 V, a short-circuit current density (J_{SC}) of 2.2 mA/cm^2, and a fill factor (FF) of 42%, yielding a total power conversion efficiency of 0.8%. Annealing led to an increase of all these values with a V_{OC} of 0.62 V, a J_{SC} of 2.8 mA/cm^2, and a FF of 46%, resulting in a PCE of 1.2%. Both devices show a significant bias dependence of the photocurrent, as can be seen by the comparably low fill factor and the steady increase of the photocurrent at more negative bias. Figure 2b shows the external quantum efficiency (EQE) spectrum of the device after annealing. The polymer:PDI layer absorbs in the relevant wavelength range up to 800 nm with EQE values approaching 30% at 460 nm, which correlates to photons absorbed by PDI molecules. From the EQE and the blend's absorption spectrum, the internal quantum efficiency (IQE) was calculated using a transfer matrix approach as recently presented by Burkhard et al.[29] Interestingly, the IQE is essentially constant across the entire wavelength range from 350 to 700 nm, indicating that the quantum efficiency loss is similarly independent of the PDI or polymer excitation. From the blend's absorption spectrum, the theoretical J_{SC} maximum was calculated according to the method presented by Burkhard et al. This approach considers the absorbance of the film as well as reflection of light at the electrodes and interference effects within the photoactive layer and takes into account an IQE of unity.[29] This results in a predicted maximum J_{SC} value for the PBDTTT-C:PDI (1:3) blend of 11.2 mA/cm^2 at a 100 nm thick active layer under irradiation of 0.7 suns, corresponding to the conditions in our experiments. Accepting a measured J_{SC} of only 2.8 mA/cm^2 means a quantum efficiency loss of about three-fourths at short-circuit conditions.

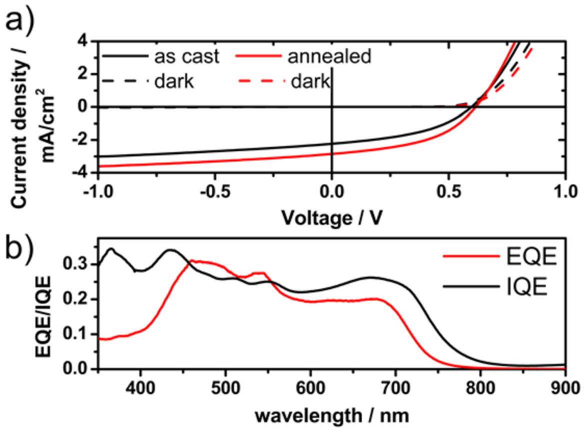

Figure 2. (a) Current density−voltage characteristics of PBDTTT-C:PDI (1:3) solar cells before (black) and after (red) annealing under AM1.5G-like conditions with 0.7 suns illumination. Dark currents of the respective devices are depicted by dashed lines. (b) Measured EQE (red) and calculated IQE (black) of the annealed PBDTTT-C:PDI (1:3) solar cell.

2.3. Early Time (Picosecond−Nanosecond) Exciton Diffusion, Charge Transfer, Dissociation, and Geminate Recombination. To track the sequence of physical events that lead to these quantum efficiency losses, we undertook a series of transient absorption experiments. TA is a two-pulse pump−probe experiment, which probes the pump-induced change of the transmission ($T_{ON} - T_{OFF}$) of the sample with respect to the sample's ground-state transmission (T_{OFF}) by using a second probe pulse. Typically, the pump pulse is a femtosecond narrowband laser pulse, while the probe pulse is a broadband supercontinuum covering a spectral range as wide as possible. The temporal delay between pump and probe pulse is variable to allow for studying the signal dynamics. The change in transmission $\Delta T/T$ is plotted versus the wavelength or energy. Here, negative signals are assigned to photoinduced absorption (PA), while positive signals indicate either stimulated emission (SE) corresponding to singlet excitons or a ground-state bleach (GSB) originating from the depopulated ground state of the material when excited states are present. Often the different species-associated contributions overlap. Consequently, the evolution of the population (concentration) of excited states as a function of time has to be obtained by factorization of the measured data matrix. In general, this factorization problem is ill-posed, so either additional physical knowledge (often in the form of rate equations or known spectra) is necessary to obtain a unique solution. However, by probing the largest spectral range possible (here the visible and entire near-infrared (NIR)) and selecting a donor and acceptor with minimal overlap in ground- and excited-state spectra, this issue can be minimized and meaningful population kinetics can be extracted from the data without the need for additional physical constraints. Also, to track the whole cascade of processes, the nano- to microsecond time range was measured in addition to the femto- to nanosecond range. Figure 3 shows the Vis−NIR pump−probe spectra of a PBDTTT-C:PDI (1:3) blend on the picosecond−nanosecond time scale (Figure 3a) as well as the TA spectra of pristine PBDTTT-C on the same time scale (Figure 3b).

The film of the pristine polymer shows a positive signal in the visible wavelength region up to 860 nm, which is assigned to the ground-state bleach and stimulated emission of the polymer according to the appearance of the absorption and emission of the polymer, respectively. Furthermore, at lower energy, a broad photoinduced absorption (PA_{Ex}) around 1415 nm is observed, which originates from the singlet excited states generated in the pristine material by photoexcitation. The isosbestic point at a $\Delta T/T$ of 0 at 860 nm indicates the decay of a single excited species to the ground state within a nanosecond. The GSB and PA_{Ex} dynamics (see Supporting Information) exhibit a pronounced intensity dependence suggesting singlet−singlet annihilation (SSA) occurs after

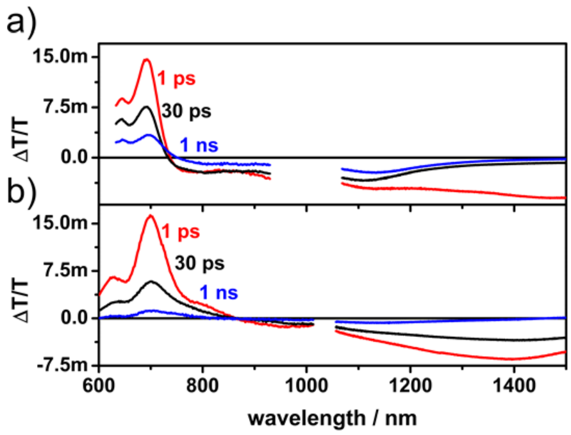

Figure 3. (a) Transient absorption spectra of PBDTTT-C:PDI (1:3) blends at delay times of 1, 30, and 1000 ps after excitation of the polymer at 650 nm with 45.5 μJ/cm^2. (b) Picosecond−nanosecond transient absorption spectra of a pristine PBDTTT-C polymer thin film after excitation at 650 nm with 20.0 μJ/cm^2.

high-intensity excitation because of the increased density of excitons. At a low pump fluence (∼1.7 μJ/cm^2), however, the signal decay could be explained by a mono-exponential fit showing an inverse rate constant of 266 ps (see Figure S2 of Supporting Information), which is in good agreement with the polymer's fluorescence lifetime (257 ps; see Figure S3 of Supporting Information) obtained by Streak Camera experiments indicating negligible SSA at the lowest pump fluences used in our TA experiments. It is noteworthy that at elevated pump intensities the TA spectra at late times (∼1 ns) exhibit a small signal remaining at 1150 nm. This indicates the creation of a small number of charges in the pristine polymer, especially after high-intensity excitation, most probably originating from SSA.

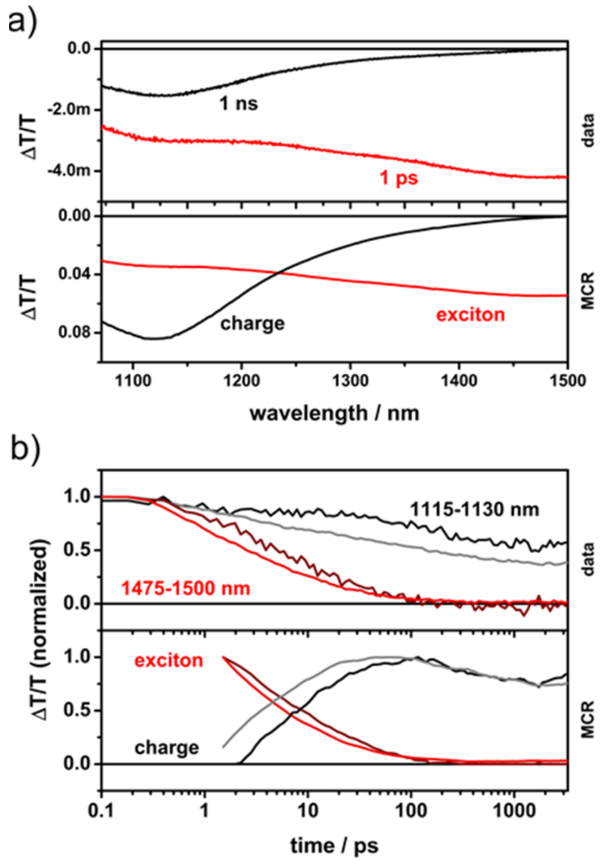

Figure 4. (a) Picosecond−nanosecond TA spectra of PBDTTT-C:PDI (1:3) blends 1 ps and 1 ns after excitation at 650 nm (polymer excitation, upper panel) and component spectra (lower panel) obtained by MCR analysis. (b) Kinetics obtained by tracking the decay of the TA signal at 1075−1125 nm (black) and 1425−1475 nm (red) (upper panel) and concentration profiles of both components obtained by MCR analysis at the highest and lowest fluence (lower panel).

The picosecond−nanosecond transient absorption spectra of the PBDTTT-C:PDI blends after excitation at 650 nm corresponding to the polymer absorption show a GSB of the polymer up to 729 nm and a broad PIA spanning the whole NIR spectral range with a peak at 1500 nm at early times. This peak vanishes within the first 100 ps, after which a PIA between 742 and 1400 nm remains, peaking at 1130 nm. These spectral changes are assigned to a population conversion from singlet excitons located on the polymer to charges, according to the appearance of the charge-induced absorption (PA$_C$) of PBDTTT-C. The assignment of this feature to the charge-induced absorption is additionally backed up by comparing the early time transient absorption spectra of a PBDTTT-C:PCBM blend (see Figure S4a of Supporting Information) and a chemically oxidized PBDTTT-C film (see Figure S5 of Supporting Information) with the spectra shown in Figure 3, which showed similar PA$_C$ of the polymer. We note that the NIR TA signal in PBDTTT-C:PCBM blends underwent a spectral evolution which has to be addressed in a separate study as it is beyond the scope of the present work. To determine the individual spectral components and species-dependent dynamics that constitute the TA data matrix, we performed multivariate curve resolution (MCR) analysis of the NIR TA data using the script provided by Jaumot et al.[30] Prior to the MCR analysis of the TA data we determined by singular value decomposition (SVD) that the entire data matrix can be described entirely by two species, which we assigned to the polymer exciton and polaron. The only constraints used for the MCR analysis were non-negativity of the population density and non-positivity of the spectral profiles, which is a physical necessity for the signals to appear in the NIR spectral region because here the TA is dominated by photoinduced absorption features. The spectra and concentration profiles obtained by MCR analysis are depicted in panels a and b of Figure 4, respectively. Comparing the component spectra obtained by MCR analysis with TA measurements on pristine PBDTTT-C polymer films and PBDTTT-C:PCBM blends (see Figure S2a of Supporting Information), from which the polymer's exciton and polaron spectra can be obtained, allowed the clear assignment of the extracted component spectra to polymer excitons (component 1) and charges (component 2), respectively. Most importantly, the decomposition by MCR shows a slow rise in the concentration of charges on the polymer, indicating that polymer exciton dissociation is diffusion-limited compared to, for instance, PBDTTT-C:PCBM blends which showed exclusively ultrafast charge generation upon excitation of the polymer (data not shown here). We note that the MCR factorization provides a unique solution, indicated by the fact that at the end of the experimentally observed time range of the TA experiment a single species, namely the polymer polaron, remained, i.e., the data matrix reached rank 1.[31]

We now turn to the intensity dependence of the dynamics obtained experimentally and extracted from the MCR analysis of the data (see Figure 4 and Figure S6 of Supporting Information). Both the exciton and the charge dynamics showed an intensity dependence. Parallel MCR analysis of the data sets with shared spectra for all excitation intensities showed a weak intensity dependence of the decay of polymer excitons as well as an intensity-dependent rise of the charge-induced absorption from 42 to 117 ps at the highest and lowest excitation intensity, respectively. Interestingly, we did not observe an intensity dependence of the charge carrier dynamics after their generation was complete at delay times up to 1 ns. This indicates that those charges recombining in the first nanosecond have most likely collapsed into bound and interfacial charge-transfer (CT) states as they have not managed to overcome their mutual Coulomb attraction. In fact, intensity-independent subnanosecond to nanosecond CT-state recombination has regularly been observed in polymer:fullerene blends, and we demonstrate here that it also appears to be a common feature in polymer:PDI blends. It is an important cause of quantum efficiency loss.

To get an estimate of the exciton-to-charge conversion efficiency of the initial charge-transfer process, we plot the maximum of the charge-induced absorption signal of the optimized PBDTTT-C:PDI blends as a function of the number of absorbed photons and compare the signal amplitudes to those obtained for a PBDTTT-C:PCBM blend (Figure 5). The above-mentioned spectral evolution seen in PCBM blends is taken into account by taking the signal height of the charge-induced absorption at the isosbestic point seen in the NIR TA spectra of PBDTTT-C:PCBM blends. The signal amplitude at the same wavelength is taken at the time of maximum charge carrier concentration as obtained by MCR analysis to get the charge yield in the PDI blends. In PBDTTT-C:PCBM, near-quantitative charge transfer occurs (see Figure S4 of Supporting Information), while in the PDI blends significantly fewer charges are generated per absorbed photon (roughly half as many). This implies that about half of the initial polymer excitons in PBDTTT-C:PDI blends decay before being converted to charges or during the electron-transfer process at the interface and hence did not contribute to the photocurrent generation.

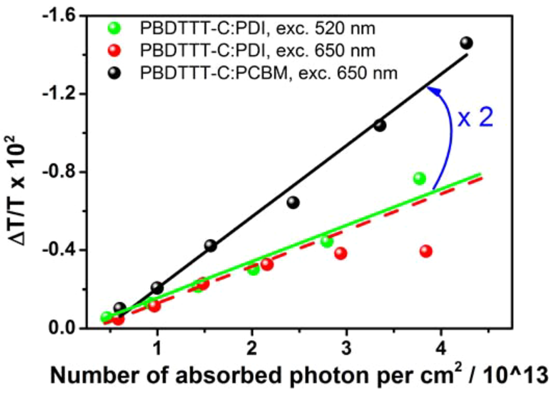

Figure 5. Maximum of the charge-induced absorption signal obtained by TA spectroscopy and MCR analysis versus the number of photons absorbed for PBDTTT-C:PDI blends excited at 520 nm (green dots) or 650 nm (red dots) and for a PBDTTT-C:PCBM blend excited at 650 nm (black dots).

The fullerene blend showed a linear relation of the maximum of the charge-induced absorption signal and the excitation intensity recalculated into the number of absorbed photons, whereas for PBDTTT-C:PDI blends this is the case for lower excitation intensities only. This is consistent with the longer-lived excitons in the PDI blend being quenched by bimolecular interactions at high excitation intensities. Furthermore, we note that the amplitude of the charge-induced absorption in PBDTTT-C:PDI blends was independent of the excitation wavelength (here 520 and 650 nm), which is consistent with a rather flat IQE spectrum (compare Figure 2).

2.4. Processes Following PDI Excitation. Here, we focus on the processes triggered by excitation of the perylene diimide acceptor. Figure 6a presents the TA spectra of the same blend as presented above after selectively exciting the PDI acceptor at 510 nm. Figure 6b displays the dynamics monitored at probe wavelengths corresponding to the polymer's ground-state bleach (650−675 nm) and the exciton-induced (1450−1475 nm) and charge-induced (from MCR analysis) absorption. The GSB of PBDTTT-C rises within 20−30 ps because of depopulation of the polymer's ground state. Concomitantly, the absorption originating from charges located on the PBDTTT-C polymer increased, indicative of delayed exciton quenching of excitons originally created in acceptor-rich regions. However, we note that the PA_{Ex} of PBDTTT-C is observed as early as 1 ps after excitation, showing that either a small number of the PBDTTT-C was excited at 510 nm in addition to PDI or energy transfer from the PDI to the polymer occurred within the temporal resolution of our TA experiment (~200 fs) as discussed below. Undoubtedly, PDI excitation resulted in delayed charge generation according to the rise of the PBDTTT-C GSB in conjunction with the rise of the charge-induced absorption. However, it is not straightforward to understand the process of delayed charge formation. Mechanistically, excitons created in PDI domains could approach the donor−acceptor interface, and subsequently hole transfer to the polymer could occur, that is, we would witness a photoinduced hole-transfer process. This process has been described in polymer:fullerene blends after fullerene excitation.[32] Nonetheless, in the example of PBDTTT-C:PDI

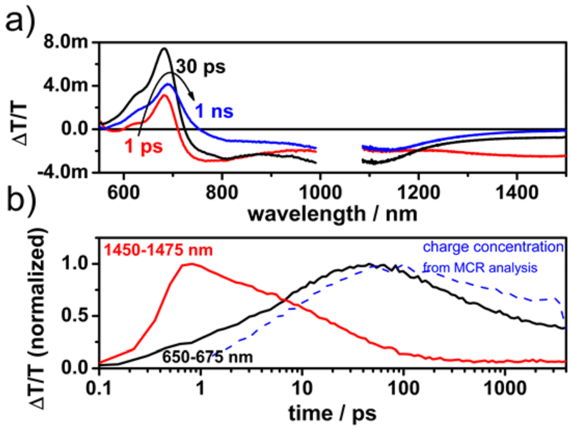

Figure 6. (a) Picosecond−nanosecond transient absorption spectra of PBDTTT-C:PDI (1:3) blends at different delay times after excitation of the PDI at 510 nm. (b) Dynamics tracked at 650−675 nm (black, polymer GSB) and 1450−1475 nm (red, exciton).

blends presented here, fluorescence resonance energy transfer by the Förster mechanism could play an important role as well, as the PDI emission entirely coincides with the polymer's absorption spectrum (see Figure S7 of Supporting Information). In fact, a rough estimate of the energy-transfer rate applying the Förster energy-transfer formalism resulted in $k > 3 \times 10^{11}$ s^{-1}, corresponding to an inverse rate of <3 ps (for $\Phi_{PL} = 0.2$, $r < 3$ nm) which indeed makes this process highly likely. However, we note that independent of the mechanism behind charge separation, it was complete after 100 ps, as thereafter the TA spectra and dynamics measured for the excitation of either the acceptor or the donor largely resembled each other.

2.5. Nano- to Microsecond Nongeminate Charge Recombination. Figure 7 depicts the nanosecond–microsecond transient spectra (a), the steady-state photoinduced absorption spectrum (b), and the intensity-dependence of the charge recombination dynamics (c) monitored at the peak of the charge-induced absorption of the polymer:PDI blend under investigation with a 532 nm excitation wavelength. The TA spectra showed the GSB of the polymer and the PA_C, virtually similar to the spectra measured after 1 ns in the picosecond–nanosecond TA measurements. The agreement of the nanosecond–microsecond transient spectra with the steady-state PIA spectrum suggests that on this time scale we recorded the recombination of long-lived states, predominantely spatially separated charges that can possibly contribute to the photocurrent. Indeed, the clear intensity dependence of the charge-related signal decay supports the assignment of the PA_C to spatially separated charges because it is indicative of a nongeminate recombination of free charges. The solid lines overlaying the experimental data in Figure 7c are global fits of the decay dynamics of all excitation intensities using a two-pool model that we have previously presented and successfully applied to describe the recombination of free charges in other polymer:fullerene blends.[33] We note that the data could be well-described by a sum of a single-exponential decay and thus intensity-independent component with an inverse rate of 1.75 ns and an intensity-dependent component with a nongeminate recombination coefficient of 1.4×10^{-15} $(cm^3)^{\lambda}$ s^{-1} and a recombination order of $n = 2.2$ which deviates from a purely bimolecular recombination process. Calculating the effective, i.e., bimolecular, recombination rate γ_{eff} assuming a charge density of 5×10^{15} cm^{-3} which is equivalent to 1 sun illumination conditions and a recombination order of $n = 2$ resulted in a value for γ_{eff} of 3.4×10^{-11} cm^3 s^{-1}, which is in the upper range of those previously obtained for polymer:fullerene blends. However, the necessity of including a single-exponential decay process implies that in the first few nanoseconds we still observed a contribution from geminate recombination of interfacial CT-states which had not managed to split entirely into free charge carriers. This is in line with the intensity-independent nanosecond geminate recombination observed in the picosecond–nanosecond TA experiments described above.

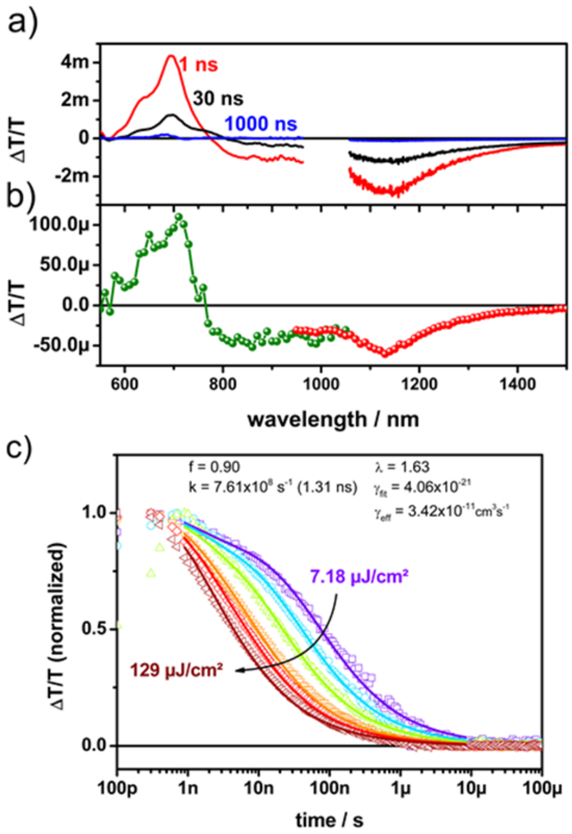

Figure 7. (a) Nanosecond–microsecond transient absorption spectra of PBDTTT-C:PDI (1:3) blends at different delay times. (b) Quasi-steady-state photoinduced absorption spectra of a PBDTTT-C:PDI (1:3) blend. (c) Intensity dependence of the recombination dynamics (symbols) and global fit according to a two-pool model (lines).

2.6. Field Dependence of Charge Generation. The photocurrent of the PBDTTT-C:PDI solar cells showed a pronounced bias dependence implying field-dependent charge carrier dissociation and/or slow and field-dependent extraction of charges from the photoactive layer causing a competition of extraction and nongeminate recombination. To better understand the origin of the field dependence also in comparison to polymer:fullerene blends, we performed time-delayed collection field experiments, the results of which are displayed in Figure 8. In TDCF experiments, the total number of charge carriers extracted by a strong extraction bias is measured as a function of the prebias applied during the pulsed laser photoexcitation. Figure 8a compares the *JV*-characteristics of a PBDTTT-C:PDI

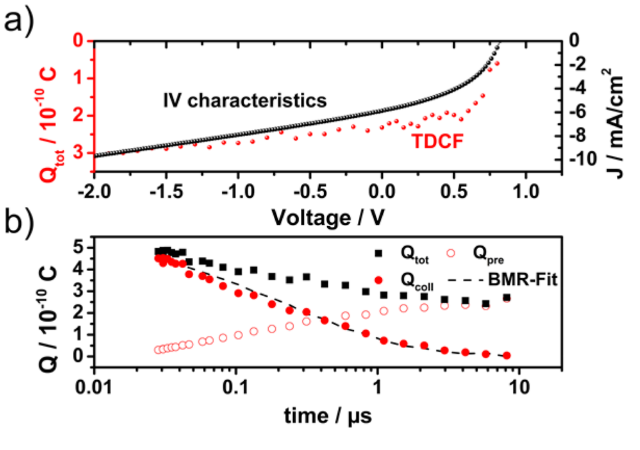

Figure 8. (a) Left scale: total amount of charges (Q_{tot}) extracted for a PBDTTT-C:PDI solar cell at different prebiases (V_{pre}) during excitation. Right scale: *JV*-characteristics of inverted devices. (b) Delay-dependent total charge (squares), pre-charge (red open circles), and collection charge (red solid circles) for a prebias of 0.2 V. The iterative bimolecular ($n = 2$) recombination fit (dashed line) determines the bimolecular recombination coefficient.

(1:3) solar cell using an inverse device architecture (black) as typically required for TDCF measurements with the total amount of charge carriers extracted in the TDCF measurement (red) as a function of the applied voltage or prebias, respectively. Clearly, the charge generation appears to be field-dependent as indicated by the pronounced dependence of the total number of extracted (and thus generated) charges on the applied prebias. In fact, the *JV*-characteristics of the device reproduced the trend of the TDCF measurements very well. Again, this indicates that the charge carrier-separation process at the interface is field-assisted and some of the geminate CT recombination observed in TA measurements can be suppressed in the device by the application of an electric field. To determine the kinetics of nongeminate recombination, TDCF measurements were performed in which the delay between the laser pulse and the collection voltage was varied. The data, namely precharge (Q_{pre}), the collected charge (Q_{coll}) and the total charge (Q_{tot}), is shown in Figure S8 of Supporting Information. Fitting the dynamics with an iterative model was consistent with bimolecular ($n = 2$) recombination. As an example, the data and the bimolecular recombination fit are shown for a prebias of 0.2 V in Figure 8b (see Figure S8 of Supporting Information for further results). We found the BMR coefficient to be field-independent, with a value of around 9.9×10^{-11} cm^{3}s^{-1}, approximately three times higher than that obtained by our TA experiments. However, given the entirely different experimental techniques and data analyses, the bimolecular recombination (BMR) coefficients are in rather good agreement. Furthermore, the BMR coefficient is rather large compared to that found by TDCF measurements on annealed P3HT:PCBM blends [34] but is similar to that obtained for the low-bandgap polymer PCPDTBT:PC$_{70}$BM blend, for which values ranging from 3.5 to 9.2×10^{-11} cm^3 s^{-1} were previously measured.[35] As a result of the rather high BMR coefficient, nongeminate recombination competes with extraction even well below open circuit, which is clearly seen by the decrease of the total charge with delay time in Figure 8b and Figure S5 of Supporting Information.

3. DISCUSSION

A key finding of this study is the observation of incomplete dissociation of excitons into free charges at the polymer:PDI interface, regardless of whether the donor polymer or PDI acceptor was excited. In fact, a comparison of the PDI blend with the respective PCBM blend revealed that the maximum charge-induced absorption signal is by a factor of 2 smaller in the PBDTTT-C:PDI system. Given that the polymer excitons in the pristine films have a lifetime of ~260 ps, which is significantly shortened in the blend with PDI, it appears that although excitons can approach the interface during their lifetime and get quenched, this process does not necessarily result in complete charge transfer between the donor and acceptor. The reason could be that during the electron-transfer process the system rather returns to the ground state, for instance by crossing a conical intersection between the excited and ground state. The yield of the charge-transfer process and the accessibility of competing photophysical pathways may be dependent on the orientation of the polymer with respect to the PDI acceptor molecules.[27] In fact, the anisotropy of the PDI acceptor molecules or, vice versa, the isotropy of fullerenes, could well be a critical factor in their different performance in solar cell devices. Accordingly, Shivanna et al. showed in a very recent study that a twisted perylene exhibits a polaron yield comparable to that of the respective polymer:fullerene blend.[36] Further evidence for an impeded charge-separation process comes from the TDCF measurements, which demonstrate that a barrier for charge separation exists in the polymer:PDI blends, which can be partially overcome by the aid of an electric field. These findings can explain the rather low quantum efficiency and fill factors observed for photovoltaic devices based on polymer:PDI blends.

For the planar PDI used in this study,[37] strong aggregation due to $\pi-\pi$ stacking results in the formation of rather extended crystallites and thus extended domains of pure PDI which is supported by AFM images of PBDTTT-C:PDI blend films (see Figure S10 of Supporting Information). In this respect, another inherent feature of planar and thus highly aggregating PDIs is the ability to form excited dimers, namely excimers, after photoexcitation.[38] The excimer states can act as traps and potentially limit the exciton diffusion length, in turn leading to less excitons reaching the interface and undergoing charge transfer.[21] However, our results show that charge transfer from the PDI to the polymer occurs on a time scale of tens of picoseconds (see Figure S6 of Supporting Information) and that the IQE is similar for excitation of PBDTTT-C or the PDI. Hence, it appears that the formation of spatially separated charge carriers at the interface is impeded and the main bottleneck in the cascade of photophysical processes determining the performance of polymer:PDI blends.

4. CONCLUSIONS

Perylene diimides are promising as nonfullerene acceptors in bulk heterojunction organic solar cells as they substantially add to the photoactive layer's absorption, unlike the often used fullerene derivatives. However, the efficiencies obtained are significantly lower than those of fullerene-based acceptors as demonstrated here for the low-bandgap polymer:PDI photovoltaic blend PBDTTT-C:PDI. Using transient absorption spectroscopy and soft modeling of the TA data by multivariate curve resolution analysis, we identified inefficient exciton dissociation at the interface to be the main bottleneck for the moderate power conversion efficiency. In addition, exciton dissociation at the interface largely creates bound charge-transfer states, which geminately recombine on a subnanosecond time scale. Furthermore, time-delayed collection field experiments demonstrated that the initial charge separation is field-dependent, largely causing the pronounced bias dependence of the photocurrent. Further experiments are still necessary to unravel the effect the interfacial morphology has on the charge separation in polymer:PDI solar cells, specifically the impact of the orientation of donor and acceptor with respect to each other.

■ ASSOCIATED CONTENT

Ⓢ Supporting Information

PCE as a function of the PDI fraction; TA of PBDTTT-C:PCBM blends and pristine PBDTTT-C films; intensity dependence of TA signals, TDCF fits, further MCR analysis, absorption spectrum of a PBDTTT-C film treated with iodine vapor; AFM image and TR-PL data of PBDTTT-C:PDI blends; and Förster transfer rate calculation. This material is available free of charge via the Internet at http://pubs.acs.org.

■ AUTHOR INFORMATION

Corresponding Author

*E-mail: laquai@mpip-mainz.mpg.de.

Present Address

§I.A.H: Karlsruhe Institute of Technology (KIT), Karlsruhe 76131, Germany.

Notes

The authors declare no competing financial interest.

ACKNOWLEDGMENTS

We thank G. Battagliarin, C. Li, and K. Müllen (all Max Planck Institute for Polymer Research) for providing the PDI acceptor. F.L. thanks the Max Planck Society for funding the Max Planck Research Group of Organic Optoelectronics and the Deutsche Forschungsgemeinschaft (DFG) for funding in the framework of the priority program SPP1355 "Elementary Processes in Organic Photovoltaics". D.G. acknowledges a Kekulé scholarship of the Fonds der Chemischen Industrie (FCI). I.A.H. thanks the Alexander von Humboldt Foundation and the Max Planck Society for research scholarships.

REFERENCES

(1) Chen, J.; Cao, Y. Development of Novel Conjugated Donor Polymers for High-Efficiency Bulk-Heterojunction Photovoltaic Devices. *Acc. Chem. Res.* **2009**, *42*, 1709−1718.

(2) Scharber, M. C.; Sariciftci, N. S. Efficiency of Bulk-Heterojunction Organic Solar Cells. *Prog. Polym. Sci.* **2013**, *38*, 1929−1940.

(3) Green, M. A.; Emery, K.; Hishikawa, Y.; Warta, W.; Dunlop, E. D. Solar Cell Efficiency Tables (Version 41). *Prog. Photovoltaics* **2013**, *21*, 1−11.

(4) Jamieson, F. C.; Domingo, E. B.; McCarthy-Ward, T.; Heeney, M.; Stingelin, N.; Durrant, J. R. Fullerene Crystallisation as a Key Driver of Charge Separation in Polymer/Fullerene Bulk Heterojunction Solar Cells. *Chem. Sci.* **2012**, *3*, 485−492.

(5) Bloking, J. T.; et al. Solution-Processed Organic Solar Cells with Power Conversion Efficiencies of 2.5% Using Benzothiadiazole/Imide-Based Acceptors. *Chem. Mater.* **2011**, *23*, 5484−5490.

(6) Schwenn, P. E.; et al. A Small Molecule Non-Fullerene Electron Acceptor for Organic Solar Cells. *Adv. Energy Mater.* **2011**, *1*, 73−81.

(7) Shu, Y.; Lim, Y.-F.; Li, Z.; Purushothaman, B.; Hallani, R.; Kim, J. E.; Parkin, S. R.; Malliaras, G. G.; Anthony, J. E. A Survey of Electron-Deficient Pentacenes as Acceptors in Polymer Bulk Heterojunction Solar Cells. *Chem. Sci.* **2011**, *2*, 363−368.

(8) Sonar, P.; Ng, G.-M.; Lin, T. T.; Dodabalapur, A.; Chen, Z.-K. Solution Processable Low Bandgap Diketopyrrolopyrrole (DPP) Based Derivatives: Novel Acceptors for Organic Solar Cells. *J. Mater. Chem.* **2010**, *20*, 3626−3636.

(9) Sullivan, P.; Duraud, A.; Hancox, l.; Beaumont, N.; Mirri, G.; Tucker, J. H. R.; Hatton, R. A.; Shipman, M.; Jones, T. S. Halogenated Boron Subphthalocyanines as Light Harvesting Electron Acceptors in Organic Photovoltaics. *Adv. Energy Mater.* **2011**, *1*, 352−355.

(10) Park, I.; Lim, Y.; Noh, S.; Lee, D.; Meister, M.; Amsden, J. J.; Laquai, F.; Lee, C.; Yoon, D. Y. Enhanced Photovoltaic Performance of ZnO Nanoparticle/Poly(Phenylene Vinylene) Hybrid Photovoltaic Cells by Semiconducting Surfactant. *Org. Electron.* **2011**, *12*, 424−428.

(11) Zhou, R.; et al. Enhancing the Efficiency of Solution-Processed Polymer:Colloidal Nanocrystal Hybrid Photovoltaic Cells Using Ethanedithiol Treatment. *ACS Nano* **2013**, *7*, 4846−4854.

(12) Lu, Z.; Jiang, B.; Zhang, X.; Tang, A.; Chen, L.; Zhan, C.; Yao, J. Perylene−Diimide Based Non-Fullerene Solar Cells with 4.34% Efficiency through Engineering Surface Donor/Acceptor Compositions. *Chem. Mater.* **2014**, *26*, 2907−2914.

(13) Ye, L.; Jiang, W.; Zhao, W.; Zhang, S.; Qian, D.; Wang, Z.; Hou, J. Selecting a Donor Polymer for Realizing Favorable Morphology in Efficient Non-fullerene Acceptor-based Solar Cells. *Small* **2014**, No. 10.1002/smll.201401082.

(14) Kamm, V.; Battagliarin, G.; Howard, I. A.; Pisula, W.; Mavrinskiy, A.; Li, C.; Müllen, K.; Laquai, F. Polythiophene:Perylene Diimide Solar Cells − The Impact of Alkyl-Substitution on the Photovoltaic Performance. *Adv. Energy Mater.* **2011**, *1*, 297−302.

(15) Shin, W. S.; Jeong, H.-H.; Kim, M.-K.; Jin, S.-H.; Kim, M.-R.; Lee, J.-K.; Lee, J. W.; Gal, Y.-S. Effects of Functional Groups at Perylene Diimide Derivatives on Organic Photovoltaic Device Application. *J. Mater. Chem.* **2006**, *16*, 384−390.

(16) Rajaram, S.; Armstrong, P. B.; Kim, B. J.; Fréchet, J. M. J. Effect of Addition of a Diblock Copolymer on Blend Morphology and Performance of Poly(3-hexylthiophene):Perylene Diimide Solar Cells. *Chem. Mater.* **2009**, *21*, 1775−1777.

(17) Lindner, S. M.; Hüttner, S.; Chiche, A.; Thelakkat, M.; Krausch, G. Charge Separation at Self-Assembled Nanostructured Bulk Interface in Block Copolymers. *Angew. Chem., Int. Ed.* **2006**, *45*, 3364−3368.

(18) Tao, Y.; McCulloch, B.; Kim, S.; Segalman, R. A. The Relationship between Morphology and Performance of Donor-Acceptor Rod-Coil Block Copolymer Solar Cells. *Soft Matter* **2009**, *5*, 4219−4230.

(19) Sommer, M.; Lindner, S. M.; Thelakkat, M. Microphase-Separated Donor−Acceptor Diblock Copolymers: Influence of HOMO Energy Levels and Morphology on Polymer Solar Cells. *Adv. Funct. Mater.* **2007**, *17*, 1493−1500.

(20) Mohamad, D. K.; Fischereder, A.; Yi, H.; Cadby, A. J.; Lidzey, D. G.; Iraqi, A. A Novel 2,7-Linked Carbazole Based "Double Cable" Polymer with Pendant Perylene Diimide Functional Groups: Preparation, Spectroscopy and Photovoltaic Properties. *J. Mater. Chem.* **2011**, *21*, 851−862.

(21) Howard, I. A.; Laquai, F.; Keivanidis, P. E.; Friend, R. H.; Greenham, N. C. Perylene Tetracarboxydiimide as an Electron Acceptor in Organic Solar Cells: A Study of Charge Generation and Recombination. *J. Phys. Chem. C* **2009**, *113*, 21225−21232.

(22) Keivanidis, P. E.; Laquai, F.; Howard, I. A.; Friend, R. H. Room-Temperature Phase Demixing in Bulk Heterojunction Layers of Solution-Processed Organic Photodetectors: The Effect of Active Layer Ageing on the Device Electro-optical Properties. *Adv. Funct. Mater.* **2011**, *21*, 1355−1363.

(23) Shoaee, S.; An, Z.; Zhang, X.; Barlow, S.; Marder, S. R.; Duffy, W.; Heeney, M.; McCulloch, I.; Durrant, J. R. Charge Photogeneration in Polythiophene-Perylene Diimide Blend Films. *Chem. Commun. (Cambridge, U.K.)* **2009**, 5445−5447.

(24) Pensack, R. D.; Guo, C.; Vakhshouri, K.; Gomez, E. D.; Asbury, J. B. Influence of Acceptor Structure on Barriers to Charge Separation in Organic Photovoltaic Materials. *J. Phys. Chem. C* **2012**, *116*, 4824−4831.

(25) Gehrig, D.; Howard, I. A.; Kamm, V.; Dyer-Smith, C.; Etzold, F.; Laquai, F. Charge Generation in Polymer:Perylene Diimide Blends Probed by Vis-NIR Broadband Transient Absorption Pump-Probe Spectroscopy. *Proc. SPIE* **2013**, DOI: 10.1117/12.2023757.

(26) Nolde, F.; Pisula, W.; Müller, S.; Kohl, C.; Müllen, K. Synthesis and Self-Organization of Core-Extended Perylene Tetracarboxdiimides with Branched Alkyl Substituents. *Chem. Mater.* **2006**, *18*, 3715−3725.

(27) Beckers, E. H. A.; Meskers, S. C. J.; Schenning, A. P. H. J.; Chen, Z.; Würthner, F.; Marsal, P.; Beljonne, D.; Cornil, J.; Janssen, R. A. J. Influence of Intermolecular Orientation on the Photoinduced Charge Transfer Kinetics in Self-Assembled Aggregates of Donor−Acceptor Arrays. *J. Am. Chem. Soc.* **2006**, *128*, 649−657.

(28) Yagai, S.; Seki, T.; Karatsu, T.; Kitamura, A.; Würthner, F. Transformation from H- to J-Aggregated Perylene Bisimide Dyes by Complexation with Cyanurates. *Angew. Chem., Int. Ed.* **2008**, *47*, 3367−3371.

(29) Burkhard, G. F.; Hoke, E. T.; McGehee, M. D. Accounting for Interference, Scattering, and Electrode Absorption to Make Accurate Internal Quantum Efficiency Measurements in Organic and Other Thin Solar Cells. *Adv. Mater. (Weinheim, Ger.)* **2010**, *22*, 3293−3297.

(30) Jaumot, J.; Gargallo, R.; de Juan, A. A Graphical User-Friendly Interface for MCR-ALS: A New Tool for Multivariate Curve Resolution in MATLAB. *Chemom. Intell. Lab. Syst.* **2005**, *76*, 101−110.

(31) Howard, I. A.; Mangold, H.; Etzold, F.; Gehrig, D.; Laquai, F. *Ultrafast Dynamics in Molecules, Nanostructures and Interfaces*; World Scientific: Singapore, 2014, Vol. *8*.

(32) Etzold, F.; Howard, I. A.; Forler, N.; Cho, D. M.; Meister, M.; Mangold, H.; Shu, J.; Hansen, M. R.; Müllen, K.; Laquai, F. The Effect of Solvent Additives on Morphology and Excited-State Dynamics in PCPDTBT:PCBM Photovoltaic Blends. *J. Am. Chem. Soc.* **2012**, *134*, 10569−10583.

(33) Howard, I. A.; Mauer, R.; Meister, M.; Laquai, F. Effect of Morphology on Ultrafast Free Carrier Generation in Polythiophene:-Fullerene Organic Solar Cells. *J. Am. Chem. Soc.* **2010**, *132*, 14866−14876.

(34) Kniepert, J.; Schubert, M.; Blakesley, J. C.; Neher, D. Photogeneration and Recombination in P3HT/PCBM Solar Cells Probed by Time-Delayed Collection Field Experiments. *J. Phys. Chem. Lett.* **2011**, *2*, 700−705.

(35) Albrecht, S.; Schindler, W.; Kurpiers, J.; Kniepert, J.; Blakesley, J. C.; Dumsch, I.; Allard, S.; Fostiropoulos, K.; Scherf, U.; Neher, D. On the Field Dependence of Free Charge Carrier Generation and Recombination in Blends of PCPDTBT/PC70BM: Influence of Solvent Additives. *J. Phys. Chem. Lett.* **2012**, *3*, 640−645.

(36) Shivanna, R.; Shoaee, S.; Dimitrov, S.; Kandappa, S. K.; Rajaram, S.; Durrant, J. R.; Narayan, K. S. Charge Generation and Transport in Efficient Organic Bulk Heterojunction Solar Cells with a Perylene Acceptor. *Energy Environ. Sci.* **2014**, *7*, 435−441.

(37) Chen, Z.; Debije, M. G.; Debaerdemaeker, T.; Osswald, P.; Würthner, F. Tetrachloro-Substituted Perylene Bisimide Dyes as Promising n-Type Organic Semiconductors: Studies on Structural, Electrochemical and Charge Transport Properties. *ChemPhysChem* **2004**, *5*, 137−140.

(38) Auweter, H.; Ramer, D.; Kunze, B.; Wolf, H. C. The Dynamics of Excimer Formation in Perylene Crystals. *Chem. Phys. Lett.* **1982**, *85*, 325−329.

Efficiency-Limiting Processes in Low-bandgap Polymer:Perylene Diimide Photovoltaic Blends

Dominik W. Gehrig,[§] Steffen Roland,[$] Ian A. Howard,[§,†] Valentin Kamm,[§] Hannah Mangold,[§] Dieter Neher,[$] Frédéric Laquai[§,]*

[§]Max Planck Research Group for Organic Optoelectronics, Max Planck Institute for Polymer Research, Ackermannweg 10, D-55128 Mainz, Germany
[$]University of Potsdam, Institut für Physik und Astronomie, Physik weicher Materie, Karl-Liebknecht-Straße 24–25, 14476 Potsdam-Golm

SUPPORTING INFORMATION

EXPERIMENTAL SECTION

Materials. Chloroform (HPLC grade) was obtained from VWR and used without further purification. PBDTTT-C was purchased from One Material and used as received. The PBDTTT-C used in the present study had a molecular weight of Mn = 132.000 kg/mol and a polydispersity of 2.8. The synthesis of *N,N'*-bis(α-ethylpropyl)-3,4:9,10-tetra-carbonic acid diimide was reported earlier.[S1] The compound was thoroughly purified by column chromatography.

Photovoltaic Devices were prepared as described earlier by our group.[S2] Solar cells were fabricated on ITO-coated glass substrates (Präzisions Glas & Optik GmbH, Germany) which were patterned by wet etching and cleaned successively by ultrasonication in detergent, acetone and subsequently *iso*-propanol. After that, the samples were treated with an argon plasma for 15 min before spin-coating of a ~40 nm thick poly(3,4-ethylene-dioxythiophene):poly-(styrenesulfonate) (PEDOT:PSS) layer (Clevios P VP Al 4083, H.C. Stark). Afterwards, the substrates were transferred into a nitrogen-filled glovebox and heated to 120 °C for 30 min. The layer was deposited by dissolving PBDTTT-C and PDI separately in chloroform at a concentration of 10 mg mL^{-1} and the solutions were stirred overnight at room temperature. 4 h before spin-coating the active layer the solutions were mixed in a ratio of 1:3 (by weight/volume) and the blend was then spin-coated at 900 rpm for 60 s, resulting in an active layer thickness of ~100 nm. Post deposition annealing of the active layer was done at 120 °C for 10 min. As a top-electrode, a bilayer of 5 nm calcium and 100 nm aluminum was evaporated through a shadow mask. Spectroscopic samples were fabricated in the same way except that quartz substrates were used and no top-electrode was evaporated. Solar cells were characterized with a solar simulator (K.H. Steuernagel Lichttechnik GmbH, Germany) employing a 575 W metal halide lamp combined with a filter system to create a spectrum according to AM1.5G conditions, however, with a lower intensity of 70 mW cm^{-2}. Current-voltage curves were taken with a Keithley 236 Source Measure Unit (SMU) in a glovebox. For external quantum efficiency (EQE) measurements between 400 and 900 nm the solar-cell was illuminated with monochromatic light from a tungsten-halogen lamp passed through a TRIAX 180 monochromator. The light intensity was measured with a calibrated silicon photodiode giving a maximum intensity of 0.7 W m^{-2} at 600 nm. EQE measurements were performed in the glovebox at short circuit conditions with a Keithley 236 Source Measure Unit.

Steady-State Spectroscopy. Steady state absorption spectra were measured with a Perkin Elmer Lambda 25 spectrometer. The layer thickness was determined with a Tencor P10 surface profilometer.

Quasi-Steady-State Photoinduced Absorption Spectroscopy. Quasi-steady-state photoinduced absorption (PIA) spectroscopy, as described earlier by our group,[S3] was performed with a pump-probe setup consisting of a 100 W tungsten-halogen lamp with a LOT-Oriel Omni-λ 300 monochromator as the probe and a Newport LED (LED-527-HP) operating at 524 nm with a power of 100 mW cm^{-2} used as a pump. The samples were placed in a nitrogen-cooled optical cryostat (Oxford Instruments Optistat CF) and cooled down to 80 K in a helium atmosphere. The transmitted light was dispersed by a second and identical monochromator and then detected by a photodetector. For measurements in the wavelength range from 500 to 1100 nm, an amplified silicon photodetector (Thorlabs PDI 100A) was employed, which was replaced by an amplified germanium detector (Thorlabs PDA 50B) for the wavelength range from 900 to 1800 nm. The pump light was chopped at 317 Hz to induce changes in the transmission ΔT, which were measured by using a lock-in amplifier (EG&G Princeton Applied Research model 5210). To calculate Δ*T/T*, the transmission was recorded prior to the PIA measurement and corrected for photoluminescence.

Time-Resolved Fluorescence. Time-resolved photoluminescence (TR-PL) spectra were taken with a C4742 Hamamatsu streak camera system in fast/slow sweep mode. Excitation pulses at 400 nm were provided by frequency doubling the output of a commercial femtosecond oscillator (Coherent MIRA Duo) or amplifier laser system (Coherent LIBRA-HE), for fast/slow sweep respectively.

Transient Absorption Spectroscopy. Transient absorption (TA) measurements were performed with a home-built pump-probe setup.[S2, S3] To measure in the time range of 1-4 ns with a resolution of ~100 fs, the output of a commercial titanium:sapphire amplifier (Coherent LIBRA-HE, 3.5 mJ, 1 kHz, 100 fs) was split into two beams that pumped two independent commercial optical parametric amplifiers (Coherent OPerA Solo). One optical parametric amplifier (OPA) was used to generate the tunable excitation pulses in the visible, while the second OPA was used to generate the pump beam for white-light generation. For measurements in the spectral range between 550-1100 nm a 1300 nm seed of a few μJ was focused into a c-cut 3 mm thick sapphire window for white-light generation. The variable delay of up to 4 ns between pump and probe was introduced by a broadband retroreflector mounted on a mechanical delay stage. Mostly reflective elements were used to guide the probe beam to the sample to minimize chirp. The excitation pulse was chopped at 500 Hz, while the white-light pulses were dispersed onto a linear silicon photodiode array, which was read out at 1 kHz by home-built electronics. Adjacent diode readings corresponding to the transmission of the sample after an excitation pulse and without an excitation pulse were used to calculate ΔT/T.

For measurements in the time range between 1 ns to 1 ms with a resolution of 600 ps, the excitation pulse was provided by an actively Q-switched Nd:YVO_4 laser (AOT Ltd. MOPA) at 532 nm. In this case the delay between pump and probe was controlled by an electronic delay generator (Stanford Research Systems DG535). TA measurements were performed at room temperature under a dynamic vacuum of $<10^{-5}$ mbar.

For TA measurements in the NIR spectral range covering 1100-2000 nm a 2100 nm pump was used to generate white-light in an yttrium vanadate window. Furthermore, a dichroic mirror was used to separate the residual seed beam (idler of the OPA at 2100 nm) from the broadband NIR supercontinuum. The NIR pulses were dispersed onto a Peltier-cooled 512 pixel long linear extended InGaAs array (Entwicklungsbüro Stresing) and read out as described above.

Multivariate Curve Resolution. MCR analysis is a soft-modelling approach used to factor experimentally measured TA data surfaces into their component spectra and respective concentration profiles applying certain physical constraints such as non-negativity of excited state concentrations or non-positivity of spectra. The MCR analysis and application to TA data has recently been reported and reviewed by us in a separate publication.[S4, S5]

Time-delayed Collection Field Experiments. In TDCF experiments charges are photo-generated by a short laser pulse from a commercial Nd:YAG laser pumping an optical parametric oscillator (NT242 EKSPLA, 5.5 ns pulse width, 500 Hz repetition rate, 500 nm excitation wavelength) at a variable pre-bias V_{pre}. After a certain delay time charge carriers are extracted completely by a high rectangular reverse bias (-3 V) applied with a pulse generator (Agilent 81150A). The current was determined with a Yokogawa DL9140 oscilloscope via a 50 Ω input resistor. The total photogenerated charge Q_{tot} of the 1 mm² sized pixels was obtained by integration of the current transient. The small pixel size reduced RC-time limitations below the required time resolution. To determine the field dependence of charge carrier generation current transients are recorded for several pre-biases at a laser intensity of 0.2 μJ/cm^2 and a short delay time of 10 ns to prevent non–geminate recombination. To obtain information about non-geminate recombination kinetics current transients were measured at a higher fluence of 0.5 μJ/cm^2 for different delay times ranging from 20 ns to 10 μs. Subsequently, sectionalized integration of the current transients yield the charge extracted while a certain pre-bias is applied (Q_{pre}) and the remaining charge (Q_{coll}) which gets extracted by the applied reverse bias after the particular delay time. The total photogenerated charge Q_{tot} will decrease with delay time if non-geminate recombination takes place. By iteratively fitting the delay dependent values of Q_{coll}, according to Kniepert et al.,[S6] with a bimolecular recombination model yields the bimolecular recombination coefficient γ_{BMR}.

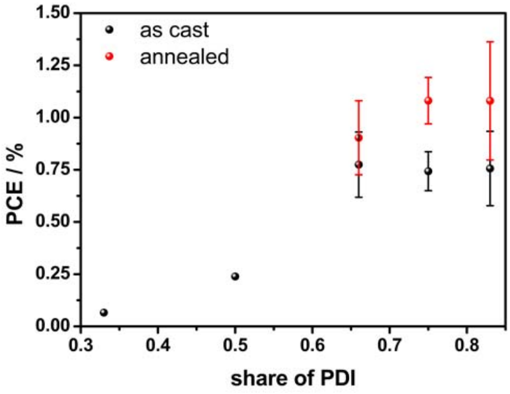

Figure S1. Power conversion efficiency of PBDTTT-C:PDI solar cells in normal device architecture with respect to the share of PDI in the active layer.

A series of solar cell devices was fabricated to obtain the optimum ratio of PBDTTT-C to PDI. The best performing cells contain a threefold excess of PDI. Annealing improved the device performance for each donor-acceptor ratio.

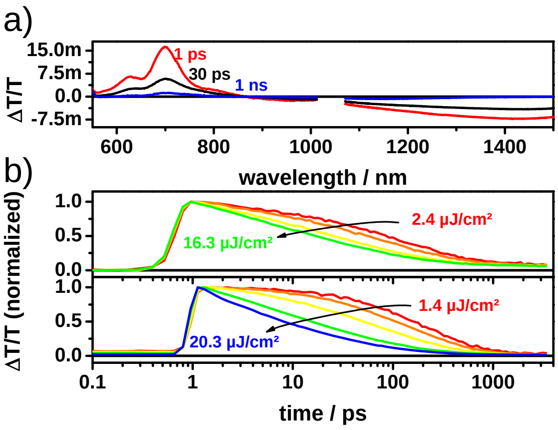

Figure S2. a) ps-ns transient absorption spectra of pure PBDTTT-C; b) intensity dependent kinetics tracked at 675-725 nm (GSB, upper panel) and 1450-1700 nm (PIA, lower panel).

The pristine polymer was measured by transient absorption spectroscopy. The spectra showed three distinct features, namely the ground-state bleach (up to 750 nm), stimulated emission (750-850 nm) and photo-induced absorption (>850 nm).

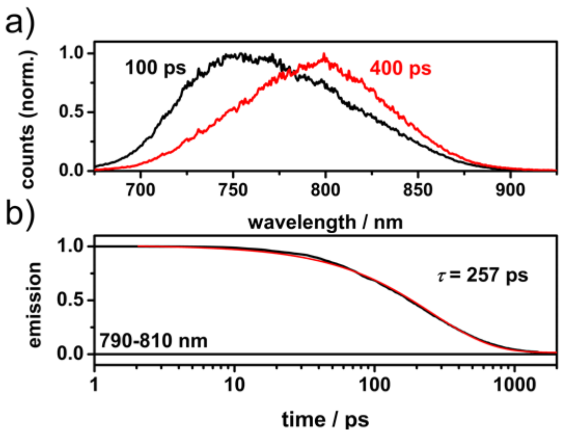

Figure S3. a) Emission spectra of pristine PBDTTT-C at 100 ps and 400 ps after excitation with 400 nm and b) emission decay tracked from 790-810 nm.

Furthermore, time-resolved photoluminescence (TR-PL) of pure PBDTTT-C was measured. Figure S8 shows the spectra (a) and dynamics (b) together with a monoexponential fit (red line). An inverse decay rate of 257 ps is determined.

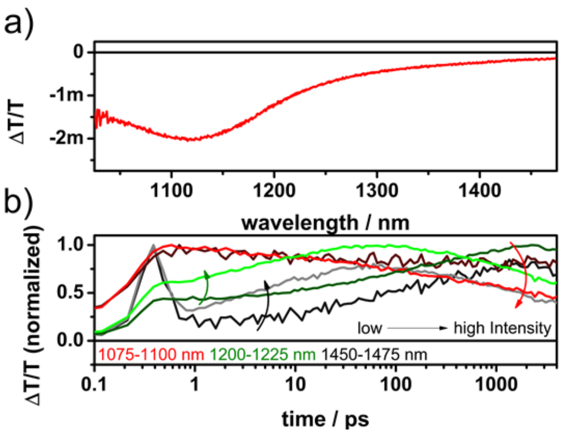

Figure S4. a) ps-ns transient absorption spectra of a PBDTTT-C:$PC_{60}BM$ blend excited at 650 nm with 6.7 µJ/cm²; b) intensity dependent dynamics tracked at different wavelengths. The dynamics at 1450-1475 nm show the ultrafast exciton quenching.

A PBDTTT-C:PCBM (1:2, spun from chlorobenzene) film was measured by transient absorption spectroscopy to get a meaningful estimate of the cross section of the charge-induced absorption. This estimate is obtained under the assumption of an exciton-to-charge conversion efficiency of unity as the PBDTTT-C-exciton-induced signal (1450-1500 nm, Figure S4(b)) vanishes on a sub-picosecond timescale.

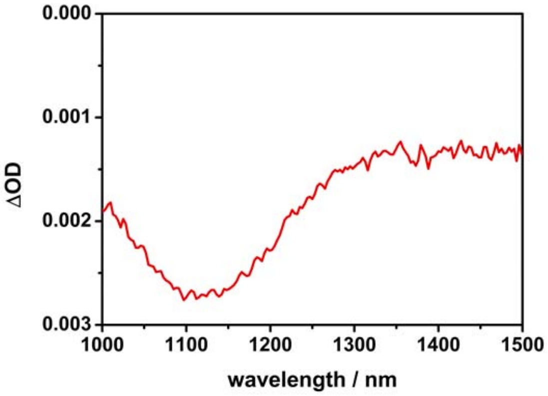

Figure S5. NIR absorption spectrum of a pristine PBDTTT-C film oxidized with Iodine vapor.

A pristine PBDTTT-C thin film was oxidized by exposure to Iodine vapor. The change in the optical density was obtained by substracting the absorption spectrum before and after Iodine vapor treatment (see Figure S5). A peak at 1120 nm is obtained and assigned to PBDTTT-C cation absorption.

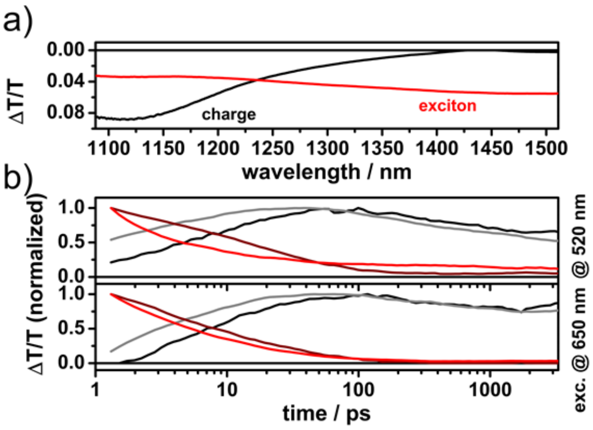

Figure S6. a) MCR spectra and b) concentration profiles obtained by parallel MCR-ALS analysis of TA data of PBDTTT-C:PDI films excited at 520 nm (upper panel) and 650 nm (lower panel).

MCR-ALS analysis was performed in parallel at a data set consisting of the data of different excitation intensities and obtained by exciting the sample at 520 nm or 650 nm, which favors an excitation of the PDI or PBDTTT-C domains, respectively. The maximum charge-induced absorption signal (red curve) at each intensity was used to obtain the signal of the respective data which is used in Figure 5.

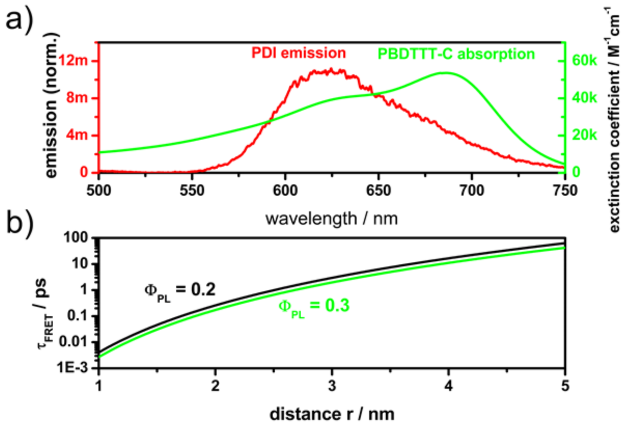

Figure S7. a) Overlap of PDI emission and PBDTTT-C absorption and b) inverse rate of Förster energy transfer with respect to the distance r.

The Förster resonance energy transfer rate was determined with the following equation

$$k_{FRET} = \frac{k_D}{r^6}\frac{9000 \cdot \ln(10) \cdot \kappa^2 \cdot \Phi_D^0}{128 \cdot \pi^5 \cdot N_A \cdot n^4}\int_0^\infty I_D(\lambda) \cdot \varepsilon_A(\lambda)\lambda^4 d\lambda$$

Where k_{FRET} is the rate of Förster resonance energy transfer, k_D is the fluorescence lifetime of the energy donor (5×10^7 s^{-1} for PDI), κ^2 is an orientation factor set to 2/3 for an isotropic orientation of donor and acceptor molecules, $\Phi^0{}_D$ is the photoluminescence quantum efficiency of the energy donor, N_A is the Avogadro constant, n is the refractive index of the medium, $I_D(\lambda)$ corresponds to the emission of the energy donor normalized to an integrated area of unity and ε_A is the molar extinction coefficient of the energy acceptor.

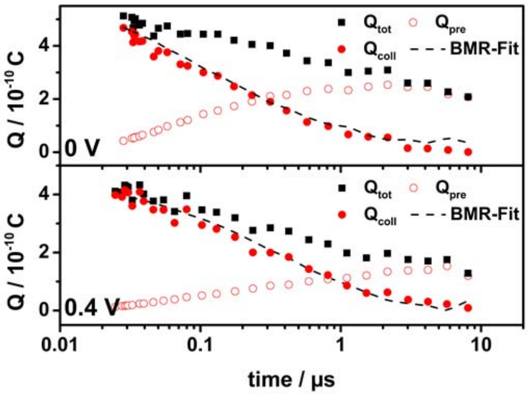

Figure S8. Bimolecular recombination fits to the total number of extracted charges for different pre-biases.

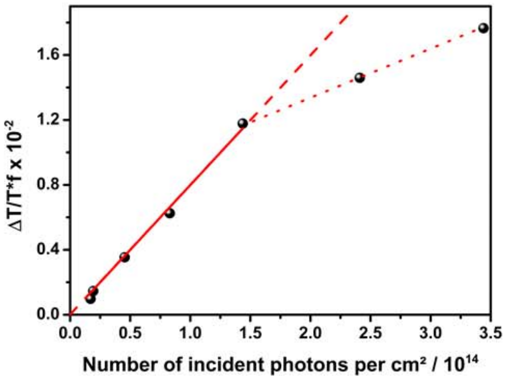

Figure S9. Signal intensity per number of absorbed photons for a PBDTTT-C:PDI blend excited with 532 nm (black) and linear fit to the data (red).

To determine the cross section of the charge-induced absorption the signal height per fraction of absorbed photons was plotted against the number of photons incident on the sample. The cross section was then obtained by a linear fit to the region of the data that did not show a sub linear behavior.

$$\frac{\Delta T}{T} = (N_0 * (1-f) * \exp(-k * (t-t_0)) + (\lambda * \gamma * (t-t_0) + (f * N_0)^{-\lambda})^{-\frac{1}{\lambda}})/N_0$$

Where N_0 is the initial charge density, that is derived from the cross section and excitation fluence, f is the fraction of non-geminate decay, k is the geminate recombination rate, $\lambda+1$ is the order of non-geminate decay and γ is the non-geminate decay rate.

f	k / s^{-1}	λ	γ_{fit} / (cm^3)$^\lambda$s^{-1}	γ_{eff} / cm^{3}s^{-1}
0.83	5.71x10^8	1.22	1.37x10^{-15}	3.61x10^{-12}

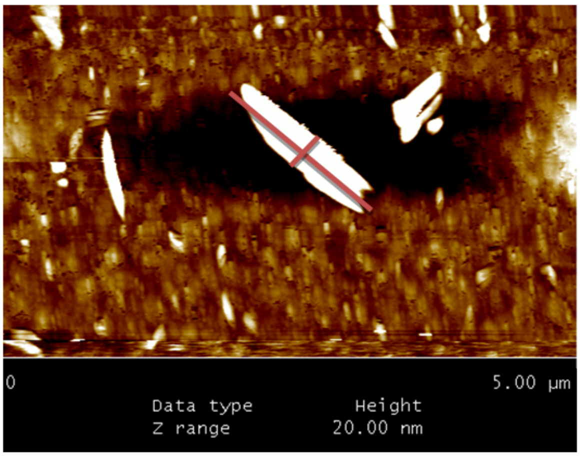

Figure S10. AFM image of an annealed PBDTTT-C:PDI (1:3) blend.

Additionally AFM measurements were conducted to analyze the morphology of annealed PBDTTT-C:PDI blends. The observation of micrometersized PDI-crystals is in good agreement with previous measurements and caused by the propensity of planar PDI to form extended π–π–stacks.

References

(S1) Nolde, F.; Pisula, W.; Müller, S.; Kohl, C.; Müllen, K., Synthesis and Self-Organization of Core-Extended Perylene Tetracarboxdiimides with Branched Alkyl Substituents. *Chem. Mater.* **2006**, *18*, 3715-3725.

(S2) Gehrig, D.; Howard, I. A.; Kamm, V.; Dyer-Smith, C.; Etzold, F.; Laquai, F. In *Charge generation in polymer:perylene diimide blends probed by Vis-NIR broadband transient absorption pump-probe spectroscopy*, 2013; pp 88111F-88111F-10.

(S3) Etzold, F.; Howard, I.A; Mauer, R.; Meister, M.; Kim, T.-D.; Lee, K.-S.; Baek, N.S.; Laquai, F.; Ultrafast Exciton Dissociation Followed by Nongeminate Charge Recombination in PCDTBT:PCBM Photovoltaic Blends. *J. Am. Chem. Soc.* **2011**, *133* (24), 9469-9479.

(S4) Jaumot, J.; Gargallo, R.; de Juan, A., A Graphical User-Friendly Interface for MCR-ALS: a New Tool for Multivariate Curve Resolution in MATLAB. *Chemom. Intell. Lab. Syst.* **2005**, *76*, 101-110.

(S5) Howard, I. A.; Mangold, H.; Etzold, F.; Gehrig, D.; Laquai, F., *Ultrafast Dynamics in Molecules, Nanostructures and Interfaces* **2014**, *Volume 8, World Scientific*.

(S6) Kniepert, J.; Schubert, M.; Blakesley, J. C.; Neher, D., Photogeneration and Recombination in P3HT/PCBM Solar Cells Probed by Time-Delayed Collection Field Experiments. *J. Phys. Chem. Lett.* **2011**, *2*, 700-705.

Charge generation in polymer:perylene diimide blends probed by Vis-NIR broadband transient absorption pump-probe spectroscopy

D. Gehrig[a], I.A. Howard[a], V. Kamm[a], C. Dyer-Smith[a], F. Etzold[a], F. Laquai*[a]
[a]Max Planck Research Group for Organic Optoelectronics, Max Planck Institute for Polymer Research, Ackermannweg 10, D-55128 Mainz, Germany

ABSTRACT

We report the photovoltaic performance of a low-bandgap polymer:perylene diimide (PDI) photovoltaic blend and study the exciton to charge carrier conversion in the photoactive layer by Vis-NIR broadband transient absorption spectroscopy over a dynamic range from pico- to microseconds. Power conversion efficiencies of 1.2 % are obtained from the polymer:PDI blends with a maximum EQE of about 30 %, which is significantly below the performance of the same polymer with fullerene as acceptor indicating that severe loss processes exist that limit the photocurrent. From the evolution of the transient absorption spectra we conclude that the photovoltaic performance of the polymer:PDI blends is mainly limited by inefficient exciton harvesting and dissociation at the interface. However, once free charge carriers are generated in the blend they can be extracted as photocurrent as their recombination occurs on a timescale similar to the time typically needed for charge extraction from the photoactive layer. Hence, strategies to improve the efficiency of polymer:PDI blends should aim at increasing exciton harvesting at the heterojunction and the dissociation efficiency into free charges at the interface.

Keywords: Organic photovoltaics, transient absorption spectroscopy, charge carrier dynamics, low-bandgap polymer, non-fullerene acceptors, perylene diimide

1. INTRODUCTION

The power conversion efficiency of state-of-the-art polymer:fullerene photovoltaic devices is heavily limited by the low absorption and thus incomplete photon harvesting of the thin photoactive organic layer. The main reasons for the low absorption are the spectrally confined absorption of the donor polymer and more importantly the intrinsically low absorbance of the typically used fullerene derivatives. The latter is even more severe in case of the use of low-bandgap polymers, which sometimes require an excess of up to 4 times as much fullerene as polymer to achieve optimum performance. Furthermore, recent calculations have forecasted the maximum power conversion efficiency of a single layer solar cell is limited to about 10-12 % [1] and the currently best-performing polymer:fullerene blends are already approaching this limit.[2] Hence, for this technology to overcome the present efficiency limits novel acceptor materials, namely non-fullerene acceptors, have to be developed. These non-fullerene acceptor molecules should ideally not only have a strong absorption and high electron mobility, but also acquire a favorable interaction with the donor polymer which facilitates charge separation at the interface, while simultaneously suppressing charge recombination. This is not a trivial set of requirements at all and may too a large extent explain the success of the fullerene derivatives as electron acceptors in organic solar cells, despite their low absorbance.

In fact, the efficiency of non-fullerene acceptors used in blends with different donor polymers still lacks substantially behind the efficiency of polymer:fullerene blends for reasons largely unknown. Several different acceptor structures have already been screened mostly resulting in poor efficiencies often less than or close to 1 %. However, some exceptions do exist, for instance the Sellinger group has recently reported an efficiency of 2.5 % for a benzothiadiazole-based acceptor in combination with poly(3-hexylthiophene) (P3HT) as donor polymer.[3] Furthermore, Rajaram et al. have very recently reported an efficiency of 2.8 % for a blend of a non-planar perylene diimide (PDI) bichromophore with a low-bandgap polymer, namely PBDTTT-C-T.[4] They assigned the high efficiency obtained for this particular system to the better mixing of the two components and thus more efficient exciton quenching at the interface. In general perylene diimide derivatives have attracted quite some interest as fullerene substitutes in organic solar cells due to their strong absorbance, photochemical stability, good electron transport properties and easily scalable synthesis. They have been

Physical Chemistry of Interfaces and Nanomaterials XII, edited by Natalie Banerji, Carlos Silva,
Proc. of SPIE Vol. 8811, 88111F · © 2013 SPIE · CCC code: 0277-786X/13/$18 · doi: 10.1117/12.2023757

used as acceptors in donor-acceptor type block-copolymers for photovoltaic devices, however with fairly moderate efficiencies so far.[5] Various small molecule PDI derivatives have also been tested with different donor polymers in solution processed devices often resulting in efficiencies below 1 %. In our own work we have recently reported that core-alkylation of PDIs can double the efficiency in blends with P3HT as donor polymer reaching moderate efficiencies of 0.5 %, however the reasons for the still low efficiency remained unclear.[6] In fact, there is only a limited number of studies that address the efficiency-limiting processes in polymer:PDI blends. Pensack et al. have recently reported that in polymer:perylene diimide blends the charge separation is temperature-activated in contrast to polymer:fullerene blends indicating that in the former an activation barrier exists for the charge separation process, which may point to a slower separation process.[7] Durrant and coworkers have also studied the photophysics of polymer:PDI blends.[8] They reported that energy transfer from the perylene diimide to the polymer prior to charge transfer occurred in their system. However, their transient absorption measurements on timescales longer than 1 μs only did not allow insight into the processes of exciton diffusion, charge generation, or sub-microsecond recombination processes. We have recently shown by using ps-ns transient absorption spectroscopy that the efficiency of polymer:PDI blends using F8BT as donor polymer is limited by exciton trapping in PDI aggregates, preventing the efficient splitting of excitons at the interface resulting in very poor efficiencies for this respective system.[9] However, the data analysis was complicated by the spectral superposition of the excited state absorption (ESA) of the many states present in the blend and by the parallel excitation of the polymer and the PDI due to the overlapping ground state absorption (GSA) spectra. Hence, we have turned to different polymer:PDI systems, which have well-separated polymer and PDI GSA and ESA spectra allowing to selectively excite one of the blend's components and to individually monitor the excited states, which, as we will show, aids the data analysis and interpretation and allows unprecedented insights into the photophysics of these systems. For the present study we selected the low-bandgap donor polymer PBDTTT-C and blended it with PDI as acceptor. We studied the charge generation and recombination processes by broadband Vis-NIR transient absorption pump-probe spectroscopy covering a wavelength range from 500 – 2000 nm and a wide dynamic range from femto- to microseconds to monitor the entire cascade of the photophysical processes from exciton generation to free charge recombination. We identified comparably slow exciton quenching and poor interfacial charge separation in conjunction with significant geminate recombination to be the major efficiency-limiting processes. However, once free charges are generated they can be efficiently extracted from the blends showing that the interfacial charge separation process is the main bottleneck of polymer:PDI solar cells.

2. METHODOLOGY

2.1 Materials

Scheme 1 depicts the chemical structures of the donor polymer, namely PBDTTT-C, and the PDI derivative used as electron acceptor. The PBDTTT-C was obtained from Solarmer and the PDI was synthesized in-house.

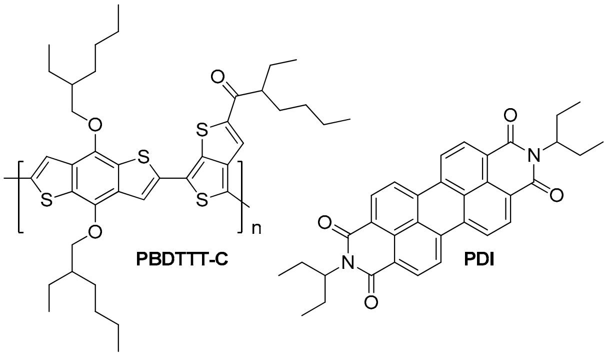

Scheme 1: Chemical structures of the low-bandgap polymer PBDTTT-C and the perylene diimide (PDI) derivative.

2.2 Photovoltaic Devices

For the preparation of solar cells ITO-coated glass substrates (Präzisions Glas & Optik GmbH, Germany) were patterned by wet etching and cleaned successively by ultrasonication in detergent, acetone and iso-propanol. Subsequently the samples were treated with an argon plasma for 15 min before spin-coating a ~ 40 nm thick poly(3,4-ethylene-dioxythiophene):poly-(styrenesulfonate) (PEDOT:PSS) (Clevios P VP Al 4083, H.C. Stark) layer. The substrates were transferred into a nitrogen-filled glovebox and heated to 120 °C for 30 min. For the preparation of the active layer, PBDTTT- C and PDI were individually dissolved in chloroform at a concentration of 10 mg mL^{-1} and the solutions were stirred overnight. Before spin-coating the active layer the solutions were mixed in a ratio of 1:3 (by weight/volume), stirred for another 4 hours and then spin-coated at 900 rpm for 60 s onto the cleaned substrates, resulting in an active layer thickness of ~100 nm. Annealing of the active layer was performed at 120 °C for 10 min. As top-electrodes a bilayer of 5 nm Ca and 100 nm Al was used. Spectroscopic samples were fabricated by spin-coating the solutions onto quartz substrates instead. Solar cells were characterized with a solar simulator (K.H. Steuernagel Lichttechnik GmbH, Germany) employing a 575 W metal halide lamp combined with a filter system to create a spectrum close to AM1.5G conditions, however, with an intensity of 70 mW cm^{-2}. Current-voltage curves were taken with a Keithley 236 Source-Measure Unit in the glovebox. For external quantum efficiency (EQE) measurements the solar-cell device was illuminated with monochromatic light from a tungsten-halogen lamp and a TRIAX 180 monochromator between 400 and 900 nm. The light intensity was measured with a calibrated silicon diode leading to a maximum intensity of 0.7 Wm^{-2} at 600 nm. EQE measurements were performed in the glovebox at short circuit conditions with a Keithley 236 Source-Measure Unit.

2.3 Steady-State Spectroscopy

Absorption properties were measured with a Perkin Elmer Lambda 25 spectrometer. The layer thickness was determined with a Tencor P10 surface profilometer.

2.4 Quasi-Steady-State Spectroscopy

Quasi-steady-state photoinduced absorption spectroscopy (PIA) was performed with a pump-probe setup consisting of a 100 W tungsten-halogen lamp with a LOT-Oriel Omni-λ 300 monochromator as the probe and a Newport LED (LED-527-HP) working at 524 nm with 100 mW cm^{-2} used as a pump. The samples were placed in a nitrogen-cooled optical cryostat (Oxford Instruments Optistat CF) at 80 K in helium atmosphere. The transmitted light was dispersed by a second identical monochromator and then detected by a photodetector. For measurements in the wavelength range from 500 to 1100 nm, an amplified silicon photodetector (Thorlabs PDI 100A) was employed, which was replaced by an amplified germanium detector (Thorlabs PDA 50B) for the wavelength range from 900 to 1800 nm. The pump light was chopped at 317 Hz to induce changes in the transmission ΔT, which were measured by using a lock-in amplifier (EG&G Princeton Applied Research model 5210). To calculate $\Delta T/T$, the transmission was recorded prior to the PIA measurement and corrected for photoluminescence.

2.5 Transient Absorption Spectroscopy

Transient absorption (TA) measurements were performed with a home-built pump-probe setup. To measure in the time range of 1 4 ns with a resolution of ~100 fs, the output of a commercial titanium:sapphire amplifier (Coherent LIBRA HE, 3.5 mJ, 1 kHz, 100 fs) was split into two beams that independently pumped two optical parametric amplifiers (Coherent OPerA Slo). One optical parametric amplifier (OPA) was used to generate the excitation pulses in the visible, while the second OPA was used to generate the seed beam for white-light generation. For measurements in the spectral range between 550-1100 nm a 1300 nm seed was focused into a c-cut 3 mm thick sapphire window for white-light generation. The variable delay of up to 4 ns between pump and probe was introduced by a broadband retroreflector mounted on a mechanical delay stage. Only reflective elements were used to guide the probe beam to the sample to minimize chirp. The excitation pulse was chopped at 500 Hz, while the white-light pulses were dispersed onto a linear silicon photodiode array, which was read out at 1 kHz. Adjacent diode readings corresponding to the transmission of the sample after an excitation pulse and without an excitation pulse were used to calculate $\Delta T/T$.

For measurements in the time range between 1 ns to 1 ms with a resolution of 600 ps, the excitation pulse was provided by an actively Q-switched Nd:YVO_4 laser (AOT Ltd. MOPA) at 532 nm. The delay between pump and probe in this case was controlled by an electronic delay generator (Stanford Research Systems DG535). TA measurements were performed at room temperature under a dynamic vacuum of $<10^{-5}$ mbar.

For TA measurements in the NIR spectral range covering 1100-2000 nm a 2100 nm seed was used to generate white-light and a polished silicon substrate was added into the path of the with light to block the visible fraction of the supercontinuum. Furthermore, a dichroic mirror was used to separate the residual idler beam (2100 nm) from the white-light supercontinuum. The NIR white-light pulses were dispersed onto a Peltier-cooled 512 pixel long linear extended InGaAs array (Entwicklungsbüro Stresing) and read out as described above.

3. RESULTS

3.1 Steady-State Absorption Spectra

Figure 1 shows the absorption spectra of a thin PBDTTT-C film, a thin film blend of the PDI derivative doped into polystyrene as inert matrix polymer and the absorption spectrum of a PBDTTT-C:PDI (1:3) blend used for the photovoltaic devices and optical experiments. The absorption spectra of the PDI and the polymer are largely complementary with the former absorbing mostly between 450 – 550 nm and the latter from 550 – 750 nm, respectively. The absorption spectrum of the PDI shows the typical features of H-aggregates, i.e. a higher oscillator strength of the 0-1 transition compared to the 0-0 transition, as previously reported for this material.[10] In the photovoltaic blend the absorption of the PDI is significantly stronger than the absorption of the polymer due to the excess of PDI molecules with respect to the polymer content necessary for optimum performance.

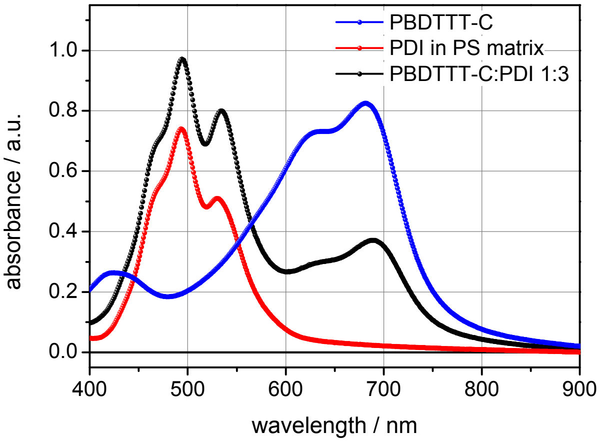

Figure 1. Absorption spectra of a PBDTTT-C thin film, a blend of perylene diimide with polystyrene (50 wt.% each) and the PBDTTT-C:PDI blend (1:3 wt.%).

We note that the well-separated absorption bands of the PDI and the low-bandgap polymer allow for selective excitation of the polymer at wavelengths longer than 650 nm and predominant excitation of the PDI at around 500 nm, where the polymer absorption has its minimum, in turn allowing us to study the photophysical processes occurring after the selective excitation of one of the two components.

3.2 Photovoltaic Performance

Figure 2(a) shows the J-V curve of a PBDTTT-C:PDI (1:3) annealed solar cell along with the dark current of the same device. The annealed solar cells showed an open circuit voltage (V_{OC}) of 0.62 V, a short circuit current (I_{SC}) of 2.8 mA/cm² and a FF of 46 % resulting in a moderate overall efficiency of 1.2 %. In figure 2(b) the external quantum efficiency (EQE) spectrum of the annealed device is presented. The polymer:PDI layer is photoactive across the entire visible spectral range up to 800 nm with a maximum EQE of 30 % at 450 nm, which corresponds to the PDI absorption. From the absorption spectrum of the blend the maximum possible I_{SC} was calculated following the approach by Burkhard et al. taking into account the absorbance of the film, the reflected light at the electrodes, interference effects within the active layer and assuming an internal quantum efficiency of unity.[11] This yields a theoretically possible maximum I_{SC} for the PBDTTT-C:PDI (1:3) blend of 11.2 mA/cm² at a film thickness of the active layer of 100 nm, when illuminated with 0.7 suns corresponding to our measurement conditions. Given that the experimentally measured I_{SC} is 2.8 mA/cm² only, this amounts to a total loss of about three fourth with respect to the number of initial excitations.

However, it is unclear where this loss occurs in the cascade of processes leading to photocurrent generation and thus we turned to transient pump-probe spectroscopy to investigate the individual loss channels.

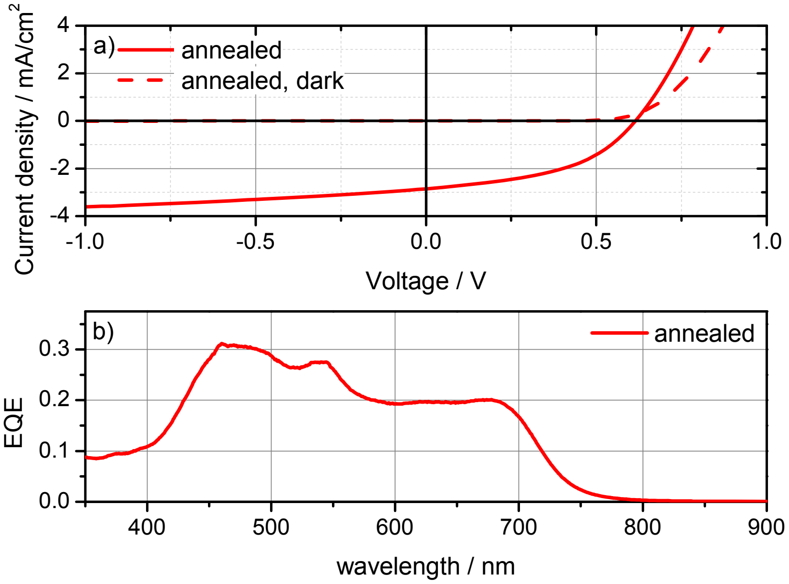

Figure 2. (a) JV-curves of as-cast (black) and annealed (red) PBDTTT-C:PDI (1:3) solar cells under AM1.5G-like conditions at 0.7 suns illumination conditions. The dashed lines show the respective dark currents of the devices. (b) External quantum efficiency of the annealed PBDTTT-C:PDI (1:3) solar cell.

3.3 Early-Time (ps-ns) Transient Absorption Spectra and Dynamics

Before we present the results of the transient absorption (TA) measurements let us briefly recall the fundamentals of the experimental technique. TA is a two pulse pump-probe experiment, which probes the pump-induced change of the transmission ($T_{ON} - T_{OFF}$) of the sample by a second probe pulse with respect to its ground state transmission (T_{OFF}). Typically the pump pulse is a femtosecond narrowband laser pulse, while the probe pulse is a broadband supercontinuum covering a spectral range preferably as wide as possible. The probe pulse can be temporally delayed with respect to the pump pulse to allow the signal dynamics to be studied. Upon plotting $\Delta T/T$ vs. the wavelength or energy, respectively, negative signals indicate photoinduced absorption (PA), while positive signals can be assigned to either stimulated emission (SE) originating from singlet excitons or a ground state bleach (GSB) caused by the depopulation of the material's ground state due to the presence of excited states. Naturally, the spectral features of the different excited states overlap which complicates data analysis. However, this issue can, at least to some extent, be overcome by probing not only the visible, but also the entire near-infrared spectral range, which, as we will show, is a prerequisite to understand the processes in low-bandgap materials. Secondly, in order to monitor the entire cascade of processes not only the femto- to nanosecond, but also the nano- to microsecond time range should be observed. Recent advances in supercontinuum generation and detection and laser technology have made all this feasible and Vis-NIR fs-µs pump-probe spectroscopy has become a ubiquitous tool in material science.

In figure 3 we show a comparison of the Vis-NIR pump-probe spectra of a PBDTTT-C:PDI (1:3) blend on the ps-ns timescale (a) along with the TA spectra of the pristine polymer (b) on the ps-ns timescale.

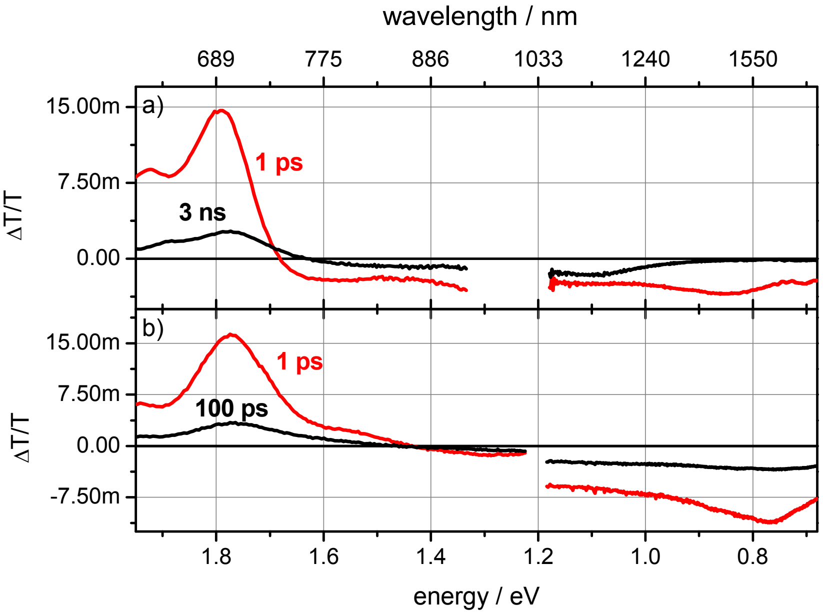

Figure 3: a) ps-ns transient absorption spectra of PBDTTT-C:PDI (1:3) blends at two different delay times. b) ps-ns transient absorption spectra of a thin PBDTTT-C polymer film at two different delay times.

The pristine polymer film showed a positive signal at short wavelength up to 860 nm, which we assigned to the GSB and SE of the polymer due to its correspondence to the ground state absorption and fluorescence of the polymer. At longer wavelength a broad photoinduced absorption (PA_{Ex}) peaking at 1620 nm can be seen, which originated from the singlet excitons created in the pristine polymer film by photoexcitation. The isosbestic point at 860 nm indicated the presence of a single excited species only, which returned to the ground state within a ns. The dynamics of the GSB and PA_{Ex} showed a pronounced intensity dependence (not shown) indicating annihilation of excited singlet states, namely singlet-singlet annihilation (SSA), due to the high exciton density created by the femtosecond pump pulse. However, at the lowest pump energy (~20 nJ) the dynamics could be described by a single exponential with an inverse rate constant of 266 ps similar to the fluorescence lifetime of the polymer indicating negligible SSA. We note that at very high pump intensities the TA spectra after 1 ns showed an additional peak at 1150 nm indicating the formation of charges in the pristine polymer, most probably as a consequence of SSA.

The ps-ns pump-probe spectra of the PBDTTT-C:PDI (1:3) blends after selective excitation of the polymer at 650 nm showed after 1 ps a ground state bleach of the polymer up to 729 nm and a broad photoinduced absorption covering the entire NIR spectral range peaking at 1500 nm. The latter vanished within the first 100 ps after excitation after which a photoinduced absorption between 742 nm and 1400 nm remained, which peaked at 1130 nm. We assigned the spectral evolution to a population flow from singlet excited states of the polymer to charges, as indicated by the emergence of the charge-induced absorption (PA_C) of the polymer. The assignment of this band to the charge-induced absorption is further supported by a comparison of the TA spectra of a PBDTTT-C:PCBM blend (not shown) with the data presented in figure 3, which showed virtually the same PA_C of the polymer. We also observed that the GSB of the polymer decayed to about 15.7% of its initial value within the timerange of 3 ns indicating a substantial fraction of the initial polymer exciton population returned to the ground state before undergoing charge separation and indicating also some nanosecond geminate recombination.

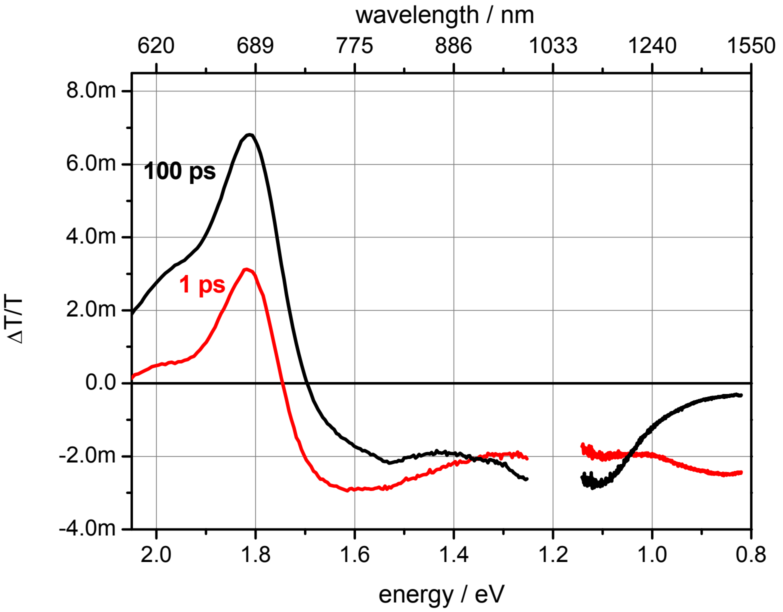

Figure 4: ps transient absorption spectra of PBDTTT-C:PDI (1:3) blends at different delay times after excitation at 520 nm.

Before presenting the results of the nano- to microsecond TA experiments we have a closer look at the processes occurring after excitation of the PDI acceptor. Figure 4 shows the Vis-NIR TA spectra of the same PBDTTT-C:PDI (1:3) blend as presented above, but excited at 520 nm, where mainly the PDI acceptor absorbed and the polymer absorption was significantly less. The ground state bleach of the polymer rose during the first 20-30 ps indicating a delayed depopulation of the polymer's ground state. Concomitantly the charge-induced absorption of the polymer increased, indicating diffusion-limited exciton dissociation from excitons primarily created in the PDI domains. However, we note that we also observed the PA_{Ex} of the polymer below 100 ps showing that some fraction of the polymer was excited at 520 nm as well. While it is clear that excitation of the PDI led to delayed charge generation as proven by the rise of the polymer bleach, it is not straightforward to unravel the mechanism behind the delayed charge separation. In principle the PDI excitons could diffuse to the heterojunction and upon approaching the interface transfer a hole to the polymer. This has previously been observed in polymer:fullerene blends upon excitation of the fullerene phase.[12] However, in the case of polymer:PDI blends also fluorescence energy transfer by the Förster mechanism can occur, as the PDI fluorescence spectrum significantly overlaps with the polymer absorption. One may speculate further that upon energy transfer the polymer exciton is created close to an interface, where it can undergo immediate charge transfer. Although we could not distinguish between these two processes and not rule out that they coexist, we could determine that the delayed charge separation is finished within 100 ps, after which the TA spectra and dynamics observed for the excitation of either the PDI or the polymer resemble each other.

3.4 Nano- to Microsecond Charge Recombination

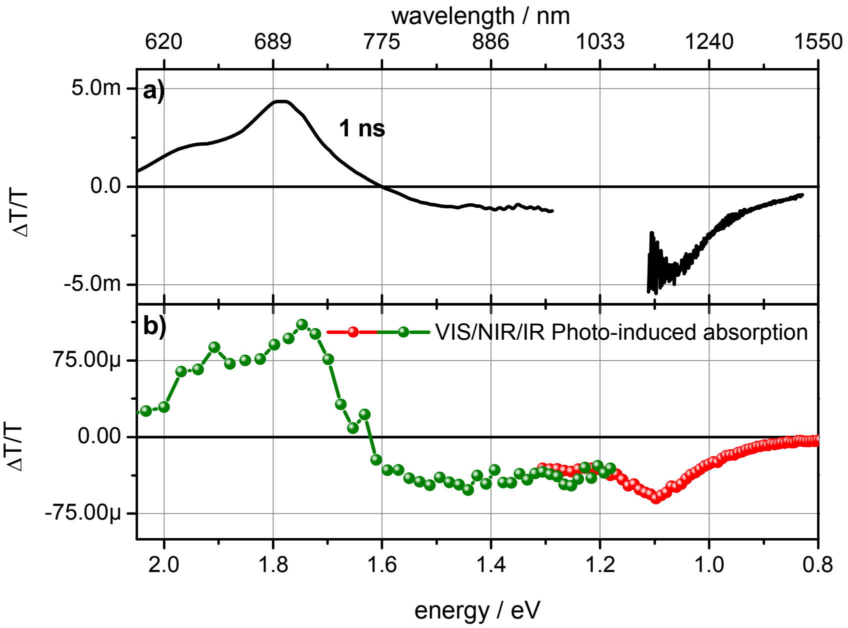

Figure 5: a) ns transient absorption spectrum of a PBDTTT-C:PDI (1:3) blend at a delay time of 1 ns. b) Quasi steady-state photoinduced absorption spectra of a PBDTTT-C:PDI (1:3) blend.

Figure 5 depicts a ns pump-probe spectrum (a) and the steady-state photoinduced absorption spectrum (b) of the PBDTTT-C:PDI blend after excitation at 532 nm. The delayed TA spectrum shows the ground state bleach of the polymer and the PA_C, in good agreement with the spectra observed after 1 ns in the early-time TA experiments. The similarity of the ns pump-probe spectrum with the steady-state PIA indicates that on this timescale we observed long-lived states, specifically free charge carriers that can be extracted as photocurrent. In fact, we also observed a pronounced intensity dependence of the decay of the charge-induced absorption supporting the assignment of the PA_C to free charges, as it points to a non-geminate recombination of mobile charge carriers.

4. DISCUSSION

The generation of photocurrent in an organic solar cell depends on a cascade of photophysical processes, each potentially also contributing a loss channel. Absorption of photons in the photoactive layer leads to the generation of a strongly-bound electron-hole pair, namely an exciton, in either the donor or acceptor component. If generated close to the heterojunction the exciton can dissociate ultrafast into free charges, as typically observed for polymer:fullerene blends. However, excitons generated in the bulk have to diffuse to the interface to undergo charge transfer. During exciton diffusion recombination of the electron-hole pair can occur leading to a loss of excited states. Furthermore, charge transfer at the interface can lead to bound charge-transfer states, which recombine geminately. Finally, spatially-separated charges can encounter each other at the interface during their drift-diffusion to the electrodes resulting in non-geminate recombination. From the evolution of the transient absorption signals of the polymer:PDI blends, namely the exciton- and charge-induced absorptions observed across the ps-µs time range, we can roughly estimate the contribution of the individual loss channels. We determine that a large fraction of polymer excitons of about 55 % recombines into the ground state without undergoing charge transfer. The remaining fraction of 45 % of excitons that do undergo charge transfer at the heterojunction splits into 19 % charge-transfer states that recombine geminately within the first few nanoseconds and 26 % spatially-separated charges that undergo non-geminate recombination and can potentially be extracted as photocurrent. The latter value of about one fourth fits very well to the experimentally observed photocurrent in relation to the theoretically predicted maximum photocurrent of the blend indicating that free charges created in the blend can in fact be extracted as photocurrent. This implies on the other hand that the performance of the investigated polymer:PDI blends is heavily limited by inefficient exciton harvesting and dissociation at the heterojunction. Hence, a potential strategy to improve the efficiency of polymer:PDI solar cells is to increase exciton harvesting, for instance by better mixing of the blend's components, and to increase the charge separation efficiency at the interface by careful design of the PDI acceptor.

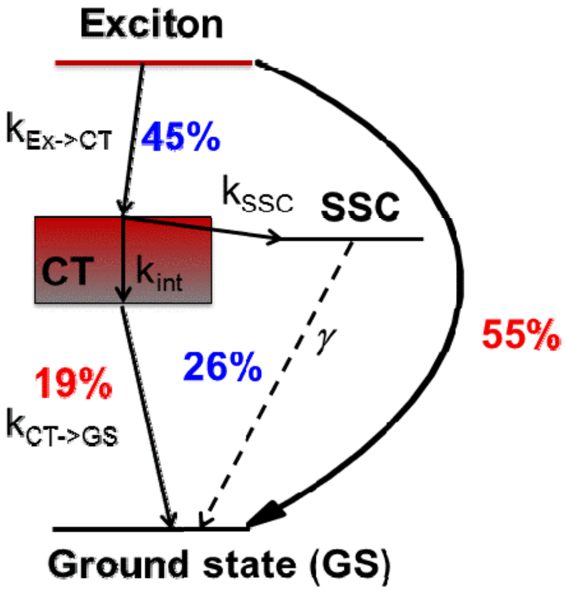

Figure 6: The estimated contributions of the individual photophysical processes in the polymer:PDI blend. CT denotes charge-transfer states, SSC spatially-separated charges.

*laquai@mpip-mainz.mpg.de; phone +49 6131 379 135; fax +49 6131 379 100; www.mpip-mainz.mpg.de/11529/Organische_Optoelektronik

REFERENCES

[1] Janssen, R. A. J. and Nelson, J., "Factors Limiting Device Efficiency in Organic Photovoltaics," Adv. Mater. 25(13), 1847-1858 (2013).

[2] Li, G., Zhu, R., Yang, Y., "Polymer solar cells," Nat. Photon. 6(3), 153-161 (2012).

[3] Bloking, J. T., Han, X., Higgs, A. T., Kastrop, J. P., Pandey, L., Norton, J. E., Risko, C., Chen, C. E., Bredas, J. L., McGehee, M. D., Sellinger, A., "Solution-Processed Organic Solar Cells with Power Conversion Efficiencies of 2.5% using Benzothiadiazole/Imide-Based Acceptors," Chem. Mater. 23(24), 5484-5490 (2011).

[4] Rajaram, S., Shivanna, R., Kandappa, S. K., Narayan, K.S., "Nonplanar Perylene Diimides as Potential Alternatives to Fullerenes in Organic Solar Cells," J. Phys. Chem. Lett. 3(17), 2405-2408 (2012).

[5] Hüttner, S., Hodgkiss, J. M., Sommer, M., Friend, R. H., Steiner, U., Thelakkat, M., "Morphology-Dependent Charge Photogeneration in Donor-Acceptor Block Copolymer Films Based on Poly(3-hexylthiophene)-block-Poly(perylene bisimide acrylate)," J. Phys. Chem. B 116(33), 10070-10078 (2012).

[6] Kamm, V., Battagliarin, G., Howard, I.A., Pisula, W., Mavrinskiy, A., Li, C., Müllen, K., Laquai, F., "Polythiophene:Perylene Diimide Solar Cells – The Impact of Alkyl-Substitution on the Photovoltaic Performance," Adv. Energy Mater. 1(2), 297-302 (2011).

[7] Pensack, R.D., Guo, C., Vakshouri, K., Gomez E.D., Asbury, J.B., "Influence of Acceptor Structure on Barriers to Charge Separation in Organic Photovoltaic Materials," J. Phys. Chem. C 116(7), 4824-4831 (2012).

[8] Shoaee, S., Clarke, T.M., Huang, C., Barlow, S., Marder, S.R., Heeney, M., McCulloch, I., Durrant, J.R., "Acceptor Energy Level Control of Charge Photogeneration in Organic Donor/Acceptor Blends," J. Am. Chem. Soc. 132(37), 12919-12926 (2010).

[9] Howard, I.A., Laquai, F., Keivanidis, P.E., Friend, R.H., Greenham, N.C., "Perylene Tetracarboxydiimide as an Electron Acceptor in Organic Solar Cells: A Study of Charge Generation and Recombination," J. Phys. Chem. C 113(50), 21225-21232 (2009).

[10] Keivanidis, P. E., Kamm, V., Dyer–Smith, C., Zhang, W., Laquai, F., McCulloch, I., Bradley, D. D. C., Nelson, J.,"Delayed luminescence spectroscopy of organic photovoltaic binary blends: probing the emissive non-geminate charge recombination," Adv. Mater. 22(45), 5183-5187 (2010).

[11] Burkhard, G. F., Hoke, E. T., McGehee, M. D., "Accounting for Interference, Scattering, and Electrode Absorption to Make Accurate Internal Quantum Efficiency Measurements in Organic and Other Thin Solar Cells," Adv. Mater. 22(30), 3293-3297 (2010).

[12] Etzold, F., Howard, I.A., Forler, N., Cho, D.M., Meister, M., Mangold, H., Shu, J., Hansen, M.R., Müllen, K., Laquai, F., "The Effect of Solvent Additives on Morphology and Excited State Dynamics in PCPDTBT:PCBM Photovoltaic Blends," J. Am. Chem. Soc. 134 (25), 10569–10583 (2012).

4.2 PBDTTT-C:Fullerene Solar Cells

The article "Charge Carrier Generation Followed by Triplet State Formation, Annihilation, and Carrier Recreation in PBDTTT-C:$PC_{60}BM$ Photovoltaic Blends" was published in the Journal of Physical Chemistry C and is available online since May 22nd, 2015. The article is reprinted with permission from reference [217]. Copyright (2015) American Chemical Society.

THE JOURNAL OF
PHYSICAL CHEMISTRY C
Article
pubs.acs.org/JPCC

Charge Carrier Generation Followed by Triplet State Formation, Annihilation, and Carrier Recreation in PBDTTT-C/PC$_{60}$BM Photovoltaic Blends

Dominik W. Gehrig, Ian A. Howard, and Frédéric Laquai*,†

Max Planck Research Group for Organic Optoelectronics, Max Planck Institute for Polymer Research, Ackermannweg 10, 55128 Mainz, Germany

Ⓢ *Supporting Information*

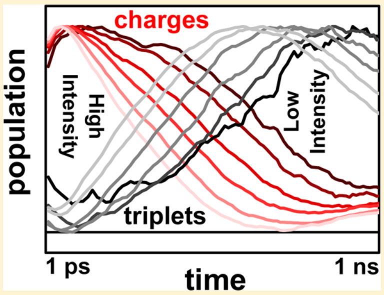

ABSTRACT: Triplet state formation after photoexcitation of low-bandgap polymer/fullerene blends has recently been demonstrated; however, the precise mechanism and its impact on solar cell performance is still under debate. Here, we study exciton dissociation, charge carrier generation, and triplet state formation in low-bandgap polymer PBDTTT-C/PC$_{60}$BM bulk heterojunction photovoltaic blends by a combination of fs−μs broadband vis-NIR transient absorption (TA) pump−probe spectroscopy and multivariate curve resolution (MCR) data analysis. We found sub-ps exciton dissociation and charge generation followed by sub-ns triplet state creation. The carrier dynamics and triplet state dynamics exhibited a very pronounced intensity dependence, indicating nongeminate recombination of free carriers is the origin of triplet formation in these blends. Triplets were found to be the dominant state present on the nanosecond time scale. Surprisingly, the carrier population increased again on the ns−μs time scale. We attribute this to triplet−triplet annihilation and the formation of higher energy excited states that subsequently underwent charge transfer. This unique dip and recovery of the charge population is a clear indication that triplets are formed by nongeminate recombination, as such a kinetic is incompatible with a monomolecular triplet state formation process.

1. INTRODUCTION

Triplet state formation is a ubiquitous phenomenon in organic semiconductors and typically occurs as a consequence of intersystem crossing from the singlet excited state or via fission of high energy excitations.[1,2] It plays a prominent role in the device physics of organic light-emitting diodes (OLEDs), in which recombination of injected charge carriers should theoretically lead to a fraction of 75% triplet state formation according to spin statistics. Recently, increasing attention is being paid to triplet states in polymer/fullerene photovoltaic blends.[3−5] In the last year, several groups have reported triplet state formation in low-bandgap polymer/fullerene solar cells, but the precise mechanism behind the triplet state formation is currently debated. An understanding of whether triplets are formed due to geminate recombination of interfacial charge-transfer (CT) states created upon exciton dissociation or due to nongeminate recombination of spatially separated charges (SSC) is still sought. It is important to know the exact nature of the triplet state formation mechanism because a geminate recombination mechanism is an intensity-independent process and thus would play a significant role even under solar illumination conditions (that is at lower carrier concentrations than transient absorption experiments). On the other hand, nongeminate recombination rates depend strongly on the charge carrier concentrations and therefore may be of more relevance after pulsed laser excitation, and less relevant for photovoltaic devices performance under standard illumination. In the past Westenhoff et al. studied all-polymer photovoltaic blends by transient absorption spectroscopy and reported triplet state formation as a consequence of recombination of interfacial charge-transfer states.[6] Di Nuzzo et al. investigated triplet state formation in PCPDTBT/PCBM blends and its dependence on film morphology by steady-state photoinduced absorption spectroscopy. The authors argued that processing of the blend in the presence of solvent additives changes the blend morphology and energy landscape and thereby reduces triplet state formation as the triplet level becomes energetically less accessible in blends prepared with additives.[7] However, a recent transient absorption study on the same material system by Chow et al. presented contradictory evidence. They showed that in fact more triplets are created in the blend processed with solvent additives, and that this is a consequence of an increased yield of free charge carriers that create triplets through nongeminate recombination.[5] Similarly, Rao et al. showed that triplet formation in PCPDTBT/PCBM blends is depending on the excitation density and concluded that triplet states are populated via bimolecular recombination events.[3] Very recently, Dimitrov et al. reported polaron pair-mediated triplet state formation caused by recombination of interfacial states created upon singlet exciton dissociation in a fluorinated low-bandgap polymer/fullerene blend.[4] Furthermore, triplet state formation via nongeminate recombination of free charges has

Received: April 10, 2015
Revised: May 20, 2015
Published: May 22, 2015

DOI: 10.1021/acs.jpcc.5b03467
J. Phys. Chem. C 2015, 119, 13509−13515

very recently been identified as a loss channel in PTB7/$PC_{60}BM$ solar cells.[8] Interestingly, the triplet state population could be suppressed by addition of a 1/2 spin-radical, namely, galvinoxyl, in turn leading to a significant improvement of the device photocurrent. In our own work we very recently compared triplet state formation in the silicon-substituted analogue of PCPDTBT, namely, PSBTBT, and showed that triplet states are created on a sub-ns time scale in PCPDTBT/PCBM supporting the findings of Chow et al. We found that triplets were also created in PSBTBT/PCBM, however, to a much lesser extent than in the PCPDTBT/PCBM, which indicated a suppressed rate of nongeminate recombination contributes to PSBTBT/PCBM's higher photovoltaic efficiency.[9]

In the present study, we investigated the excited state dynamics, specifically the charge recombination and triplet state formation, following pulsed laser excitation of another widely used prototypic low-bandgap polymer/fullerene blend, namely, PBDTTT-C/$PC_{60}BM$ (see Scheme 1 for chemical structures), by ps−μs broadband vis-NIR transient absorption spectroscopy in combination with multivariate curve resolution (MCR) analysis of the experimental data. The BDT comonomer is a common structural motif often used in alternating donor−acceptor low-bandgap polymers, thus the investigated PBDTTT-C polymer belongs to a whole family of structurally related materials very often used in polymer solar cells such as PTB1 and PTB7 for instance. Compared to the PBDTTT-C polymer studied by us, in which the thienothiophene (TT) comonomer is substituted with an ethyl-hexyloxy side group and the BDT unit is substituted with a 2-ethyl-hexan-1-one side group, PTB1 is substituted with a dodecyl-ester group at the TT unit and *n*-octyloxy side chains at the BDT comonomer, while in PTB7 the BDT unit is the same as in PBDTTT-C and the TT unit is substituted with an ethyl-hexyl ester and in addition also fluorinated in comparison to PTB1 and PBDTTT-C.[10−12] Guo et al. and Rolczynski et al. have previously studied the correlation between bulk morphology, excited state dynamics and power conversion efficiency of bulk heterojunction solar cells using structurally related donor polymers including PTB1,[13−15] while Carsten et al. and Szarko et al. have studied the photophysics of PTB7 blended with fullerenes.[16−18] However, in the aforementioned studies the authors limited their spectroscopic experiments to the ps−ns time scale mostly relevant for exciton dissociation and charge carrier formation, while the ns−μs time range relevant for charge carrier recombination was not investigated, and furthermore, none of the studies reported triplet state formation in blends of these polymers with fullerene derivatives. Here, we use a combination of broadband vis-NIR transient absorption spectroscopy across a dynamic range from femto- to milliseconds in conjunction with sophisticated MCR analysis to separate the individual components contributing to the experimentally observed data and thereby to determine the component-associated spectra and their dynamics. Specifically, we demonstrate in the following that in the investigated PBDTTT-C/PCBM blends triplet states are rapidly generated by nongeminate recombination on a sub-ns time scale and subsequently undergo fast triplet−triplet annihilation on the ns−μs time scale that leads to a recreation of the charge carrier population.

Scheme 1. Chemical Structures of the Material System Investigated in the Present Study, Namely, the Low-Bandgap Donor Polymer PBDTTT-C and the Electron Acceptor $PC_{60}BM$

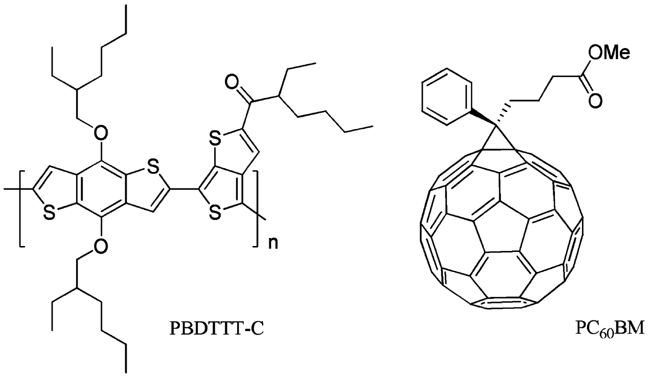

2. RESULTS AND DISCUSSION

Figure 1a shows the near-infrared ps−ns transient absorption spectra of a PBDTTT-C/PCBM (1:2) bulk heterojunction blend film as typically used in photovoltaic devices and (c) the signal dynamics monitored in selected wavelength regions, which, as we will show, correspond to specific excited states (thereafter named components) present in the blend film after photoexcitation. The sub-ps TA spectrum (shown in the SI) exhibits contributions of the excited state absorption of the primary photoexcitations, namely, singlet exciton-induced absorption (PA_{ex}). Polymer singlet excitons undergo ultrafast charge transfer in the blend as indicated by the rapid decay of the PA_{ex} at around 1450−1475 nm, that is a wavelength range, in which singlet excitons clearly dominate the TA spectra at early delay times. For comparison we have included a TA spectrum of a pristine polymer film in the SI. The TA spectrum 1 ps after photoexcitation peaks at 1120 nm, but rapidly undergoes a spectral evolution on the sub-ns time scale. In fact, a progressive red-shift of the maximum of the TA signal with time was observed until at about 1 ns the photoinduced absorption peaked at 1190 nm. Interestingly, we also observed an isosbestic point at 1135 nm indicating that we witnessed a transition between two components without any significant loss of the total excited state population by recombination of the excited states to the ground state. In conjunction with the red-shift of the photoinduced absorption, we also observed an increase in the total signal amplitude, indicating that the product created on the sub-ns time scale, hereafter referred to as component 2, has a larger excited state absorption cross section than component 1, that is the product of exciton dissociation obtained on the ps time scale. In order to gain more detailed insight into the nature of the components, we performed multivariate curve resolution analysis on the experimentally measured TA data, a soft-modeling data analysis technique previously introduced by Jaumot et al.[19] We have recently reviewed this technique and its usefulness for the analysis of TA data and we have previously applied it for TA data analysis of different photovoltaic systems, for instance, polymer/perylene diimide (PDI) blends, small molecule donor/PDI acceptor systems, and low-bandgap polymer/fullerene blends.[9,20−22] A brief introduction to the principles of MCR analysis is also presented in the Supporting Information. The MCR analysis of the experimental TA data yielded two separate component spectra and component-associated dynamics as shown in Figure 1b and d, respectively.

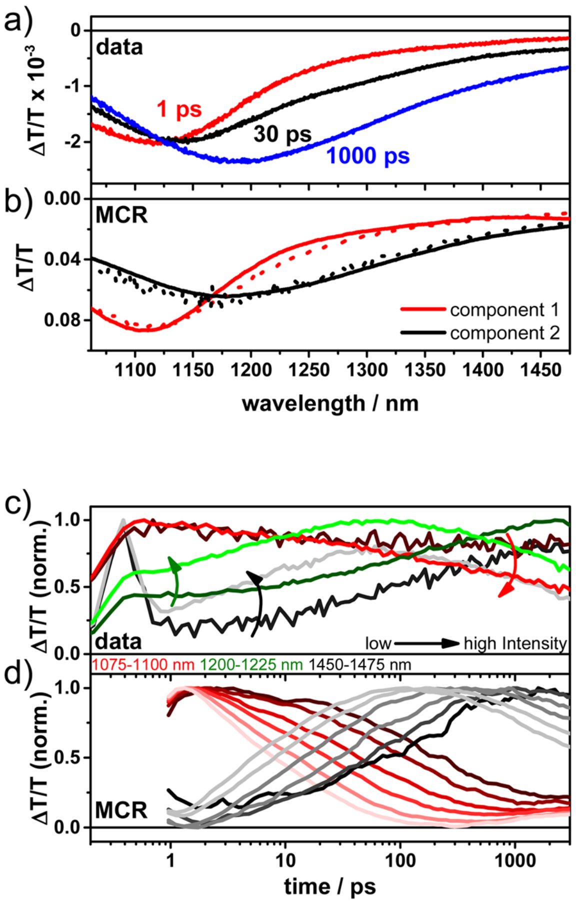

Figure 1. (a) ps−ns transient absorption spectra at different delay times after excitation of the polymer at 650 nm with a fluence of 6.7 μJ/cm^2. (b) Component spectra obtained by MCR-ALS analysis of the ps−ns TA data using non-negativity as a constraint for the concentration profiles and non-positivity as spectral constraint. The dotted spectra represent the charge- and triplet-induced absorption spectra obtained by separate measurements on a polymer/PDI blend and a triplet sensitizer-doped polymer film, respectively. (c) Dynamics extracted at 1075−1100 nm (red), 1200−1225 nm (green), and 1450−1475 nm (gray) at different excitation densities. (d) Dynamics of components 1 (charges) and 2 (triplets) obtained by MCR-ALS analysis of the TA data after 1 ps. Note the pronounced intensity dependence of the dynamics.

However, the precise nature of the excited states is a priori unknown, and thus, we performed control experiments to identify the two components. In fact, component 1, which is already present at 1 ps after photoexcitation when polymer exciton dissociation is completed and which peaks at 1120 nm could be assigned to charges, as the peak position of the component-associated spectrum matches very closely that of the charge-induced absorption (PA_{charge}) obtained on an iodine-oxidized polymer film (see SI) and also previously reported for the same polymer but blended with PDI as acceptor instead of fullerene (see Figure 1).[21] We note that this component spectrum is also similar in shape and position as the charge-induced absorption spectrum reported earlier by Guo et al. for the structurally related polymer PTB1 when blended with PCBM.[13] The spectrum of component 2 was found to be virtually the same as the triplet-induced absorption ($PA_{triplet}$) obtained by TA experiments on polymer films doped with different metalated porphyrins as sensitizers (see SI and Figure 1). Hence, we can confidently conclude that component 1 represents charges, while component 2 triplet states in the PBDTTT-C/$PC_{60}BM$ blend. Furthermore, the excellent agreement of the spectra obtained from the MCR with the known spectra means that the factorization provided by the MCR is accurate, and the dynamics it extracted accurately correspond to the real evolution of the charge and triplet concentrations. The component-associated dynamics from the MCR analysis are shown in Figure 1d. Both the charge carrier dynamics as well as the triplet state dynamics exhibit a very pronounced dependence on the excitation fluence on the sub-ns time scale, that is, on the total concentration of excited states. The decrease in the charge population occurs more quickly at higher fluences, in line with the observation that the increase in the triplet population also occurs more quickly at higher fluences. The time scale of the charge decay and triplet formation are clearly linked and change similarly as a function of fluence. These observations clearly point to a mechanism of triplet state formation via nongeminate recombination of charges, in line with previous reports for TQ1/PCBM by Rao et al., PCPDTBT/PCBM by Chow et al. and PSBTBT/PCBM by Etzold et al.[3,5,9] In order to estimate the sub-ns recombination coefficient we parametrized the intensity-dependent dynamics of component 1 by a combination of a concomitant single exponential and nongeminate (power law) process. The former accounts for any fast recombination and annihilation process of charges, while the latter describes the carrier population undergoing sub-ns nongeminate recombination. Interestingly, this simplified approximation yields a nongeminate recombination coefficient on the order of 10^{-9} cm^3 s^{-1}, which translates into an effective bimolecular recombination coefficient at a carrier concentration of 5×10^{15} cm^{-3} (approximately that under solar illumination) on the order of 10^{-10} cm^3 s^{-1}. This is very high and in line with the fast sub-ns charge recombination observed experimentally. Using the latter value to calculate the minimum mobility of electrons and holes according to the approach previously reported by Koster et al.[23] yields a mobility value of ~1 cm^2 (Vs)$^{-1}$. This rather high mobility is in good agreement with values used in Kinetic Monte Carlo simulations by Burke et al. to explain the high exciton dissociation yield in bulk heterojunction solar cells and it is also compatible with conductivity values derived from ultrafast terahertz spectroscopy experiments on polymer/fullerene blends.[24,25] This is also consistent with the picture that charges created by ultrafast exciton dissociation are located in the upper part of the density of states (DOS) and thus are very mobile as they have not yet relaxed within the density of states to sites of lower energy in the tail of the DOS.

Furthermore, we determined the TA signal amplitude of charges and triplets from the MCR analysis and plotted the maximum TA signal versus the excitation energy or pump fluence (see SI). Interestingly, the maximum charge carrier and triplet concentration exhibit a similar and linear dependence on the excitation fluence. For the charge carriers this is obvious, as the initial carrier concentration at 1 ps should be directly proportional to the fluence as long as sub-ps higher order annihilation processes do not play a role and the ground state absorption is not saturated. However, the reason for the linear increase of the triplet yield with fluence is not immediately apparent, but it does not necessarily indicate that the triplets are created from a monomolecular process such as spin-flipping in a CT state. Rather, charge recombination is clearly dominated by nongeminate recombination in the range of fluences we investigated, as indicated by the intensity dependent dynamics. This supports that for all of these fluences or charge carrier densities created by pulsed laser excitation essentially all generated charges undergo nongeminate recombination and thereby cause the triplet yield of this bimolecular process nonetheless to be linearly dependent on the initial charge carrier concentration. In this case the rate of triplet formation should depend on fluence and in fact, we observed a clear correlation between the rate of nongeminate recombination and triplet formation across the measured fluences as obvious from Figure 1d). Furthermore, we note that, although most of the initially created charges had recombined by 1 ns, the decay dynamics on the ns−μs time scale were still intensity-dependent indicating, as we will discuss later, that triplet−triplet annihilation is a major recombination mechanism for triplets at these fluences. Nevertheless, we still obtained a reasonable photovoltaic performance (see SI) from the PBDTTT-C/PC$_{60}$BM blends, which would not be the case, if the same processes occurred to a similar extent under solar illumination, that is, at much lower charge carrier densities. Hence, our results clearly point to a nongeminate mechanism as the origin of triplet state formation in this particular material system.

Figure 2a shows the experimentally determined ns−μs TA spectra after pulsed laser excitation of the same blend as used for the ps−ns experiments. The signal dynamics tracked between 1140 and 1160 nm are clearly intensity-dependent as shown in Figure 2c. Similar to the analysis of the ps−ns dynamics we also performed MCR-ALS analysis of the TA data obtained on the ns−μs time scale. Again, we observed two components are required to describe the entire TA data matrix, of which component 1 represents the charge-induced absorption very similar to the charge-induced absorption spectrum of a PBDTTT-C/PDI blend. Component 2 represents the triplet-induced absorption, as supported by comparison of this component spectrum with the separately obtained absorption spectrum of triplet states also depicted in Figure 2b. We observed that the triplet decay dynamics are only weakly intensity-dependent, as shown in Figure 2d, and exhibit a rather complex decay pattern, which can neither be described by an exponential decay nor a power law indicating that several parallel processes determine the triplet decay including the recombination of triplets to the ground state, as well as triplet−triplet and perhaps triplet−charge annihilation. In fact, the observed triplet state decay dynamics are similar to those observed in the porphyrin-doped polymer film at high excitation densities, that is, under conditions which lead to a significant population of polymer triplet states and thus cause triplet−triplet annihilation to be the main decay channel of the triplet state population.

Surprisingly, we also observed a pronounced rise of the charge-induced absorption up to ~200 ns (see Figure 2d), which is the time scale on which the main part of the triplet population decays. This is rather unexpected and indicates that a substantial fraction of the triplet population indeed underwent triplet−triplet annihilation, thereby created higher energy triplet and singlet excitons, which in turn had sufficient energy to undergo charge separation and led to a delayed (re)generation of charge carriers in the polymer. As these regenerated charges create a charge density that is much lower than the original charge density immediately after optical excitation, the regenerated charges live much longer and are not immediately lost to nongeminate recombination. This longer lifetime of the regenerated charges allows them to be clearly observed. The triplet−triplet annihilation is supported by the fast decay of the triplet states observed in the polymer/fullerene blend which is similar to the high excitation conditions in the triplet sensitizer-doped film as outlined above.

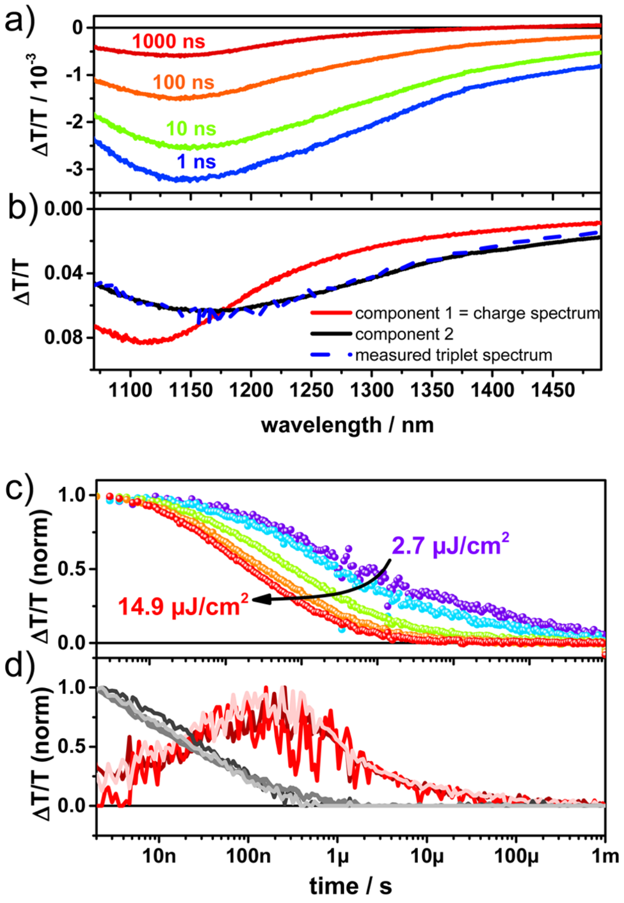

Figure 2. (a) ns−μs TA spectra in the near-infrared spectral region measured after pulsed laser excitation at 532 nm and 8.5 μJ/cm^2 per pulse. (b) Absorption spectra extracted from the ns−μs data surface by MCR-ALS analysis. The black spectrum represents component 2 obtained by using the charge-induced absorption spectrum of a PBDTTT-C/PDI blend as input, while the dashed blue spectrum corresponds to the triplet-induced absorption spectrum obtained on a PtOEP-sensitized film. (c) Dynamics observed at different excitation densities extracted in the spectral region from 1140 to 1160 nm. (d) Intensity dependence of the concentration profiles for components 1 (red, charges) and 2 (gray, triplets).

Figure 3 shows a combined contour plot of the ps−μs experimental TA data and the corresponding charge-induced and triplet-induced absorption spectra and dynamics as obtained by MCR analysis of the ps−ns TA data and ns−μs TA data. Clearly, the charge carrier concentration is minimal at around 1 ns after excitation. This depletion of the pool of charge carriers in conjunction with the isosbestic point observed in the ps−ns TA data points to a very high triplet state yield, likely close to being quantitative under the experimental conditions. Furthermore, the combination of the TA data across the entire ps−μs timerange allows us to estimate that the charge carrier regeneration on the ns−μs time scale leads to not more than a quarter of the initial carrier population that was initially present after photoexcitation. In principle, if all processes, that is nongeminate recombination, triplet formation, triplet−triplet annihilation, and carrier regeneration, were quantitative, the delayed carrier population

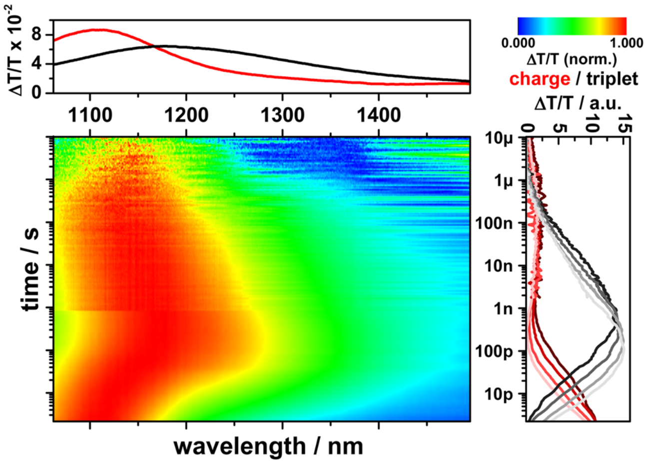

Figure 3. Normalized contour plot of the ps−μs NIR transient absorption data obtained at an excitation density of 11.5 μJ/cm^2. The panel on top shows the component spectra and the panel on the right side the ps−μs component dynamics obtained by MCR analysis of the experimental data. Note the fast and intensity-dependent recombination of charge carriers and concomitant population of the triplet state on the sub-ns time scale. On the ns−μs time scale triplet states undergo annihilation and repopulate the pool of charge carriers.

could reach about half of the initial value as the recreation of one charge carrier requires the annihilation of two triplet states. Taking into account the close to quantitative triplet state formation process on the ns time scale, this observation, precisely that only about a quarter of the initial carrier population is regenerated, points to the presence of additional loss channels, which likely occur during the triplet−triplet annihilation and charge carrier recreation process.

3. CONCLUSIONS

In summary, we have demonstrated by a combination of vis-NIR transient absorption spectroscopy over 9 orders of magnitude in time and multivariate curve resolution analysis of the experimental TA data that after photoexcitation of PBDTTT-C/PC$_{60}$BM blends by pulsed laser excitation a cascade of photophysical processes is initiated starting with ultrafast exciton dissociation, followed by a fast sub-ns decay of the charge carrier population and almost quantitative formation of triplet states. Further analysis of the carrier and triplet state dynamics revealed a pronounced intensity dependence of the dynamics pointing to a nongeminate recombination of charges and origin of triplet state formation. A nongeminate recombination coefficient around 10^{-10} cm^3 s^{-1} was determined for the sub-ns charge recombination pointing to an initial mobility of carriers as high as 1 cm^2 (Vs)$^{-1}$. The triplet state population is followed by triplet−triplet annihilation on the ns−μs time scale, while in parallel a significant charge carrier population is recreated. We believe that the charges are recreated by dissociation of high energy singlet and triplet states created by triplet−triplet annihilation. Despite the close to quantitative triplet formation on the sub-ns time scale following pulsed laser excitation, we still obtained a moderate photovoltaic performance from this blend under solar illumination indicating that the yield of triplets must be significantly reduced at lower photon flux. Overall, our results provide insight into the ongoing debate of the mechanism of triplet state formation in low-bandgap polymer/fullerene blends, the fate of triplet states after their generation and implications for the photovoltaic device performance and future material development.

4. EXPERIMENTAL METHODS

Thin Film Preparation. PBDTTT-C (M_n = 132.000 g/mol, PDI = 2.8), obtained from 1-Material Inc., and PC$_{60}$BM were dissolved separately in chlorobenzene at a concentration of 15 mg mL^{-1} and stirred at 70 °C overnight. The solutions were mixed at a 1:2 ratio 2 h prior to spin coating at a rotation speed of 1000 rpm. For spectroscopic experiments the active layer was spin-coated on quartz substrates which were cleaned by ultrasonication in detergent, acetone and *iso*-propanol and subsequently treated with an argon plasma for 15 min. For photovoltaic devices, a ∼40 nm thick poly(3,4-ehylenedioxythiophene)/poly(styrenesulfonate) (PEDOT/PSS; Clevios P VP Al 4083, H.C. Stark) was spin-coated on ITO-coated glass substrates (Präzisions Glas and Optic GmbH, Germany). After active layer deposition, a bilayer of 5 nm calcium and 100 nm aluminum was evaporated through a shadow mask. Solar cells were characterized with a solar simulator (K.H. Steuernagel Lichttechnik GmbH, Germany) employing a 575 W metal halide lamp combined with a filter system to create a spectrum according to AM1.5G conditions, however, with a lower intensity of 70 mW cm^{-2}. Current−voltage curves were taken with a Keithley 236 Source Measure Unit (SMU) in a glovebox.

Steady-State Spectroscopy. Steady state absorption spectra were measured with a PerkinElmer Lambda 25 spectrometer. The layer thickness was determined with a Tencor P10 surface profilometer.

Transient Absorption Spectroscopy. Transient absorption (TA) measurements were performed with a home-built pump−probe setup.[26,27] To measure in the time range of 1−4 ns with a resolution of ∼100 fs, the output of a commercial titanium/sapphire amplifier (Coherent LIBRA-HE, 3.5 mJ, 1 kHz, 100 fs) was split into two beams that pumped two independent commercial optical parametric amplifiers (Coherent OPerA Solo). One optical parametric amplifier (OPA) was used to generate the tunable excitation pulses in the visible, while the second OPA was used to generate the pump beam for white-light generation. For TA measurements in the NIR spectral range covering 1100−2000 nm a 2100 nm pump was used to generate white-light in an yttrium vanadate window. Furthermore, a dichroic mirror was used to separate the residual seed beam (idler of the OPA at 2100 nm) from the broadband NIR supercontinuum. The variable delay of up to 4 ns between pump and probe was introduced by a broadband retroreflector mounted on a mechanical delay stage. Mostly reflective elements were used to guide the probe beam to the sample to minimize chirp. The excitation pulse was chopped at 500 Hz, while the white-light pulses were dispersed onto a Peltier-cooled 512 pixel long linear extended InGaAs array (Entwicklungsbüro Stresing), which was read out at 1 kHz by home-built electronics. Adjacent diode readings corresponding to the transmission of the sample after an excitation pulse and without an excitation pulse were used to calculate $\Delta T/T$.

For measurements in the time range between 1 ns to 1 ms with a resolution of 600 ps, the excitation pulse was provided by an actively Q-switched Nd:YVO$_4$ laser (AOT Ltd. MOPA) at 532 nm. In this case the delay between pump and probe was controlled by an electronic delay generator (Stanford Research Systems DG535). TA measurements were performed at room temperature under a dynamic vacuum of <10^{-5} mbar.

Multivariate Curve Resolution. MCR analysis is a soft-modeling approach used to factor experimentally measured TA data surfaces into their component spectra and respective concentration profiles applying certain physical constraints such as non-negativity of excited state concentrations or non-positivity of spectra. The MCR analysis and application to TA data has recently been reported and reviewed by us in a separate publication.[19,20]

■ ASSOCIATED CONTENT

Ⓢ Supporting Information

J−*V* curves of photovoltaic devices, additional TA spectra and dynamics of pristine and triplet sensitizer-doped polymer films, and absorption spectra oxidized polymer films. The Supporting Information is available free of charge on the ACS Publications website at DOI: 10.1021/acs.jpcc.5b03467.

■ AUTHOR INFORMATION

Corresponding Author

*E-mail: laquai@mpip-mainz.mpg.de.

Present Address

[†]Physical Sciences and Engineering Division (PSE), Material Science and Engineering (MSE), Solar and Photovoltaics Engineering Research Center (SPERC), King Abdullah University of Science and Technology (KAUST), Thuwal 23955−6900, Kingdom of Saudi Arabia. E-mail: frederic.laquai@kaust.edu.sa.

Notes

The authors declare no competing financial interest.

■ ACKNOWLEDGMENTS

D.W.G. acknowledges a Kekulé scholarship of the Fonds der Chemischen Industrie (FCI). I.A.H. thanks the Alexander von Humboldt Foundation, Carl-Zeiss-Stiftung, and Max Planck Society for postdoctoral fellowships. F.L. acknowledges the Max Planck Society for funding the Max Planck Research Group.

■ REFERENCES

(1) Congreve, D. N.; Lee, J.; Thompson, N. J.; Hontz, E.; Yost, S. R.; Reusswig, P. D.; Bahlke, M. E.; Reineke, S.; Van Voorhis, T.; Baldo, M. A. External Quantum Efficiency Above 100% in a Singlet-Exciton-Fission−Based Organic Photovoltaic Cell. *Science* **2013**, *340*, 334−337.

(2) Chan, W.-L.; Ligges, M.; Jailaubekov, A.; Kaake, L.; Miaja-Avila, L.; Zhu, X.-Y. Observing the Multiexciton State in Singlet Fission and Ensuing Ultrafast Multielectron Transfer. *Science* **2011**, *334*, 1541−1545.

(3) Rao, A.; Chow, P. C. Y.; Gelinas, S.; Schlenker, C. W.; Li, C.-Z.; Yip, H.-L.; Jen, A. K. Y.; Ginger, D. S.; Friend, R. H. The Role of Spin in the Kinetic Control of Recombination in Organic Photovoltaics. *Nature* **2013**, *500*, 435−439.

(4) Dimitrov, S. D.; Wheeler, S.; Niedzialek, D.; Schroeder, B. C.; Utzat, H.; Frost, J. M.; Yao, J.; Gillett, A.; Tuladhar, P. S.; McCulloch, I.; et al. Polaron Pair Mediated Triplet Generation in Polymer/Fullerene Blends. *Nat. Commun.* **2015**, *6*, 6501.

(5) Chow, P. C. Y.; Gélinas, S.; Rao, A.; Friend, R. H. Quantitative Bimolecular Recombination in Organic Photovoltaics through Triplet Exciton Formation. *J. Am. Chem. Soc.* **2014**, *136*, 3424−3429.

(6) Westenhoff, S.; Howard, I. A.; Hodgkiss, J. M.; Kirov, K. R.; Bronstein, H. A.; Williams, C. K.; Greenham, N. C.; Friend, R. H. Charge Recombination in Organic Photovoltaic Devices with High Open-Circuit Voltages. *J. Am. Chem. Soc.* **2008**, *130*, 13653−13658.

(7) Di Nuzzo, D.; Aguirre, A.; Shahid, M.; Gevaerts, V. S.; Meskers, S. C. J.; Janssen, R. A. J. Improved Film Morphology Reduces Charge Carrier Recombination into the Triplet Excited State in a Small Bandgap Polymer-Fullerene Photovoltaic Cell. *Adv. Mater.* **2010**, *22*, 4321−4324.

(8) Basel, T.; Huynh, U.; Zheng, T.; Xu, T.; Yu, L.; Vardeny, Z. V. Optical, Electrical, and Magnetic Studies of Organic Solar Cells Based on Low Bandgap Copolymer with Spin 1/2 Radical Additives. *Adv. Funct. Mater.* **2015**, *25*, 1895−1902.

(9) Etzold, F.; Howard, I. A.; Forler, N.; Melnyk, A.; Andrienko, D.; Hansen, M. R.; Laquai, F. Sub-ns Triplet State Formation by Non-Geminate Recombination in PSBTBT:PC70BM and PCPDTBT:PC60BM Organic Solar Cells. *Energy Environ. Sci.* **2015**, *8*, 1511−1522.

(10) Liang, Y.; Xu, Z.; Xia, J.; Tsai, S.-T.; Wu, Y.; Li, G.; Ray, C.; Yu, L. For the Bright Future—Bulk Heterojunction Polymer Solar Cells with Power Conversion Efficiency of 7.4%. *Adv. Mater.* **2010**, *22*, E135−E138.

(11) Chen, H.-Y.; Hou, J.; Zhang, S.; Liang, Y.; Yang, G.; Yang, Y.; Yu, L.; Wu, Y.; Li, G. Polymer Solar Cells with Enhanced Open-Circuit Voltage and Efficiency. *Nat. Photonics* **2009**, *3*, 649−653.

(12) Liang, Y.; Feng, D.; Wu, Y.; Tsai, S.-T.; Li, G.; Ray, C.; Yu, L. Highly Efficient Solar Cell Polymers Developed via Fine-Tuning of Structural and Electronic Properties. *J. Am. Chem. Soc.* **2009**, *131*, 7792−7799.

(13) Guo, J.; Liang, Y.; Szarko, J.; Lee, B.; Son, H. J.; Rolczynski, B. S.; Yu, L.; Chen, L. X. Structure, Dynamics, and Power Conversion Efficiency Correlations in a New Low Bandgap Polymer: PCBM Solar Cell. *J. Phys. Chem. B* **2010**, *114*, 742−748.

(14) Rolczynski, B. S.; Szarko, J. M.; Son, H. J.; Liang, Y.; Yu, L.; Chen, L. X. Ultrafast Intramolecular Exciton Splitting Dynamics in Isolated Low-Band-Gap Polymers and Their Implications in Photovoltaic Materials Design. *J. Am. Chem. Soc.* **2012**, *134*, 4142−4152.

(15) Rolczynski, B. S.; Szarko, J. M.; Son, H. J.; Yu, L.; Chen, L. X. Effects of Exciton Polarity in Charge-Transfer Polymer/PCBM Bulk Heterojunction Films. *J. Phys. Chem. Lett.* **2014**, *5*, 1856−1863.

(16) Carsten, B.; Szarko, J. M.; Son, H. J.; Wang, W.; Lu, L.; He, F.; Rolczynski, B. S.; Lou, S. J.; Chen, L. X.; Yu, L. Examining the Effect of the Dipole Moment on Charge Separation in Donor−Acceptor Polymers for Organic Photovoltaic Applications. *J. Am. Chem. Soc.* **2011**, *133*, 20468−20475.

(17) Szarko, J. M.; Guo, J.; Rolczynski, B. S.; Chen, L. X. Current Trends in the Optimization of Low Band Gap Polymers in Bulk Heterojunction Photovoltaic Devices. *J. Mater. Chem.* **2011**, *21*, 7849−7857.

(18) Szarko, J. M.; Rolczynski, B. S.; Lou, S. J.; Xu, T.; Strzalka, J.; Marks, T. J.; Yu, L.; Chen, L. X. Photovoltaic Function and Exciton/Charge Transfer Dynamics in a Highly Efficient Semiconducting Copolymer. *Adv. Funct. Mater.* **2014**, *24*, 10−26.

(19) Jaumot, J.; Gargallo, R.; de Juan, A. A Graphical User-Friendly Interface for MCR-ALS: a New Tool for Multivariate Curve Resolution in MATLAB. *Chemom. Intell. Lab. Syst.* **2005**, *76*, 101−110.

(20) Howard, I. A.; Mangold, H.; Etzold, F.; Gehrig, D.; Laquai, F. Ultrafast Dynamics. *Molecules, Nanostructures and Interfaces*; World Scientific: Singapore, 2014; Vol. *8*.

(21) Gehrig, D. W.; Roland, S.; Howard, I. A.; Kamm, V.; Mangold, H.; Neher, D.; Laquai, F. Efficiency-Limiting Processes in Low-Bandgap Polymer:Perylene Diimide Photovoltaic Blends. *J. Phys. Chem. C* **2014**, *118*, 20077−20085.

(22) Sharenko, A.; Gehrig, D.; Laquai, F.; Nguyen, T.-Q. The Effect of Solvent Additive on the Charge Generation and Photovoltaic Performance of a Solution-Processed Small Molecule:Perylene Diimide Bulk Heterojunction Solar Cell. *Chem. Mater.* **2014**, *26*, 4109−4118.

(23) Koster, L. J. A.; Mihailetchi, V. D.; Blom, P. W. M. Bimolecular Recombination in Polymer/Fullerene Bulk Heterojunction Solar Cells. *Appl. Phys. Lett.* **2006**, *88*, 052104.

(24) Burke, T. M.; McGehee, M. D. How High Local Charge Carrier Mobility and an Energy Cascade in a Three-Phase Bulk Heterojunction Enable >90% Quantum Efficiency. *Adv. Mater.* **2014**, *26*, 1923−1928.

(25) Vukmirović, N.; Ponseca, C. S.; Němec, H.; Yartsev, A.; Sundström, V. Insights into the Charge Carrier Terahertz Mobility in Polyfluorenes from Large-Scale Atomistic Simulations and Time-Resolved Terahertz Spectroscopy. *J. Phys. Chem. C* **2012**, *116*, 19665−19672.

(26) Etzold, F.; Howard, I. A.; Mauer, R.; Meister, M.; Kim, T.-D.; Lee, K.-S.; Baek, N. S.; Laquai, F. Ultrafast Exciton Dissociation Followed by Nongeminate Charge Recombination in PCDTBT:PCBM Photovoltaic Blends. *J. Am. Chem. Soc.* **2011**, *133*, 9469−9479.

(27) Gehrig, D.; Howard, I. A.; Kamm, V.; Dyer-Smith, C.; Etzold, F.; Laquai, F. Charge Generation in Polymer:Perylene Diimide Blends Probed by Vis-NIR Broadband Transient Absorption Pump-Probe Spectroscopy. *Proc. SPIE* **2013**, *8811*, 88111F−88111F-10.

Supporting Information

Charge Carrier Generation Followed by Triplet State Formation, Annihilation, and Carrier Recreation in PBDTTT-C:PC$_{60}$BM Photovoltaic Blends

Dominik. W. Gehrig, Ian A. Howard, Frédéric Laquai†*

Supporting Information. J-V curves of photovoltaic devices, additional TA spectra and dynamics etc. can be found in the supporting information. This material is available free of charge via the Internet at http://pubs.acs.org.

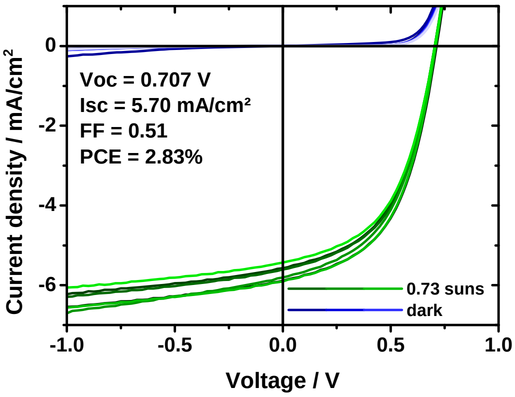

Figure S1. J-V curves of PBDTTT-C:PCBM (1:2) photovoltaic devices obtained under AM1.5G-like conditions at 0.73 suns. Each curve represents one pixel of the device.

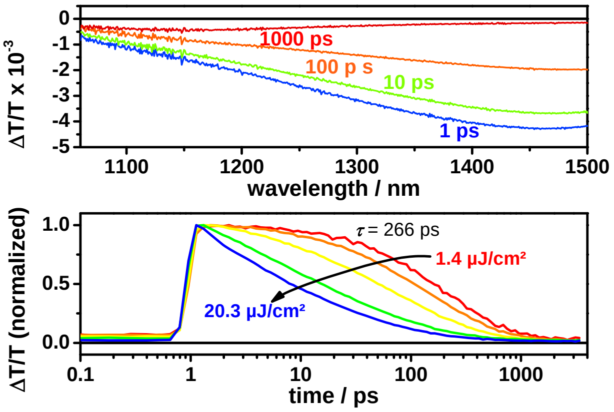

Figure S2. a) ps-ns transient absorption spectra of a pristine PBDTTT-C film excited at 650 nm with 5.3 µJ/cm^2 showing the singlet exciton-induced absorption. Note that at long delay time around 1 ns the spectrum peaks at 1150 nm corresponding to the triplet-induced absorption. b) Intensity dependence of the kinetics monitored at 1450-1500 nm. At the lowest fluence used in the TA experiments the dynamics fit to a single exponential with a lifetime of 266 ps indicating the absence of exciton-exciton annihilation processes.

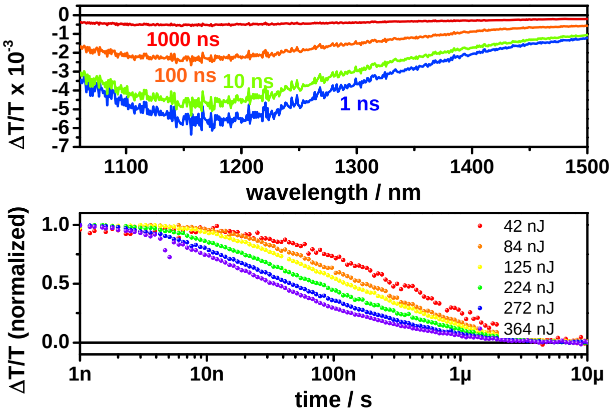

Figure S3. a) ns-µs NIR TA spectra of a platinum porphyrin-sensitized PBDTTT-C polymer film and b) intensity dependence of the dynamics monitored at 1140-1190 nm.

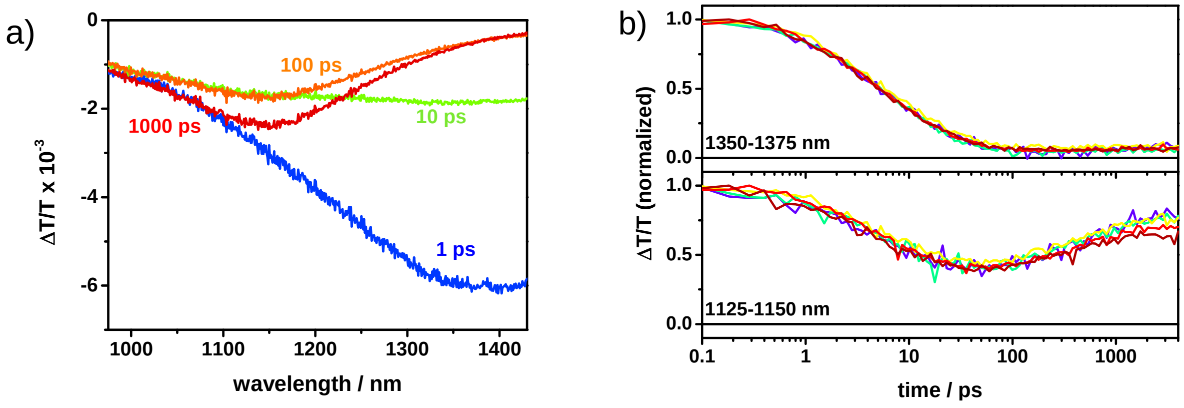

Figure S4. a) ps-ns NIR TA spectra of a 5 wt.% palladium anthraporphyrin-doped PBDTTT-C polymer film. Initially the TA spectrum peaked at 1400 nm corresponding to the singlet exciton-induced absorption. At later delay times the triplet-induced absorption peaking at 1160 nm was observed. b) Signal dynamics tracked at different wavelength regions corresponding to the singlet exciton-induced absorption (1350-1375 nm) and the region of triplet-induced absorption (1125-1150 nm).

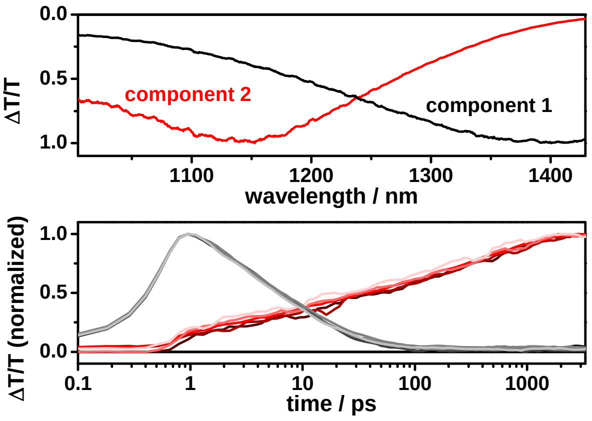

Figure S5. MCR-ALS analysis of the TA data presented in figure S4. a) Component spectra: component 1 corresponds to the singlet exciton-induced absorption and component 2 to the triplet exciton-induced absorption. b) Dynamics of the two components at different excitation intensities. Note that the triplet-induced absorption rises even after all polymer singlet excitons have been quenched by the sensitizer indicating that intersystem crossing on the sensitizer requires several nanoseconds.

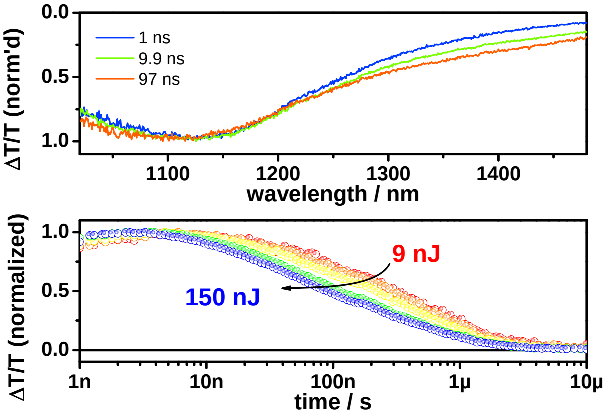

Figure S6. a) ns-µs NIR TA spectra of a 5 wt.% palladium anthraporphyrin-doped PBDTTT-C polymer film. b) Intensity dependence of the decay dynamics.

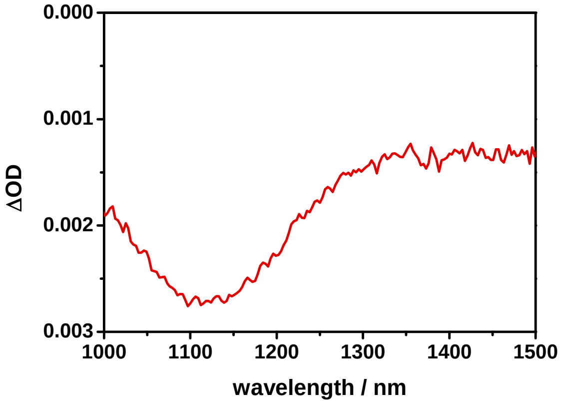

Figure S7. Absorption spectrum of a PBDTTT-C polymer film after oxidation with iodine. Note that the peak position at 1120 nm corresponds to the peak position of component 1 obtained by MCR-ALS analysis of the TA data of a PBDTTT-C:PCBM blend supporting the assignment of component 1 to charges.

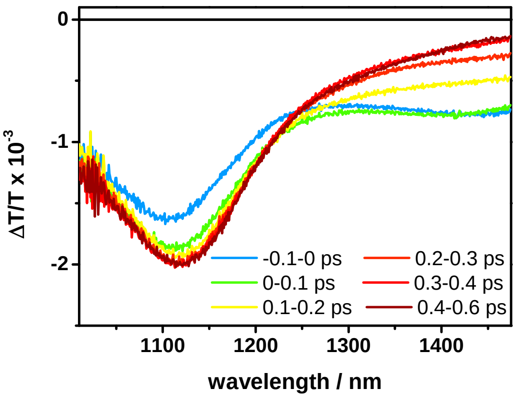

Figure S8. Sub-ps transient absorption spectra of a PBDTTT-C:PCBM film excited at 650 nm with 6.7 µJ/cm².

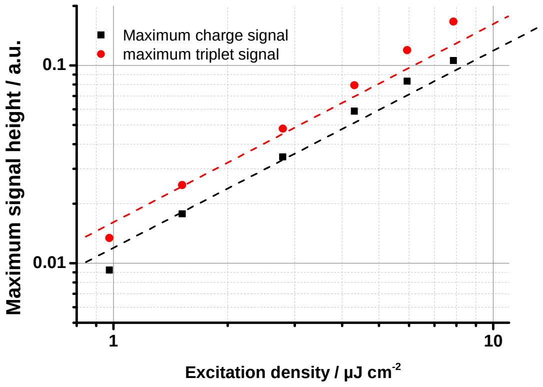

Figure S9. Maximum charge-induced (black symbol) and triplet-induced (red symbol) absorption signal height of a PBDTTT-C:PCBM film after excitation at 650 nm extracted from the MCR analysis. Dashed lines are guides to the eye with a slope of 1 indicating a linear increase of the charge and triplet concentration with excitation density.

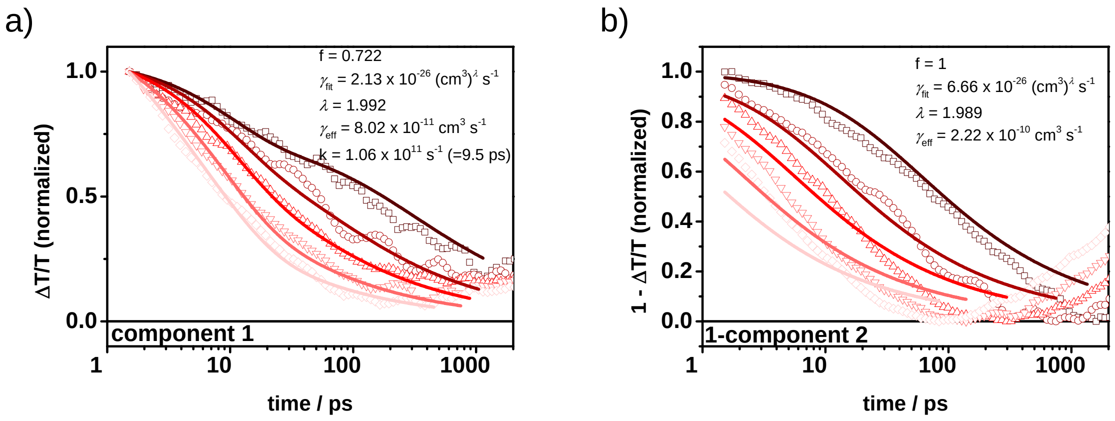

Figure S10. Decay dynamics of a) component 1 and b) ‘1-component 2’ at various excitation densities (dark to light color corresponds to low to high excitation intensities). Open symbols represent experimental data and solid lines fits taking into account geminate (that is monomolecular) and non-geminate (that is bimolecular) recombination. The fitting parameter *f* corresponds to the fraction of non-geminate recombination.

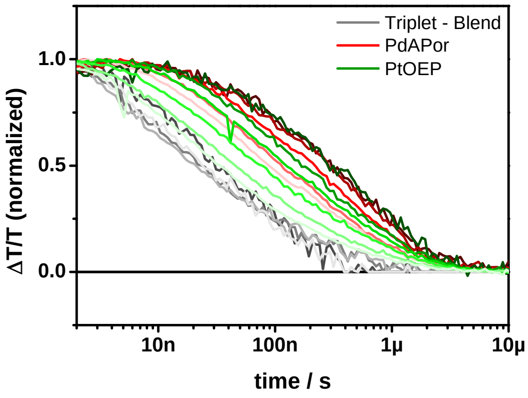

Figure S11. Decay dynamics on the ns-µs timescale of the triplet-induced absorption signal observed in blends of PBDTTT-C with i.) PCBM (grey), ii.) Palladium-Anthraporphyrin (PdAPor , red), and iii.) Platinum-Octaethylporphyrin (PtOEP, green) at different excitation intensities (color shade).

Multi-variate curve resolution. The result of a transient absorption experiment is a two-dimensional data matrix containing the transient absorption spectra of each time point of the experiment. Assuming that the spectra of the individual excited states do not evolve or shift with time, the data matrix D can be written as a bilinear decomposition, in such a way that

$$D = CS + E.$$

C contains the concentration profiles of the excited states, the rows of S represent the transient absorption spectra of the states, and E ideally only contains experimental noise. In order to factorize the experimentally obtained data matrix and to determine the concentration profiles and cross-sections of the individual excited states, we employed multivariate curve resolution. Multivariate curve resolution is a soft-modeling approach used to analyze transient absorption data, independent of any a priori knowledge of the excited states that constitute the data matrix. Our analysis is based on the MCR-ALS algorithm developed by Tauler et al.,[1-3] and a detailed discussion of the application of this technique to TA data has recently been presented by us.[4] The inherent advantage of a soft-modeling method is its intrinsic independence from any photophysical model typically required for the data analysis. Compared to hard-modeling, in which a kinetic model of coupled rate equations is used on the basis of an a priori known number of excited and ground states and interconversion channels between them, neither any assumption of the number of excited states nor their decay processes is required to perform an MCR-ALS analysis. Instead, the number of excited states and the initial concentration profiles describing the transient data surface are determined in an evolving factor analysis (EFA).

In order to determine the number of excited states contributing to the TA data matrix, we performed an evolving factor analysis (EFA), starting right after the polymer singlet exciton quenching was completed. EFA is based on singular value decompositions (SVDs) performed on a sequence of sub-matrices, which are generated by successively increasing the number of columns contained in the sub-matrix considered for each decomposition. This procedure is repeatedly performed starting from the right side and from the left side of the data matrix. EFA yields information about the rank of the data matrix at each time point and thus it determines the number of relevant states that comprise the TA data matrix. EFA was performed on the PBDTTT-C:PC$_{60}$BM blend's sub-ns TA NIR data for five different excitation densities after excitation of the polymer at 650 nm. At approximately 2 ps, that is, the time required to ensure complete exciton quenching, all measurements are dominated by one excited state, namely component 1. However, a second component (2) is observed at later times whose onset shifts to earlier times with increasing pump fluence, indicating a fluence-dependent generation process. Subsequent matrix division yields the corresponding spectra, while constraints such as non-negativity of concentrations and non-positivity / non-negativity of the spectra can be applied. From the obtained spectra, a new set of concentration profiles is calculated and the procedure is repeated until a given tolerance criterion is met.

(1) Jaumot, J.; Gargallo, R.; de Juan, A., A Graphical User-Friendly Interface for MCR-ALS: a New Tool for Multivariate Curve Resolution in MATLAB. *Chemom. Intell. Lab. Syst.* **2005**, *76*, 101-110.

(2) de Juan, A.; Tauler, R., Multivariate curve resolution (MCR) from 2000: progress in concepts and applications. *Crit. Rev. Anal. Chem.* **2006**, *36*, 163-176.

(3) De Juan, A.; Tauler, R., Chemometrics applied to unravel multicomponent processes and mixtures: Revisiting latest trends in multivariate resolution. *Anal. Chim. Acta* **2003**, *500*, 195-210.

(4) Howard, I. A.; Mangold, H.; Etzold, F.; Gehrig, D.; Laquai, F., *Ultrafast Dynamics in Molecules, Nanostructures and Interfaces* **2014**, *Volume 8, World Scientific*.

4.3 p-DTS(FBTTh$_2$)$_2$:Perylene Diimide Solar Cells

The article "The Effect of Solvent Additive on the Charge Generation and Photovoltaic Performance of a Solution-Processed Small Molecule:Perylene Diimide Bulk Heterojunction Solar Cell" was published in Chemistry of Materials and is available online since July 1st, 2014. The article is reprinted with permission from reference [115]. Copyright (2014) American Chemical Society.

CHEMISTRY OF MATERIALS

The Effect of Solvent Additive on the Charge Generation and Photovoltaic Performance of a Solution-Processed Small Molecule:Perylene Diimide Bulk Heterojunction Solar Cell

Alexander Sharenko,[†,‡,#] Dominik Gehrig,[§,#] Frédéric Laquai,[*,§] and Thuc-Quyen Nguyen[*,‡,∥,⊥]

[†]Materials Department, University of California, Santa Barbara, California 93106, United States
[‡]Center for Polymers and Organic Solids, University of California, Santa Barbara, California 93106, United States
[§]Max Planck Research Group for Organic Optoelectronics, Max Planck Institute for Polymer Research, Mainz, Germany
[∥]Department of Chemistry, Faculty of Science, King Abdulaziz University, Jeddah, Saudi Arabia
[⊥]Department of Chemistry and Biochemistry, University of California, Santa Barbara, California 93106, United States

Ⓢ *Supporting Information*

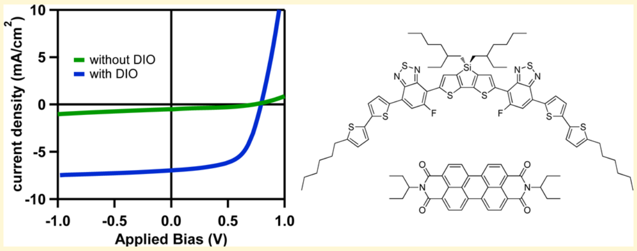

ABSTRACT: The photovoltaic performance and charge generation dynamics in thin film bulk heterojunction organic photovoltaic (BHJ OPV) devices comprising the small molecule donor 7,7′-(4,4-bis(2-ethylhexyl)-4H-silolo[3,2-b:4,5-b′]dithiophene-2,6-diyl)bis(6-fluoro-4-(5′-hexyl-[2,2′-bithiophen]-5-yl)benzo[c][1,2,5]thiadiazole) (p-DTS(FBTTh$_2$)$_2$) and a perylene diimide (PDI) electron acceptor are investigated with and without the processing additive 1,8-diiodooctane (DIO). UV−vis absorption spectroscopy indicates that the use of DIO during processing increases the structural order of both p-DTS(FBTTh$_2$)$_2$ and PDI compared to films cast from chlorobenzene alone. Excitation intensity dependent broadband vis−NIR transient absorption pump−probe experiments over a dynamic range from 100 fs to 100 μs reveal that, in blends processed without DIO, essentially none of the interfacial charge transfer states generated after exciton dissociation at the donor−acceptor interface split into spatially separated charge carriers. In contrast, in blends processed with 0.4 vol% DIO, geminate recombination is significantly reduced, and spatially separated charge carriers are generated. It appears that the drastic increase in the power conversion efficiency in p-DTS(FBTTh$_2$)$_2$:PDI BHJ OPV devices upon the use of DIO, from 0.13% to 3.1%, is a consequence of the increased solid state order of both p-DTS(FBTTh$_2$)$_2$ and PDI, which leads to a significant improvement of the exciton dissociation efficiency and makes this system among the most efficient non-fullerene BHJ organic solar cells to date.

1. INTRODUCTION

Organic photovoltaics (OPVs) have been fabricated with power conversion efficiencies (PCEs) exceeding 10% and are additionally capable of being solution-processed at low temperatures on mechanically flexible substrates using high volume manufacturing techniques such as roll-to-roll coating.[1−3] Efforts to commercialize this technology, however, may be hindered by the difficulties and expense associated with the production of the functionalized fullerenes utilized in the vast majority of OPV devices.[4,5] Functionalized fullerenes also exhibit relatively low absorption coefficients within the terrestrial solar spectrum. Therefore, it would be advantageous to replace fullerenes in OPVs with materials that likewise exhibit high electron mobility and efficient charge separation but are additionally inexpensive and absorb more solar photons.

While balanced, sufficiently high hole and electron mobilities and relatively thin photoactive layers are generally considered necessary for the efficient sweep out of free charge carriers and thus the suppression of nongeminate recombination in bulk heterojunction (BHJ) OPVs, much less is known about the processes that lead to efficient charge separation in these devices.[6−9] In contrast to inorganic materials, organic semiconductors do not directly generate free charge carriers upon photoexcitation due to their low permittivity. Photoexcitation instead leads to the formation of a Coulombically bound electron−hole pair referred to as an exciton that must then be split in order to produce spatially separated charges, i.e. a free electron and hole.[9,10] It has been suggested that this Coulombic attraction is overcome during charge separation via the occupation of higher energy, delocalized charge transfer (CT) states.[11−13] Recent work, however, has shown the internal quantum efficiency (IQE) of multiple BHJ OPV systems to be relatively independent of photon energy, suggesting exciton splitting does not require excess electronic or vibrational energy.[14] A correlation between the size of the donor−acceptor frontier energy level offsets and the efficiency of charge

Received: March 24, 2014
Revised: June 20, 2014
Published: July 1, 2014

generation has also been observed.[15,16] Others have suggested that high charge carrier mobility is responsible for the suppression of geminate recombination.[17,18] Morphology has additionally been shown to strongly influence the charge generation process in BHJ OPVs. Donor−acceptor interfacial geometry has been demonstrated to influence the energy of the donor−acceptor electronic coupling and CT state and therefore the probability of charge separation.[19−21] An increase in polymer donor solid state order has been correlated with an increase in the efficiency of charge generation.[22,23] Likewise, fullerene aggregation has been suggested to aid in the charge separation process.[8,24−28] Needless to say, charge generation in BHJ OPVs is a complex process that is still subject to much debate within the field.

The lack of a complete theoretical understanding of charge generation in BHJ OPVs, however, has not prevented the fabrication of BHJ OPV devices exhibiting extremely efficient conversion of absorbed photons into free charge carriers. Several BHJ OPV systems utilizing fullerene acceptors have been reported to exhibit IQEs approaching unity, indicating nearly all photons are converted into free charge carriers that are then collected at the device electrodes and converted into electrical current.[8,14,29] In contrast, whereas relatively efficient BHJ OPV devices utilizing non-fullerene acceptors are capable of overcoming nongeminate recombination, existing data suggest they are plagued by significant geminate recombination and consequently low short-circuit current densities (J_{sc}) and PCEs compared to high performance fullerene-based devices.[30,31] Whereas significant trial and error experimentation has led to extremely efficient OPVs utilizing fullerene acceptors, this approach to date has not led to the same success with devices utilizing non-fullerene acceptors. Therefore, a better understanding of the charge generation process in BHJ OPVs utilizing non-fullerene acceptors is required to reduce the amount of geminate recombination in these systems. The suppression of geminate recombination in non-fullerene systems is thus crucial to the fabrication of efficient non-fullerene BHJ OPVs that overcome many of the shortcomings associated with fullerenes.

Perylene diimides (PDIs) are a class of organic dye molecules with high electron affinity similar to fullerenes, large extinction coefficients within the terrestrial solar spectrum, and relatively high electron mobilities, thus making them attractive for use as electron acceptors in organic solar cells.[32,33] In the work presented herein, we investigate the photovoltaic performance, morphology, and charge generation in the 7,7′-(4,4-bis(2-ethylhexyl)-4H-silolo[3,2-b:4,5-b′]dithiophene-2,6-diyl)bis(6-fluoro-4-(5′-hexyl-[2,2′-bithiophen]-5-yl)benzo[c][1,2,5]-thiadiazole):PDI (p-DTS(FBTTh$_2$)$_2$:PDI) BHJ OPV system without and with the use of the solvent additive 1,8-diiodooctane (DIO; Figure 1a). Whereas PDI has demonstrated the ability to function as an electron acceptor in OPVs,[34] PDI OPVs have largely underperformed OPVs utilizing fullerene acceptors for reasons that are still largely not understood. The p-DTS(FBTTh$_2$)$_2$:PDI system has recently exhibited a PCE of 3.0% when fabricated with DIO, making it among the highest performing non-fullerene BHJ OPVs but still significantly less efficient than optimized p-DTS(FBTTh$_2$)$_2$:fullerene BHJ OPV devices.[29,30] As we demonstrate here, the p-DTS(FBTTh$_2$)$_2$:PDI system exhibits drastically different photovoltaic performance when processed without and with DIO, allowing the correlation of differences in blend morphology induced by DIO with OPV photophysical processes to produce a processing-property-performance relationship for a non-fullerene BHJ OPV device. Film morphology is inferred from UV−vis spectroscopy while charge generation is probed using broadband vis−NIR transient absorption (TA) pump−probe spectroscopy. It is found that an increase in donor and acceptor crystallinity upon the use of DIO correlates with a significant increase in the charge generation efficiency, consistent with the drastic increase in device PCE when using the solvent additive.

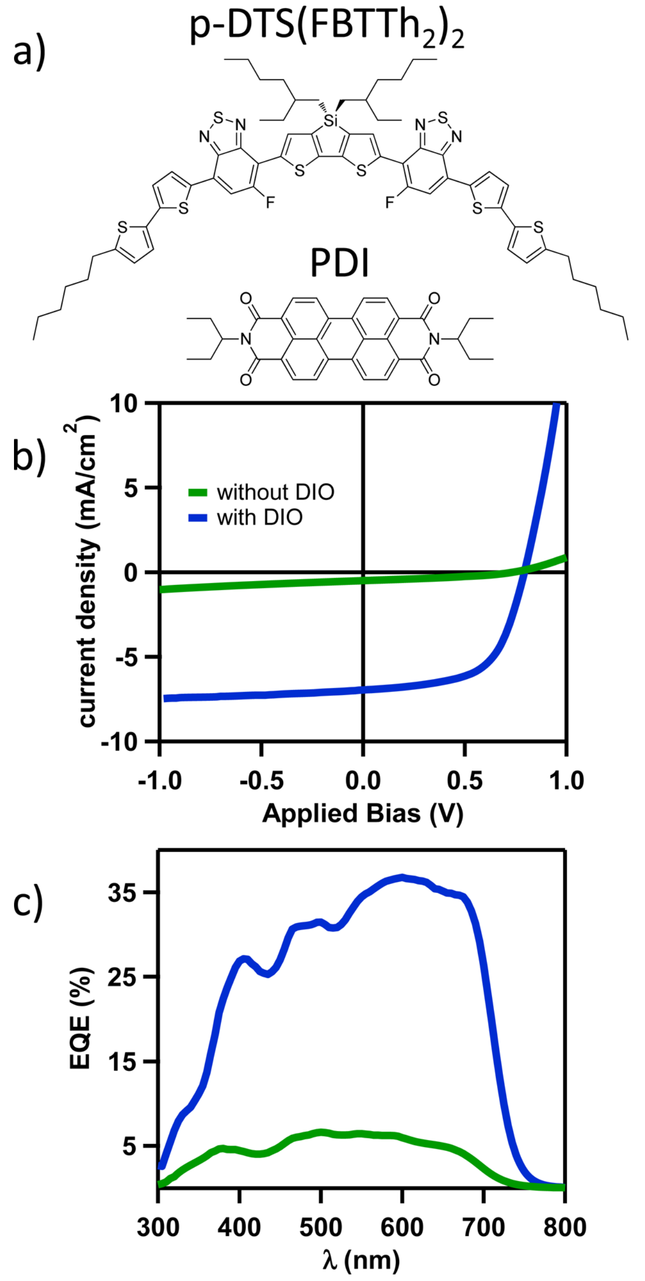

Figure 1. (a) Chemical structures of the donor, p-DTS(FBTTh$_2$)$_2$, and acceptor, PDI, used in this study. (b) $J-V$ curves and (c) EQE spectra of BHJ OPV devices processed without (green) and with (blue) DIO.

2. RESULTS AND DISCUSSION

2.1. Photovoltaic Performance. Figure 1b displays the current density−voltage ($J-V$) curves of p-DTS-(FBTTh$_2$)$_2$:PDI BHJ OPV devices processed from pure chlorobenzene (without DIO) and chlorobenzene with 0.4 vol% DIO (with DIO) under simulated AM 1.5 sun illumination. The device processed with DIO exhibits an open-circuit voltage (V_{oc}) of 0.78 V, a J_{sc} of 7.0 mA/cm^2, a fill factor (FF) of 0.57, and a PCE of 3.1%. The device processed without DIO, however, displays very low photovoltaic performance with a V_{oc} of 0.74 V, a J_{sc} of 0.50 mA/cm^2, a FF of 0.35, and a PCE of 0.13%. The external quantum efficiency (EQE) spectra of the blends processed without and with DIO are displayed in Figure 1c. The relative magnitudes of the EQE spectra correlate well to the J_{sc} values determined from the $J-V$ curves with the EQE of the device processed with DIO exhibiting a maximum value of approximately 37% while the EQE of the device processed without DIO never exceeds 7%. The use of the solvent additive DIO thus results in a drastic increase in photovoltaic performance due to simultaneous increases in all figures of merit (V_{oc}, J_{sc}, and FF). Furthermore, it has previously been shown that the device processed with DIO exhibits a relatively wavelength-independent IQE of approximately 50% across a broad wavelength range.[30]

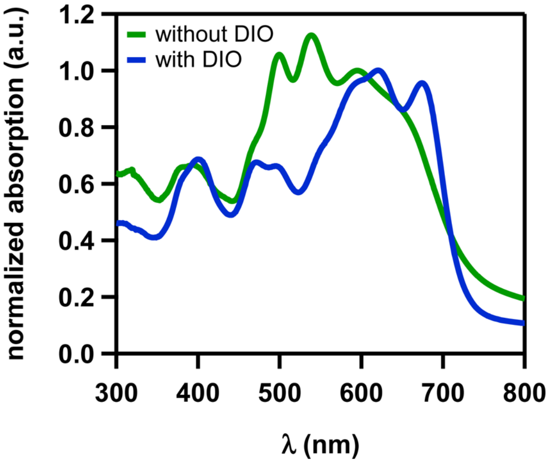

Figure 2. UV−vis absorption spectra of p-DTS(FBTTh$_2$)$_2$:PDI BHJ films processed without (green) and with (blue) DIO.

2.2. UV−Vis and Photoluminescence Spectroscopy.

The normalized UV−vis absorption spectra of the blends spin-cast without and with DIO are displayed in Figure 2. These spectra exhibit significant differences. Both spectra display approximately the same number and position of peaks with the major exception being the additional peak at 675 nm observed in the blend processed with DIO compared to the blend processed without DIO. The relative magnitude of the peaks in the two spectra, however, is significantly different. The most intense peaks in the blend processed without DIO are those at 500 and 539 nm, whereas the most intense peaks in the blend processed with DIO are those at 620 and 675 nm. Information on the structural order of organic semiconductors can be obtained by careful analysis of the position and relative intensities of their optical transitions.[35,36] The peak at 675 nm in the blend processed with DIO can be assigned to p-DTS(FBTTh$_2$)$_2$ and is present in the pristine molecule's thin film absorption spectra but absent in its solution spectra (Figure S1). Additionally, the relative intensity of this transition has previously been observed to increase with increasing p-DTS(FBTTh$_2$)$_2$ crystallinity.[29] The presence of the p-DTS-(FBTTh$_2$)$_2$ transition at approximately 675 nm is therefore indicative of p-DTS(FBTTh$_2$)$_2$ solid state order, whereas its absence in the blend cast without DIO indicates a relative lack of p-DTS(FBTTh$_2$)$_2$ structural order. DIO has previously been shown to have a similar effect on p-DTS(FBTTh$_2$)$_2$:phenyl-C$_{71}$-butyric acid methyl ester (PC$_{71}$BM) BHJ blends in that its use was shown to increase the solid state ordering of p-DTS(FBTTh$_2$)$_2$ during spin-casting.[37] The peaks at 500 and 539 nm orrespond to PDI's 0−1 and 0−0 transition, respectively. It has been shown that PDI crystallization results in a reduction of the intensity of the 0−0 and 0−1 peaks as these transitions are associated with absorption from individual chromophores rather than PDI crystallites.[38,39] We therefore interpret the relative decrease in intensity of these peaks upon the addition of DIO to the casting solution as indicating that in the blend spin-cast without DIO PDI is predominantly structurally disordered but that DIO directly or indirectly induces the nucleation of PDI crystallites in the blend spin-cast with DIO. By analyzing the blend UV−vis spectra cast without and with DIO, it can therefore be deduced that the blend film cast without DIO predominantly consists of structurally disordered p-DTS(FBTTh$_2$)$_2$ and PDI molecules, while the addition of DIO results in an increase in the crystallinity of both p-DTS(FBTTh$_2$)$_2$ and PDI. Notably, the increase in both donor and acceptor structural order correlates to a drastic improvement in device photovoltaic performance. We emphasize that our characterization of the solid state order of the p-DTS(FBTTh$_2$)$_2$:PDI BHJ without and with DIO should be considered on a relative scale as quantifying the absolute order of organic semiconductors is notoriously difficult.[40]

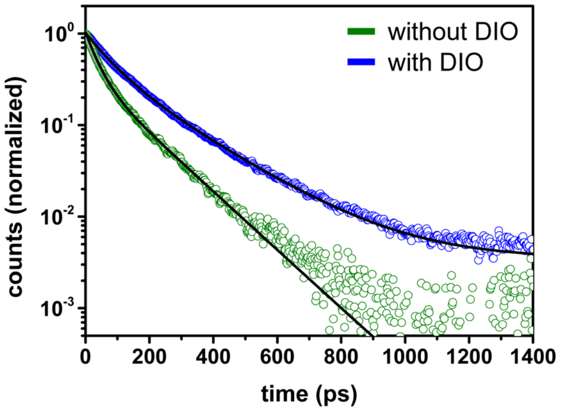

Figure 3. p-DTS(FBTTh$_2$)$_2$ PL emission lifetimes in p-DTS-(FBTTh$_2$)$_2$:PDI BHJ films processed without (green) and with (blue) DIO integrated between 730 and 750 nm and fit (black lines) with biexponential functions. Films were excited at 400 nm.

In order to better understand the photophysical processes in p-DTS(FBTTh$_2$)$_2$:PDI BHJ OPV devices, these blends were first investigated with photoluminescence (PL) spectroscopy. Figure 3 displays the p-DTS(FBTTh$_2$)$_2$ PL emission lifetime in p-DTS(FBTTh$_2$)$_2$:PDI BHJ blend films processed without and with DIO. In the blend processed without DIO the fluorescence of p-DTS(FBTTh$_2$)$_2$ shows a biexponential decay with lifetimes of τ_1 = 34.7 ps (65.5%) and τ_2 = 135.9 ps (34.5%), whereas its lifetimes increase to τ_1 = 71.6 ps (55.1%) and τ_2 = 200.4 ps (44.9%) in the blend processed with DIO. Likewise, integration of the p-DTS(FBTTh$_2$)$_2$ PL emission intensities reveals that the PL amplitude of p-DTS(FBTTh$_2$)$_2$ in the blend processed with DIO is approximately 4 times larger than in the blend processed without DIO. The quenching of the p-DTS(FBTTh$_2$)$_2$

emission is a consequence of electron transfer from p-DTS(FBTTh$_2$)$_2$ to PDI. The PDI emission in p-DTS-(FBTTh$_2$)$_2$:PDI BHJ films is very weak in contrast to the strong emission observed from pristine PDI films (data not shown). Quenching of the PDI fluorescence can be due to hole and/or energy transfer from PDI to p-DTS(FBTTh$_2$)$_2$. The latter mechanism is feasible as the PDI's emission spectrum significantly overlaps with the p-DTS(FBTTh$_2$)$_2$ absorption spectrum, allowing Förster resonance energy transfer (Figure S2). The longer lifetime and more intense emission from the blend spin-cast with DIO compared to the blend spin-cast without DIO suggests that some amount of phase separation occurs concomitantly with the increase in p-DTS(FBTTh$_2$)$_2$ and PDI crystallinity as inferred from the UV−vis spectra.[24,41] Crystallization-induced phase separation has previously been observed in BHJ OPVs consisting of a small molecule donor and a fullerene acceptor.[42] A similar process is likely occurring in the p-DTS(FBTTh$_2$)$_2$:PDI system, albeit further complicated by the crystallization of both donor and acceptor molecules in the present case. PL spectroscopy then indicates that the p-DTS(FBTTh$_2$)$_2$:PDI BHJ blend is relatively more phase separated when processed with DIO than without.

2.3. Transient Absorption Spectroscopy. TA spectroscopy was used to study the charge generation and recombination dynamics of p-DTS(FBTTh$_2$)$_2$:PDI blends spin-cast without and with DIO. TA pump−probe spectroscopy involves the excitation of a sample with an ultrashort pump laser pulse followed by exposing the sample to an optical supercontinuum probe pulse. Excited states generated by the pump pulse induce a differential absorption that is measured by the probe pulse. The difference in sample transmission between the excited and nonexcited state ($\Delta T/T$) can then be used to infer the population dynamics of the excited states as a function of pump−probe time delay.

2.3.1. Selective Excitation of PDI and p-DTS(FBTTh$_2$)$_2$ in BHJ Films. Figure 4A displays the TA spectra of p-DTS(FBTTh$_2$)$_2$:PDI blends cast without and with DIO after excitation at 485 nm. This excitation wavelength is at the absorption minimum of p-DTS(FBTTh$_2$)$_2$ and near the absorption maximum of PDI, thus predominantly creating excitations on the PDI molecules within the blend (Figure S1). At both 1 ps and 1 ns after excitation, the blend processed without DIO exhibits a broad and featureless ground state bleach (GSB, positive $\Delta T/T$ signal) while the blend processed with DIO shows a more structured GSB with peaks at approximately 615 and 675 nm. This is consistent with the UV−vis absorption spectroscopy measurements of both blends as described above. Additionally, the spectra at 1 ps after excitation show significant differences in the wavelength range associated with photoinduced absorption (PIA, negative $\Delta T/T$ signal) when comparing the blend processed without and with DIO. The PIA signal of the 1 ps spectrum of the blend processed without DIO exhibits two distinct peaks at approximately 730 and 825 nm that are not present in the 1 ps spectrum of the blend processed with DIO. These peaks correspond to the absorption of a chemically reduced PDI film (Figure S3). We therefore assign these peaks to PDI anion-induced absorption. The appearance of PIA peaks associated with PDI anions in the blend spin-cast without DIO directly after excitation but not in the blend processed with DIO implies charge transfer from PDI to p-DTS(FBTTh$_2$)$_2$ is very fast in the blend processed without DIO compared to the blend processed with DIO. This implies that the blend processed without DIO consists of an intimate mixture of p-DTS-(FBTTh$_2$)$_2$ and PDI molecules as already suggested by the much less intense PL emission, i.e. stronger PL quenching, of this blend.[43,44] This charge transfer can occur via direct hole transfer from PDI to p-DTS(FBTTh$_2$)$_2$ or energy transfer from PDI to p-DTS(FBTTh$_2$)$_2$ and subsequent electron transfer from p-DTS(FBTTh$_2$)$_2$ to PDI. Recent investigations of efficient polymer:PDI BHJ blends identified electron and hole transfer processes on a similar picosecond time scale.[44] As both charge and energy transfer occur on the same time scale, it is not possible to distinguish between these two pathways with our measurements. Furthermore, the observation of PDI anion-induced absorption does not imply the formation of unbound (spatially separated) charges, it could also be the result of the formation of a bound p-DTS(FBTTh$_2$)$_2$:PDI interfacial CT state, as in many cases both species have similar photoinduced absorption spectra and cross sections.

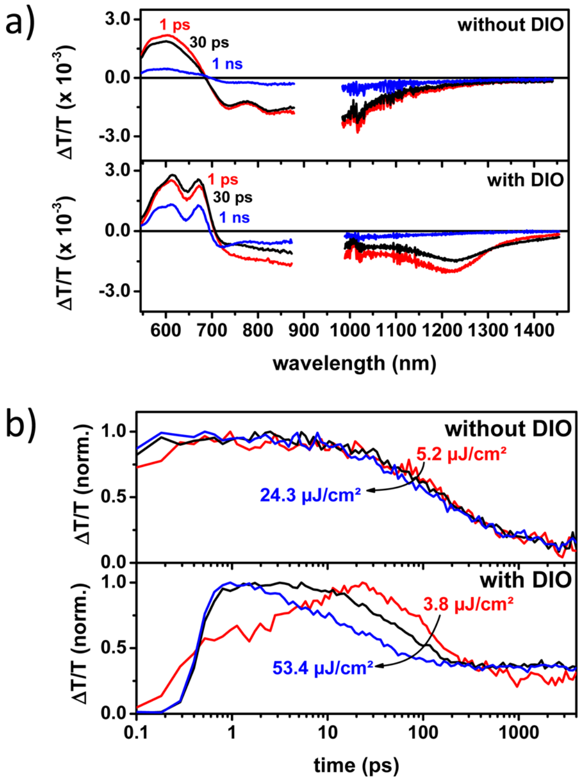

Figure 4. (a) TA spectra and (b) GSB kinetics of p-DTS-(FBTTh$_2$)$_2$:PDI films processed without (600−625 nm) and with DIO (670−695 nm) excited at 485 nm.

Distinct differences can also be observed in the near-infrared region (1000−1450 nm) of the spectra. The sample processed without DIO shows a charge-induced absorption signal from p-DTS(FBTTh$_2$)$_2$ directly after excitation, which is indicative of ultrafast charge transfer due to an intimate intermixing of donor and acceptor and thus is in good agreement with the findings obtained from time-resolved PL measurements as well as TA spectroscopy measurements in the visible part of the spectrum. Conversely, samples processed with the solvent additive exhibit a pronounced p-DTS(FBTTh$_2$)$_2$ exciton-induced absorption. Thus, either ultrafast energy-transfer from PDI to p-DTS-(FBTTh$_2$)$_2$ occurs or a fraction of the donor is also excited at 485 nm.

Figure 4b displays the excitation intensity dependent TA kinetics associated with the GSB of blends processed without and with DIO. The dynamics are virtually intensity independent in blends processed without DIO, while a pronounced intensity dependence is observed in blends processed with DIO. This suggests that monomolecular processes dominate in blends processed without DIO whereas bimolecular processes dominate in blends processed with DIO. Furthermore, the intensity dependent dynamics of the blends processed without and with DIO exhibit significant differences. The low intensity spectra of the blend processed with DIO exhibit a steady rise of the p-DTS(FBTTh$_2$)$_2$ bleach that continues up to 25 ps which is not present in the spectra of the blend processed without DIO. This delayed rise of the bleach is likely the result of an exciton diffusion-limited process such as energy or charge transfer from PDI to p-DTS(FBTTh$_2$)$_2$, suggesting larger domain sizes in the blend spin-cast with DIO as compared to the blend processed without DIO.[43] This result is consistent with the PL measurements discussed above.

TA measurements were also performed by exciting films at 625 nm, near a local maximum in p-DTS(FBTTh$_2$)$_2$ absorption but red-shifted with respect to the PDI's absorption spectrum. Thus, p-DTS(FBTTh$_2$)$_2$ molecules within the blend are predominantly excited at this wavelength. The TA spectra in the visible spectral region of the samples spin-cast without and with DIO are displayed in Figure 5a. These spectra are similar to those measured upon exciting the films at 485 nm. Once again, the GSB of the blend processed without DIO is broad and featureless whereas the GSB of the blend processed with DIO exhibits peaks at 620 and 675 nm. Additionally, the PIA peaks associated with PDI anions are present in the blend spin-cast without DIO, while they are absent in the blend spin-cast with DIO at 1 ps after excitation. Furthermore, the early time spectra of blends processed with the solvent additive are clearly modulated by the stimulated emission of p-DTS(FBTTh$_2$)$_2$ in the wavelength region spanning from 750 to 850 nm. This is further evidence for larger pure domains that cause diffusion-limited exciton dissociation and thus allow the observation of the donor's stimulated emission. The peak at 950 nm in samples processed without DIO is assigned to p-DTS-(FBTTh$_2$)$_2$ polarons. Figure 5b displays the GSB dynamics as a function of excitation intensity. Similar to excitation of the PDI, the blend spin-cast without DIO displays only a weak intensity dependence, whereas the blend processed with DIO exhibits a significantly more pronounced intensity dependence indicating geminate recombination dominates in the blend processed without DIO, while nongeminate recombination dominates in the blend processed with DIO. However, a significant and important difference compared to the excitation of PDI is that the GSB dynamics of the blend processed with DIO does not display the slow rise of the charge-induced absorption observed after excitation of the PDI. As the slow rise after excitation of the PDI is the result of an exciton diffusion-limited process in the PDI crystallites, its absence is expected when directly exciting p-DTS(FBTTh$_2$)$_2$.

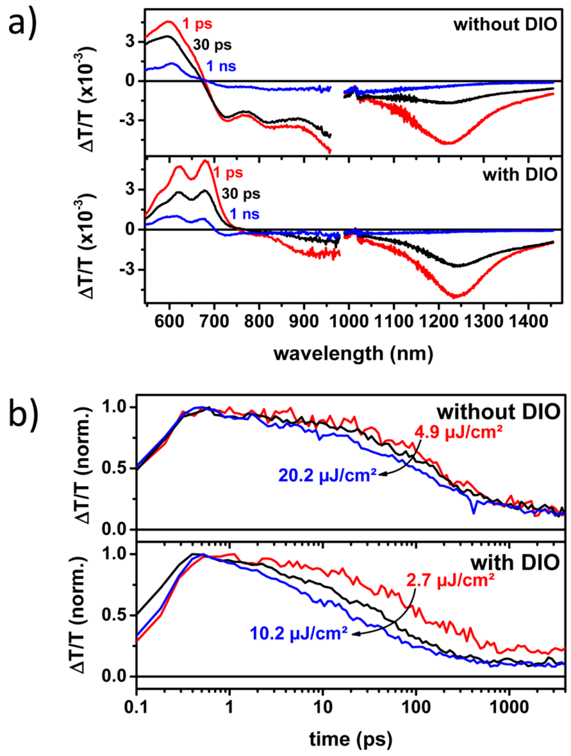

Figure 5. (a) TA spectra and (b) GSB kinetics of p-DTS-(FBTTh$_2$)$_2$:PDI films processed without (550−575 nm) and with DIO (665−690 nm) excited at 625 nm.

The near-infrared region (1000 to 1450 nm) of the TA spectra shown in Figure 5a also differ depending on whether the blend is processed without or with DIO. The PIA peak in this spectral region shifts from approximately 1225 to 1245 nm upon processing with DIO. This peak is assigned to singlet excited states located on p-DTS(FBTTh$_2$)$_2$ as determined by TA measurements of pristine p-DTS(FBTTh$_2$)$_2$ films (Figure S4). Such a red shift has previously been observed when using a solvent additive to increase the solid state order of a polymer donor in a polymer:fullerene BHJ OPV device.[23] This red shift is then consistent with the increase in solid state order of p-DTS(FBTTh$_2$)$_2$ in the present system. Additionally, the spectra of the blend processed with DIO exhibit a weak shoulder at longer wavelengths that is not present in the spectra of the blend processed without DIO. This shoulder is present in the TA spectra of pristine films of p-DTS(FBTTh$_2$)$_2$ but not in spectra obtained from p-DTS(FBTTh$_2$)$_2$ in solution (Figure S4). Thus, this shoulder is likely the result of increased intermolecular interaction between p-DTS(FBTTh$_2$)$_2$ molecules. The presence of this shoulder in the blend processed with DIO and its absence in the blend processed without DIO is once again consistent with the results of UV−vis absorption spectroscopy, indicating p-DTS(FBTTh$_2$)$_2$ is relatively structurally disordered in the blend spin-cast without DIO, whereas in the blend processed with DIO it is structurally more ordered.

2.3.2. Long Delay Measurements and Quantitative Recombination Modeling of BHJ Films. In order to study the recombination of longer-lived species such as free charges that contribute to the device photocurrent, we used nanosecond to microsecond TA spectroscopy to probe the carrier dynamics from approximately 100 ps to 100 μs after excitation at 532 nm. This excitation wavelength results in significant absorption by both the p-DTS(FBTTh$_2$)$_2$ donor and the PDI acceptor. Figure 6a displays the long delay TA spectra of p-DTS(FBTTh$_2$)$_2$:PDI blends processed without and with DIO. The spectra display the same GSB and PIA features of the short delay measurements as described above. The GSB of the blend processed without DIO is again broad and featureless; however, the GSB of the blend processed with DIO shows three distinct, narrow peaks that are slightly red-shifted compared to the GSB observed in the short delay TA measurements. This implies that in the blend processed with DIO, after a delay time of 1 ns,

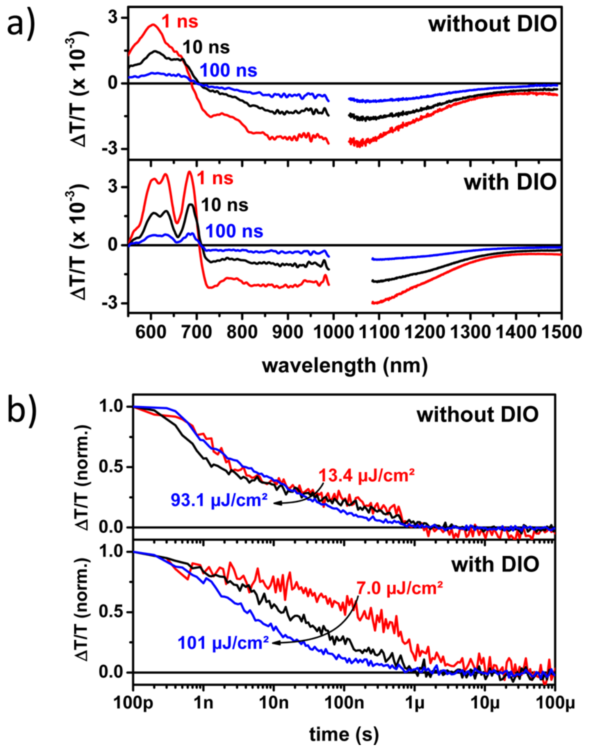

Figure 6. (a) TA spectra after excitation with 47.9 μJ/cm^2 and 53.6 μJ/cm^2 and (b) PIA dynamics of p-DTS(FBTTh$_2$)$_2$:PDI films processed without and with DIO excited at 532 nm. Dynamics were monitored from 875 to 925 nm of the TA spectra.

excited states still present in the film reside in more ordered regions of the p-DTS(FBTTh$_2$)$_2$ donor. Figure 6b shows the long delay dynamics of the PIA region of the spectrum over a broad range of excitation intensities. As found for the short delay measurements, the blend processed without DIO exhibits negligible intensity dependence, while the blend processed with DIO shows a pronounced intensity dependence of the dynamics after 1 ns. Hence, these data indicate that in blends processed without DIO bound charge pairs are formed, which do not split into free charge carriers, while in blends processed with DIO a significant population of free charge carriers is produced upon absorption of photons.

To further analyze the charge recombination dynamics occurring in the blend processed with DIO, the intensity dependent PIA dynamics were fit with a previously reported model assuming concomitant recombination of CT states via a monomolecular and geminate recombination process parallel to recombination of free charges via a nongeminate recombination process (Figure 7).[22] Here, the PIA of the spectra was used because this negative $\Delta T/T$ signal yields information on the temporal evolution of the charge carrier concentration in the film. The initial charge carrier concentrations, i.e. charges remaining after 1 ns, needed to fit the data were estimated from the signal amplitude of the charge-induced absorption of the ps-ns TA experiments, thereby taking into account the sub-ns carrier losses. By fitting the nanosecond to microsecond TA data with the recombination model we determined that in the blend processed with DIO, approximately 76% of the charges surviving the first nanosecond are free charge carriers as opposed to bound CT states. The bimolecular recombination coefficient was determined to be ~4.3 × 10^{-12} cm^3 s^{-1}, which is comparable to previously published polymer:fullerene systems.[23] This is in contrast to the blend processed without DIO in which the lack of any excitation intensity dependence as seen in Figure 6b indicates that a negligible amount of free charge carriers are produced. In fact, the intensity-independent recombination of the blend processed without DIO on the longer nanosecond to microsecond time scale indicates trap-assisted recombination of nonmobile charge carriers in addition to the geminate recombination identified using the ps TA spectroscopy.[22] Therefore, processing p-DTS(FBTTh$_2$)$_2$:PDI devices with DIO drastically increases the splitting efficiency of excitons into free charge carriers, in turn explaining to a large extent why p-DTS(FBTTh$_2$)$_2$:PDI OPV devices processed without DIO exhibit negligible photovoltaic efficiency, whereas OPV devices made from blends processed with DIO demonstrate rather efficient photovoltaic performance. Moreover, Friend and co-workers recently studied the effect of PCBM aggregation in p-DTS(FBTTh$_2$)$_2$:PC$_{71}$BM blends and linked the positive effect of DIO on the charge separation efficiency to the observation of a pronounced electro-absorption (EA) signal, which is indicative of spatially separated electron−hole pairs.[26] Here, the EA signal is observed at 710 nm in Figure 6a and consequently overlaps with the PDI anion-induced absorption signal. Therefore, the PIA present in the data shown above is likely a superposition of both features in the blend processed with DIO. Additionally, Friend et al. found two time constants that describe the exciton-to-charge conversion process. One is ultrafast and below 100 fs, the other on the picosecond time scale.[26] This is consistent with our measurements of the short time scale where even for the lowest intensity shown in Figure 4 (lower panel) a certain portion of the GSB is present directly after excitation (i.e., within the temporal resolution of our measurement), while a subsequent rise on the picosecond time scale is also observed.

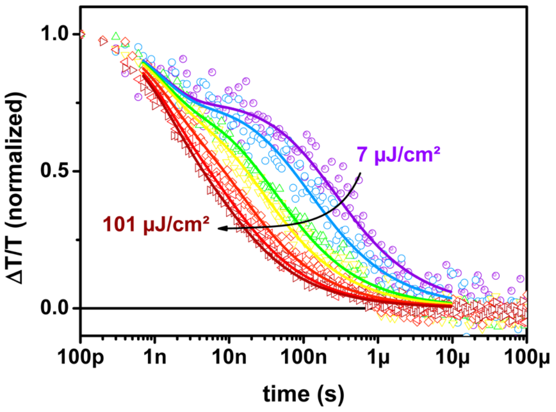

Figure 7. Excitation intensity dependence of the PIA dynamics (symbols) and respective fits (lines) using the recombination model detailed in reference 22. Data sampled from between 875 and 925 nm of TA spectra.

2.4. Use of Perylene Diimides as Electron Acceptors in Bulk Heterojunction Solar Cells. In this section, we discuss the implications of the presented data on the use of PDIs as electron acceptors in BHJ OPV devices.

2.4.1. PDI Excimer Formation. Upon aggregation and/or crystallization, PDIs are known to readily form lower energy, intermolecular excited states known as excimers.[45,46] Excimer formation has been shown to lead to exciton trapping, in turn limiting the exciton diffusion length in PDIs.[47−49] Strategies to avoid the formation of PDI excimers or to harvest them as photocurrent must therefore be developed in order to fabricate high efficiency OPV devices utilizing PDIs as electron acceptors. To date, molecular design has been used to influence PDI excimer formation in PDIs used as electron acceptors in OPV devices, for instance via the addition of bulky substituents that modify the packing motif of PDI crystallites.[50−53] This strategy has been successfully used to produce relatively efficient BHJ OPVs utilizing PDI acceptors,[50,52] however, at the cost of the additional synthetic complexity associated with these substituted PDI acceptors. These bulky substituents can also reduce the electron mobility and therefore the PCE if not carefully selected.[54] The presented TA experiments on p-DTS(FBTTh$_2$)$_2$:PDI films processed with DIO show that, in these films, photogenerated excitons readily dissociate into free charge carriers at the donor−acceptor interface. These TA data combined with the largely wavelength independent IQE data presented previously for this system[30] as well as its comparably efficient photovoltaic behavior suggest that PDI excimers are not a significant loss mechanism in p-DTS(FBTTh$_2$)$_2$:PDI OPV devices processed with DIO. To correlate this observation with the direct characterization of film morphology, grazing incidence wide-angle X-ray scattering (GIWAXS) measurements were used to quantify the PDI's crystalline order in p-DTS(FBTTh$_2$)$_2$:PDI films processed with DIO (Figure S5). GIWAXS data were used to calculate the crystalline correlation length (CCL) of PDI crystallites in the blend film processed with DIO. The CCL is a measure of the distance over which crystalline order is preserved[55] and can therefore likely be considered the maximum distance over which exciton trapping by PDI excimers could occur. The PDI's CCL was determined to be 7.4 ± 3.3 nm. This is consistent with the absence of large PDI crystallites in atomic force microscopy images of p-DTS(FBTTh$_2$)$_2$:PDI BHJ blends (Figure S6). Given the exciton diffusion length of PDI is approximately 5 nm,[48] PDI excimers in optimized p-DTS(FBTTh$_2$)$_2$:PDI BHJ OPV devices can likely be harvested because PDI crystallites are small enough to allow the majority of excited states to escape and undergo charge transfer. Furthermore, long-range Förster-type energy transfer from the PDI to the p-DTS(FBTTh$_2$)$_2$ due to the pronounced overlap of the PDI emission and p-DTS(FBTTh$_2$)$_2$ absorption spectra can help to harvest the PDI excitations, even if they are unable to diffuse out of PDI domains to a donor−acceptor interface as has previously been suggested in a low-bandgap polymer:PDI BHJ OPV system.[56] We have thus shown that PDI excimer formation, a commonly cited loss pathway in solar cells utilizing PDIs as electron acceptors, can be overcome without complicated synthetic modification of the PDI structural core by combining PDI with a donor molecule and/or using processing techniques that encourage the formation of PDI crystalline order on a length scale that does not significantly exceed the PDI's excited state diffusion length and by utilizing energy transfer from the PDI molecule to the donor molecule and successive charge transfer, as is expected for blends of PDIs with low-bandgap donor materials. It is unclear, however, why the large PDI crystallites commonly observed in PDI:polymer BHJ blends[52,56,57] are not formed in p-DTS(FBTTh$_2$)$_2$:PDI BHJ blends and the extent to which the processing conditions used in this blend will suppress the formation of large PDI crystallites in BHJ blends with different donor molecules.

2.4.2. Relationship Between Solid State Order and Charge Generation. The remarkable increase in the efficiency of interfacial charge separation associated with the use of the processing additive DIO in p-DTS(FBTTh$_2$)$_2$:PDI films corresponds to a significant increase in the solid state order of both p-DTS(FBTTh$_2$)$_2$ and PDI as inferred from UV−vis measurements. TA spectroscopy has previously been used to observe similar behavior in polymer:PCBM BHJ films. For example, the efficiency of charge generation increases from approximately 68% to 85% upon thermal annealing of poly(3-hexylthiopene):PCBM (P3HT:PCBM) films,[22] and in poly-[2,6-(4,4-bis(2-ethylhexyl)-4H-cyclopenta[2,1-b;3,4-b′]-dithiophene)-*alt*-4,7-(2,1,3-benzothiadiazole)]:PCBM (PCPDTBT:PCBM) films, the charge generation efficiency additionally increases upon using the processing additive DIO during film casting.[23] Thermal annealing of P3HT:PCBM films and the use of the processing additive DIO during spin-casting of PCPDTBT:PCBM films improves the solid state order of these donor polymers.[58,59] The p-DTS(FBTTh$_2$)$_2$:PDI BHJ system differs from these polymer:PCBM BHJ systems, however, as here the use of the processing additive DIO leads to crystallization of both donor and acceptor, which may explain the much more significant increase in the charge separation efficiency between disordered and ordered morphologies compared to previous observations of polymer:PCBM films. In order to gain insight into this observation it is useful to compare the relationship between solid state order and charge generation in p-DTS(FBTTh$_2$)$_2$:PDI BHJ OPV devices to p-DTS(FBTTh$_2$)$_2$:PC$_{71}$BM BHJ OPV devices. p-DTS(FBTTh$_2$)$_2$:PC$_{71}$BM BHJ OPV devices cast without DIO form a structurally disordered BHJ morphology lacking significant phase separation, very similar to p-DTS-(FBTTh$_2$)$_2$:PDI films cast without DIO. However, p-DTS-(FBTTh$_2$)$_2$:PC$_{71}$BM devices processed without DIO exhibit a J_{sc} over 6 mA/cm^2, even though they absorb approximately the same number of photons as optimized p-DTS(FBTTh$_2$)$_2$:PDI BHJ OPV devices.[29,30] Comparing the results reported herein on p-DTS(FBTTh$_2$)$_2$:PDI BHJ OPVs to previous observations on p-DTS(FBTTh$_2$)$_2$:PC$_{71}$BM BHJ OPVs then further supports the suggestion that PDIs require greater solid state order compared to PCBM in order to achieve efficient charge generation.[60] This relationship between solid state order and efficient charge generation may be general for BHJ electron acceptors capable of forming crystalline domains as evidenced by recent work comparing the efficiency of charge generation with the crystallinity of C$_{60}$ and CdS acceptors.[61,62] It is still unclear, however, specifically why increased solid state order leads to more efficient charge separation in PDI acceptors. Given the delocalization of excited states associated with crystalline molecular semiconductors[63,64] and the crucial role delocalization is thought to play in efficient charge generation at organic heterojunctions,[11,13,14,61] it is possible that the increased solid state order in p-DTS(FBTTh$_2$)$_2$:PDI films associated with the use of DIO facilitates the delocalization of photogenerated excited states, thereby allowing these states to successfully overcome Coulombic forces and produce free charge carriers. It is difficult to determine what exactly prevents the remaining CT states from dissociating into free charge carriers in p-DTS(FBTTh$_2$)$_2$:PDI films processed with DIO. Perhaps additional increases in the solid state order of p-DTS(FBTTh$_2$)$_2$ and/or the PDI would result in more efficient charge generation, provided this could be achieved without leading to phase separation on a length scale larger than the exciton diffusion length. PDIs, however, may lack some fundamental property fullerene derivatives possess that enables extremely efficient charge generation.[65] More work is needed to better understand the charge generation process, especially in systems utilizing non-fullerene acceptors, before these questions can be answered.

3. CONCLUSIONS

We have demonstrated that using the processing additive DIO during spin-casting of p-DTS(FBTTh$_2$)$_2$:PDI BHJ OPV devices leads to a drastic improvement in PCE compared to devices processed without the additive, increasing the PCE from 0.13% to 3.1%. Using UV−vis absorption spectroscopy and transient PL measurements we have shown that the increased PCE is associated with a significant increase in both p-DTS(FBTTh$_2$)$_2$ and PDI solid state order as well as donor−acceptor phase separation. TA spectroscopy measurements are consistent with this morphological characterization and are additionally used to characterize the charge generation and recombination dynamics of p-DTS(FBTTh$_2$)$_2$:PDI films processed without and with DIO. Fast, intensity independent geminate recombination was found to be the dominant loss process in blends spin-cast without DIO, while geminate recombination was significantly reduced in blends cast with DIO, thereby increasing the yield of free charge carriers in these blends as demonstrated by the occurrence of intensity dependent nongeminate recombination in their charge carrier dynamics. Devices processed without DIO are therefore relatively structurally disordered and homogeneous compared to the blend processed with DIO and display negligible photovoltaic efficiency because the vast majority of excitons form interfacial CT states that recombine prior to dissociation. In contrast, in blends processed with DIO both p-DTS(FBTTh$_2$)$_2$ and PDI exhibit increased structural order as well as phase separation and a much higher PCE, largely due to a drastic increase of the efficiency with which excitons dissociate into free charge carriers. Our results thus provide useful insight into the conditions under which photogenerated excitons are able to overcome Coulombic forces to produce spatially separated free charge carriers in a BHJ architecture when using a non-fullerene acceptor. By using a donor molecule and processing conditions that produce PDI crystalline order on a length scale corresponding to the PDI's excited state diffusion length and Förster resonance energy transfer, we have shown that PDI excimers, a commonly cited loss mechanism in PDI OPVs, can be avoided and/or harvested without the need for the synthetic complexity associated with the addition of bulky substituents to the PDI core. The blend processed with DIO, however, still displays a significant amount of geminate recombination of Coulombically bound CT states that do not form free charge carriers. This relatively low efficiency of charge separation compared to fullerene acceptors largely explains why p-DTS(FBTTh$_2$)$_2$:PDI devices exhibit less efficient photovoltaic performance compared to p-DTS-(FBTTh$_2$)$_2$:PCBM devices, which exhibit a PCE of 7.0% and an IQE exceeding 90%.[29] It remains unclear, however, why the use of the PDI as an electron acceptor leads to less efficient charge generation compared to the use of PCBM as an electron acceptor. Accordingly, we emphasize that further advances in the fabrication of high efficiency BHJ OPV devices utilizing PDI acceptors are dependent on developing a more thorough understanding of the relationship between PDI chemical structure, BHJ processing conditions, thin film morphology, and the fundamental processes associated with charge generation in these devices.

4. EXPERIMENTAL PROCEDURES

4.1. Photovoltaic Device Fabrication and Testing. Bulk heterojunction organic solar cells were fabricated on UV−O$_3$ treated ITO substrates coated with approximately 45 nm of PEDOT:PSS (Clevios P VP Al 4083). Solutions of p-DTS(FBTTh$_2$)$_2$ and PDI were prepared in a 1:1 weight ratio at a total solids concentration of 30 mg/mL in either pure chlorobenzene or chlorobenzene with 0.4 vol % diiodooctane. Solutions were heated overnight and residual solids filtered prior to casting at 90 °C to produce films approximately 100-nm-thick as measured with an Ambios XP-100 stylus profilometer. Approximately 5 nm of Ca and 100 nm of Al were then subsequently thermally evaporated on top of the organic layer. Device characteristics were measured under illumination by a simulated 100 mW cm^{-2} AM 1.5 G light source using a 300 W Xe arc lamp with an AM 1.5 global filter using an aperture to define a device area of 0.13 cm^2. Solar-simulator irradiance was calibrated using a standard silicon photovoltaic cell with a protective KG1 filter calibrated by the National Renewable Energy Laboratory. External quantum efficiencies were determined using a 75 W Xe source, monochromator, optical chopper, and lock-in amplifier, and a National Institute of Standards and Technology calibrated silicon photodiode was used for power-density calibration. The presented OPV device data and $J-V$ curves are representative of approximately 20 devices of each processing condition (with and without DIO) made over the course of several months. The average and standard deviation of the PCE is 0.2% ± 0.1 and 3.0% ± 0.2 for the devices processed without and with DIO respectively.

4.2. Photoluminescence Measurements. Time-resolved photoluminescence (TR-PL) spectra were taken with a C4742 Hamamatsu streak camera system in fast sweep mode. Excitation pulses at 400 nm were provided by frequency doubling the output of a commercial femtosecond laser system (Coherent LIBRA-HE).

4.3. Transient Absorption Measurements. Transient absorption (TA) measurements were performed with a home-built pump−probe setup. To measure in the time range of 1−4 ns with a resolution of ~100 fs, the output of a commercial titanium:sapphire amplifier (Coherent LIBRA-HE, 3.5 mJ, 1 kHz, 100 fs) was split into two beams that pumped two independent commercial optical parametric amplifiers (Coherent OPerA Solo). One optical parametric amplifier (OPA) was used to generate the tunable excitation pulses in the visible, while the second OPA was used to generate the seed beam for white-light generation. For measurements in the spectral range between 550 and 1100 nm, a 1300 nm seed of a few microjoules was focused into a c-cut 3-mm-thick sapphire window for white-light generation. The variable delay of up to 4 ns between pump and probe was introduced by a broadband retroreflector mounted on a mechanical delay stage. Mostly reflective elements were used to guide the probe beam to the sample to minimize chirp. The excitation pulse was chopped at 500 Hz, while the white-light pulses were dispersed onto a linear silicon photodiode array, which was read out at 1 kHz by home-built electronics. Adjacent diode readings corresponding to the transmission of the sample after an excitation pulse and without an excitation pulse were used to calculate $\Delta T/\mathrm{T}$.

For measurements in the time range between 1 ns to 1 ms with a resolution of 600 ps, the excitation pulse was provided by an actively Q-switched Nd:YVO$_4$ laser (AOT Ltd. MOPA) at 532 nm. In this case, the delay between pump and probe was controlled by an electronic delay generator (Stanford Research Systems DG535). TA measurements were performed at room temperature under a dynamic vacuum of <10^{-5} mbar.

For TA measurements in the NIR spectral range covering 1100−2000 nm, a 2100 nm seed was used to generate white-light in a yttrium vanadate window. Furthermore, a dichroic mirror was used to separate the residual seed beam (idler of the OPA at 2100 nm) from the broadband NIR supercontinuum. The NIR pulses were dispersed onto a Peltier-cooled 512 pixel long linear extended InGaAs array (Entwicklungsbüro Stresing) and read out as described above.

■ ASSOCIATED CONTENT

Ⓢ Supporting Information

p-DTS(FBTTh$_2$)$_2$, PDI, and PDI anion absorption spectra; p-DTS(FBTTh$_2$)$_2$ and PDI PL spectra; TA spectra of pure p-DTS(FBTTh$_2$)$_2$ as a thin film and in solution; atomic force microscopy; and GIWAXS data. This material is available free of charge via the Internet at http://pubs.acs.org.

■ AUTHOR INFORMATION

Corresponding Authors

*E-mail: laquai@mpip-mainz.mpg.de.
*E-mail: quyen@chem.ucsb.edu.

Author Contributions

$^{\#}$These authors contributed equally.

Notes

The authors declare no competing financial interest.

■ ACKNOWLEDGMENTS

The authors thank the Office of Naval Research (N000141410076) for support and funding. F.L. thanks the Max Planck Society for funding of the Max Planck Research Group and the Deutsche Forschungsgemeinschaft (DFG) for funding in the framework of the priority program SPP1355 "Elementary Processes in Organic Photovoltaics." D.G. acknowledges a Kekulé scholarship of the Fonds der Chemischen Industrie (FCI). A.S. acknowledges support from a National Science Foundation Graduate Research Fellowship. Portions of this research were conducted at the Stanford Synchrotron Radiation Lightsource user facility, operated by Stanford University on behalf of the U.S. Department of Energy, Office of Basic Energy Sciences under Contract No. DE-AC02-76SF00515. The authors thank G. C. Bazan and Z. B. Henson for synthesis of PDI and J. A. Love for helpful discussions regarding structural characterization. T.-Q.N. thanks the Camille Dreyfus Teacher Scholar Award.

■ REFERENCES

(1) Green, M. A.; Emery, K.; Hishikawa, Y.; Warta, W.; Dunlop, E. D. *Prog. Photovolt. Res. Appl.* **2014**, *22*, 1−9.

(2) Krebs, F. C.; Gevorgyan, S. A.; Alstrup, J. *J. Mater. Chem.* **2009**, *19*, 5442−5451.

(3) Krebs, F. C.; Espinosa, N.; Hösel, M.; Søndergaard, R. R.; Jørgensen, M. *Adv. Mater.* **2014**, *26*, 29−39.

(4) Anctil, A.; Babbitt, C. W.; Raffaelle, R. P.; Landi, B. J. *Environ. Sci. Technol.* **2011**, *45*, 2353−2359.

(5) Anctil, A.; Babbitt, C.; Landi, B.; Raffaelle, R. P. In *2010 35th IEEE Photovoltaic Specialists Conference (PVSC)*; IEEE: Piscataway, NJ, 2010; pp 000742−000747.

(6) Wagenpfahl, A.; Deibel, C.; Dyakonov, V. *IEEE J. Sel. Top. Quantum Electron.* **2010**, *16*, 1759−1763.

(7) Proctor, C. M.; Kim, C.; Neher, D.; Nguyen, T.-Q. *Adv. Funct. Mater.* **2013**, *23*, 3584−3594.

(8) Bartelt, J. A.; Beiley, Z. M.; Hoke, E. T.; Mateker, W. R.; Douglas, J. D.; Collins, B. A.; Tumbleston, J. R.; Graham, K. R.; Amassian, A.; Ade, H.; Fréchet, J. M. J.; Toney, M. F.; McGehee, M. D. *Adv. Energy Mater.* **2012**, *3*, 364−374.

(9) Proctor, C. M.; Kuik, M.; Nguyen, T.-Q. *Prog. Polym. Sci.* **2013**, *38*, 1941−1960.

(10) Dimitrov, S. D.; Durrant, J. R. *Chem. Mater.* **2013**, DOI: 10.1021/cm402403z.

(11) Bakulin, A. A.; Rao, A.; Pavelyev, V. G.; Loosdrecht, P. H. M.; van Pshenichnikov, M. S.; Niedzialek, D.; Cornil, J.; Beljonne, D.; Friend, R. H. *Science* **2012**, *335*, 1340−1344.

(12) Dimitrov, S. D.; Bakulin, A. A.; Nielsen, C. B.; Schroeder, B. C.; Du, J.; Bronstein, H.; McCulloch, I.; Friend, R. H.; Durrant, J. R. *J. Am. Chem. Soc.* **2012**, *134*, 18189−18192.

(13) Jailaubekov, A. E.; Willard, A. P.; Tritsch, J. R.; Chan, W.-L.; Sai, N.; Gearba, R.; Kaake, L. G.; Williams, K. J.; Leung, K.; Rossky, P. J.; Zhu, X.-Y. *Nat. Mater.* **2013**, *12*, 66−73.

(14) Vandewal, K.; Albrecht, S.; Hoke, E. T.; Graham, K. R.; Widmer, J.; Douglas, J. D.; Schubert, M.; Mateker, W. R.; Bloking, J. T.; Burkhard, G. F.; Sellinger, A.; Fréchet, J. M. J.; Amassian, A.; Riede, M. K.; McGehee, M. D.; Neher, D.; Salleo, A. *Nat. Mater.* **2014**, *13*, 63−68.

(15) Bakulin, A. A.; Dimitrov, S. D.; Rao, A.; Chow, P. C. Y.; Nielsen, C. B.; Schroeder, B. C.; McCulloch, I.; Bakker, H. J.; Durrant, J. R.; Friend, R. H. *J. Phys. Chem. Lett.* **2013**, *4*, 209−215.

(16) Ohkita, H.; Cook, S.; Astuti, Y.; Duffy, W.; Tierney, S.; Zhang, W.; Heeney, M.; McCulloch, I.; Nelson, J.; Bradley, D. D. C.; Durrant, J. R. *J. Am. Chem. Soc.* **2008**, *130*, 3030−3042.

(17) Vithanage, D. A.; Devižis, A.; Abramavičius, V.; Infahsaeng, Y.; Abramavičius, D.; MacKenzie, R. C. I.; Keivanidis, P. E.; Yartsev, A.; Hertel, D.; Nelson, J.; Sundström, V.; Gulbinas, V. *Nat. Commun.* **2013**, *4*, 2334.

(18) Shoaee, S.; An, Z.; Zhang, X.; Barlow, S.; Marder, S. R.; Duffy, W.; Heeney, M.; McCulloch, I.; Durrant, J. R. *Chem. Commun.* **2009**, 5445−5447.

(19) Holcombe, T. W.; Norton, J. E.; Rivnay, J.; Woo, C. H.; Goris, L.; Piliego, C.; Griffini, G.; Sellinger, A.; Brédas, J.-L.; Salleo, A.; Fréchet, J. M. J. *J. Am. Chem. Soc.* **2011**, *133*, 12106−12114.

(20) Rand, B. P.; Cheyns, D.; Vasseur, K.; Giebink, N. C.; Mothy, S.; Yi, Y.; Coropceanu, V.; Beljonne, D.; Cornil, J.; Brédas, J.; Genoe, J. *Adv. Funct. Mater.* **2012**, *22*, 2987.

(21) Ojala, A.; Petersen, A.; Fuchs, A.; Lovrincic, R.; Pölking, C.; Trollmann, J.; Hwang, J.; Lennartz, C.; Reichelt, H.; Höffken, H. W.; Pucci, A.; Erk, P.; Kirchartz, T.; Würthner, F. *Adv. Funct. Mater.* **2012**, *22*, 86−96.

(22) Howard, I. A.; Mauer, R.; Meister, M.; Laquai, F. *J. Am. Chem. Soc.* **2010**, *132*, 14866−14876.

(23) Etzold, F.; Howard, I. A.; Forler, N.; Cho, D. M.; Meister, M.; Mangold, H.; Shu, J.; Hansen, M. R.; Müllen, K.; Laquai, F. *J. Am. Chem. Soc.* **2012**, *134*, 10569−10583.

(24) Jamieson, F. C.; Domingo, E. B.; McCarthy-Ward, T.; Heeney, M.; Stingelin, N.; Durrant, J. R. *Chem. Sci.* **2012**, *3*, 485−492.

(25) Shoaee, S.; Subramaniyan, S.; Xin, H.; Keiderling, C.; Tuladhar, P. S.; Jamieson, F.; Jenekhe, S. A.; Durrant, J. R. *Adv. Funct. Mater.* **2013**, *23*, 3286−3298.

(26) Gélinas, S.; Rao, A.; Kumar, A.; Smith, S. L.; Chin, A. W.; Clark, J.; Poll, T. S.; van der Bazan, G. C.; Friend, R. H. *Science* **2013**, 1239947.

(27) Savoie, B. M.; Rao, A.; Bakulin, A. A.; Gelinas, S.; Movaghar, B.; Friend, R. H.; Marks, T. J.; Ratner, M. A. *J. Am. Chem. Soc.* **2014**, *136*, 2876−2884.

(28) Kesava, S. V.; Fei, Z.; Rimshaw, A. D.; Wang, C.; Hexemer, A.; Asbury, J. B.; Heeney, M.; Gomez, E. D. *Adv. Energy Mater.* **2014**, DOI: 10.1002/aenm.201400116.

(29) Love, J.; Proctor, C.; Liu, J.; Takacs, C.; Sharenko, A.; van der Poll, T.; Heeger, A.; Bazan, G.; Nguyen, T.-Q. *Adv. Funct. Mater.* **2013**, *23*, 5019−5026.

(30) Sharenko, A.; Proctor, C. M.; van der Poll, T. S.; Henson, Z. B.; Nguyen, T.-Q.; Bazan, G. C. *Adv. Mater.* **2013**, *25*, 4403−4406.

(31) Bloking, J. T.; Giovenzana, T.; Higgs, A. T.; Ponec, A. J.; Hoke, E. T.; Vandewal, K.; Ko, S.; Bao, Z.; Sellinger, A.; McGehee, M. D. *Adv. Energy Mater.* **2014**, DOI: 10.1002/aenm.201301426.

(32) Huang, C.; Barlow, S.; Marder, S. R. *J. Org. Chem.* **2011**, *76*, 2386−2407.

(33) Li, C.; Wonneberger, H. *Adv. Mater.* **2012**, *24*, 613−636.

(34) Schmidt-Mende, L.; Fechtenkötter, A.; Müllen, K.; Moons, E.; Friend, R. H.; MacKenzie, J. D. *Science* **2001**, *293*, 1119−1122.

(35) Salleo, A.; Kline, R. J.; DeLongchamp, D. M.; Chabinyc, M. L. *Adv. Mater.* **2010**, *22*, 3812−3838.

(36) Würthner, F. *Chem. Commun.* **2004**, 1564−1579.

(37) Perez, L. A.; Chou, K. W.; Love, J. A.; van der Poll, T. S.; Smilgies, D.-M.; Nguyen, T.-Q.; Kramer, E. J.; Amassian, A.; Bazan, G. C. *Adv. Mater.* **2013**, *25*, 6380−6384.

(38) Balakrishnan, K.; Datar, A.; Oitker, R.; Chen, H.; Zuo, J.; Zang, L. *J. Am. Chem. Soc.* **2005**, *127*, 10496−10497.

(39) Keivanidis, P. E.; Howard, I. A.; Friend, R. H. *Adv. Funct. Mater.* **2008**, *18*, 3189−3202.

(40) Rivnay, J.; Mannsfeld, S. C. B.; Miller, C. E.; Salleo, A.; Toney, M. F. *Chem. Rev.* **2012**, *112*, 5488−5519.

(41) Massip, S.; Oberhumer, P. M.; Tu, G.; Albert-Seifried, S.; Huck, W. T. S.; Friend, R. H.; Greenham, N. C. *J. Phys. Chem. C* **2011**, *115*, 25046−25055.

(42) Sharenko, A.; Kuik, M.; Toney, M. F.; Nguyen, T.-Q. *Adv. Funct. Mater.* **2014**, *24*, 3543−3550.

(43) Marsh, R. A.; Hodgkiss, J. M.; Albert-Seifried, S.; Friend, R. H. *Nano Lett.* **2010**, *10*, 923−930.

(44) Shivanna, R.; Shoaee, S.; Dimitrov, S.; Kandappa, S. K.; Rajaram, S.; Durrant, J. R.; Narayan, K. S. *Energy Environ. Sci.* **2013**, *7*, 435−441.

(45) Walker, B.; Port, H.; Wolf, H. C. *Chem. Phys.* **1985**, *92*, 177−185.

(46) Giaimo, J. M.; Lockard, J. V.; Sinks, L. E.; Scott, A. M.; Wilson, T. M.; Wasielewski, M. R. *J. Phys. Chem. A* **2008**, *112*, 2322−2330.

(47) Fink, R. F.; Seibt, J.; Engel, V.; Renz, M.; Kaupp, M.; Lochbrunner, S.; Zhao, H.-M.; Pfister, J.; Würthner, F.; Engels, B. *J. Am. Chem. Soc.* **2008**, *130*, 12858−12859.

(48) Howard, I. A.; Laquai, F.; Keivanidis, P. E.; Friend, R. H.; Greenham, N. C. *J. Phys. Chem. C* **2009**, *113*, 21225−21232.

(49) Yago, T.; Tamaki, Y.; Furube, A.; Katoh, R. *Phys. Chem. Chem. Phys.* **2008**, *10*, 4435.

(50) Zhang, X.; Lu, Z.; Ye, L.; Zhan, C.; Hou, J.; Zhang, S.; Jiang, B.; Zhao, Y.; Huang, J.; Zhang, S.; Liu, Y.; Shi, Q.; Liu, Y.; Yao, J. *Adv. Mater.* **2013**, *25*, 5791−5797.

(51) Kozma, E.; Kotowski, D.; Luzzati, S.; Catellani, M.; Bertini, F.; Famulari, A.; Raos, G. *RSC Adv.* **2013**, *3*, 9185−9188.

(52) Rajaram, S.; Shivanna, R.; Kandappa, S. K.; Narayan, K. S. *J. Phys. Chem. Lett.* **2012**, *3*, 2405−2408.

(53) Kamm, V.; Battagliarin, G.; Howard, I. A.; Pisula, W.; Mavrinskiy, A.; Li, C.; Müllen, K.; Laquai, F. *Adv. Energy Mater.* **2011**, *1*, 297−302.

(54) Guide, M.; Pla, S.; Sharenko, A.; Zalar, P.; Fernández-Lázaro, F.; Sastre-Santos, Á.; Nguyen, T.-Q. *Phys. Chem. Chem. Phys.* **2013**, *15*, 18894−18899.

(55) Rivnay, J.; Noriega, R.; Kline, R. J.; Salleo, A.; Toney, M. F. *Phys. Rev. B* **2011**, *84*, 045203.

(56) Ye, T.; Singh, R.; Butt, H.-J.; Floudas, G.; Keivanidis, P. E. *ACS Appl. Mater. Interfaces* **2013**, *5*, 11844−11857.

(57) Li, J.; Dierschke, F.; Wu, J.; Grimsdale, A. C.; Müllen, K. *J. Mater. Chem.* **2006**, *16*, 96−100.

(58) Verploegen, E.; Mondal, R.; Bettinger, C. J.; Sok, S.; Toney, M. F.; Bao, Z. *Adv. Funct. Mater.* **2010**, *20*, 3519−3529.

(59) Rogers, J. T.; Schmidt, K.; Toney, M. F.; Kramer, E. J.; Bazan, G. C. *Adv. Mater.* **2011**, *23*, 2284−2288.

(60) Pensack, R. D.; Guo, C.; Vakhshouri, K.; Gomez, E. D.; Asbury, J. B. *J. Phys. Chem. C* **2012**, *116*, 4824−4831.

(61) Bernardo, B.; Cheyns, D.; Verreet, B.; Schaller, R. D.; Rand, B. P.; Giebink, N. C. *Nat. Commun.* **2014**, *5*, 3245.

(62) Bansal, N.; Reynolds, L. X.; MacLachlan, A.; Lutz, T.; Ashraf, R. S.; Zhang, W.; Nielsen, C. B.; McCulloch, I.; Rebois, D. G.; Kirchartz, T.; Hill, M. S.; Molloy, K. C.; Nelson, J.; Haque, S. A. *Sci. Rep.* **2013**, *3*, 1531.

(63) Haskal, E. I.; Shen, Z.; Burrows, P. E.; Forrest, S. R. *Phys. Rev. B* **1995**, *51*, 4449−4462.

(64) Shen, Z.; Forrest, S. R. *Phys. Rev. B* **1997**, *55*, 10578−10592.

(65) Liu, T.; Troisi, A. *Adv. Mater.* **2013**, *25*, 1038−1041.

Supporting Information

The Effect of Solvent Additive on the Charge Generation and Photovoltaic Performance of a Solution-Processed Small Molecule:Perylene Diimide Bulk Heterojunction Solar Cell

Alexander Sharenko,[†‡‖] Dominik Gehrig,[§‖] Frédéric Laquai,[§*] Thuc-Quyen Nguyen[‡#⊥*]

[†]Materials Department, University of California, Santa Barbara, CA, United States
[‡]Center for Polymers and Organic Solids, University of California, Santa Barbara, CA, United States
[§] Max Planck Research Group for Organic Optoelectronics , Max Planck Institute for Polymer Research, Mainz, Germany
[#]Department of Chemistry, Faculty of Science, King Abdulaziz University, Jeddah, Saudi Arabia
[⊥]Department of Chemistry and Biochemistry, University of California, Santa Barbara, CA, United States
[‖]These authors contributed equally

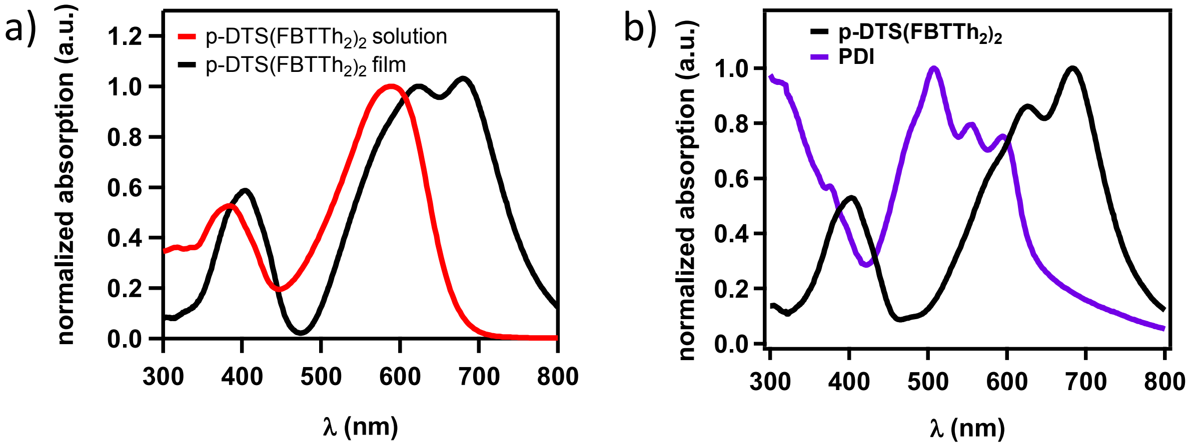

Figure S1. a) Solution and film absorption spectra of p-DTS(FBTTh$_2$)$_2$. Solution spectra in chloroform and film cast from chlorobenzene. b) Film absorption spectra of p-DTS(FBTTh$_2$)$_2$ and PDI cast from chlorobenzene with 0.4% DIO.

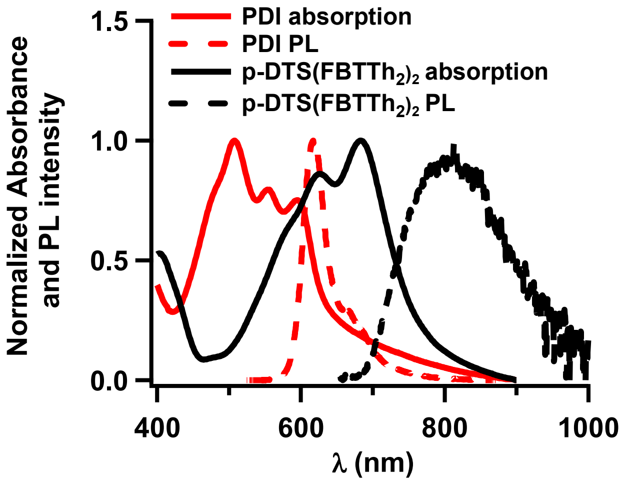

Figure S2. UV-Vis absorption spectra and PL spectrum of p-DTS$(FBTTh_2)_2$ and PDI films. The significant overlap of p-DTS$(FBTTh_2)_2$'s absorption spectrum and PDI's PL spectrum enables the possibility of Förster resonance energy transfer from PDI to p-DTS$(FBTTh_2)_2$.

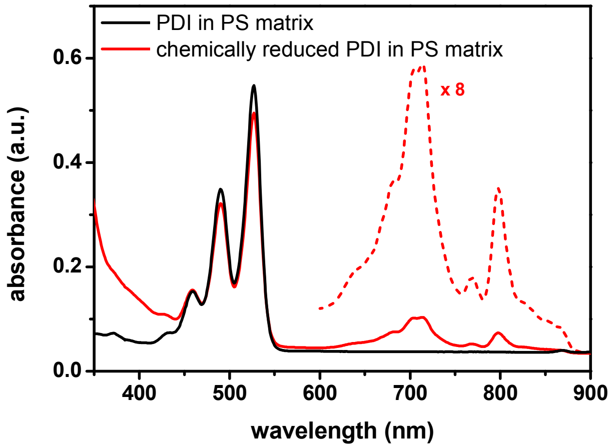

Figure S3. UV-Vis absorption spectra of PDI in a polystyrene (PS) matrix and chemically-reduced PDI in a PS matrix. PDI was chemically reduced in a chlorobenzene solution using 10 equivalents of cobaltocene.

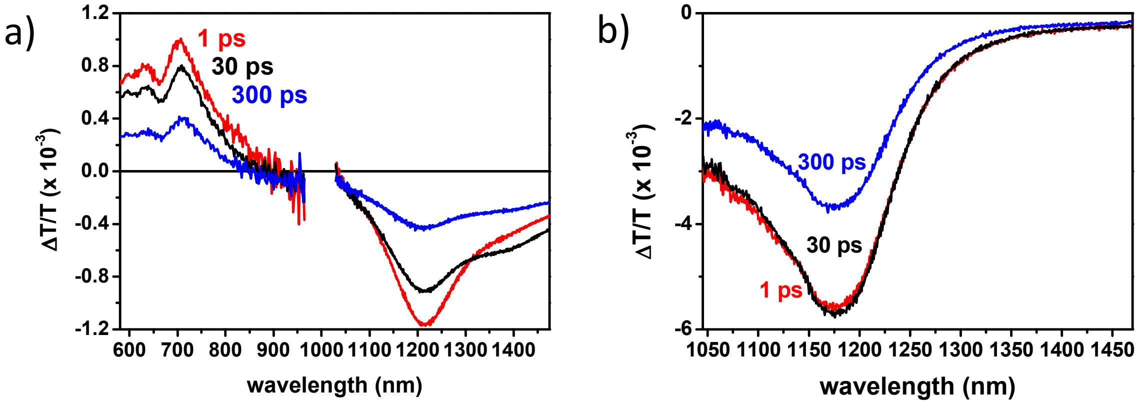

Figure S4. Transient absorption spectra of a) pristine p-DTS$(FBTTh_2)_2$ film and b) p-DTS$(FBTTh_2)_2$ in chlorobenzene.

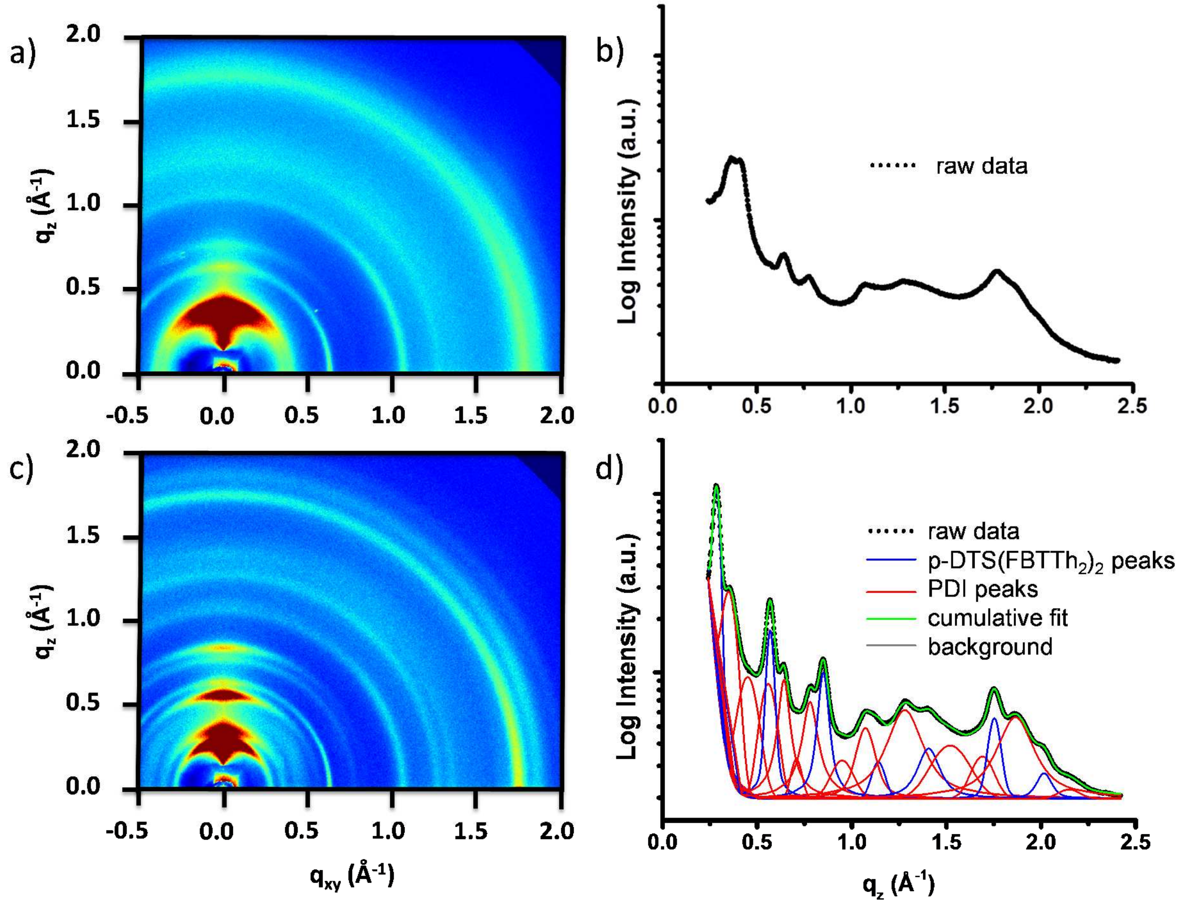

Figure S5. 2D GIWAXS images (a, c) and out of plane (chi = 75° to 105°) cake segments (b, d) of p-DTS(FBTTh$_2$)$_2$:PDI BHJ film processed without (a, b) and with (c, d) 0.4 vol. % DIO.

GIWAXS measurements were performed at Stanford Synchrotron Radiation Lightsource beamline 11-3 using a photon energy of 12.7 keV with a sample to detector distance of 400 mm. Experiments were performed under a helium environment to minimize background scattering and sample damage from the x-ray beam at an incident angle of 0.12° (above the critical angle of the BHJ blend, but below the critical angle of the substrate to ensure probing of the BHJ blend and not the substrate). Images were collected with a MAR-345 2D image plate and processed with the software package WxDiff, provided by Dr. Stefan Mannsfeld. Samples for GIWAXS were spin-cast from solutions identical to those used for BHJ OPV device fabrication onto silicon substrates previously coated with PEDOT:PSS to mimic a solar cell architecture. Silicon substrates were used instead of ITO to reduce background scattering from the substrate.

p-DTS(FBTTh$_2$)$_2$ and PDI peaks were indexed, deconvoluted and fit with pseudo-voigt peak functions using their respective single crystal structures as reference.[1,2] Background scattering was fit using a biexponential function. The full-width-at-half-maximum (FWHM) of PDI's (200) peak ($q_z = 0.35$ Å^{-1}) was used for calculation of PDI's crystal correlation length (CCL). The (001) peak ($q_z = 0.28$ Å^{-1}) of p-DTS(FBTTh$_2$)$_2$ was used to calculate a CCL of 15.5 ± 0.3 nm for p-DTS(FBTTh$_2$)$_2$. Scherrer's equation was used to calculate the CCL[3]:

$$CCL = \frac{2\pi}{FWHM}$$

The GIWAXS data of the blend cast without DIO lacks several of the well-defined p-DTS(FBTTh$_2$)$_2$ and PDI peaks exhibited in the GIWAXS data of the blend with DIO. This observation largely supports our interpretation of the UV-Vis data included in the main text. The GIWAXS of the blend without DIO, however, appears to contain some peaks partially obscured by broadening and/or background amorphous scattering. The presence of these peaks is suggestive that some amount of solid state order exists even in the blend without DIO. As GIWAXS is an x-ray diffraction technique, however, it is only sensitive to crystalline regions of the film capable of satisfying Bragg's condition and is therefore severely biased towards characterization of crystalline order within a film, regardless of the fraction of film containing such order. Alternatively, UV-Vis probes all regions of the film (regardless of solid state order) and the resulting UV-Vis spectrum is therefore representative of the dominant morphological features in the film.[4] Because of the wealth of information about molecular order associated with UV-Vis data[4], its ability to probe both ordered and disordered regions of a film, and the unambiguous and well established indicators of structural order in the UV-Vis spectra of both p-DTS(FBTTh$_2$)$_2$[1,5] and PDI[6,7], we are able to use UV-Vis spectroscopy as the more insightful tool to qualitatively characterize the overall relative structural order in p-DTS(FBTTh$_2$)$_2$:PDI BHJ films.

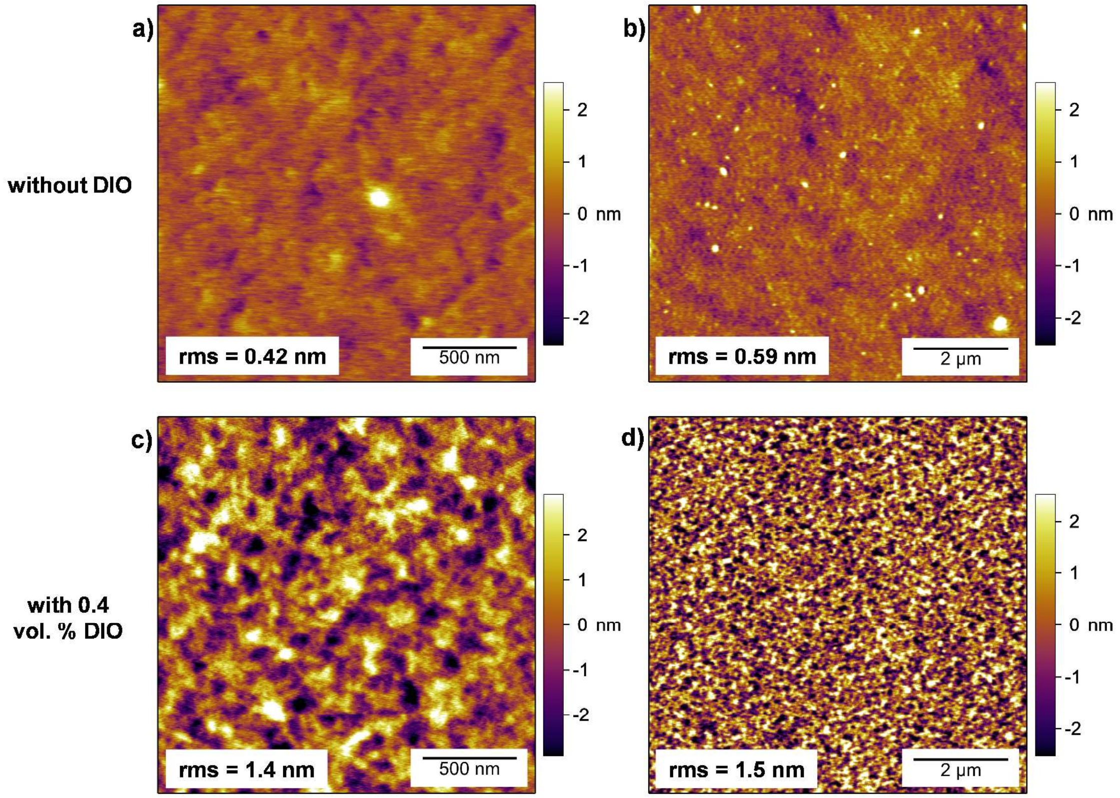

Figure S6. Atomic force microscopy topography images of p-DTS(FBTTh$_2$)$_2$:PDI BHJ blends processed without (a, b) and with (c, d) 0.4 vol. % DIO. The increase in surface roughness associated with use of DIO is consistent with an increase in film crystallinity as inferred from UV-Vis spectroscopy.[8]

Table 1. Complete results from modeling transient absorption excitation intensity dependent PIA dynamics.[9]

Parameter	**Result from model**
Fraction of non-geminate decay (f)	75.7%
Order of non-geminate decay (λ+1)	1.61
Non-geminate decay rate (γ)	$1.32 \text{ x } 10^{-21} (\text{cm}^3)^{\lambda} \text{ s}^{-1}$
Effective non-geminate recombination rate (γ_{eff})	$4.27 \text{ x } 10^{-12} \text{ cm}^3\text{s}^{-1}$
Bimolecular recombination rate	$8.25\text{x } 10^{8} \text{ cm}^3\text{s}^{-1}$

References

(1) Love, J.; Proctor, C.; Liu, J.; Takacs, C.; Sharenko, A.; van der Poll, T.; Heeger, A.; Bazan, G.; Nguyen, T.-Q. *Adv. Funct. Mater.* **2013**, *23*, 5019–5026.

(2) Maniukiewicz, W.; Bojarska, J.; Olczak, A.; Dobruchowska, E.; Wiatrowski, M. *Acta Crystallogr.* **2010**, *66*, o2570–o2571.

(3) *Methods of X-Ray and Neutron Scattering in Polymer Science*; Roe, R. J., Ed.; Oxford University Press, Inc., 2000.

(4) Salleo, A.; Kline, R. J.; DeLongchamp, D. M.; Chabinyc, M. L. *Adv. Mater.* **2010**, *22*, 3812–3838.

(5) Van der Poll, T. S.; Love, J. A.; Nguyen, T.-Q.; Bazan, G. C. *Adv. Mater.* **2012**, *24*, 3646–3649.

(6) Würthner, F. *Chem. Commun.* **2004**, 1564–1579.

(7) Balakrishnan, K.; Datar, A.; Oitker, R.; Chen, H.; Zuo, J.; Zang, L. *J. Am. Chem. Soc.* **2005**, *127*, 10496–10497.

(8) Verploegen, E.; Mondal, R.; Bettinger, C. J.; Sok, S.; Toney, M. F.; Bao, Z. *Adv. Funct. Mater.* **2010**, *20*, 3519–3529.

(9) Howard, I. A.; Mauer, R.; Meister, M.; Laquai, F. *J. Am. Chem. Soc.* **2010**, *132*, 14866–14876.

4.4 p-DTS(FBTTh$_2$)$_2$:Fullerene Solar Cells

The article "High open-circuit voltage small-molecule p-DTS(FBTTh$_2$)$_2$:ICBA bulk heterojunction solar cells – morphology, excited-state dynamics, and photovoltaic performance" was published in the Journal of Material Chemistry C and is available online since November 27th, 2014. The article is reprinted with permission (open access) from reference [205]. Copyright (2015) Royal Society of Chemistry.

Journal of
Materials Chemistry A

PAPER

View Article Online
View Journal | View Issue

Cite this: *J. Mater. Chem. A*, 2015, **3**, 1530

High open-circuit voltage small-molecule p-DTS(FBTTh$_2$)$_2$:ICBA bulk heterojunction solar cells – morphology, excited-state dynamics, and photovoltaic performance†

Aung Ko Ko Kyaw,‡[a] Dominik Gehrig,‡[b] Jie Zhang,[a] Ye Huang,[c] Guillermo C. Bazan,[c] Frédéric Laquai*[b] and Thuc-Quyen Nguyen*[c]

Received 18th November 2014
Accepted 18th November 2014

DOI: 10.1039/c4ta06256f

www.rsc.org/MaterialsA

The photovoltaic performance of bulk heterojunction solar cells using the solution-processable small molecule donor 7,7′-(4,4-bis(2-ethylhexyl)-4*H*-silolo[3,2-*b*:4,5-*b*′]dithiophene-2,6-diyl)bis(6-fluoro-4-(5′-hexyl-[2,2′-bithiophene]-5-yl)benzo[c][1,2,5]thiadiazole) (p-DTS(FBTTh$_2$)$_2$ in combination with indene-C60 bis-adduct (ICBA) as an acceptor is systematically optimized by altering the processing conditions. A high open-circuit voltage of 1 V, more than 0.2 V higher than that of a p-DTS(FBTTh$_2$)$_2$:PC$_{70}$BM blend, is achieved. However, the power conversion efficiency remains around 5% and thus is lower than ~8% previously reported for p-DTS(FBTTh$_2$)$_2$:PC$_{70}$BM. Transient absorption (TA) pump–probe spectroscopy over a wide spectral (Vis-NIR) and dynamic (fs to μs) range in combination with multivariate curve resolution analysis of the TA data reveals that generation of free charges is more efficient in the blend with PC$_{70}$BM as an acceptor. In contrast, blends with ICBA create more coulombically bound interfacial charge transfer (CT) states, which recombine on the sub-nanosecond timescale by geminate recombination. Furthermore, the ns to μs charge carrier dynamics in p-DTS(FBTTh$_2$)$_2$:ICBA blends are only weakly intensity dependent implying a significant contribution of recombination from long-lived CT states and trapped charges, while those in p-DTS(FBTTh$_2$)$_2$:PC$_{70}$BM decay *via* an intensity-dependent recombination mechanism indicating that spatially separated (free) charge carriers are observed, which can be extracted as photocurrent from the device.

1. Introduction

The open-circuit voltage (V_{OC}) is one of the figures of merit determining the power conversion efficiency (PCE) of solar cells. It is also a critical parameter in electrochemical reactions such as photocatalytic splitting of water into hydrogen and oxygen using solar fuels.[1–4] What exactly determines the V_{OC} is still intensely investigated. In fact several factors influencing the V_{OC} of a bulk-heterojunction (BHJ) solar cell have already been suggested, for instance the work-function difference of the device electrodes according to the metal–insulator–metal model,[5–7] Fermi level pinning between the metal electrode and the fullerene reduction potential,[8] the surface dipoles at the interfaces,[9,10] the formation of ground-state charge-transfer complexes between the acceptor and donor material,[11] and shunts in the photoactive layer causing leakage currents.[12] However, it appears that the V_{OC} mainly depends on the energy offset between the highest occupied molecular orbital (HOMO) of the donor and the lowest unoccupied molecular orbital (LUMO) of the acceptor.[8,13]

Based on this rather simple and empiric design rule, donor materials with deep HOMO levels have been designed to increase the V_{OC} of BHJ organic solar cells. The V_{OC} of the heavily researched poly(3-hexylthiophene):phenyl-C61-butyric acid methyl ester blend (P3HT:PC$_{60}$BM) is only 0.6 V (in fact it varies between 0.58 V and 0.67 V depending on the film processing conditions and interfacial layer structure)[14,15] as P3HT has a rather high HOMO level of −5.2 eV, whereas conjugated polymers with lower HOMO levels such as poly(*N*-9″-heptadecanyl-2,7-carbazole-*alt*-5,5-(4′,7′-di-2-thienyl-2′,1′,3′-benzothiadiazole)) (PCDTBT) and poly[2,3-bis-(3-octyloxyphenyl)quinoxaline-5,8-diyl-*alt*-thiophene-2,5-diyl] (PTQ1) (HOMO levels of −5.5 eV and −5.7 eV, respectively) show significantly higher

---

[a] *Institute of Materials Research and Engineering (IMRE), Agency for Science Technology and Research (A*STAR), Singapore 117602, Republic of Singapore*

[b] *Max Planck Research Group for Organic Optoelectronics, Max Planck Institute for Polymer Research, Ackermannweg 10, D-55128 Mainz, Germany. E-mail: laquai@mpip-mainz.mpg.de*

[c] *Center for Polymers and Organic Solids, Department of Chemistry and Biochemistry, University of California at Santa Barbara, Santa Barbara, California 93106-5090, USA. E-mail: quyen@chem.ucsb.edu*

† Electronic supplementary information (ESI) available: Further details are given in Fig. S1–S12. See DOI: 10.1039/c4ta06256f

‡ These authors contributed equally to this work.

V_{OC}s of ~0.88 V and 0.89 V, respectively.[16,17] Furthermore, fullerene bis-adduct acceptors have been used to increase the V_{OC}, because of their higher LUMO level compared to the ubiquitously used $PC_{60}BM$. For instance, replacing $PC_{60}BM$ with indene-C60 bis-adduct (ICBA) (LUMO levels around −3.74 eV *vs.* −3.91 eV for $PC_{60}BM$) significantly increases the V_{OC} of a P3HT-based solar cell from 0.58 V to 0.84 V.[18–21] However, there are limitations in the tunability of energy levels of materials. Firstly, lowering the HOMO level of the donor without changing its LUMO level increases the optical bandgap of the donor and hence blue-shifts the absorption spectrum of the photoactive layer thereby reducing the spectral overlap with the solar radiation. Secondly, if the LUMO level of the donor is lowered concomitantly to maintain the bandgap, then the effective energy offset between the LUMO levels of the donor and acceptor decreases and the probability of exciton dissociation into free charges can be reduced.[22] Similarly, lifting the LUMO level of the acceptor to increase V_{OC} also decreases the energy offset and can reduce the yield of free charges. However, the minimum energy offset required to overcome the exciton binding energy for efficient charge separation is still controversially debated and is a subject of recent studies and reports vary from 0.1 eV to 0.5 eV depending on the donor properties.[23,24] Furthermore, the reduction of the energy offset leads to the condition, in which the energy level of the triplet state is lower than that of the interfacial charge transfer state, resulting in relaxation of the charge transfer state to the triplet state.[25] Thus, while the V_{OC} of some BHJ systems has reached values higher than 1 V, the fill factor (FF) and PCE often remained low.[26,27] In fact, a BHJ system with decent efficiency (PCE > 5%) and V_{OC} approaching 1 V is a very rare case.[28]

Recently, we reported a BHJ solar cell with a PCE of ~8% and a V_{OC} of ~0.78 V using a small molecule (SM) donor, namely 7,7′-(4,4-bis(2-ethylhexyl)-4*H*-silolo[3,2-*b*:4,5-*b*′]dithiophene-2,6-diyl)bis(6-fluoro-4-(5′-hexyl-[2,2′-bithiophene]-5-yl)benzo[*c*]-[1,2,5]thiadiazole) (p-DTS(FBTTh$_2$)$_2$), and phenyl-C71-butyric acid methyl ester ($PC_{70}BM$) as an acceptor.[29] The energy offset between the LUMO levels of p-DTS(FBTTh$_2$)$_2$ and $PC_{70}BM$, however, is very large (~1 eV), as illustrated in Fig. 1. Thus, a significant fraction of the photon energy is lost in the charge transfer process. However, there is huge potential to improve the V_{OC} by reducing the energy offset between the LUMO levels of the donor and acceptor in this BHJ system. Hence, in the present study we investigate the photovoltaic performance of blends of p-DTS(FBTTh$_2$)$_2$ and ICBA, as the ICBA has a higher LUMO level than the $PC_{70}BM$ previously used. We demonstrate a high V_{OC} (~1 V) with a PCE of ~5% using the p-DTS(FBTTh$_2$)$_2$:ICBA system. Despite a more than 200 mV improvement in V_{OC}, the PCE of the p-DTS(FBTTh$_2$)$_2$:ICBA system is lower than that of our previously reported p-DTS(FBTTh$_2$)$_2$:$PC_{70}BM$ system mainly due to a low FF. Transient absorption spectroscopy covering a wide wavelength region (that is from the visible to the near-infrared) and spanning a wide dynamic range (from 100 fs to several μs) reveals that the formation of weakly bound charge transfer (CT) states in the p-DTS(FBTTh$_2$)$_2$:ICBA system, and their subsequent recombination, plus trap-assisted recombination of free charges are the main reasons for the low FF.

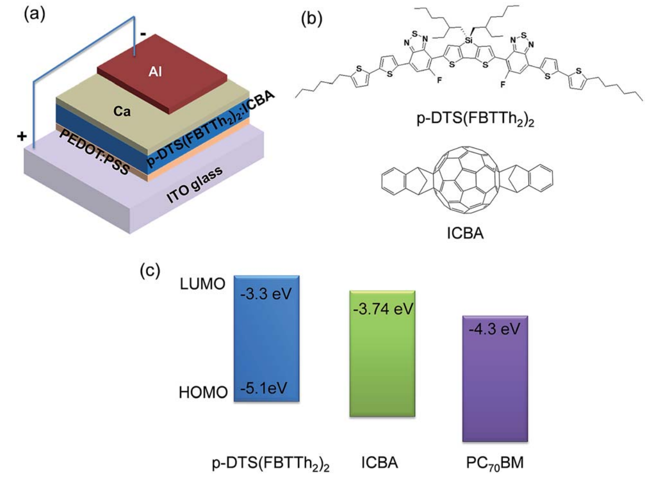

Fig. 1 Device structure of an organic solar cell with p-DTS(FBTTh$_2$)$_2$:ICBA blend used in this study (a). Molecular structure (b) and energy level (c) of p-DTS(FBTTh$_2$)$_2$ and ICBA, respectively. LUMO level of $PC_{70}BM$ is shown in (c) for comparison with ICBA.

2. Results and discussion

2.1. Photovoltaic performance of p-DTS(FBTTh$_2$)$_2$:ICBA blends

In this section, we present the photovoltaic performance of p-DTS(FBTTh$_2$)$_2$:ICBA blends prepared under various processing conditions. The use of solvent additives is an effective and common method to influence the nanomorphology of the BHJ. To examine the effect of solvent additives on the morphology and efficiency of p-DTS(FBTTh$_2$)$_2$:ICBA blends, we spin-cast films from solutions containing 0% to 0.6% (v/v%) 1,8-diiodooctane (DIO) and compared the photovoltaic performance of the devices. The photovoltaic parameters of the p-DTS(FBTTh$_2$)$_2$:ICBA solar cells processed with various contents of DIO are listed in Table 1 and their *J–V* characteristics under AM 1.5G irradiation at 100 mW cm^{-2} are shown in Fig. S1, ESI.† The results demonstrate that the device processed without any additive exhibits a PCE of only 3.01% with a short-circuit current density (J_{SC}) of 7.42 mA cm^{-2}, a V_{OC} of 1.017 V and a FF

Table 1 Photovoltaic parameters of devices with various DIO contents in the p-DTS(FBTTh$_2$)$_2$:ICBA blend. The values shown in the table are average results from five devices. The D : A weight ratio is 1.5 : 1 and the total concentration in solution is 35 mg mL^{-1} unless otherwise stated

DIO content	J_{SC} [mA cm^{-2}]	V_{OC} [V]	FF [%]	PCE [%]
0%	7.42	1.017	39.9	3.01
0.2%	8.29	1.012	42.6	3.58
0.4%	9.71	0.963	46.1	4.31
0.6%	8.69	0.956	42.8	3.56

of 39.9%. The device processed with 0.4% DIO shows the best performance with J_{SC} = 9.71 mA cm^{-2}, V_{OC} = 0.963 V, FF = 46.1%, and PCE = 4.31%. The V_{OC} has increased to ~1 V as expected, which represents a 25% increase compared to that of the p-DTS(FBTTh$_2$)$_2$:PC$_{70}$BM blend (~0.8 V).[29,30]

When the 0.4% DIO BHJ film was annealed at 120 °C, the PCE increased to 5.07% with J_{SC} = 10.45 mA cm^{-2}, V_{OC} = 0.962 V and FF = 50.4%. In contrast to other BHJ systems,[31–34] one observes that the figures of merit of the p-DTS(FBTTh$_2$)$_2$:ICBA system are not strongly dependent on the annealing temperature. The PCE remains almost unchanged in the annealing temperature range from 100 °C to 130 °C (Table 2).

While the device processed without DIO exhibits a low PCE (3.01%), its PCE significantly increased to 4.95% with J_{SC} = 9.99 mA cm^{-2}, V_{OC} = 1.0 V and FF = 49.5% after annealing at 100 °C (Table 2). Hence, the PCE of this device (that is without DIO, but with annealing) becomes similar to that of the device prepared with 0.4% DIO and annealing, suggesting that the impact of annealing supersedes the effect of additive in this system. We also investigated the thermal stability of the devices processed without DIO. The PCE changed from 4.95% to 4.78% by varying the temperature from 100 °C to 120 °C. More interestingly, the p-DTS(FBTTh$_2$)$_2$:ICBA system is also less susceptible to a variation in the donor : acceptor (D : A) ratio. We varied the D : A ratio from 1.5 : 1 to 2.3 : 1 resulting in a virtually constant PCE of 4.95% and 4.94%, respectively, as shown in Table 2. Based on the photovoltaic performance, we conclude that the p-DTS(FBTTh$_2$)$_2$:ICBA system is less sensitive to the processing conditions compared to other BHJ systems.

The *J*–*V* characteristics under AM 1.5G irradiation at 100 mW cm^{-2} and the corresponding external quantum efficiency (EQE) spectra of the champion devices fabricated under different processing conditions are shown in Fig. 2. The calculated J_{SC} obtained by integrating the EQE data convoluted with the AM 1.5G solar spectrum deviates only by 1.5% from the experimentally determined value. The maximum EQE of ~60% is obtained between 570 nm and 700 nm. A decrease in EQE at 550 nm and below can be assigned to the poor absorption of C60-based fullerene in the visible region compared to C70-based fullerenes. The *J*–*V* characteristics of the other devices are displayed in Fig. S2–S4, ESI.†

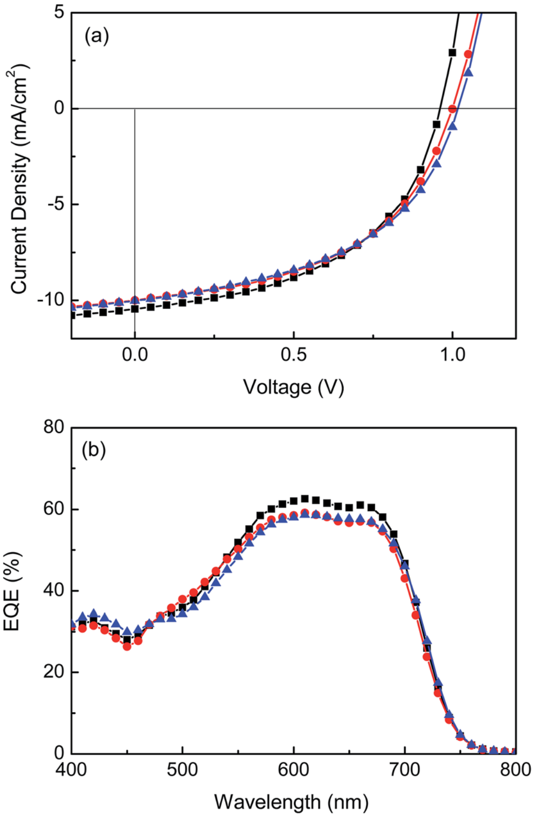

Fig. 2 (a) *J*–*V* characteristics under AM 1.5G irradiation at 100 mW cm^{-2} and (b) EQE spectra of the champion cells fabricated under different processing conditions: (i) D : A = 1.5 : 1, 0.4% DIO and annealed at 120 °C (black square), (ii) D : A = 1.5 : 1, 0% DIO and annealed at 100 °C (red circle) and (iii) D : A = 2.3 : 1, 0% DIO and annealed at 100 °C (blue triangle).

2.2. Morphological characterization of BHJ films

The interpenetration of the acceptor and donor is an important factor in determining the efficiency of a BHJ solar cell. Thus, the nanomorphology of the p-DTS(FBTTh$_2$)$_2$:ICBA BHJ obtained under different processing conditions was studied by tapping mode Atomic Force Microscopy (AFM). Fig. 3 presents the AFM topographic and phase images of as-cast films and films

Table 2 Photovoltaic parameters of devices fabricated from different annealing temperatures and donor : acceptor weight ratios. The values shown in the table are average results from five devices

D : A ratio	Additive	Annealing temperature	J_{SC} [mA cm^{-2}]	V_{OC} [V]	FF [%]	PCE [%]	J_{SC} (calc.) [mA cm^{-2}]	Error [%]
1.5 : 1	0.4% DIO	100 °C	10.30	0.964	49.9	4.95		
		110 °C	10.35	0.962	49.7	4.95		
		120 °C	10.45	0.962	50.4	5.07	10.34	1.05
		130 °C	10.71	0.962	47.8	4.92		
1.5 : 1	Nil	100 °C	9.99	1.000	49.5	4.95	9.97	0.2
		110 °C	9.86	1.013	48.4	4.83		
		120 °C	9.83	1.000	48.6	4.78		
2.3 : 1	Nil	100 °C	10.02	1.017	48.5	4.94	9.99	0.3
		110 °C	10.14	1.000	47.8	4.84		

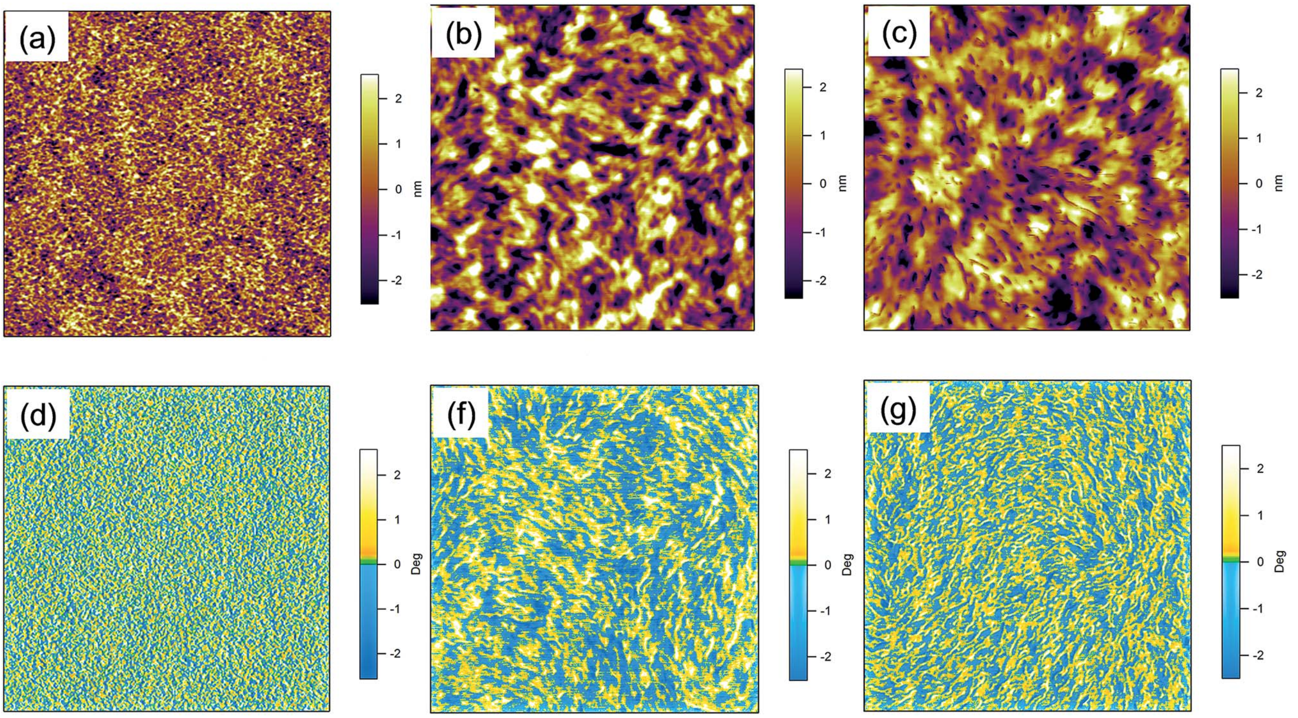

Fig. 3 Taping mode AFM topography (top) and phase (bottom) images of p-DTS(FBTTh$_2$)$_2$:ICBA films fabricated under different processing conditions: as-cast (a & d), 0.4% DIO and annealed at 120 °C (b & f), and 0% DIO and annealed at 100 °C (c & g). D : A ratio is 1.5 : 1 for all films. The scan size is 2 μm × 2 μm.

processed with DIO and/or annealing. The topographic and phase images of as-cast films are featureless with a surface roughness of only ~1 nm (Fig. 3a and d). No obvious sign of phase separation can be identified implying intimate donor and acceptor mixing. The use of DIO and/or thermal annealing resulted in significant changes of the surface topography. Overall, the films processed with DIO and/or annealing reveal rather fine and evenly distributed domains of a size of tens of nanometers in conjunction with continuous interpenetrating networks without any large-scale aggregation of either the donor or the acceptor with a slight increase in the surface roughness (~1.4 nm, Fig. 3b and c). From the phase images (Fig. 3e and f), one observes fiber-like network formation for films processed with DIO and/or thermally annealed films. It is widely accepted that the phase separation must be sufficiently large to create percolation pathways for charge carrier transport, yet small enough to form a large interfacial area for efficient exciton dissociation and charge separation (typically on the order of tens of nanometers). It is likely that the formation of interpenetrating networks of acceptor and donor compounds without large-scale aggregation by the use of DIO and/or annealing fulfils the above conditions, and hence leads to an improved J_{SC}, FF, and PCE.

Since AFM reveals information limited to the surface of the film only, we also probed the morphology of the bulk film by grazing incidence wide angle X-ray scattering (GIWAXS). Fig. 4 presents 2D GIWAXS patterns of as-cast films and films processed with DIO and/or annealing atop of PEDOT:PSS-coated substrates. As shown in Fig. 4, 2D GIWAXS patterns of as-cast films as well as films processed with DIO and/or annealing exhibit a (100) peak as well as higher order scattering peaks ((200) and (300)) along the q_z (normal to the substrate) axis due to a lamella-like layered structure, and the (010) peak along the q_{xy} (parallel to the substrate) axis due to π–π interchain stacking. This implies that p-DTS(FBTTh$_2$)$_2$:ICBA BHJ films have highly ordered edge-on orientation with side chains sitting perpendicular to the substrate and the π-stacking direction is parallel to the substrate, even for the as-cast conditions. The (100) peak at $q_z = 0.288$ Å^{-1} and (010) peak at $q_{xy} = 1.744$ Å^{-1} correspond to the alkyl stacking distance of 21.8 Å and π–π stacking distance of 3.6 Å, respectively (note: the intense peak at $q_{xy} \sim 2.16$ Å^{-1} is caused by scattering from the underlying PEDOT:PSS layer). However, the films processed with DIO and/or annealing have a higher scattering intensity, especially the higher order scattering peaks (200) and (300), associated with both lamella-like layers and π–π stacking, respectively than as-cast films, suggesting that the crystallinity of the film is further improved by using the co-solvent DIO and/or annealing. The crystal correlation length (CCL) which is the estimated crystal size of the films processed with DIO and/or annealing, calculated from the peak width, is ~17 nm, which is in good agreement with the AFM images.

2.3. Comparison with PC$_{70}$BM-based blends

The p-DTS(FBTTh$_2$)$_2$:ICBA system exhibits a PCE of ~5% with a high V_{OC} of ~1 V under optimized conditions. Compared to our previously reported p-DTS(FBTTh$_2$)$_2$:PC$_{70}$BM system, which

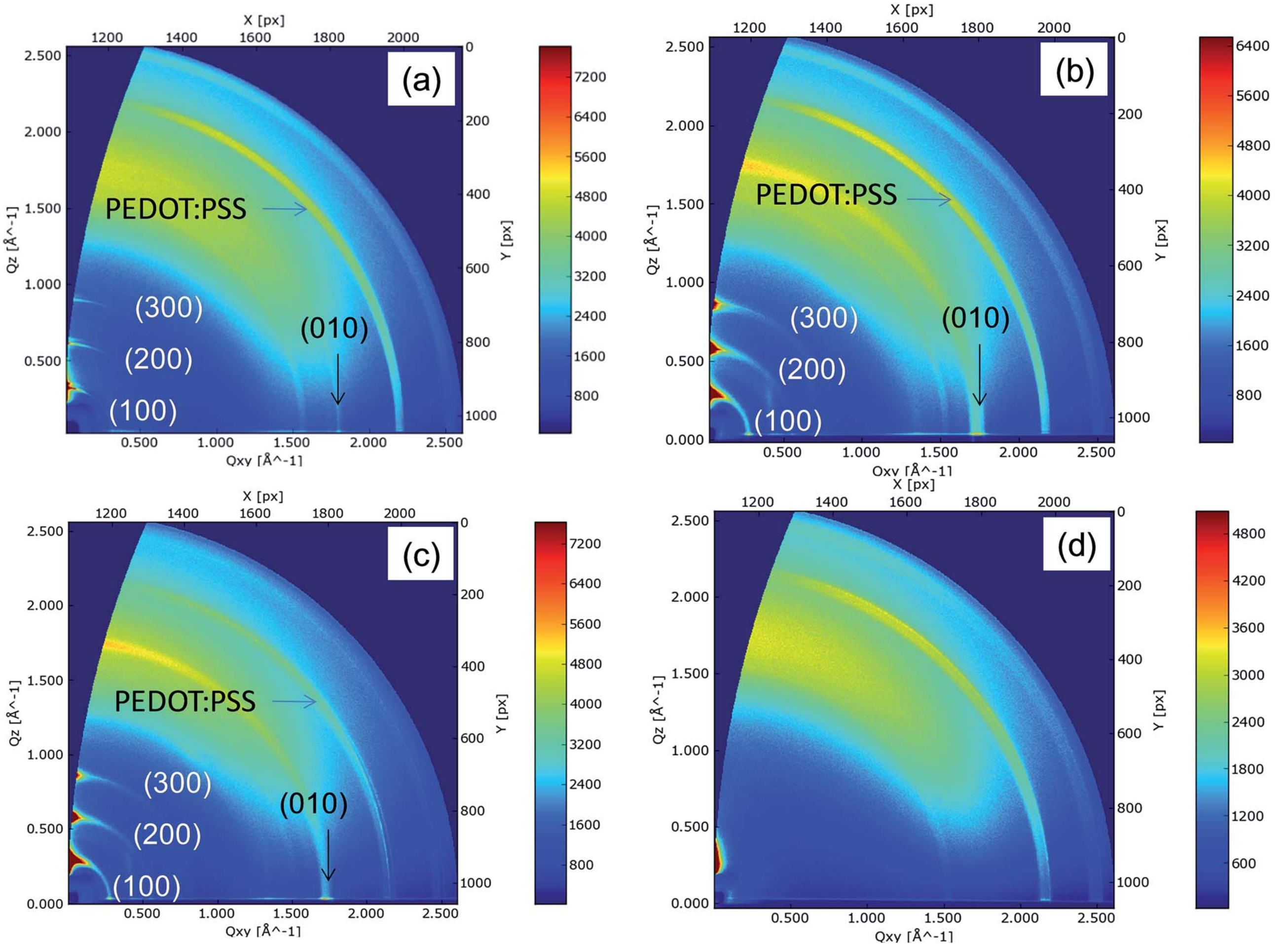

Fig. 4 2D GIWAXS patterns of p-DTS(FBTTh$_2$)$_2$:ICBA films fabricated on the PEDOT:PSS coated substrate under different processing conditions: as-cast (a), 0.4% DIO and annealed at 120 °C (b), 0% DIO and annealed at 100 °C (c). The 2D GIWAXS patterns of the PEDOT:PSS film is shown in (d).

showed a PCE of ~8% with $J_{SC} = 14.2$ mA cm^{-2}, $V_{OC} = 0.775$ V and FF = 72.8%, the PCE of p-DTS(FBTTh$_2$)$_2$:ICBA is still lower even under optimized preparation conditions, despite the more than 0.2 V increase in V_{OC}. The decrease in PCE originates from a low J_{SC} (~10 mA cm^{-2}) as well as moderate FF (~50%). It is straightforward to understand that a lower absorption of the p-DTS(FBTTh$_2$)$_2$:ICBA photoactive layer compared to that of p-DTS(FBTTh$_2$)$_2$:PC$_{70}$BM, due to the lack of the absorption of ICBA in the visible region, causes a decrease in J_{SC} (Fig. S5 and S6, ESI†). However, the origin of the lower FF is not so clear. The dark J–V curve of a p-DTS(FBTTh$_2$)$_2$:ICBA device exhibited a high rectification ratio and low leakage current in turn ensuring that there is a high quality interface between the BHJ photoactive layer and the electrodes and that the low FF is not due to the interfacial layers (Fig. S7, ESI†). Thus, to gain insight into the origin of the low FF in the p-DTS(FBTTh$_2$)$_2$:ICBA system, we studied the excited states dynamics and related charge carrier recombination mechanisms of these two systems by ultrafast and ns to μs transient absorption spectroscopy.

2.4. Charge generation in p-DTS(FBTTh$_2$)$_2$:ICBA and p-DTS(FBTTh$_2$)$_2$:PC$_{70}$BM

All samples were excited at 700 nm, that is into the absorption band of the p-DTS(FBTTh$_2$)$_2$ donor molecules. The TA spectra of both blends are compared in Fig. 5. All TA spectra exhibit a

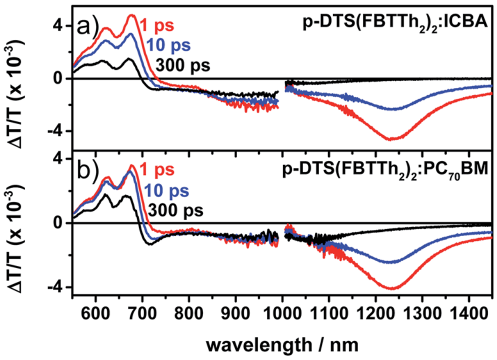

Fig. 5 Spectra of (a) p-DTS(FBTTh$_2$)$_2$:ICBA and (b) p-DTS(FBTTh$_2$)$_2$:PC$_{70}$BM after excitation at 700 nm with 8.1/2.4 μJ cm^{-2} (a) and 4.1/2.3 μJ cm^{-2} (b), respectively.

ground-state bleach present immediately after excitation. In addition to the ground-state bleach, both films show a negative feature peaking at 1250 nm at early delay times, which we assigned to exciton-induced absorption of the singlet excited-state of p-DTS$(FBTTh_2)_2$. This assignment is further confirmed by TA measurements on a neat p-DTS$(FBTTh_2)_2$ film (Fig. S8, ESI†). In both films, a photoinduced absorption at shorter wavelengths, precisely between 900 and 1100 nm, appears on a timescale of tens to hundreds of picoseconds, which we assigned to the charge carrier-induced absorption of p-DTS$(FBTTh_2)_2$ molecules (see Fig. 5).

A noteworthy difference between the two investigated blends is the occurrence of a peak at 720 nm. This is attributed to electro-absorption (EA) as reported and discussed recently by Friend and co-workers.[35] They demonstrated that a large EA signal is caused by long-range charge separation across the donor–acceptor interface and is therefore an indication of the formation of free charge carriers. Clearly, this feature is less pronounced in p-DTS$(FBTTh_2)_2$:ICBA blends compared to p-DTS$(FBTTh_2)_2$:$PC_{70}BM$ blends. Thus, it appears that blends containing $PC_{70}BM$ exhibit more efficient generation of spatially separated (free) charges compared to ICBA blends. We analyzed the TA data by means of multivariate curve resolution (MCR) analysis as recently reviewed by us[36] and also applied to other donor : acceptor systems.[37] The transition of the initial excitonic state (component 1) to the charge-separated state (component 2) can be clearly seen as shown in Fig. 6. Fitting the concentration profiles obtained by MCR analysis showed an inverse rate constant between 10 and 40 ps, depending on the excitation intensity used.

This is consistent with TA measurements in the near-infrared (NIR) spectral region on the ps to ns timescale, where the ICBA sample showed a fast and intensity-independent decay in the spectral region around 1050 nm, which is related to charge-induced absorption as shown in the upper panel of Fig. 7. A straightforward explanation for this observation is the geminate recombination of tightly bound CT states at the interface, which did not manage to split into free charge carriers. In contrast, the $PC_{70}BM$ sample showed a rather constant TA signal at low excitation intensities. This is further supported by MCR analysis of the NIR TA data, which is presented in Fig. S9, ESI.† Component 1 is assigned to singlet exciton-induced absorption in agreement with measurements on the pristine donor material (see Fig. S8, ESI†). Component 2 is assigned to charge-induced absorption according to spectra obtained from a chemically oxidized p-DTS$(FBTTh_2)_2$ film (see Fig. S10, ESI†). From the MCR analysis it appears that only a small fraction of charges recombine on the early timescale up to 4 ns at low excitation densities in the p-DTS$(FBTTh_2)_2$:$PC_{70}BM$ blend. However, we note that the ground-state bleach does not remain constant on the same timescale. This indicates that either a fraction of the singlet excitons decay without being quenched at the interface or during the charge transfer process at the interface or alternatively that a negative charge-induced absorption signal is superimposed on the ground-state bleach and hence reduces the positive ground-state bleach signal. This interpretation is supported by MCR analysis of the visible data as shown in Fig. 6. Here, component 2 is assigned to the spatially separated charges, as the EA signal could clearly be observed. Component 1 is assigned to p-DTS$(FBTTh_2)_2$ excitons with a ground-state bleach and additionally a strong contribution from the stimulated emission ranging from 750–850 nm. In contrast to the rather constant signal observed for p-DTS$(FBTTh_2)_2$:$PC_{70}BM$, the concentration profile of the second (charge carrier-related) component in p-DTS$(FBTTh_2)_2$:ICBA decreases by 50–70% on the short timescale.

The TA data also allowed us to draw some conclusions on the nanoscale morphology of the investigated samples. The evolution of the spectra at the 0–0-transition on the short timescale (see lower panels of Fig. S11, ESI†) as well as the evolution of the charge-induced absorption peak obtained by MCR analysis from both the visible and the NIR data (Fig. 6 and S9 ESI,† lower panels, grey solid lines) implies that exciton diffusion plays a more dominant role in p-DTS$(FBTTh_2)_2$:$PC_{70}BM$ blends compared to p-DTS$(FBTTh_2)_2$:ICBA, as the respective maxima are reached after a longer delay time in the $PC_{70}BM$ containing blends. A further indication is the amplitude of the charge carrier-induced absorption observed directly after excitation and obtained by MCR analysis (lower panels of Fig. S9, ESI†).

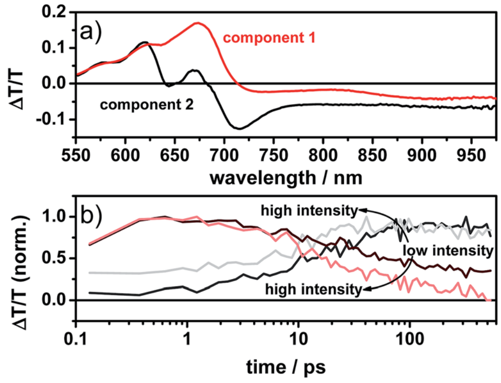

Fig. 6 (a) Spectra and (b) concentration profiles according to MCR-ALS analysis of p-DTS$(FBTTh_2)_2$:$PC_{70}BM$.

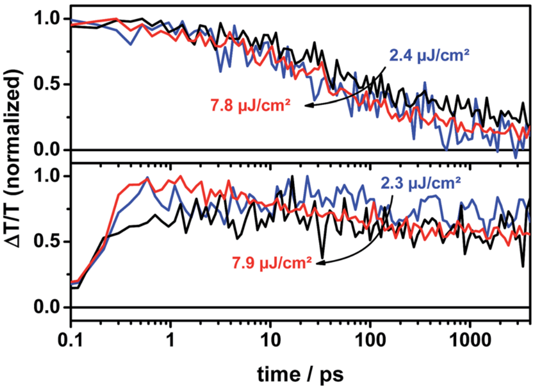

Fig. 7 Kinetics of p-DTS$(FBTTh_2)_2$:ICBA (upper panel) and p-DTS$(FBTTh_2)_2$:$PC_{70}BM$ (lower panel) tracked at 1025–1075 nm (charge induced absorption).

The initial carrier-induced absorption in p-DTS(FBTTh$_2$)$_2$:PC$_{70}$BM is below 25% with respect to the maximum charge carrier concentration at later times, whereas in p-DTS(FBTTh$_2$)$_2$:ICBA blends more than 50% of the signal is obtained from the very beginning suggesting a more intimate mixing of donor and acceptor domains and thus a larger fraction of ultrafast charge transfer. This is supported by the AFM images and GIWAXS experiments as presented above. In fact, the domain size in the p-DTS(FBTTh$_2$)$_2$:ICBA system is ~17 nm, whereas p-DTS(FBTTh$_2$)$_2$:PC$_{70}$BM blends show domain sizes of up to 40 nm as reported recently.[38] This can be explained by the stronger tendency of PC$_{70}$BM to cluster and crystallize as the steric hindrance introduced by the side groups is less pronounced than in ICBA. We note also that Gelinas *et al.* recently observed two charge generation pathways for p-DTS(FBTTh$_2$)$_2$:PC$_{70}$BM blends – an ultrafast component contributing about 70% weight with an inverse rate constant of ~82 fs and a second component contributing 30% of the amplitude, which was diffusion-limited and had an inverse rate constant of ~22 ps. A very similar inverse rate constant of 26.6 ps is also observed in our TA measurements, however, only at the highest excitation fluence, while lower excitation fluences resulted in values as high as 44.4 ps. This is indicative of some exciton-exciton annihilation. The faster femtosecond component could not be resolved by our setup, as it is below the temporal resolution of ~200 fs. However, MCR analysis suggested a smaller fraction of ultrafast charge generation, as the initial signal amplitude related to charges is below 25%.

2.5. Charge recombination in p-DTS(FBTTh$_2$)$_2$:ICBA and p-DTS(FBTTh$_2$)$_2$:PC$_{70}$BM

On the ns to μs timescale the TA spectra exhibit similar features as on the ps to ns timescale, specifically the EA signal is also observed (see Fig. 8). The EA signal is still more pronounced in the case of p-DTS(FBTTh$_2$)$_2$:PC$_{70}$BM blends, again indicating that a higher fraction of free charge carriers contribute to the signal in the more efficient device.

Furthermore, the TA signal of p-DTS(FBTTh$_2$)$_2$:ICBA in the spectral range between 1055 and 1080 nm is significantly longer-lived (up to 10 μs) and its decay is only weakly intensity dependent over the entire dynamic range (Fig. 9, upper panel). In contrast, the TA signal of p-DTS(FBTTh$_2$)$_2$:PC$_{70}$BM is vanished after 1 μs and shows a strongly intensity dependent decay (Fig. 9, lower panel). It has been reported previously that ICBA blends tend to form trapped CT states at the interface that are loosely bound, but in which charges still experience their mutual coulombic attraction.[39] Decay times between 60 and 100 ns were reported for this type of geminate recombination. Additionally, the reduced tendency to aggregate, which is inherent to ICBA compared to PCBM, can lead to the formation of small isolated fullerene domains. CT states formed within these domains also decay *via* a quasi-geminate recombination mechanism.[40] Aggregated fullerene domains have also been assigned to be "energetic sinks" that drive charge separation in donor–acceptor blends. ICBA largely lacks this type of thermodynamic driving force thus reducing efficient charge generation.[41] Taking the extended lifetime into account, losses *via* recombination of trapped CT states appear to be in p-DTS(FBTTh$_2$)$_2$:ICBA blends.

Nonetheless, both blends produce a relatively high amount of extractable charge carriers as confirmed by a PCE exceeding 5%. This is supported by the dynamics of the photo-induced absorption (PIA) between 720 and 1000 nm (see lower panels of Fig. S12, ESI†). Here, both blends show intensity dependent dynamics. The discrepancy between intensity dependent and intensity independent dynamics observed for different spectral regions might result from convoluted free as well as bound charge-induced absorption spectra. Interestingly, both blends show only a weak intensity dependence of the dynamics of the ground-state bleaching (see the upper panel of Fig. S12, ESI†).

The ns to μs data of the p-DTS(FBTTh$_2$)$_2$:PC$_{70}$BM blend was further analyzed using a previously reported two-pool model that combines an intensity independent geminate decay of coulombically bound CT states (first pool) and an intensity dependent non-geminate decay of spatially separated charges (second pool). The fit results are displayed in Fig. 10, where the open symbols represent the experimentally measured data and the solid lines correspond to the fits of the data according to the two pool model. However, this model could not be applied to the p-DTS(FBTTh$_2$)$_2$:ICBA. While some intensity dependence

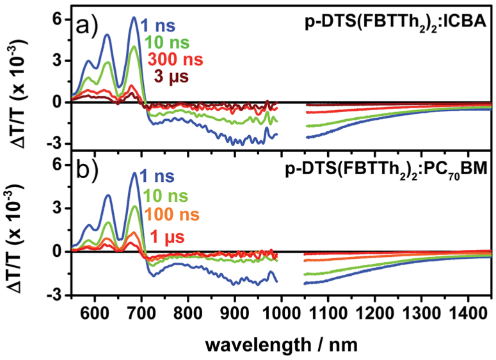

Fig. 8 Spectra of (a) p-DTS(FBTTh$_2$)$_2$:ICBA and (b) p-DTS(FBTTh$_2$)$_2$:PC$_{70}$BM after excitation with 532 nm (9.5 μJ cm^{-2} and 5.5 μJ cm^{-2} respectively).

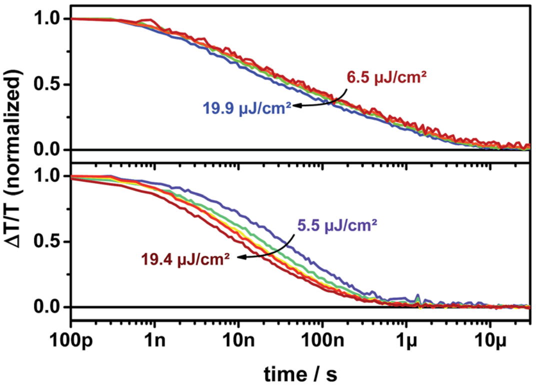

Fig. 9 Kinetics of p-DTS(FBTTh$_2$)$_2$:ICBA (upper panel) and p-DTS(FBTTh$_2$)$_2$:PC$_{70}$BM (lower panel) films tracked at 1055–1080 nm.

was observed in the range of 900–950 nm, a signal offset was also observed, indicating that the formation of trapped CT states influences the kinetics (see the lower panel of Fig. S12, ESI†) in this spectral range. Therefore, an analysis using only two pools would not be meaningful due to the likely superposition of spectral features from different species with unknown concentrations and cross-sections.

The results obtained for p-DTS(FBTTh$_2$)$_2$:PC$_{70}$BM blends show that a large fraction of free charge carriers are present in the sample after excitation, precisely ~85%, that can, in principle, contribute to the device photocurrent. We note that the fraction of free charge carrier formation of 85% is in line with the high IQE of the blend of around 85% indicating that those charges can be extracted as photocurrent. Furthermore, the inverse geminate recombination rate is determined to be ~2 ns, which is very similar to previously reported lifetimes of geminate pairs in polymer–fullerene blends as they were observed for example in samples prepared with P3HT,[42] PCDTBT,[43] PCPDTBT,[44] and PPE–PPV.[45] The fits also yield an effective bimolecular recombination (BMR) coefficient of 1.25×10^{-11} cm^3 s^{-1} obtained by recalculating the extracted non-geminate recombination coefficient to a bimolecular recombination coefficient at a charge carrier density of 5×10^{15} cm^{-3}. This value is rather high compared to other polymer:fullerene blends, such as P3HT:PC$_{60}$BM or PCDTBT:PC$_{60}$BM,[43] which have BMR coefficients about two to one order of magnitude lower, respectively. Interestingly, charge carrier mobility measurements using the space charge limited current (SCLC) model revealed a rather high and balanced electron and hole mobility of 1.08×10^{-3} cm^2 V^{-1} s^{-1} and 1.20×10^{-3} cm^2 V^{-1} s^{-1}, respectively, in the p-DTS(FBTTh$_2$)$_2$:PC$_{70}$BM blends. In fact, mobilities reported for PCDTBT and P3HT are in the range of 10^{-5} cm^2 V^{-1} s^{-1},[46,47] and thus two orders of magnitude lower than the hole mobility of p-DTS(FBTTh$_2$)$_2$. This could very well explain the larger effective BMR coefficient in p-DTS(FBTTh$_2$)$_2$:PC$_{70}$BM blends as, in principle, charge carriers with a higher mobility more often encounter the donor–acceptor interface where they can recombine. However, the comparably high mobility of charges also explains why the solar cells still exhibit decent efficiencies, despite fast non-geminate recombination. In fact, the high mobility allows fast carrier extraction from the photoactive layer in operating solar cells, thereby shifting the competition between charge carrier extraction and non-geminate recombination towards carrier extraction.

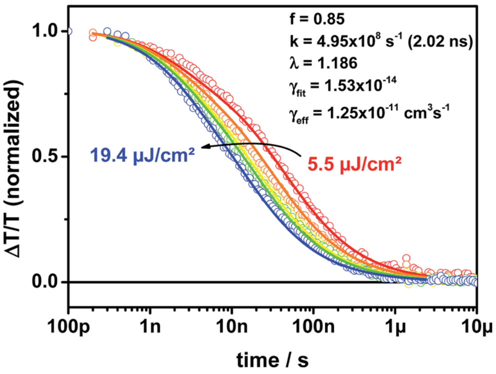

Fig. 10 Fit of the ns to μs data of p-DTS(FBTTh$_2$)$_2$:PC$_{70}$BM (1055–1080 nm) with a two-pool model based on concomitant geminate and non-geminate recombination.

3. Conclusions

We demonstrate high V_{OC} (~1 V) BHJ solar cells with a PCE of ~5% using the p-DTS(FBTTh$_2$)$_2$:ICBA system. While compared to the previously reported p-DTS(FBTTh$_2$)$_2$:PC$_{70}$BM system a more than 0.2 V improvement in V_{OC} was achieved, the overall PCE remains lower than that of the p-DTS(FBTTh$_2$)$_2$:PC$_{70}$BM system. Transient spectroscopic experiments on p-DTS(FBTTh$_2$)$_2$ blended with either PC$_{70}$BM or ICBA revealed that using PC$_{70}$BM as an acceptor leads to more efficient generation of free charges. In addition, soft modeling of the TA data by MCR analysis suggested that charge separation is not only ultrafast but also in large part diffusion-limited. We note that the MCR analysis also provides limited information about the sample morphology and domain sizes, which are in line with AFM and XRD studies on these blends. Furthermore, we find that the charge carriers in p-DTS(FBTTh$_2$)$_2$:PC$_{70}$BM decay *via* an intensity-dependent recombination, while the dynamics in p-DTS(FBTTh$_2$)$_2$:ICBA blends are only weakly intensity-dependent implying the recombination of long-lived CT states and trapped charges in the latter. A closer analysis of the ns to μs recombination dynamics of photogenerated charges in the p-DTS(FBTTh$_2$)$_2$:PC$_{70}$BM based devices by a two-pool model suggests that about 85% of the charges are free and can potentially contribute to the photocurrent, which is in line with the internal quantum efficiency of these blends.

All in all, the measurements provide insight into the question why blends consisting of p-DTS(FBTTh$_2$)$_2$ and PC$_{70}$BM outperform those using ICBA as an acceptor with PCEs of 8.01% and 5.07%, respectively. Moreover, the present study supports recent findings that aggregated (crystalline) fullerene domains are beneficial for charge separation at the donor–acceptor interface.[39,41] In contrast, blends containing ICBA form smaller domains giving rise to long-lived CT states and carrier trapping. Whilst previous work suggests that one crystalline component is sufficient to oppress the formation of bound states, we found that although 2D-GIWAXS experiments suggest a pronounced crystallinity of ICBA, it is not sufficient to generate as many free charges as in PCBM blends. Further experiments are required to better understand the initial charge separation such as ultrafast mobility measurements using different fullerene derivatives to evaluate the role of the initial carrier mobility of different acceptors in the charge separation process.

4. Experimental

4.1. Device fabrication and characterization

The ITO-coated glass was first cleaned by detergent, acetone and isopropyl alcohol with ultra-sonication sequentially, followed by the UV/ozone treatment for 10 min. The hole transport material of PEDOT:PSS (Clevious PH) was spin-coated at 5000 rpm for 40 s to obtain a film thickness of ~30 nm. The p-DTS(FBTTh$_2$)$_2$:ICBA blend solution was prepared from a total of 35 mg mL^{-1} in chlorobenzene with various DIO amounts. The solution is dissolved at 60 °C overnight. Before spin-casting, the solution was heated at 90 °C for 15 min. The BHJ film was obtained from spin-casting the solution at 2000 rpm for 45 s. The films were baked to 80 °C for 10 min to evaporate residual solvent and then annealed between 100 °C and 130 °C for 5 min. The thickness of the BHJ film is ~100 nm as determined using a profilometer. Then, the Ca layer was thermally evaporated with a thickness of 20 nm, and the Al cathode was continuously deposited to ~80 nm under the vacuum condition of 4×10^{-6} Torr. The fabricated solar cells were encapsulated with epoxy and cover glass. The *J–V* characteristics of the solar cells were measured using a Keithley 2400 source meter unit. The light source was calibrated by using silicon reference cells with an AM 1.5G solar simulator with an intensity of 100 mW cm^{-2}. During the testing, an aperture with an area of 4.5 mm^2 was used to accurately measure the performance of solar cells. All solar cells were tested in ambient air. The EQE was measured using a QE measurement system (PV measurements, Inc.) after monochromatic power calibration to confirm the J_{SC} value.

4.2. Thin film characterization

The nano-morphology of the pristine p-DTS(FBTTh$_2$)$_2$ film and p-DTS(FBTTh$_2$)$_2$:PC$_{70}$BM BHJ film were investigated by AFM (AFM Asylum MFP3D) to characterize the surface morphology. 2D grazing-incidence wide-angle X-ray scattering (GIWAXS) measurements were performed at the Stanford Synchrotron Radiation Lightsource (SSRL) on Beamline 11-3, with a MAR345 image plate area detector, at 12.7 keV incident photon energy, and at incident angles of 0.10–0.12°. Thin film illumination occurred in a helium atmosphere to minimize X-ray beam damage. The films were spin cast on PEDOT:PSS coated glass for AFM and GIWAXS measurements.

4.3. Transient absorption spectroscopy

Transient absorption (TA) measurements were performed with a home-built pump–probe setup. To measure in the time range of 1–4 ns with a resolution of ~100 fs, the output of a commercial titanium:sapphire amplifier (Coherent LIBRA-HE, 3.5 mJ, 1 kHz, 100 fs) was split into two beams that pumped two independent commercial optical parametric amplifiers (Coherent OPerA Solo). One optical parametric amplifier (OPA) was used to generate the tunable excitation pulses in the visible range, while the second OPA was used to generate the seed beam for white-light generation. For measurements in the spectral range between 550 and 1100 nm a 1300 nm seed of a few μJ was focused into a c-cut 3 mm thick sapphire window for white-light generation. Mostly reflective elements were used to guide the probe beam to the sample to minimize chirp. The excitation pulse was chopped at 500 Hz, while the white-light pulses were dispersed onto a linear silicon photodiode array, which was read out at 1 kHz by home-built electronics. Adjacent diode readings corresponding to the transmission of the sample after an excitation pulse and without an excitation pulse were used to calculate $\Delta T/T$.

For measurements in the time range between 1 ns and 1 ms with a resolution of 600 ps, the excitation pulse was provided by an actively Q-switched Nd:YVO$_4$ laser (AOT Ltd. MOPA) at 532 nm. In this case, the delay between the pump and probe was controlled by an electronic delay generator (Stanford Research Systems DG535). TA measurements were performed at room temperature under a dynamic vacuum of $<10^{-5}$ mbar.

For TA measurements in the NIR spectral range covering 1100–2000 nm, a 2100 nm seed was used to generate white-light in an yttrium vanadate window. Furthermore, a dichroic mirror was used to separate the residual seed beam (idler of the OPA at 2100 nm) from the broadband NIR supercontinuum. The NIR pulses were dispersed onto a Peltier-cooled 512 pixel long linear extended InGaAs array (Entwicklungsbüro Stresing) and read out as described above.

MCR-ALS analysis is a soft-modeling technique that decomposes a three-dimensional data matrix into spectra and the corresponding concentration profiles. The data here can be described by two components unraveled by singular-value decomposition (SVD).

Acknowledgements

The authors are grateful to support from the Office of Naval Research and A*STAR SERC TSRP grant (Grant #102 170 0137). TQN thanks the Camille Dreyfus Teacher Scholar Award program. F.L. thanks the Max Planck Society for funding the Max Planck Research Group of Organic Optoelectronics and the Deutsche Forschungsgemeinschaft (DFG) for funding in the framework of the priority program SPP1355 "Elementary Processes in Organic Photovoltaics". A.K.K.K. thanks BMBF for funding "Green Talents-Research Stay in Germany". D.G. acknowledges a Kekulé scholarship of the Fonds der Chemischen Industrie (FCI). Use of the Stanford Synchrotron Radiation Lightsource, SLAC National Accelerator Laboratory, is supported by the U.S. Department of Energy, Office of Science, Office of Basic Energy Sciences under Contract no. DE-AC02-76SF00515.

Notes and references

1 A. J. Bard and M. A. Fox, *Acc. Chem. Res.*, 1995, **28**, 141–145.
2 S. Esiner, H. van Eersel, M. M. Wienk and R. A. J. Janssen, *Adv. Mater.*, 2013, **25**, 2932–2936.
3 M. G. Walter, E. L. Warren, J. R. McKone, S. W. Boettcher, Q. Mi, E. A. Santori and N. S. Lewis, *Chem. Rev.*, 2010, **110**, 6446–6473.
4 T. R. Cook, D. K. Dogutan, S. Y. Reece, Y. Surendranath, T. S. Teets and D. G. Nocera, *Chem. Rev.*, 2010, **110**, 6474–6502.
5 I. D. Parker, *J. Appl. Phys.*, 1994, **75**, 1656–1666.
6 V. D. Mihailetchi, P. W. M. Blom, J. C. Hummelen and M. T. Rispens, *J. Appl. Phys.*, 2003, **94**, 6849–6854.
7 J. Liu, Y. Shi and Y. Yang, *Adv. Funct. Mater.*, 2001, **11**, 420–424.

8 J. Brabec, A. Cravino, D. Meissner, N. S. Sariciftci, T. Fromherz, M. T. Rispens, L. Sanchez and J. C. Hummelen, *Adv. Funct. Mater.*, 2001, **11**, 374–380.

9 G. Li, C.-W. Chu, V. Shrotriya, J. Huang and Y. Yang, *Appl. Phys. Lett.*, 2006, **88**, 253503.

10 C. Zhang, S. W. Tong, C. Zhu, C. Jiang, E. T. Kang and D. S. H. Chan, *Appl. Phys. Lett.*, 2009, **94**, 103305.

11 K. Vandewal, K. Tvingstedt, A. Gadisa, O. Inganas and J. V. Manca, *Nat. Mater.*, 2009, **8**, 904–909.

12 N. Li, B. E. Lassiter, R. R. Lunt, G. Wei and S. R. Forrest, *Appl. Phys. Lett.*, 2009, **94**, 023307.

13 M. C. Scharber, D. Mühlbacher, M. Koppe, P. Denk, C. Waldauf, A. J. Heeger and C. J. Brabec, *Adv. Mater.*, 2006, **18**, 789–794.

14 G. Li, Y. Yao, H. Yang, V. Shrotriya, G. Yang and Y. Yang, *Adv. Funct. Mater.*, 2007, **17**, 1636–1644.

15 A. K. K. Kyaw, X. W. Sun, C. Y. Jiang, G. Q. Lo, D. W. Zhao and D. L. Kwong, *Appl. Phys. Lett.*, 2008, **93**, 221107.

16 S. H. Park, A. Roy, S. Beaupre, S. Cho, N. Coates, J. S. Moon, D. Moses, M. Leclerc, K. Lee and A. J. Heeger, *Nat. Photonics*, 2009, **3**, 297–302.

17 E. Wang, L. Hou, Z. Wang, S. Hellström, F. Zhang, O. Inganäs and M. R. Andersson, *Adv. Mater.*, 2010, **22**, 5240–5244.

18 Y. He, H.-Y. Chen, J. Hou and Y. Li, *J. Am. Chem. Soc.*, 2010, **132**, 1377–1382.

19 Y.-J. Cheng, C.-H. Hsieh, Y. He, C.-S. Hsu and Y. Li, *J. Am. Chem. Soc.*, 2010, **132**, 17381–17383.

20 X. Fan, C. Cui, G. Fang, J. Wang, S. Li, F. Cheng, H. Long and Y. Li, *Adv. Funct. Mater.*, 2012, **22**, 585–590.

21 S.-H. Liao, Y.-L. Li, T.-H. Jen, Y.-S. Cheng and S.-A. Chen, *J. Am. Chem. Soc.*, 2012, **134**, 14271–14274.

22 Z. Sun and S. Stafström, *J. Chem. Phys.*, 2013, **138**, 164905.

23 M. Muntwiler, Q. Yang, W. A. Tisdale and X. Y. Zhu, *Phys. Rev. Lett.*, 2008, **101**, 196403.

24 X. Y. Zhu, Q. Yang and M. Muntwiler, *Acc. Chem. Res.*, 2009, **42**, 1779–1787.

25 A. Rao, P. C. Y. Chow, S. Gelinas, C. W. Schlenker, C.-Z. Li, H.-L. Yip, A. K. Y. Jen, D. S. Ginger and R. H. Friend, *Nature*, 2013, **500**, 435–439.

26 X. Gong, M. Tong, F. G. Brunetti, J. Seo, Y. Sun, D. Moses, F. Wudl and A. J. Heeger, *Adv. Mater.*, 2011, **23**, 2272–2277.

27 D. Yang, Q. Yang, L. Yang, Q. Luo, Y. Huang, Z. Lu and S. Zhao, *Chem. Commun.*, 2013, **49**, 10465–10467.

28 J. Yuan, Z. Zhai, H. Dong, J. Li, Z. Jiang, Y. Li and W. Ma, *Adv. Funct. Mater.*, 2013, **23**, 885–892.

29 A. K. K. Kyaw, D. H. Wang, V. Gupta, W. L. Leong, L. Ke, G. C. Bazan and A. J. Heeger, *ACS Nano*, 2013, **7**, 4569–4577.

30 T. S. van der Poll, J. A. Love, T.-Q. Nguyen and G. C. Bazan, *Adv. Mater.*, 2012, **24**, 3646–3649.

31 Y. Kim, S. A. Choulis, J. Nelson, D. D. C. Bradley, S. Cook and J. R. Durrant, *Appl. Phys. Lett.*, 2005, **86**, 063502.

32 G. Li, V. Shrotriya, Y. Yao and Y. Yang, *J. Appl. Phys.*, 2005, **98**, 043704.

33 Z. M. Beiley, E. T. Hoke, R. Noriega, J. Dacuña, G. F. Burkhard, J. A. Bartelt, A. Salleo, M. F. Toney and M. D. McGehee, *Adv. Energy Mater.*, 2011, **1**, 954–962.

34 B. Walker, A. B. Tamayo, X.-D. Dang, P. Zalar, J. H. Seo, A. Garcia, M. Tantiwiwat and T.-Q. Nguyen, *Adv. Funct. Mater.*, 2009, **19**, 3063–3069.

35 S. Gélinas, A. Rao, A. Kumar, S. L. Smith, A. W. Chin, J. Clark, T. S. van der Poll, G. C. Bazan and R. H. Friend, *Science*, 2014, **343**, 512–516.

36 I. A. Howard, H. Mangold, F. Etzold, D. Gehrig and F. Laquai, in *Ultrafast Dynamics in Molecules, Nanostructures and Interfaces*, pp. 53–78, DOI: 10.1142/9789814556927_0004.

37 D. W. Gehrig, S. Roland, I. A. Howard, V. Kamm, H. Mangold, D. Neher and F. Laquai, *J. Phys. Chem. C*, 2014, **118**, 20077–20085.

38 J. A. Love, C. M. Proctor, J. Liu, C. J. Takacs, A. Sharenko, T. S. van der Poll, A. J. Heeger, G. C. Bazan and T.-Q. Nguyen, *Adv. Funct. Mater.*, 2013, **23**, 5019–5026.

39 S. Shoaee, S. Subramaniyan, H. Xin, C. Keiderling, P. S. Tuladhar, F. Jamieson, S. A. Jenekhe and J. R. Durrant, *Adv. Funct. Mater.*, 2013, **23**, 3286–3298.

40 M. A. Faist, S. Shoaee, S. Tuladhar, G. F. A. Dibb, S. Foster, W. Gong, T. Kirchartz, D. D. C. Bradley, J. R. Durrant and J. Nelson, *Adv. Energy Mater.*, 2013, **3**, 744–752.

41 F. C. Jamieson, E. B. Domingo, T. McCarthy-Ward, M. Heeney, N. Stingelin and J. R. Durrant, *Chem. Sci.*, 2012, **3**, 485–492.

42 I. A. Howard, R. Mauer, M. Meister and F. Laquai, *J. Am. Chem. Soc.*, 2010, **132**, 14866–14876.

43 F. Etzold, I. A. Howard, R. Mauer, M. Meister, T.-D. Kim, K.-S. Lee, N. S. Baek and F. Laquai, *J. Am. Chem. Soc.*, 2011, **133**, 9469–9479.

44 F. Etzold, I. A. Howard, N. Forler, D. M. Cho, M. Meister, H. Mangold, J. Shu, M. R. Hansen, K. Müllen and F. Laquai, *J. Am. Chem. Soc.*, 2012, **134**, 10569–10583.

45 H. Mangold, A. A. Bakulin, I. A. Howard, C. Kastner, D. A. M. Egbe, H. Hoppe and F. Laquai, *Phys. Chem. Chem. Phys.*, 2014, **16**, 20329–20337.

46 T. Wang, A. J. Pearson, A. D. F. Dunbar, P. A. Staniec, D. C. Watters, H. Yi, A. J. Ryan, R. A. L. Jones, A. Iraqi and D. G. Lidzey, *Adv. Funct. Mater.*, 2012, **22**, 1399–1408.

47 R. Mauer, M. Kastler and F. Laquai, *Adv. Funct. Mater.*, 2010, **20**, 2085–2092.

Electronic Supplementary Material (ESI) for Journal of Materials Chemistry A.

Supplementary Information

High Open-Circuit Voltage Small-Molecule p-DTS(FBTTh$_2$)$_2$:ICBA Bulk Heterojunction Solar Cells - Morphology, Excited-State Dynamics, and Photovoltaic Performance

Aung Ko Ko Kyaw,[a] Dominik Gehrig,[b] Jie Zhang,[a] Ye Huang,[c] Guillermo C. Bazan,[c] Frédéric Laquai*[b] and Thuc-Quyen Nguyen*[c]

[a]Institute of Materials Research and Engineering (IMRE), Agency for Science Technology and Research (A*STAR), Singapore 117602, Republic of Singapore

[b]Max Planck Research Group for Organic Optoelectronics, Max Planck Institute for Polymer Research, Ackermannweg 10, D-55128 Mainz, Germany
E-mail: laquai@mpip-mainz.mpg.de

[c]Center for Polymers and Organic Solids, Department of Chemistry and Biochemistry, University of California at Santa Barbara, Santa Barbara, California 93106-5090, USA
E-mail: quyen@chem.ucsb.edu

J-V characteristics of p-DTS(FBTTh$_2$)$_2$:ICBA solar cells

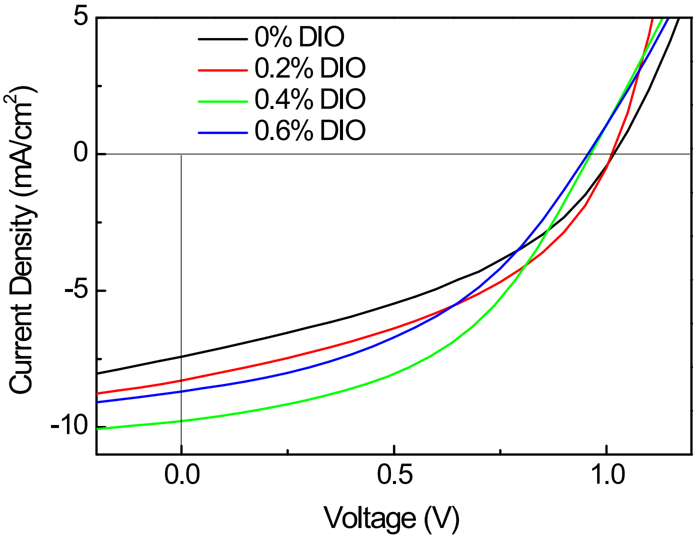

Fig. S1 *J-V* characteristics of p-DTS(FBTTh$_2$)$_2$:ICBA solar cells processed with various contents of DIO (0%, 0.2%, 0.4% and 0.6%) under AM 1.5G irradiation at 100 mW/cm^2. The blend ratio of p-DTS(FBTTh$_2$)$_2$:ICBA is 1.5:1.

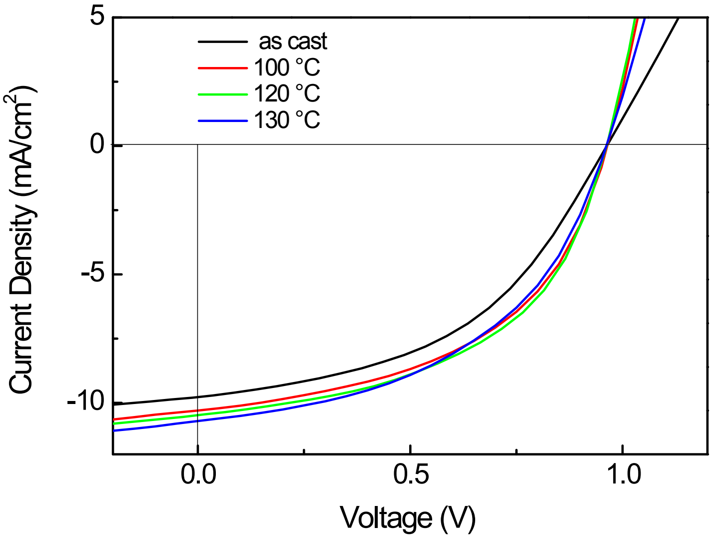

Fig. S2 *J-V* characteristics of p-DTS(FBTTh$_2$)$_2$:ICBA solar cell after annealing at different temperatures. The solar cells were fabricated from 1.5:1 blend ratio of p-DTS(FBTTh$_2$)$_2$:ICBA with 0.4% DIO.

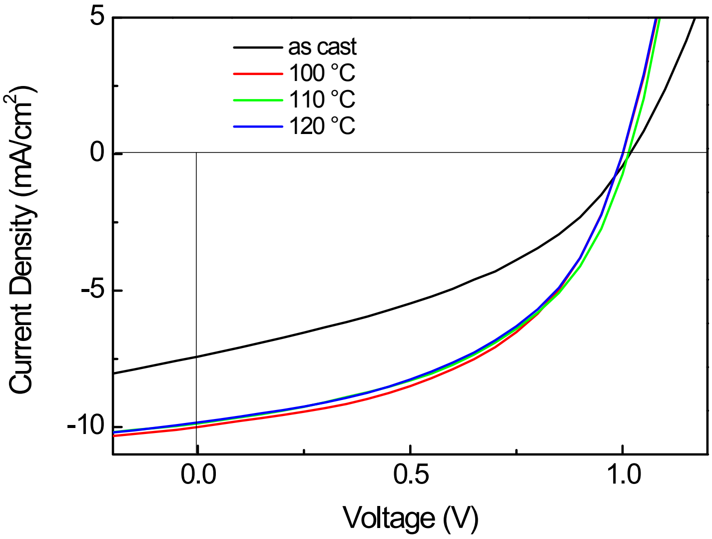

Fig. S3 *J-V* characteristics of p-DTS(FBTTh$_2$)$_2$:ICBA solar cell after annealing at different temperatures. The solar cells were fabricated from 1.5:1 blend ratio of p-DTS(FBTTh$_2$)$_2$:ICBA without DIO.

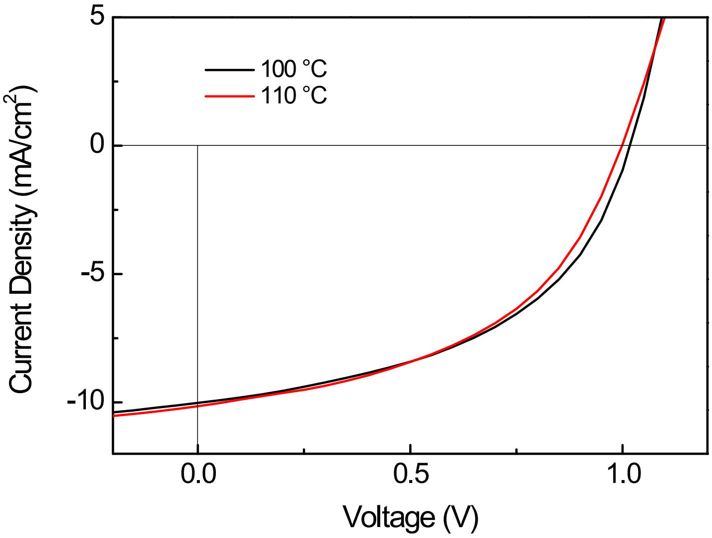

Fig. S4 *J-V* characteristics of p-DTS(FBTTh$_2$)$_2$:ICBA solar cell fabricated from 2.3:1 blend ratio of p-DTS(FBTTh$_2$)$_2$:ICBA (without DIO) and annealed at different temperatures.

Comparison between p-DTS($FBTTh_2$)$_2$:ICBA and p-DTS($FBTTh_2$)$_2$:$PC_{70}BM$ (Absorption and EQE spectrum)

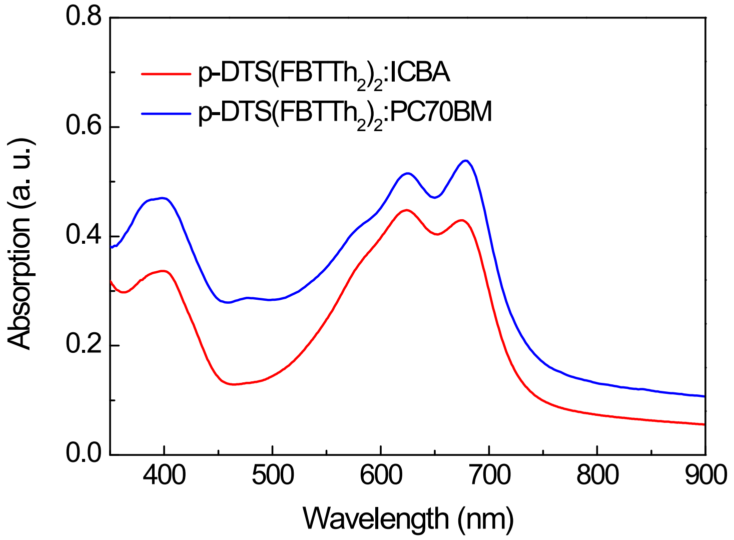

Fig. S5 UV-Vis absorption spectrum of p-DTS($FBTTh_2$)$_2$:ICBA and p-DTS($FBTTh_2$)$_2$:$PC_{70}BM$ blend under optimized condition.

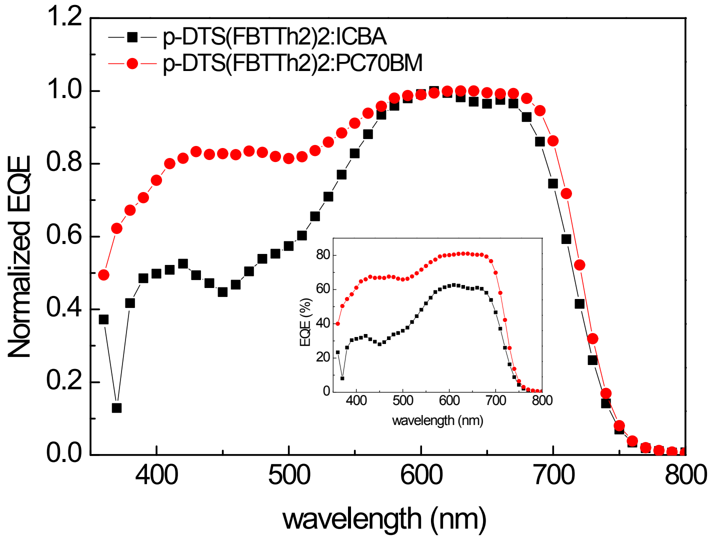

Fig. S6 Normalized EQE spectrum of p-DTS($FBTTh_2$)$_2$:ICBA and p-DTS($FBTTh_2$)$_2$:$PC_{70}BM$ solar cells. Inset shows the absolute EQE spectrum of two cells.

U-Vis absorption spectra show that absorption of p-DTS($FBTTh_2$)$_2$:ICBA is lower than that of p-DTS($FBTTh_2$)$_2$:$PC_{70}BM$, especially in the region below 580 nm, owing to the lack of absorption tail of ICBA in visible region. The normalized EQE spectra (normalized by peak value of individual device) also reveal that EQE sharply drops below the wavelength of 580 nm. Since internal quantum efficiency (IQE) is pretty flat throughout the spectrum, EQE reflects the absorption of BHJ film. The sharp drop in absorption below the wavelength of 580 nm is the main reason for low Jsc in p-DTS($FBTTh_2$)$_2$:ICBA solar cell.

Comparison between p-DTS(FBTTh$_2$)$_2$:ICBA and p-DTS(FBTTh$_2$)$_2$:PC$_{70}$BM solar cells (Dark J-V characteristics)

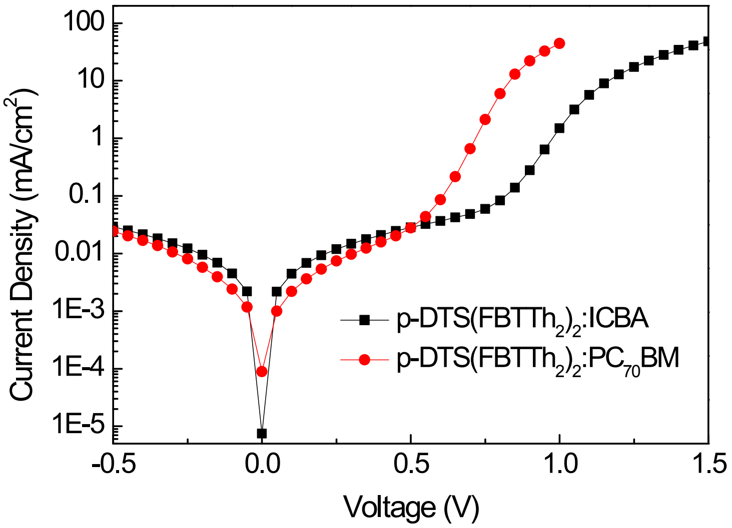

Fig. S7 *J-V* characteristics of p-DTS(FBTTh$_2$)$_2$:ICBA and p-DTS(FBTTh$_2$)$_2$:PC$_{70}$BM solar cells in the dark.

The dark *J-V* curve of p-DTS(FBTTh$_2$)$_2$:ICBA solace cell shows high rectification ratio and low leakage current which are comparable to that of p-DTS(FBTTh$_2$)$_2$:PC$_{70}$BM solar cell. The high rectification ratio and low leakage current ensure the good quality interface between the BHJ and electrodes.

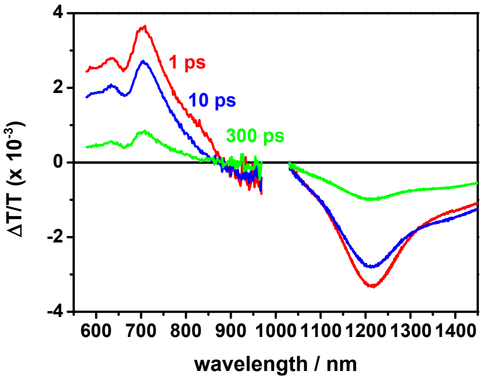

Fig. S8 Spectra of neat p-DTS(FBTTh$_2$)$_2$ film after excitation with 520 nm.

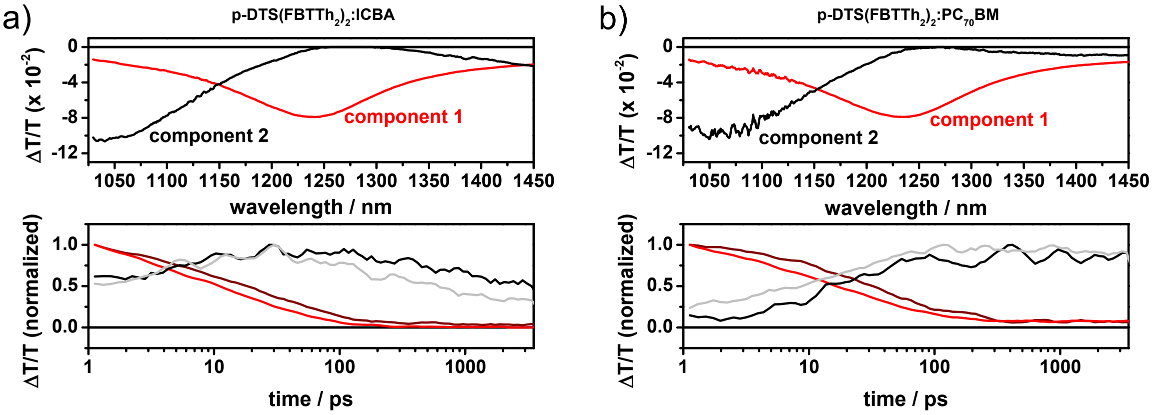

Fig. S9. Spectra (upper panel) and concentration profiles (lower panel) obtained from MCR-ALS analysis of a) p-DTS(FBTTh$_2$)$_2$:ICBA and b) p-DTS(FBTTh$_2$)$_2$:PC$_{70}$BM NIR data.

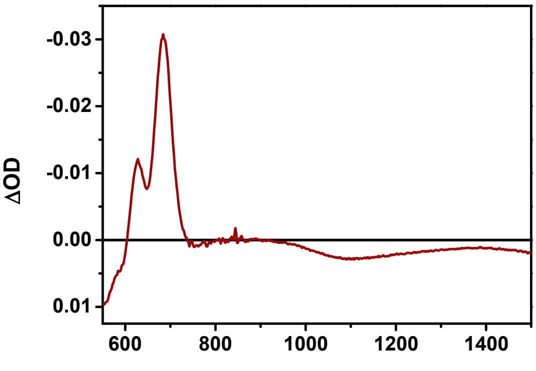

Fig. S10. Iodine vapour oxidized film of p-DTS(FBTTh$_2$)$_2$:PC$_{70}$BM

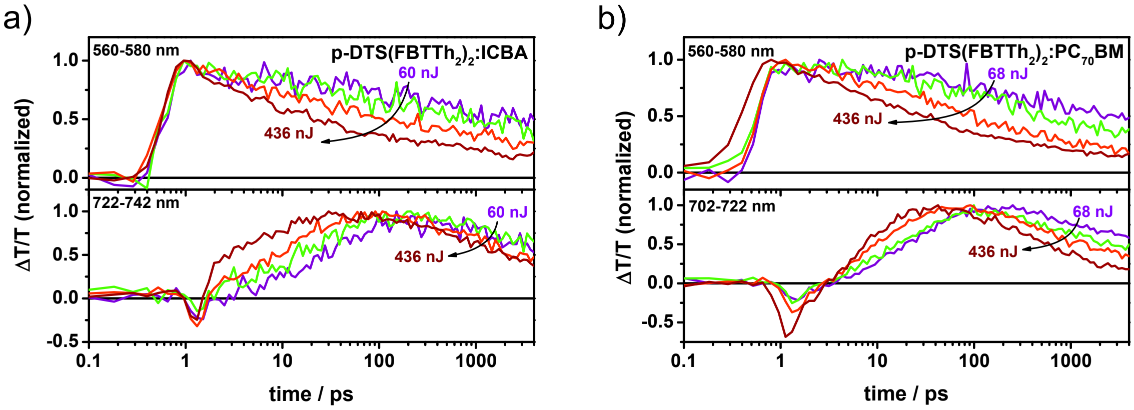

Fig. S11 Kinetics of p-DTS(FBTTh$_2$)$_2$:ICBA tracked at 560-580 nm (ground-state bleach, upper panel) and 722-742 (0-transition at 1 ps, lower panel) and b) p-DTS(FBTTh$_2$)$_2$:PC$_{70}$BM at 560-580 nm (ground-state bleach, upper panel) and 702-722 (0-0 transition at 1 ps, lower panel).

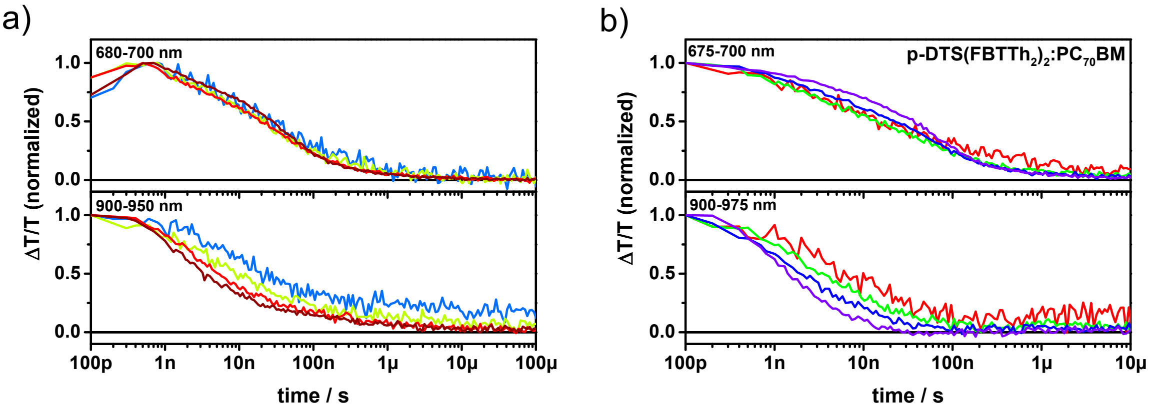

Fig. S12 a) Kinetics of p-DTS(FBTTh$_2$)$_2$:ICBA films tracked at 680-700 nm (upper panel, GSB) and at 900-950 nm (lower panel, PIA); b) Kinetics of p-DTS(FBTTh$_2$)$_2$:PC$_{70}$BM films tracked at 675-700 nm (upper panel, GSB) and at 900-975 nm (lower panel, PIA).

4.5 Influence of Nanoscale Morphology in pBTTT:PCBM Blends of Different Donor-Acceptor Ratios

The article "The Impact of Donor–Acceptor Phase Separation on the Charge Carrier Dynamics in pBTTT:PCBM Photovoltaic Blends" was published in Macromolecular Rapid Communications and is available online since April 7th, 2015. The article is reprinted with permission from reference [222]. Copyright (2015) WILEY-VCH Verlag GmbH & Co. KGaA, Weinheim.

The Impact of Donor–Acceptor Phase Separation on the Charge Carrier Dynamics in pBTTT:PCBM Photovoltaic Blends

Dominik W. Gehrig, Ian A. Howard, Sean Sweetnam, Timothy M. Burke, Michael D. McGehee, Frédéric Laquai*

The effect of donor–acceptor phase separation, controlled by the donor–acceptor mixing ratio, on the charge generation and recombination dynamics in pBTTT-C14:$PC_{70}BM$ bulk heterojunction photovoltaic blends is presented. Transient absorption (TA) spectroscopy spanning the dynamic range from pico- to microseconds in the visible and near-infrared spectral regions reveals that in a 1:1 blend exciton dissociation is ultrafast; however, charges cannot entirely escape their mutual Coulomb attraction and thus predominantly recombine geminately on a sub-ns timescale. In contrast, a polymer:fullerene mixing ratio of 1:4 facilitates the formation of spatially separated, that is free, charges and reduces substantially the fraction of geminate charge recombination, in turn leading to much more efficient photovoltaic devices. This illustrates that spatially extended donor or acceptor domains are required for the separation of charges on an ultrafast timescale (<100 fs), indicating that they are not only important for efficient charge transport and extraction, but also critically influence the initial stages of free charge carrier formation.

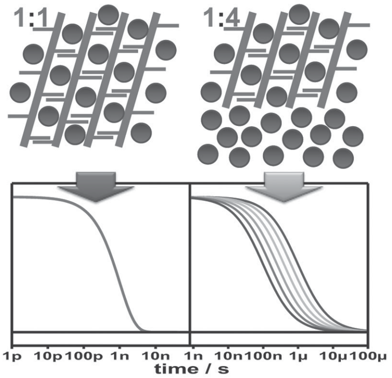

D. W. Gehrig, Assoc. Prof. F. Laquai[+]
Max Planck Research Group for Organic Optoelectronics
Max Planck Institute for Polymer Research
Ackermannweg 10, D-55128 Mainz, Germany
E-mail: laquai@mpip-mainz.mpg.de; frederic.laquai@kaust.edu.sa
Dr. I. A. Howard
Institute of Microstructure Technology (IMT)
Karlsruhe Institute of Technology (KIT)
Hermann-von-Helmholtz-Platz 1
D-76344 Eggenstein-Leopoldshafen, Germany
S. Sweetnam, T. M. Burke, Prof. M. D. McGehee
Materials Science and Engineering
Stanford University
476 Lomita Mall, Stanford, CA 94305-4045, USA
[+]Present address: Physical Sciences and Engineering Division (PSE), Material Science and Engineering (MSE), Solar and Photovoltaics Engineering Research Center (SPERC), King Abdullah University of Science and Technology (KAUST), Thuwal 23955-6900, Kingdom of Saudi Arabia

1. Introduction

The growing global demand of energy is a major challenge that motivates the search for sustainable solutions for energy production, which satisfy requirements including long-term availability as well as economic and ecological constraints. Amongst the variety of renewable energy sources, organic photovoltaics are a promising and steadily developing technology. Recently, single-junction solar cells have been demonstrated with power conversion efficiencies exceeding 10%, thus approaching the efficiency of amorphous silicon solar cells.[1,2] However, a proper choice of processing conditions is required to reach optimum performance of each material system. The most often used layout is a bulk heterojunction (BHJ) organic solar cell consisting of intermixed phases of an electron donor (D) and acceptor (A) material. Upon absorption of a photon a tightly bound exciton is

Macromol. Rapid Commun. **2015**, DOI: 10.1002/marc.201500112

DOI: 10.1002/marc.201500112

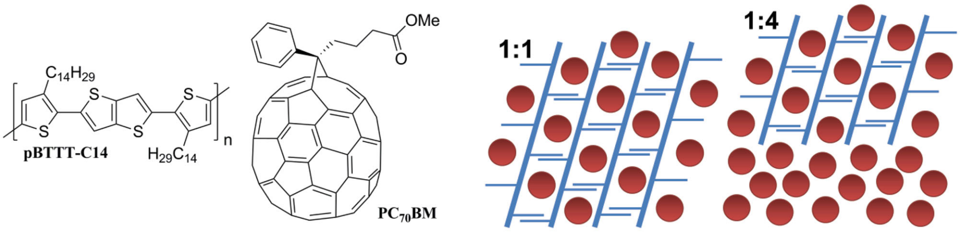

Scheme 1. Chemical structures of pBTTT-C14 and PC$_{70}$BM, as well as a schematic representation of the film morphology for blends using a 1:1 and 1:4 donor:acceptor ratio.

created in the photoactive layer, which can be split into free charges at the D–A interface, a process driven by the energy offset between the energy levels of the two components.[3] However, the mechanism of charge separation is still debated and thought to depend on parameters such as the crystallinity and the extent of the donor[4–6] and acceptor domains,[7,8] the conjugation length of the polymeric donor,[9] the charge carrier mobility of the single components[10] and the orientation of donor and acceptor molecules with respect to each other.[11,12] Free charges created at the interface upon exciton dissociation are collected at the electrodes after transport in the donor and acceptor networks; however, they are prone to nongeminate recombination during transport before extraction. In fact, a large interfacial area ensures virtually quantitative exciton dissociation; however, it simultaneously increases recombination, if the interface is not well connected to the bulk materials as charge carriers cannot escape their mutual attraction. Thus, finding the optimum morphology is a complex optimization problem and a tradeoff exists between maximizing the D–A interface, where charge separation occurs, and the optimization of percolation pathways that allow for efficient separation and charge carrier collection. Recent literature provides more insight into these complex relations between the donor–acceptor phase separation and the efficiency of charge generation; however, an entirely conclusive picture has not been developed yet.[7,13–16]

Changing the donor and acceptor ratio is one important parameter to control the phase separation, aggregation, and crystallinity of the blend. Its tuning is critical for the optimization of many BHJ systems. This has been very precisely studied in blends of the donor polymer poly[2,5-bis(3-tetradecylthiophen-2-yl)thieno[3,2-*b*]thiophene] (pBTTT-C14) and the fullerene derivative PC$_{70}$BM. Specifically, specular X-ray diffraction demonstrated that PCBM intercalates between the side chains of pBTTT-C16, thereby creating a well-defined cocrystal at a blending ratio of 1:1.[17] However, at increased fullerene fractions the acceptor molecules cannot all be accommodated in the cocrystal phase anymore, and thus extended PCBM domains are additionally created.

This clear and well characterized morphology makes pBTTT an ideal system to study the photophysics of charge generation under strongly intermixed (cocrystal) and phase-separated (high fullerene loading) conditions. It was recently shown that an excess of PC$_{60}$BM (D:A = 1:3) yields a higher fraction of long-lived (>1.5 ns) charges in contrast to samples with a 1:1 donor–acceptor ratio.[18] A separate study on pBTTT and other donor polymers suggested that charge generation is limited to the intermixed phases of donor and acceptor.[16] Zusan et al.[19] showed that charge separation is less field-dependent in a 1:4 blend of pBTTT:PC$_{60}$BM compared with a 1:1 composition and concluded that pure and spatially extended fullerene domains facilitate field-independent charge separation. It has also been found that there is an energetic offset between the mixed and pure phases that enhances separation of electrons and holes into free carriers.[7,20–23] In the following, we present the charge carrier dynamics in pBTTT:PC$_{70}$BM (see Scheme 1 for chemical structures) for 1:1 blends that exclusively contain the cocrystal phase and for 1:4 blends that contain both the cocrystal phase and extended fullerene clusters. Precisely, we demonstrate by pico- to microsecond broadband transient absorption pump-probe spectroscopy, an all-optical technique complementary to the electro-optical experiments recently presented by Zusan et al.[19] that the improvement of the photovoltaic performance with higher than 1:1 fullerene loadings is a consequence of the generation of spatially separated, that is free, charges, whereas in the cocrystal (D:A = 1:1) sub-ns geminate recombination dominates the photophysics in turn significantly limiting the device performance. This illustrates that extended PCBM domains play a role in the generation and spatial separation of charges on an ultrafast timescale, showing that they are not only important for charge extraction, but also critically influence the initial stages of free charge formation very well in line with the recently reported results of Zusan et al.[19]

2. Experimental Section

The preparation of the organic solar cells is described in detail in the supplementary material. Spectroscopic samples were prepared by spincoating the active layer on quartz substrates with a donor–acceptor ratio of 1:1 (c/c) and 1:4 (w/w), respectively. Our transient absorption spectroscopy setup has been described earlier[24] 25 and additional information can be found in the Supporting information.

3. Results and Discussion

Table 1 shows the figures of merit of solar cells made with the two different donor–acceptor blending ratios. The 1:1 blend exhibits a rather poor photovoltaic efficiency of 0.55%, whereas the 1:4 blend exhibits a moderate power conversion efficiency of 2.4%, largely due to an improved short circuit current. The current–voltage characteristics of the respective devices are shown in Figure S1 (Supporting Information).

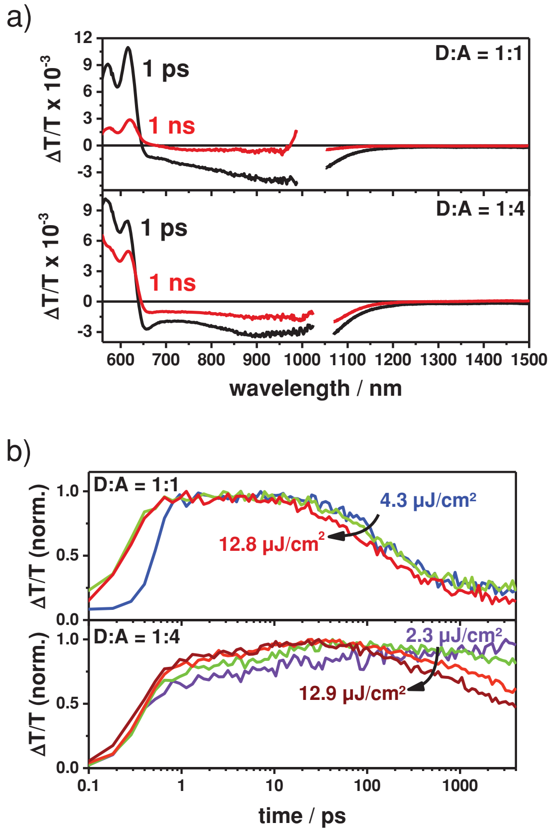

Figure 1. a) ps–ns TA spectra of a pBTTT:PC$_{70}$BM thin film blend with a donor–acceptor ratio of 1:1 (upper panel, 11.2 μJ cm^{-2}) and 1:4 (lower panel, 8.7 μJ cm^{-2}). b) Ground-state bleaching kinetics of a pBTTT:PC$_{70}$BM 1:1 blend (upper panel, 610–635 nm) and a 1:4 blend (lower panel, 585–605 nm) at different excitation intensities.

The sub-ns TA spectra of the blends are presented in Figure 1a. The samples were excited at a wavelength of 520 nm, which excites both the polymer and the fullerene. The spectra of both blends exhibit a ground-state bleaching (GSB) below 650 nm and a photo-induced absorption (PA) spanning the spectral range from 650 nm up to ≈1200 nm. No photo-induced absorption could be observed beyond 1200 nm at time delays greater than 1 ps. The TA spectra show two remarkable differences. First, the ratio of the two peaks of the ground-state bleaching changes with the donor–acceptor ratio. Although in the 1:1 blend the peak at 616 nm is more pronounced than the peak at 572 nm, the situation is reversed in the 1:4 blend, in which the peak at 614 nm is smaller than that at 567 nm. Second, the 1:4 sample shows a distinct peak at 647 nm, which is not present in the 1:1 sample. Both observations can be explained by the phenomenon of electro-absorption (EA) occurring at the donor–acceptor interface, as reported recently for other polymer:fullerene blends.[26] EA is caused by the presence of an electric field across the donor–acceptor interface itself created by the presence of oppositely charged carriers sufficiently close to the interface to create a local electric field across it. The local electric field shifts the ground-state absorption spectrum of nearby polymer molecules, effectively leading to a first derivative shape of the transient absorption spectrum in the region of the ground-state bleaching [see Figure S2b in Supporting Information]. In fact, a superposition of the thin film absorption and the first derivative of the absorption [Figure S2c, Supporting Information] matches the measured spectrum of the 1:4 blend at early times and explains the change in the ground-state bleaching, as well as the feature observed at 647 nm very well. The observation of a pronounced EA in the 1:4 blend and its absence in the 1:1 blend indicate that in the 1:4 blend spatial separation of charge carriers occurs, which in turn creates a local electric field across the interface that affects the absorption of nearby polymer molecules, whereas in the 1:1 blend, in which the EA feature is absent, charges appear to be trapped close to the interface, thereby limiting the spatial extension of the electric field to a small volume in between the two carriers. The presence of these EA features in the 1:4 blend from the earliest times onward also suggests that the carrier separation is ultrafast.[26] A further analysis of the intensity-dependent kinetics is shown in Figure 1b, and Figures S3a and S3b (Supporting Information). First, the evolution of the pBTTT ground-state bleaching after the excitation of the donor and acceptor molecules is analyzed. The maximum signal amplitude in the 1:1 blend is

Table 1. Photovoltaic parameters of pBTTT:PC$_{70}$BM solar cells at donor–acceptor ratios of 1:1 and 1:4.

D:A ratio	V_{OC} [V]	I_{SC} [mA cm^{-2}]	FF	PCE [%]
1:1	0.5	2.6	0.43	0.55
1:4	0.5	8.3	0.50	2.4

observed directly after photoexcitation, and the spectra resemble the same shape as time progresses. This implies ultrafast charge transfer from $PC_{70}BM$ to pBTTT and vice versa taking place on the sub-100 fs timescale. Given the intercalation of fullerene molecules between the side chains of the polymer backbone, it appears that excitons are always created close to the donor–acceptor interface, and hence ultrafast charge generation is facilitated. After the exciton dissociation, a fast and intensity-independent signal decay is observed indicating that the excited-state population consists mostly of geminate pairs that quickly recombine at the interface to the ground state by geminate recombination.

In contrast, the 1:4 blend shows a steady rise of the polymer's ground-state bleaching up to several tens of picoseconds. This indicates that exciton dissociation in this system is not exclusively ultrafast, but that a fraction of exciton dissociation is diffusion-limited, likely because excitons created in fullerene-rich domains must travel to the interface. The rise time observed depends on the excitation intensity, a consequence of exciton–charge and exciton–exciton annihilation in the fullerene domains at higher excitation intensities. These observations are in line with the formation of large, polymer-free domains of PCBM molecules within the photoactive layer of the 1:4 blend.

The rate of electron transfer from the pBTTT to the fullerene can be qualitatively assessed by looking at the pBTTT exciton-induced absorption in the spectral region above 1200 nm. Tracking the dynamics in this wavelength region reveals a signal decaying on a sub-picosecond timescale [Figure S3b, Supporting Information]. This indicates that in both samples, namely the 1:1 and 1:4 blends, the pBTTT polymer exciton does not have to diffuse prior to electron transfer to an acceptor molecule because the polymer exciton is generated in the cocrystal, where all polymer sites are located at a polymer:fullerene interface, whereas in the 1:4 blend a fraction of the photogenerated fullerene excitons diffuse prior to exciton dissociation.

The kinetics of the charge-induced absorption signal in the 1055–1075 nm spectral region supports our analysis of the GSB. In the 1:1 sample, the charge-induced absorption decays to about 10% of the initial value within 1 ns independent of the excitation intensity. This is consistent with the decay of the GSB, indicating geminate recombination of charges. The 1:4 blend, on the other hand, shows a diffusion-limited rise of the charge-induced absorption signal in line with a rise of the GSB. At longer delay times the intensity-dependent decay of the charge-induced absorption and GSB of the 1:4 blend are consistent with nongeminate recombination of free charges, as discussed in more detail below.

To sum up the aforementioned results of the ps–ns TA experiments, we observed ultrafast exciton dissociation in the 1:1 blend followed by a significant amount of sub-ns geminate recombination of charges, whereas in the 1:4 blend ultrafast plus diffusion-limited exciton dissociation and charge formation is observed, and charge carriers are initially separated over a significantly larger distance as indicated by a pronounced EA signal at around 650 nm and by the intensity-dependent carrier dynamics. Our results support recent findings presented by Zusan et al.,[19] who demonstrated by time-delayed collection field experiments that the field dependence of charge separation in pBTTT-C_{16}:$PC_{60}BM$ is much more pronounced in 1:1 blends than in 1:4 blends, indicating less spatial separation of charges upon charge transfer in the former compared with the latter and highlighting the importance of extended and pure fullerene domains for efficient charge separation.

We now turn to the results obtained on longer timescales, which is ns–µs measurements of the 1:1 and 1:4 blends. The dynamics in this time range reveals the recombination of longer lived charge carriers. The respective TA spectra and decay dynamics of the GSB are shown in Figure 2. In the 1:1 blend, we primarily observe recombination of charges following a decay process that does not depend on the excitation intensity or charge carrier

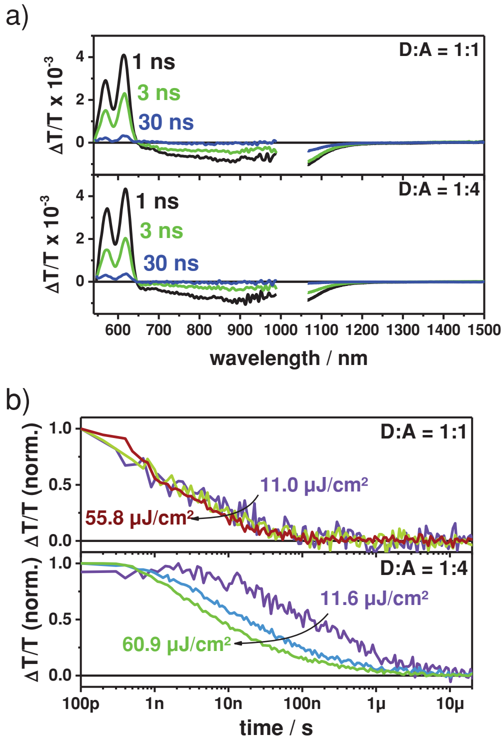

Figure 2. a) ns–µs TA spectra of thin film blends of pBTTT:$PC_{70}BM$ with a donor–acceptor ratio of 1:1 (upper panel, 28.3 µJ cm^{-2}) and 1:4 (lower panel, 52.7 µJ cm^{-2}). b) Ground-state bleaching kinetics of the same pBTTT:$PC_{70}BM$ 1:1 (upper panel, 610–630 nm) and 1:4 blend (lower panel, 610–630 nm) at different excitation densities.

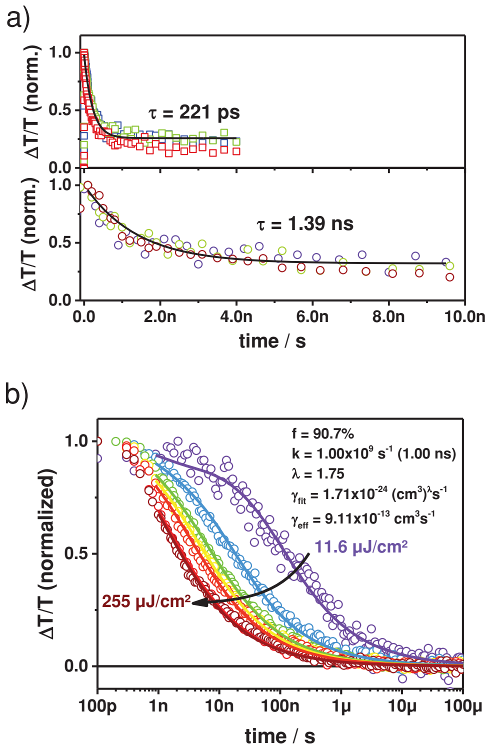

Figure 3. a) Monoexponential fit (black solid line) to the ground-state bleaching dynamics (open symbols) of a pBTTT:$PC_{70}BM$ (1:1) thin film blend to the ps–ns dynamics (upper panel, 610–635 nm) and ns–µs dynamics (lower panel, 610–630 nm). b) Intensity dependence of the ns–µs decay dynamics of the ground-state bleaching of a pBTTT:$PC_{70}BM$ (1:4) blend (open symbols, 610–630 nm) and fit to a two-pool model (solid lines). The inset depicts the obtained fitting parameters describing the experimentally measured decay dynamics.

density pointing to geminate and trap-assisted recombination. In contrast, the 1:4 blend exhibits intensity-dependent dynamics associated with non-geminate recombination of free charges.

The short (ps–ns) and long-time (ns–µs) decay dynamics of the 1:1 blend can be very well approximated by a mono-exponential fit (see Figure 3a) including an offset. The data collected on the sub-ns and the ns–µs timescales are both fitted with a single exponential resulting in inverse decay rates of 221 ps and 1.39 ns, respectively, the latter likely being a convolution of the signal decay and temporal resolution of our ns–µs TA setup limited by the ns pulse width of the pump laser. These decays account for 68–75% of the total signal decay in the 1:1 blend. The remaining signal decays in an intensity-independent manner, indicating trap-assisted recombination and/or recombination of long-lived charge-transfer states. In fact, intensity-independent recombination on the ns–µs time scale was previously demonstrated by Durrant and co-workers[21] in polymer:ICBA blends and assigned to loosely bound polaron pairs.

The charge carrier dynamics of the 1:4 blend was fitted by a two-pool model considering two separate noninteracting pools of charges generated on a sub-ns timescale, the first pool decaying by a single-exponential process accounting for geminate recombination and the second pool decaying by nongeminate recombination of free charge carriers.[27] We determine that in the 1:4 blend about 10% of the charges undergo geminate recombination with a rate of ≈1 ns, whereas 90% of the decay on the ns–µs timescale can be assigned to free charge recombination following nongeminate and thus intensity-dependent recombination dynamics. The effective nongeminate recombination coefficient at a charge carrier concentration of 5×10^{15} cm^{-3}, which is relevant for solar illumination conditions, was calculated to be 9.11×10^{-13} cm^3 s^{-1} and is comparable to that measured in other polymer:PCBM systems previously reported by us such as PCDTBT:$PC_{60}BM$ and P3HT:$PC_{60}BM$.[27,28]

The efficiency of free charge generation in organic solar cells is crucial for the overall power conversion efficiency of the solar cell device. The detailed mechanism, however, is still under debate and more complex than simple diffusion of charges from the interface to the bulk after charge transfer. Accordingly, several different pictures have been suggested to explain the astonishingly high efficiency of charge separation in organic bulk heterojunctions.

Very recently, Gélinas et al.[29] demonstrated long-range charge separation over a distance of 4 nm on a timescale as short as 40 fs. In fact, at this distance, the mutual Coulomb attraction between the electron and the hole is significantly lowered and the remaining attraction may be overcome by additional driving forces such as energy differences between the disordered interface and more ordered bulk, energy level bending due to interfacial dipoles or other effects.[30] Gélinas et al. emphasized the importance of charge delocalization in fullerene clusters that facilitates ultrafast long-range charge separation.

The necessity of the concept of delocalization to ensure ultrafast charge separation is, however, debated and the ultrafast and very efficient charge separation may alternatively be explained by the high carrier mobility (1–10 cm^2 V^{-1} s^{-1}) observed directly after exciton dissociation. In fact, it was recently demonstrated by kinetic Monte Carlo (KMC) simulations that the high local charge carrier mobility typically determined on bulk heterojunctions by ultrafast time-resolved THz measurements[31] enables fast electron–hole pair separation over distances sufficiently large to overcome the Coulomb attraction.[22,23,32] For instance, Esenturk et al. determined a lower limit of the mobility for holes in P3HT of 1 cm^2 V^{-1} s^{-1}.[33] Static disorder at the interface and entropy changes are also discussed as additional driving forces aiding charge separation.[34,35] The issue of the charge separation and recombination mechanism and its correlation with charge carrier

Macromol. Rapid Commun. **2015**, DOI: 10.1002/marc.201500112

mobility and disorder at the interface has recently been addressed for PCDTBT:$PC_{60}BM$ by Howard et al.[36] without involving any coherent processes. The authors showed that charge separation is facilitated by an initially high, nonequilibrium mobility and relaxation within the density of states results in fast hopping of charges away from the interface.

A third concept used to explain the high efficiency of charge separation is the existence of an energy cascade between the pure and mixed phases in the BHJ morphology. It has been found that there is an energetic offset between the pure and mixed phases of polymer:fullerene BHJs due to both differences in molecular aggregation,[7,21] and the presence of intermolecular interactions between the polymer and fullerene at the molecular interface.[20] These energetic offsets have been found to enhance charge separation efficiency both experimentally[21] and in kinetic Monte Carlo simulations.[22,23] The energetic offsets enhance charge separation efficiency by producing a driving force for charges to move from the mixed phase into the pure phase. Once charges encounter an energetic offset they are efficiently moved into the pure phase from the mixed phase and prevented from returning to the mixed phase, allowing them to be transported away from the polymer:fullerene interface and reducing their likelihood of recombination.

In summary, all concepts used to explain the high efficiency of charge separation observed in several polymer:fullerene blends have in common that an electron–hole separation of about 4–5 nm[22,29] is required to overcome the Coulomb binding energy at room temperature. However, they differ in the exact nature of the process of charge separation, that is, whether delocalization across neighboring molecules is a necessary prerequisite for efficient charge separation, whether an initially high charge carrier mobility is sufficient to ensure efficient charge separation, or whether the presence of an energetic offset between the pure and mixed phases is required to ensure charge separation.

4. Conclusions

In the present work, we show that solar cells prepared from pBTTT:$PC_{70}BM$ at a donor–acceptor ratio of 1:1 exhibit mainly sub-ns geminate recombination after exciton dissociation. The free carrier generation yield is, however, significantly improved by changing the donor–acceptor ratio to 1:4, which introduces extended fullerene domains and thus percolation paths for the charge carriers. In fact, the efficiency of separation on the sub-nanosecond timescale is greatly enhanced by this morphological difference, indicating that extended fullerene domains are not only important as extraction pathways for the free charge carrier, but also play a key role during the charge separation process. This finding is compatible with the aforementioned concepts, as the charge separation can be facilitated either by delocalization over fullerene aggregates or by a high initial charge carrier mobility plus an energy offset between mixed and pure phases. Hence, further experiments are necessary to address this issue and to obtain a conclusive picture of the underlying physics of charge separation in polymer:fullerene blends.

Supporting Information

Supporting Information is available from the Wiley Online Library or from the author.

Acknowledgements: The authors gratefully acknowledge Professor M. Heeney for providing pBTTT and Professor Brad Chmelka for fruitful discussions at the early stage of this work. F.L. thanks the Max Planck Society for funding the Max Planck Research Group for Organic Optoelectronics and the Deutsche Forschungsgemeinschaft (DFG) for funding in the framework of the priority program SPP1355 "Elementary Processes in Organic Photovoltaics." D.G. acknowledges a Kekulé scholarship of the Fonds der Chemischen Industrie (FCI). I.A.H. thanks the Carl-Zeiss-Stiftung and the Max Planck Society for research scholarships.

Received: February 19, 2015; Revised: March 11, 2015; Published online: ; DOI: 10.1002/marc.201500112

Keywords: carrier dynamics; pBTTT; phase separation; polymer solar cells; transient absorption spectroscopy

[1] Y. Liu, C.-C. Chen, Z. Hong, J. Gao, Y. Yang, H. Zhou, L. Dou, G. Li, *Sci. Rep.* **2013**, *3*, 3356.
[2] M. A. Green, K. Emery, Y. Hishikawa, W. Warta, E. D. Dunlop, *Prog. Photovolt. Res. Appl.* **2014**, *22*, 1.
[3] J.-L. Brédas, D. Beljonne, V. Coropceanu, J. Cornil, *Chem. Rev.* **2004**, *104*, 4971.
[4] Y. Kim, S. Cook, S. M. Tuladhar, S. A. Choulis, J. Nelson, J. R. Durrant, D. D. C. Bradley, M. Giles, I. McCulloch, C.-S. Ha, M. Ree, *Nat. Mater.* **2006**, *5*, 197.
[5] H. Mangold, A. A. Bakulin, I. A. Howard, C. Kastner, D. A. M. Egbe, H. Hoppe, F. Laquai, *Phys. Chem. Chem. Phys.* **2014**, *16*, 20329.
[6] Y. Tamai, K. Tsuda, H. Ohkita, H. Benten, S. Ito, *Phys. Chem. Chem. Phys.* **2014**, *16*, 20338.
[7] F. C. Jamieson, E. B. Domingo, T. McCarthy-Ward, M. Heeney, N. Stingelin, J. R. Durrant, *Chem. Sci.* **2012**, *3*, 485.
[8] N. C. Miller, S. Sweetnam, E. T. Hoke, R. Gysel, C. E. Miller, J. A. Bartelt, X. Xie, M. F. Toney, M. D. McGehee, *Nano Lett.* **2012**, *12*, 1566.
[9] C. Schwarz, H. Bässler, I. Bauer, J.-M. Koenen, E. Preis, U. Scherf, A. Köhler, *Adv. Mater.* **2012**, *24*, 922.
[10] W. L. Rance, A. J. Ferguson, T. McCarthy-Ward, M. Heeney, D. S. Ginley, D. C. Olson, G. Rumbles, N. Kopidakis, *ACS Nano* **2011**, *5*, 5635.
[11] D. M. Guldi, C. Luo, M. Prato, A. Troisi, F. Zerbetto, M. Scheloske, E. Dietel, W. Bauer, A. Hirsch, *J. Am. Chem. Soc.* **2001**, *123*, 9166.

[12] E. H. A. Beckers, S. C. J. Meskers, A. P. H. J. Schenning, Z. Chen, F. Würthner, P. Marsal, D. Beljonne, J. Cornil, R. A. J. Janssen, *J. Am. Chem. Soc.* **2005**, *128*, 649.

[13] J. A. Bartelt, Z. M. Beiley, E. T. Hoke, W. R. Mateker, J. D. Douglas, B. A. Collins, J. R. Tumbleston, K. R. Graham, A. Amassian, H. Ade, J. M. J. Fréchet, M. F. Toney, M. D. McGehee, *Adv. Energy Mater.* **2013**, *3*, 364.

[14] K. Schmidt, C. J. Tassone, J. R. Niskala, A. T. Yiu, O. P. Lee, T. M. Weiss, C. Wang, J. M. J. Fréchet, P. M. Beaujuge, M. F. Toney, *Adv. Mater.* **2014**, *26*, 300.

[15] B. A. Collins, Z. Li, J. R. Tumbleston, E. Gann, C. R. McNeill, H. Ade, *Adv. Energy Mater.* **2013**, *3*, 65.

[16] M. Scarongella, A. A. Paraecattil, E. Buchaca-Domingo, J. D. Douglas, S. Beaupre, T. McCarthy-Ward, M. Heeney, J. E. Moser, M. Leclerc, J. M. J. Frechet, N. Stingelin, N. Banerji, *J. Mater. Chem. A* **2014**, *2*, 6218.

[17] N. C. Cates, R. Gysel, Z. Beiley, C. E. Miller, M. F. Toney, M. Heeney, I. McCulloch, M. D. McGehee, *Nano Lett.* **2009**, *9*, 4153.

[18] I.-W. Hwang, J. Young Kim, S. Cho, J. Yuen, N. Coates, K. Lee, M. Heeney, I. McCulloch, D. Moses, A. J. Heeger, *J. Phys. Chem. C* **2008**, *112*, 7853.

[19] A. Zusan, K. Vandewal, B. Allendorf, N. H. Hansen, J. Pflaum, A. Salleo, V. Dyakonov, C. Deibel, *Adv. Energy Mater.* **2014**, *4*, DOI: 10.1002/aenm.201400922.

[20] S. Sweetnam, K. R. Graham, G. O. Ngongang Ndjawa, T. Heumüller, J. A. Bartelt, T. M. Burke, W. Li, W. You, A. Amassian, M. D. McGehee, *J. Am. Chem. Soc.* **2014**, *136*, 14078.

[21] S. Shoaee, S. Subramaniyan, H. Xin, C. Keiderling, P. S. Tuladhar, F. Jamieson, S. A. Jenekhe, J. R. Durrant, *Adv. Funct. Mater.* **2013**, *23*, 3286.

[22] T. M. Burke, M. D. McGehee, *Adv. Mater.* **2014**, *26*, 1923.

[23] C. Groves, *Energy Environ. Sci.* **2013**, *6*, 1546.

[24] F. Etzold, I. A. Howard, R. Mauer, M. Meister, T.-D. Kim, K.-S. Lee, N. S. Baek, F. Laquai, *J. Am. Chem. Soc.* **2011**, *133*, 9469.

[25] F. Etzold, I. A. Howard, N. Forler, A. Melnyk, D. Andrienko, M. R. Hansen, F. Laquai, *Energy Environ. Sci.* **2015**, DOI: 10.1039/c4ee03630a.

[26] S. Gélinas, A. Rao, A. Kumar, S. L. Smith, A. W. Chin, J. Clark, T. S. van der Poll, G. C. Bazan, R. H. Friend, *Science* **2013**, *343*, 512.

[27] I. A. Howard, R. Mauer, M. Meister, F. Laquai, *J. Am. Chem. Soc.* **2010**, *132*, 14866.

[28] F. Etzold, I. A. Howard, N. Forler, D. M. Cho, M. Meister, H. Mangold, J. Shu, M. R. Hansen, K. Müllen, F. Laquai, *J. Am. Chem. Soc.* **2012**, *134*, 10569.

[29] S. Gélinas, A. Rao, A. Kumar, S. L. Smith, A. W. Chin, J. Clark, T. S. van der Poll, G. C. Bazan, R. H. Friend, *Science* **2014**, *343*, 512.

[30] M. Schrader, R. Fitzner, M. Hein, C. Elschner, B. Baumeier, K. Leo, M. Riede, P. Bäuerle, D. Andrienko, *J. Am. Chem. Soc.* **2012**, *134*, 6052.

[31] N. Vukmirović, C. S. Ponseca, H. Němec, A. Yartsev, V. Sundström, *J. Phys. Chem. C.* **2012**, *116*, 19665.

[32] M. L. Jones, R. Dyer, N. Clarke, C. Groves, *Phys. Chem. Chem. Phys.* **2014**, *16*, 20310.

[33] O. Esenturk, J. S. Melinger, E. J. Heilweil, *J. Appl. Phys.* **2008**, *103*, 023102.

[34] T. M. Clarke, J. R. Durrant, *Chem. Rev.* **2010**, *110*, 6736.

[35] B. A. Gregg, *J. Phys. Chem. Lett.* **2011**, *2*, 3013.

[36] I. A. Howard, F. Etzold, F. Laquai, M. Kemerink, *Adv. Energy Mater.* **2014**, *4*, DOI: 10.1002/aenm.201301743.

Supporting Information

for *Macromol. Rapid Commun.*, DOI: 10.1002/marc.201500112

The Impact of Donor–Acceptor Phase Separation on the Charge Carrier Dynamics in pBTTT:PCBM Photovoltaic Blends

*Dominik W. Gehrig, Ian A. Howard, Sean Sweetnam, Timothy M. Burke, Michael D. McGehee, and Frédéric Laquai**

Supporting Information

for *Macromol. Rapid Commun.*, DOI: 10.1002/marc.201500112

The Impact of Donor-Acceptor Phase Separation on the Charge Carrier Dynamics in pBTTT:PCBM Photovoltaic Blends

Dominik W. Gehrig, Ian A. Howard, Sean Sweetnam, Tim M. Burke, Michael D. McGehee, Frédéric Laquai*

Materials. pBTTT-C14 was provided by Martin Heeney and coworkers. The synthesis was described earlier in the literature.[1] $PC_{70}BM$ was used as received.

Sample preparation. For the preparation of solar cells ITO-coated glass substrates were patterned by wet etching and cleaned by successive ultrasonication in detergent, acetone then *iso*-propanol. Subsequently, the samples were treated with an argon plasma for 15 min prior to spin-coating of a ~40 nm thick poly(3,4-ethylene-dioxythiophene):poly-(styrenesulfonate) (PEDOT:PSS) layer. The substrates were transferred into a nitrogen-filled glovebox and heated to 120 °C for 30 min. For the active layer deposition, pBTTT-C14 and $PC_{70}BM$ were dissolved in 1,2-dichlorobenzene at a total concentration of 12.5 mg mL^{-1} in a 1:1 molar ratio (4:6 by weight) or at a total concentration of 25 mg mL^{-1} with a 1:4 ratio by weight. Solutions were stirred overnight at 60 °C. Samples were spun at 60 °C at 800 rpm for 45 s and then placed into a closed petri dish to dry slowly in a solvent rich atmosphere. After drying overnight, the 1:1 molar samples were annealed at 180 °C for 10 min. The 1:4 samples were not annealed. As a top-electrode, a bilayer of 7 nm calcium and 150 nm aluminum was evaporated through a shadow mask. Spectroscopic samples were fabricated in the same way except that quartz substrates were used and no top-electrode was evaporated.

Steady-State Spectroscopy. Steady state absorption spectra were measured with a Perkin Elmer Lambda 25 spectrometer. The layer thickness was determined with a Tencor P10 surface profilometer.

Transient Absorption Spectroscopy. Transient absorption (TA) measurements were performed with a home-built pump-probe setup. To measure in the time range of 1-4 ns with a resolution of ~100 fs, the output of a commercial titanium:sapphire amplifier (Coherent LIBRA-HE, 3.5 mJ, 1 kHz, 100 fs) was split into two beams that pumped two independent commercial optical parametric amplifiers (Coherent OPerA Solo). One optical parametric amplifier (OPA) was used to generate the tunable excitation pulses in the visible, while the second OPA was used to generate the pump beam for white-light generation. For measurements in the spectral range between 550-1100 nm a 1300 nm pump of a few µJ was focused into a c-cut 3 mm thick sapphire window for white-light generation. The variable delay of up to 4 ns between pump and probe was introduced by a broadband retroreflector mounted on a mechanical delay stage. Mostly reflective elements were used to guide the probe beam to the sample to minimize chirp. The excitation pulse was chopped at 500 Hz, while the white-light pulses were dispersed onto a linear silicon photodiode array, which was read out at 1 kHz by home-built electronics. Adjacent diode readings corresponding to the transmission of the sample after an excitation pulse and without an excitation pulse were used to calculate ΔT/T.

For measurements in the time range between 1 ns to 1 ms with a resolution of ~1 ns, the excitation pulse was provided by an actively Q-switched Nd:YVO_4 laser (AOT Ltd. MOPA) at 532 nm. In this case the delay between pump and probe was controlled by an electronic delay generator (Stanford Research Systems DG535). TA measurements were performed at room temperature under a dynamic vacuum of $<10^{-5}$ mbar.

For TA measurements in the NIR spectral range covering 1100-2000 nm a 2100 nm pump was used to generate white-light in an yttrium vanadate window. Furthermore, a dichroic mirror was used to separate the residual pump beam (idler of the OPA at 2100 nm) from the broadband NIR supercontinuum. The NIR pulses were dispersed onto a Peltier-cooled 512 pixel long linear extended InGaAs array (Entwicklungsbüro Stresing) and read out as described above.

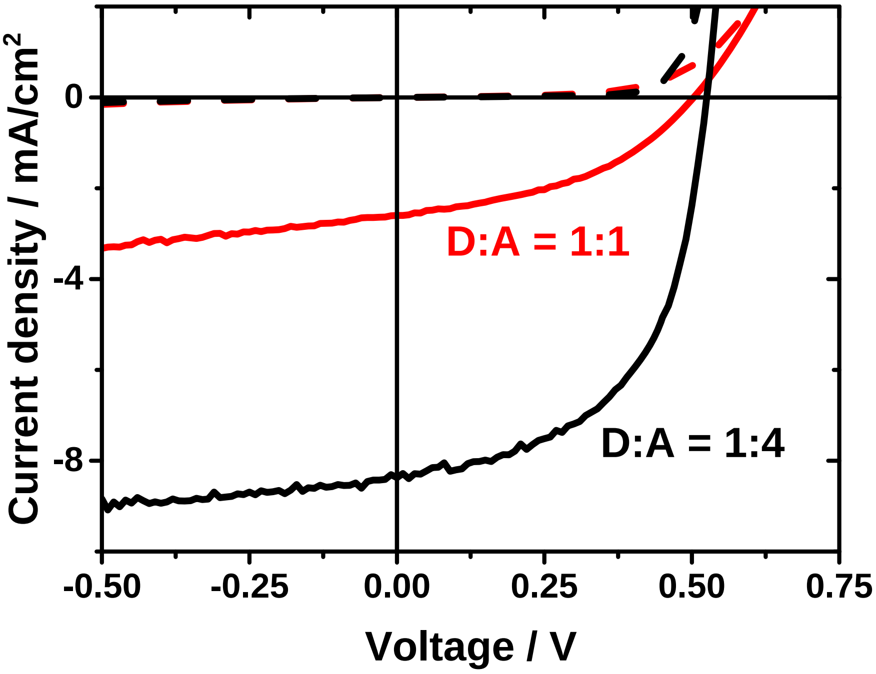

Figure S1. Current-Voltage (J-V) characteristics of pBTTT:PC$_{70}$BM solar cells at a donor-acceptor ratio of 1:1 (solid red line) and 1:4 (solid black line) and respective dark currents (dashed lines).

a)

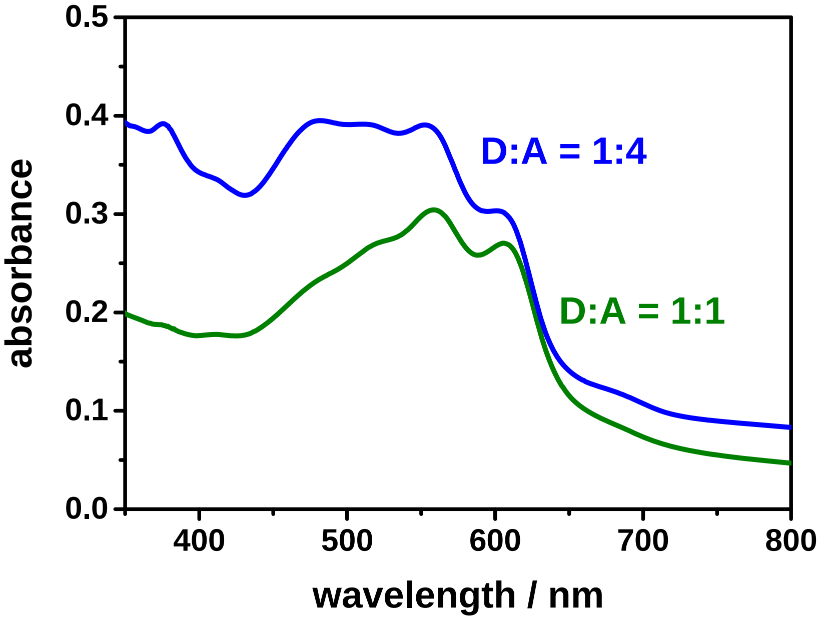
0.5
0.4
0.3
0.2
0.1
0.0
absorbance
400
500
600
700
800
wavelength / nm
D:A = 1:4
D:A = 1:1

b)

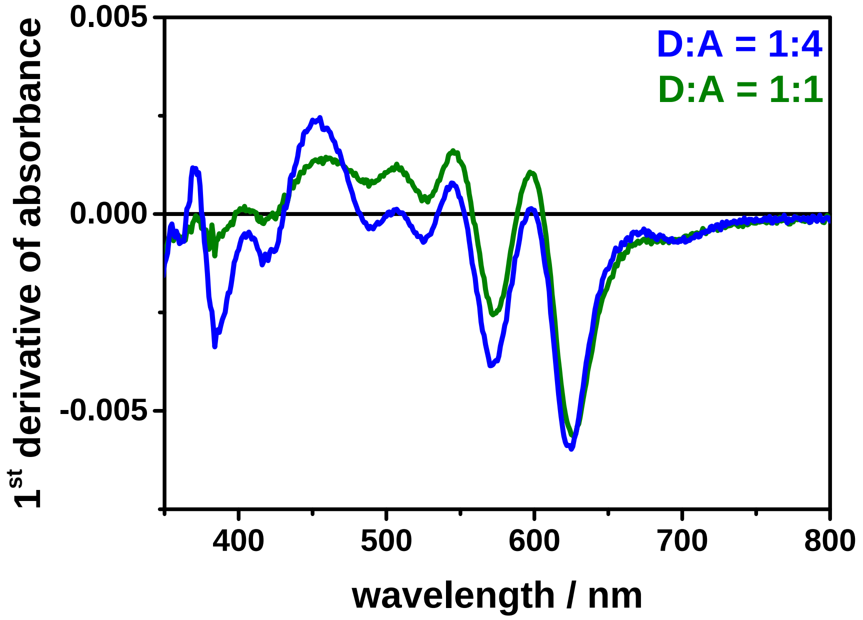
0.005
0.000
-0.005
1st derivative of absorbance
400
500
600
700
800
wavelength / nm
D:A = 1:4
D:A = 1:1

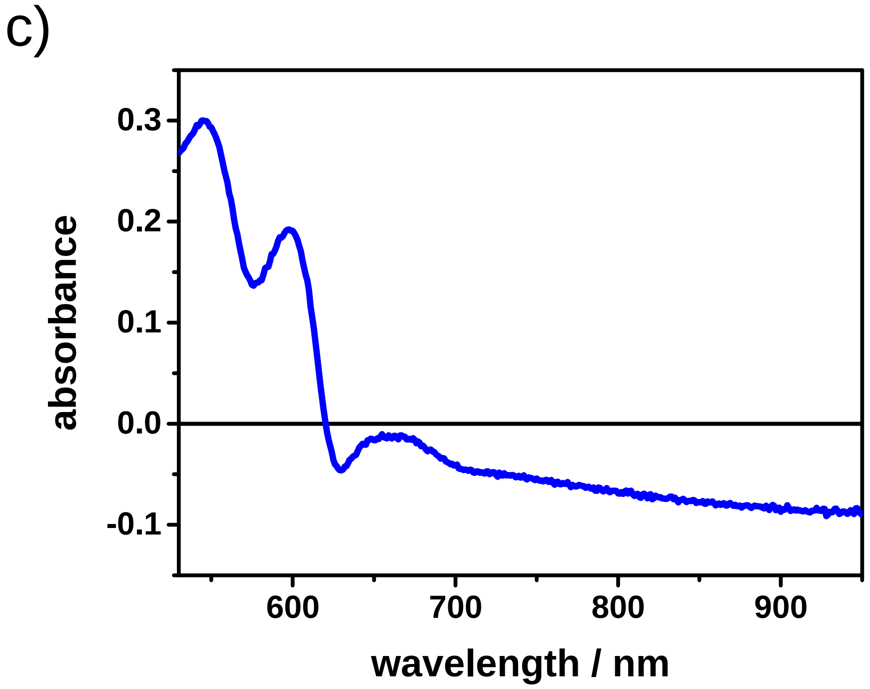

*Figure S2***.** (a) Thin film absorption of pBTTT:PC$_{70}$BM at a donor-acceptor ratio of 1:1 (green line) and 1:4 (blue line). (b) First derivative of the absorption of a 1:1 (green line) and 1:4 (blue line) blend of pBTTT:PC$_{70}$BM. This signal is equivalent to the electro-absorption.

(c) Superposition of the ground state absorption spectrum of a pBTTT:PC$_{70}$BM (1:4) blend and the first derivative of the absorption spectrum plus a Gaussian-shape photoinduced absorption profile the former accounting for the electroabsorption (EA) and the latter for the photo-induced absorption of charges, respectively.

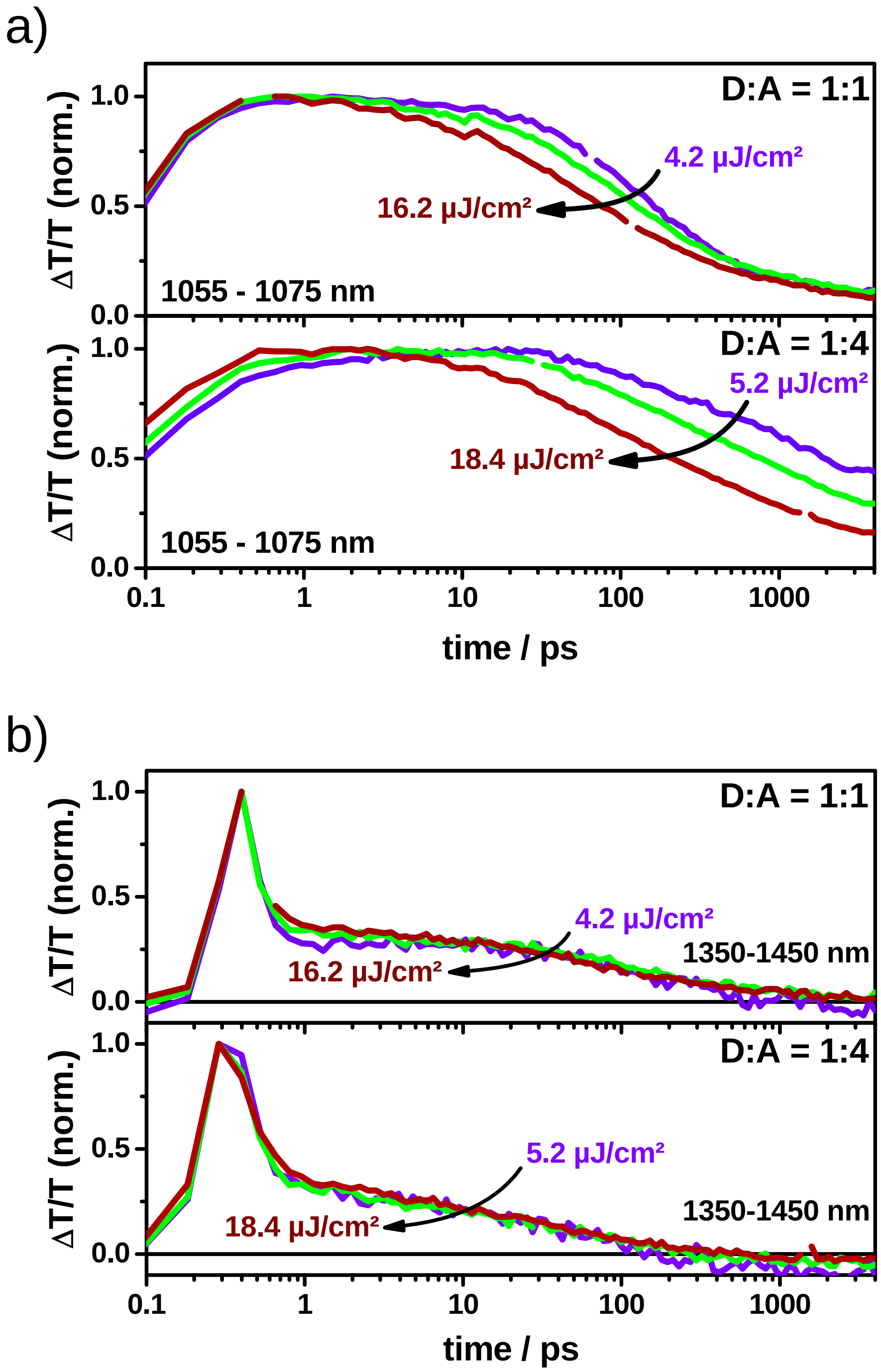

Figure S3. (a) Intensity-dependence of the dynamics of the charge-induced absorption in the spectral range from 1055-1075 nm of a pBTTT:PC$_{70}$BM blend at ratios of 1:1 (upper panel) and 1:4 (lower panel). (b) Dynamics tracked between 1350-1450 nm, that is the spectral range, in which the pBTTT exciton-induced and charge-induced absorption occur.

Note the fast sub-ps signal decay indicating ultrafast polymer exciton dissociation in both blends.

[1] I. McCulloch, M. Heeney, C. Bailey, K. Genevicius, I MacDonald, M. Shkunov, D. Sparrowe, S. Tierney, R. Wagner, W. Zhang, M. L. Chabinyc, R. J. Kline, M. D. McGehee, M. F. Toney, *Nat. Mater.***2006**, *5*, 328.

5 Comprehensive Discussion

In the following sections the findings of the case studies presented in Chapter 4 will be revisited and compared from different perspectives. Section 5.1.1 will give a comparison of Sections 4.1 and 4.2 which is the comparison of PDI *vs.* $PC_{61}BM$ blended with the low-bandgap donor polymer PBDTTT-C. Section 5.1.2 puts Sections 4.3 and 4.4 in context and thus is a comparison of PDI *vs.* fullerenes in combination with the small molecule donor p-DTS$(FBTTh_2)_2$. Furthermore, Section 5.2.1 will contrast Sections 4.1 and 4.3 *i.e.* polymer:PDI *vs.* small molecule:PDI, while Section 5.2.2 highlights the differences observed in Sections 4.2 and 4.4, namely the distinction of polymer:fullerene *vs.* small molecule:fullerene.

5.1 Comparison of PDI- and Fullerene-based Blends

5.1.1 Combination with PBDTTT-C

The investigation of the efficiency-limiting processes in PBDTTT-C:PDI blends implied that the main bottleneck in the cascade of processes in the perylene derivative-based devices was charge generation. This became evident when the maximum charge-induced signal height of the PBDTTT-C:PDI blend was compared to the signal height obtained in a PBDTTT-C:PCBM blend. In fact, the charge generation efficiency in the fullerene-based blend outperformed that of the perylene-based blend by a factor of 2 as shown with the charge signal yield in Figure 5 of the publication in Section 4.1.[210] The reason for the difference in performance is probably related to a series of factors, among them being the unfavorable domain size in PBDTTT-C:PDI blends. This resulted in slow, exciton-diffusion limited charge generation which opened up the pathway for radiative and non-radiative exciton decay. Additionally, the PDI used in this study is a two-

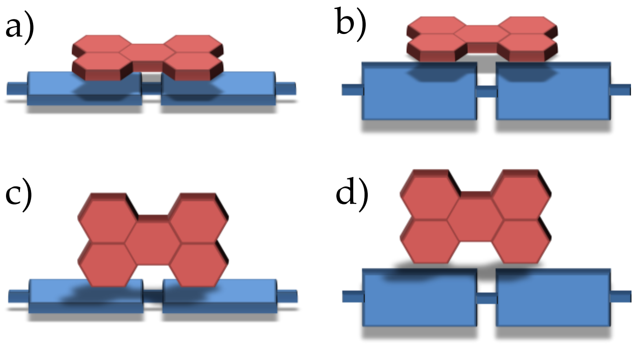

Figure 52. a) Face-on-face-on, b) edge-on-face-on, c) face-on-edge-on, and d) edge-on-edge-on orientation of the π–surfaces of a donor polymer with a two-dimensional perylene diimide.

dimensional, planar molecule and thus fundamentally different from the isotropic fullerene derivative $PC_{61}BM$. Consequently, different scenarios for the donor-acceptor intermolecular orientation of the π-surfaces of the PBDTTT-C:PDI blends are thinkable including *face-on-face-on*, *face-on-edge-on*, *edge-on-face-on*, and *edge-on-edge-on* as extreme configurations as shown schematically in Figure 52. The role of interfacial orientation will be discussed in more detail in Section 5.1.3.

In contrast to the exciton-diffusion limited charge generation observed in the perylene-based material system, charge generation occurred on a sub-ps timescale in blends composed of PBDTTT-C and $PC_{61}BM$. However, the further evolution of the charges differed enormously from PDI-based blends. When PDI was used as electron acceptor, ~90% of charges returned *via* bimolecular recombination on a timescale of tens of microseconds back to the ground state as obtained from the fit of a two-pool model to the data developed by Howard *et al*.[57] In stark contrast, the charges formed in PBDTTT-C:PCBM blends recombined already on the timescale of hundreds of picoseconds resulting in the formation of PBDTTT-C triplet excitons. This was explained by the bimolecular recombination of free charges with uncorrelated spins which results in singlet and triplet CT states according to spin statistics as shown schematically in Figure 53. This process could not be observed in PBDTTT-C:PDI blends.

The origin of the fundamentally different behavior can be explained by the energetic landscape of the two

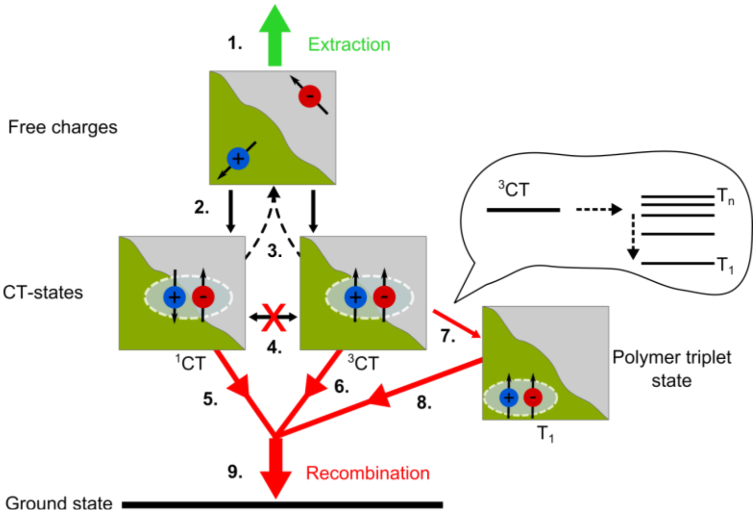

Figure 53. Mechanism for polymer triplet state population *via* bimolecular recombination of free charges into a triplet CT state. Step 1 is the favored process of charge extraction at the electrodes. Step 2 is the non-geminate recombination of free charges at the donor-acceptor interface to the singlet CT states (^{1}CT) or triplet CT states (^{3}CT). The ISC (step 4) between ^{1}CT and ^{3}CT is spin-forbidden and does not occur. Steps 5 and 6 are the recombination of CT states to the ground state. ^{3}CT states can recombine to the triplet state of the polymer (T_n) if the former is higher in energy than the latter. Polymer triplet states then recombine *via* phosphorescence, triplet-triplet or triplet-charge annihilation back to the ground state (step 8). Reprinted from reference with permission from the author.[223]

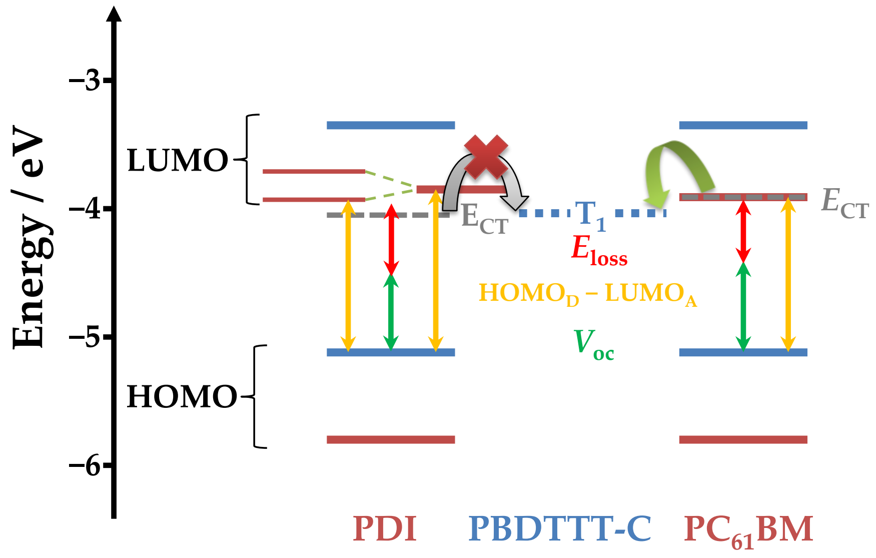

$\text{HOMO}_\text{D} = -5.12$ eV

$\text{LUMO}_\text{PDI} = -3.85$ eV

$E_\text{splitting} = 0.08$ eV → $\text{LUMO}_{\text{PDI}'} = -3.93$ eV

E_g $(\text{HOMO}_\text{D} - \text{LUMO}_\text{PDI}) = 1.27$ eV

E_g $(\text{HOMO}_\text{D} - \text{LUMO}_{\text{PDI}'}) = 1.19$ eV

$V_\text{OC} = 0.62$ V

E_loss $(E_\text{g} - \text{q}V_\text{OC}) = 0.65$ eV; $E'_\text{loss} = 0.57$ eV

E_CT (est.) $= \text{q}V_\text{oc} + 0.5$ eV $= 1.12$ eV

$\text{LUMO}_\text{PC61BM} = -3.91$ eV

E_g $(\text{HOMO}_\text{D} - \text{LUMO}_\text{A}) = 1.21$ eV

$V_\text{OC} = 0.71$ V

$E_\text{loss} = 0.5$ eV

E_CT (est.) $= \text{q}V_\text{oc} + 0.5$ eV $= 1.21$ eV

$\text{T}_1 = \text{S}_1 - 0.68$ eV $= 1.09$ eV

(Triplet of donor calculated from $\text{S}_1 - \text{T}_1$ splitting from calculations)

Figure 54. Proposed energetic landscape in blends of PBDTTT-C with PDI (left) and PC_{61}BM (right). Blue and red lines represent the energy levels of the donor and acceptor, respectively. The difference between the HOMO of the donor and the LUMO of the acceptor is indicated with orange arrows, the obtained V_OC with green arrows and the difference between both, *i.e.* E_loss, is shown with red arrows. The splitting of the LUMO of PDI originates from aggregation in thin films as seen from Figure 55. The energy of the CT state E_CT (grey dashed lines) is estimated by adding 0.5 eV to $\text{q}V_\text{OC}$ according to Janssen and co-workers.[228] The higher E_CT of PBDTTT-C:PCBM could allow for the conversion of ^{3}CT states to T_1 states located on the polymer (green curved arrow) while the lower E_CT of PBDTTT-C:PDI does not provide sufficient driving force (grey curved arrow).

blend systems which is shown in Figure 54. The values for the LUMO levels of PC_{61}BM are given as −3.7 eV[224], −3.90 eV[221], and −3.91 eV[205] in literature and of the *N*-alkyl substituted PDI as −3.80 eV[225] to −3.85 eV[226, 227] determined by cyclic voltammetry (CV). Thus, one would expect to obtain similar or even higher V_{OC} values if PDI is used as electron acceptor instead of PCBM according to Equation 5 which related V_{OC} to the LUMO and HOMO level of the acceptor and donor, respectively. However, it was found that for the specific material combination the V_{OC} of PCBM-based samples was as high as 0.71 V, while devices using PDI showed V_{OC} values which were reduced by ~0.1 V with respect to the fullerene. The energy loss E_{loss} as shown in Figure 54 is the difference between the HOMO$_D$–LUMO$_A$ gap and qV_{OC} and is larger for PDI compared to PCBM. According to Equation 6, V_{OC} and the energy of the CT state E_{CT} are directly related, which implies a lower E_{CT} in PBDTTT-C:PDI samples if the same losses are assumed. The difference between qV_{OC} (q = elementary charge) and E_{CT} reported in literature are in the range from 0.5 eV[228] and 0.6 eV.[41]

The lower V_{OC} and E_{CT} values in PDI-based blends can be a consequence of the PDI aggregation which results in the reduction of the LUMO level (which was determined from cyclic voltammetry for monomers in solution) according to the level splitting observed in H- and J-aggregates as shown in Section 2.1.2, Figure 9. This becomes obvious when the absorption of PDI in solution, *i.e.* of isolated PDI chromophores, is compared to the absorption of aggregated PDI in thin film as shown in Figure 55. The change in the absorption spectrum between solution and thin film suggests H-aggregation of the PDI derivative in thin films and a narrowing of the bandgap by 0.08 eV which is in line with the reduced V_{OC} and E_{CT} value. The aggregation effect, which lowers the LUMO level of PDI, also reduces the obtained V_{OC} and the CT energy. Thus, the conversion of ^{3}CT states to T_1 states located on the polymer is hindered as this process becomes less favorable due to a reduced driving force.

To conclude, the recombination of separated charge carriers on the sub-ns timescale in PBDTTT-C:PC$_{61}$BM occurs via a non-geminate recombination mechanism and is consequently depending on the excited-state

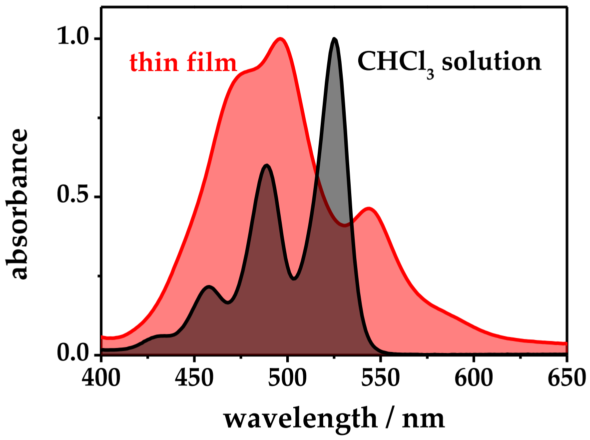

Figure 55. Normalized absorption of *N*-alkyl substituted perylene diimide (see **14** in Figure 30 on page 39) in chloroform solution at a concentration of 1 × 10^{-5} mol L^{-1} (black line) and in a thin film in a polystyrene matrix processed from chloroform solution (red line).

density as discussed in the publication shown in Section 4.2. Therefore, this process might be less relevant at solar illumination intensity which is lower than the intensity applied in spectroscopic experiments. Hence, the formation of triplets is not necessarily relevant for the operation of photovoltaic devices but shows that the energy of the CT state might be higher in PBDTTT-C:PCBM compared to PBDTTT-C:PDI blends which allows for a higher V_{OC} in turn contributing to a higher efficiency.

5.1.2 Combination with p-DTS(FBTTh$_2$)$_2$

The case study in Section 4.3 presented a blend consisting of p-DTS(FBTTh$_2$)$_2$ and a *N*-alkyl substituted perylene diimide derivative and the influence of the solvent additive DIO on the performance of the respective photovoltaic devices. Larger domains with a higher degree of intermolecular order were obtained when the solvent additive was used as confirmed by AFM and GIWAXS measurements, respectively, and as a result the power conversion efficiency of the blends was strongly improved from 0.13% to 3.1%.[115] This improvement in the efficiency was reflected in the photophysical properties which were revealed by time-resolved photoluminescence and TA spectroscopy. The increased domain size resulted in a less pronounced photoluminescence quenching as well as in a slower conversion of excitons to charges, while the higher degree of crystallinity became obvious in the more structured GSB in the transient absorption spectra. Additionally, the intensity dependence of the signal decay was more pronounced in the samples processed with DIO, pointing towards a higher fraction of free charge carriers that recombined *via* a bimolecular recombination mechanism.

p-DTS(FBTTh$_2$)$_2$:PC$_{71}$BM outperformed the respective blends based on PDI with a PCE value of 8.0%.[201] The photophysical properties were investigated by TA spectroscopy and – comparable to the donor:PDI blend – an exciton-diffusion limited charge generation was observed in agreement with the domain coarsening upon addition of DIO.[205] A fit to the ns-µs data revealed a fraction of ~85% of non-geminate recombination explaining the high efficiency of the respective photovoltaic blends.

In the following, only the most efficient blends, *i.e.* the optimized p-DTS(FBTTh$_2$)$_2$:PDI and the optimized p-DTS(FBTTh$_2$)$_2$:PC$_{71}$BM blends which are both obtained from spin-coating the active layer from chlorobenzene solution with 0.4 vol% DIO, are compared.

Within the cascade of processes, exciton quenching at the donor-acceptor interface is an important factor which determines the efficiency of an organic solar cell. Therefore, the initial exciton induced absorption is plotted *versus* the signal height at 1050 nm after 1 ns where charge-induced absorption is observed as shown in Figure 56. As both blends show an exciton-diffusion limited formation of charges, the initial signal height at 1220–1260 nm reflects the amount of excitonic states which are created upon absorption of a photon. Furthermore, at 1 ns all excitons have either decayed to the ground state or have been quenched at the donor-acceptor interface, thus no exciton contribution is observed at that delay time. Additionally, the majority of coulombically bound CT states have recombined to the ground state, so that only charges that might potentially contribute to the photocurrent of the solar cell remain. The graph includes linear fits to different selections of the data with varying excitation intensities. It becomes obvious from the plot in Figure 56 that blends that utilize the fullerene derivative PC$_{71}$BM as electron acceptor generate a higher amount of charges by a factor of 2.6 at low fluence. This value becomes even larger at higher excitation densities indicating a stronger contribution of non-linear processes *e.g.* exciton-exciton annihilation in PDI-based blends.

Reported PCE values for p-DTS(FBTTh$_2$)$_2$:PC$_{71}$BM and p-DTS(FBTTh$_2$)$_2$:PDI blends are 8.0% and 3.1%, respectively, which corresponds to an improvement by a factor of 2.58. This is in excellent agreement with the observation of the improved exciton-to-charge conversion efficiency observed for fullerene-based blends in the spectroscopic experiments as depicted in Figure 56. From this finding, one can conclude that the bottleneck *i.e.* the efficiency-limiting process in this small molecule:PDI blend is the process of charge generation and not charge transport or extraction. This is analogous to the polymer-based solar cells which were analyzed in Section 4.1 where charge generation limited the efficiency of the polymer:PDI blend.

However, a clear difference exists between the p-DTS(FBTTh$_2$)$_2$ and the PBDTTT-C-case study. In the polymer case, only blends using PDI as acceptor showed exciton-diffusion limited charge generation while

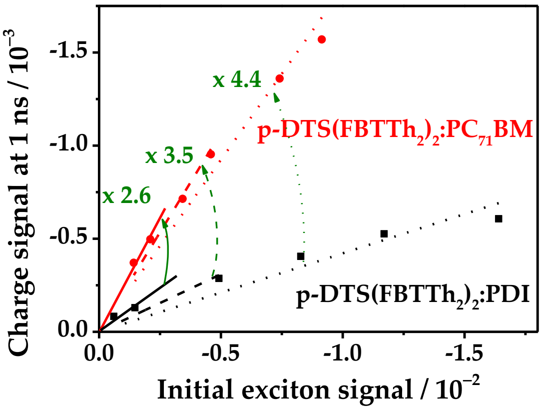

Figure 56. Signal height ΔT/T of the charge-induced absorption (1050–1090 nm) plotted *versus* the initial exciton-induced absorption height (1220–1260 nm) for p-DTS(FBTTh$_2$)$_2$ blended with PC$_{71}$BM (red) and PDI (black). Both blends show a non-linear dependence for higher excitation densities indicating exciton-exciton annihilation. Solid lines represent linear fits to the data with lower excitation densities, dashed lines fits to medium excitation densities, and dotted lines show linear fits to all data points.

the fullerene-based blends exhibited sub-ps charge generation. In the case of p-DTS(FBTTh$_2$)$_2$ both blends with PDI and PCBM showed slow exciton quenching and thus slow charge generation. This observation allows the conclusion that exciton-diffusion limited charge generation is not exclusively responsible for the low charge yield in PBDTTT-C:PDI but also other factors such as the interfacial orientation of the donor and acceptor must be important.

Furthermore, the LUMO levels of the acceptor molecules and the obtained open-circuit voltage are of interest. Reported LUMO values measured by CV are −4.3 eV[201] to −3.91 eV[229] for PC$_{71}$BM and −3.85 eV[227] for PDI. According to that, a higher V_{OC} value is expected if PDI is used as electron acceptor if Equation 5 is applied which relates V_{OC} to the HOMO$_D$−LUMO$_A$ gap. However, the reported V_{OC} values are 0.78 V in both cases which shows that bigger losses occur for PDI as compared to PCBM and stresses again the important role of aggregation in PDI blends and the concomitant effect of the altered LUMO level in the PDI based solar cells as discussed before.

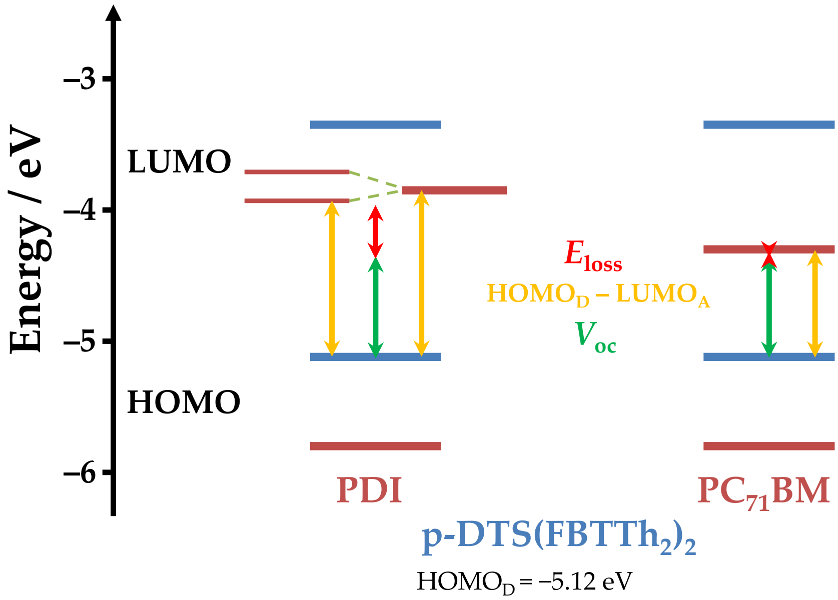

PDI
LUMO$_{PDI}$ = −3.85 eV
E_g (HOMO$_D$ – LUMO$_{PDI}$) = 1.27 eV
E_g (HOMO$_D$ – LUMO$_{PDI'}$) = 1.19 eV
V_{OC} = 0.78 V
E_{loss} (E_g – V_{OC}) = 0.49 eV/0.41 eV

PC$_{71}$BM
LUMO$_{PC71BM}$ = −4.3 eV
E_g (HOMO$_D$ – LUMO$_{PCBM}$) = 0.82 eV
V_{OC} = 0.78 V
E_{loss} = 0.04 eV

Figure 57. Proposed energetic landscape in blends of p-DTS(FBTTh$_2$)$_2$ with PDI (left) and PC$_{71}$BM (right). Blue and red lines represent the energy levels of the donor and acceptor, respectively. The difference between the HOMO of the donor und the LUMO of the acceptor is indicated with orange arrows, the obtained V_{OC} with green arrows and the difference between both, *i.e.* E_{loss}, is shown with red arrows.

The situation in p-DTS(FBTTh$_2$)$_2$:PC$_{71}$BM deserves more attention. In this blend the offset between the HOMO of the donor and the LUMO of the acceptor is 0.82 eV according to values taken from literature.[201, 205] On the other hand, the qV_{OC} (q is the elementary charge) obtained from these devices is 0.78 eV which results in a minor energetic loss of 0.04 eV with respect to E_g if a LUMO level of −4.3 eV is taken into account. However, the deviations in the reported LUMO values for PC$_{71}$BM should be noted which makes a clear discussion difficult. For instance, if a higher LUMO level of −3.91 eV is taken into account, the theoretical loss is increased to −0.43 eV.

5.1.3 Summarizing Remarks – The Role of Interfacial Orientation

To summarize the previous two sections, it became obvious that the main bottleneck in photovoltaic blends which use a planar perylene diimide derivative is the process of exciton quenching and charge generation at the donor-acceptor interface. Therefore, the role of interfacial orientation will be discussed in the following paragraphs.

Janssen and co-workers showed in 2005 with a model system based on perylene diimide and oligo(*p*-phenylene vinylene) that charge transfer kinetics depended strongly on the orientation in the self-assembled aggregates of the donor-acceptor compounds shown in Figure 58.[230] The nature of the aggregated species, *i.e.* H- and J-aggregates, was adjusted by the substitution of the bay-position of the PDI core. The analysis of UV/Vis spectra revealed that **83** and **84** formed J-aggregates in methylcyclohexane while **85** assembled in H-aggregates. The authors showed by TA spectroscopy that the rate of charge transfer is faster in J-aggregates than in H-aggregates. Furthermore, in J-aggregates charge transfer occurred as an intermolecular process while in H-aggregates charge-transfer was intramolecular. These experiments highlighted that the intermolecular orientation of donor- and acceptor-type moieties was essential for the

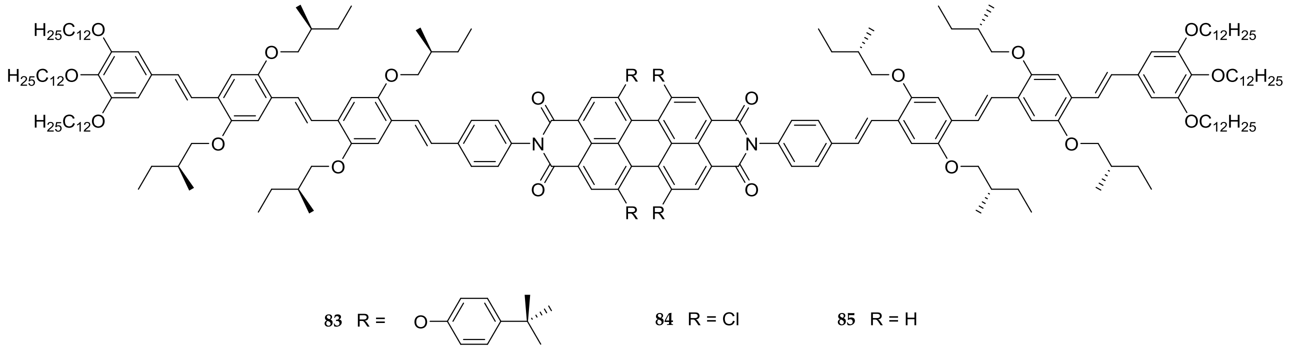

Figure 58. Chemical structures of the perylene diimide and oligo(*p*-phenylene vinylene) (OPV-PERY-OPV) structures used in the study by Janssen and co-workers as model systems to investigate charge-transfer kinetics as a function of the aggregation behavior.[230]

process of charge transfer. Yet, these experiments were performed in solution and electron-donating and electron-accepting units were covalently linked. Consequently, the findings cannot necessarily be transferred to thin films of blends of donor and acceptor molecules.

Moreover, the role of interfacial orientation was addressed recently by Aghamohammadi *et al.*[231] by an investigation of *N,N′*-octyl-3,4:9,10-perylenetetracarboxylic acid diimide (PTCDI-C_8, **86**) and diindenoperylene (DIP, **87**). The authors achieved control over the nanoscale morphology and fabricated vertical (Figure 59 c, left) and horizontal (Figure 59 c, right) DIP/PTCDI-C_8 heterojunctions. Both samples were investigated by means of emission spectroscopy. Blends with a vertical alignment of donor and acceptor showed an emission profile consisting of the single components as shown by the red, orange, and blue lines in Figure 59 b. In contrast, samples with a horizontal, *i.e.* face-on orientation of donor and acceptor

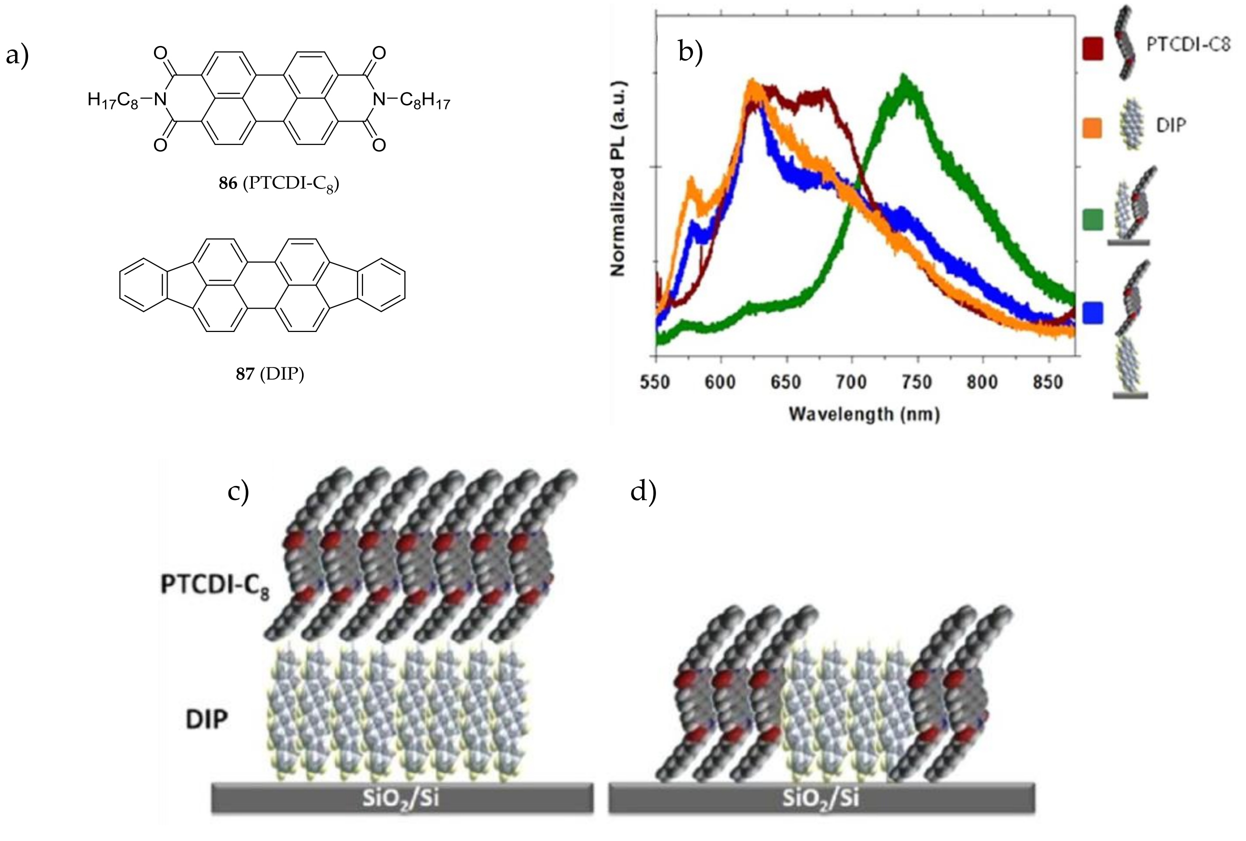

Figure 59. a) Chemical structures of PTCDI-C_8 and DIP; b) Emission measurements of PTCDI-C_8 (red line), DIP (orange line) and blend films with edge-on orientation (blue line, configuration c.) and blend films with face-on orientation (green line, configuration d); c) packing motif with edge-on configuration that does not allow for exciton quenching in which the resulting emission spectrum (blue line) shows a superposition of the single components (red and orange lines); d) PTCDI-C_8 and DIP in face-on configuration. In that case a new emission band (green line) evolves which is assigned to CT state emission. Reprinted with permission from reference [231]. Copyright (2014) American Chemical Society.

molecules showed a new emission (green line) which was assigned to the radiative decay of interfacial CT states which are enabled by the better overlap of π-orbitals. The authors inferred on basis of their data that charge transfer, and thus charge generation leading to efficiently working devices is only possible if a favorable orientation of donor and acceptor is achieved.

The question about the influence of the interfacial orientation of the donor and acceptor has also been addressed very recently by Schubert *et al.* on a polymer-polymer-based material system, namely a combination of P3HT (structure **1** in Figure 15 on page 19) as electron donating material and P(NDI2OD-T2) (**57** in Figure 34 on page 50) as electron acceptor.[165] The authors characterized the optical and electrical properties of the blend films depending on different processing solvents and used different techniques to analyze the thin film morphology including x-ray experiments. The findings of these experiments were correlated with information about the photophysics obtained by TA spectroscopy. The most efficient dissociation of CT states and thus the maximum PCE of 1.07% were obtained when blends were processed from a 1:1 mixture of xylene and chloronaphthalene as solvent. Under this condition, the donor and acceptor polymer backbone showed a face-to-face orientation. If samples were processed from pure xylene a mainly perpendicular orientation between donor and acceptor was obtained which resulted in devices with a decreased PCE of 0.08% which clearly showed the importance of a favorable orientation of the conjugated π-surfaces.

In a BHJ, as in the case of the investigated donor:PDI blends, a distribution of the orientation of the π-surfaces of donor and acceptor can be obtained. Consequently, the BHJ will exhibit donor-acceptor orientations that allow for efficient charge transfer but also donor-acceptor combinations that will lead to a return of the system to the ground state without undergoing charge transfer. This could explain why the initial process of exciton quenching at the donor-acceptor interface is the efficiency-limiting process in PBDTTT-C:PDI as well as in p-DTS(FBTTh$_2$)$_2$:PDI devices which both used planar PDI derivatives as electron acceptor. On the contrary, isotropic fullerene derivatives overcome this problem and are more likely to exhibit a favorable orientation at the D-A interface. Furthermore, this is in line with recent TA experiments of Durrant and co-workers who observed a similar charge generation efficiency in blends of PBDTTT-CT and a twisted PDI-dimer in which two perylene units are linked *via* hydrazine at the imide position (see structure **15** in Figure 30 on page 39) compared to PBDTTT-CT:PCBM.[117] The twisted PDI-dimer did not suffer from unfavorable D-A interfacial orientation and therefore showed similar behavior as the isotropic fullerene.

5.2 Comparison of Polymer- and Small Molecule-based Blends

This section will compare the photophysical behavior of the donors PBDTTT-C and p-DTS(FBTTh$_2$)$_2$ in combination with PDI (Section 5.2.1) and fullerene derivatives (Section 5.2.2).

5.2.1 Combination with PDI

The behavior of PDI with the polymer donor and small molecule donor was rather similar as shown in the framework of this thesis. As discussed before, the main efficiency-limiting process was the process of charge generation in both donor:PDI blends. PDI showed exciton-diffusion limited charge generation with PBDTTT-C as well as with p-DTS(FBTTh$_2$)$_2$ which could be explained by the propensity of the planar PDI to form rather large, pure domains enabled by the flat π-surface without sterically demanding substituents. Additionally, it could be shown that the decreased charge generation efficiency in comparison to their fullerene counterparts is related to the non-isotropic nature of the planar PDI derivative.

However, p-DTS(FBTTh$_2$)$_2$:PDI based solar cells outperformed their polymeric PBDTTT-C:PDI counterparts in every respect, namely V_{OC}, J_{SC}, FF, and thus also PCE as summarized in Table 1. Furthermore, the current-voltage characteristics revealed a stronger field-dependence as shown by time-delayed collection field (TDCF) measurements in the case of PBDTTT-C:PDI blends compared to the J-V curve of p-DTS(FBTTh$_2$)$_2$:PDI blends which saturated for high negative bias. This in turn limits the FF in the polymer-based devices. Moreover, V_{OC} differs strongly between the two blends although the energy levels of PBDTTT-C and p-DTS(FBTTh$_2$)$_2$ are virtually identical. This indicates that recombination losses in PBDTTT-C:PDI blends are more pronounced.

Table 1. Summary of the figures of merit of PBDTTT-C:PDI and p-DTS(FBTTh$_2$)$_2$:PDI solar cells.[115, 210]

Photovoltaic parameters	PBDTTT-C:PDI	p-DTS(FBTTh$_2$)$_2$:PDI
V_{OC} / V	0.62	0.78
J_{SC} / mA cm^{-2}	4.0 *	7.0
FF	0.46	0.57
PCE / %	1.2	3.1

* corrected for 0.7 suns illumination

In addition the photovoltaic figures of merit, differences in the recombination dynamics between PBDTTT-C:PDI and p-DTS(FBTTh$_2$)$_2$:PDI blends could be identified. The bimolecular recombination γ rate should scale with the sum of electron and hole mobility for Langevin-type bimolecular recombination according to the following equation:[232]

$$\gamma = \frac{q}{\varepsilon}(\mu_e + \mu_h) \qquad \text{Equation } \mathbf{26}$$

It should be taken into account that larger mobility values favor faster non-geminate recombination on the one hand, but also enable faster charge extraction on the other hand. Consequently, a high recombination rate is not detrimental if charge extraction is also high due to large charge carrier mobility.

Mobility values for PBDTTT-C, p-DTS(FBTTh$_2$)$_2$, and PDI as found in literature and photophysical parameters are given in Table 2. From these mobility values one would expect faster non-geminate recombination in blends of p-DTS(FBTTh$_2$)$_2$:PDI than in PBDTTT-C:PDI as the mobility of the former donor is twofold increased compared to the mobility of the latter donor. However, the non-geminate recombination rate was larger in the polymer:PDI blend than in the small molecule:PDI blend. This might indicate that non-geminate recombination was competing stronger with extraction and hence limiting the efficiency and V_{OC} in PBDTTT-C:PDI compared to p-DTS(FBTTh$_2$)$_2$:PDI blends. Furthermore, the extraction of free charges was hindered which limited both the obtainable current density and the fill factor.

Table 2. Parameters extracted from TA spectroscopy and mobility values of the materials.

Parameter	**PBDTTT-C:PDI**	**p-DTS(FBTTh$_2$)$_2$:PDI**
GSB loss after 1 ns	75-83%	72-91%
Fraction of non-geminate decay (f)	90.0%	75.7%
Order of non-geminate decay (λ+1)	1.63	1.61
Non-geminate decay rate (γ)	4.06×10^{-21} $(\text{cm}^3)^l$ s^{-1}	1.32×10^{-21} $(\text{cm}^3)^l$ s^{-1}
Effective non-geminate recombination rate (γ_{eff})	3.42×10^{-11} cm^3 s^{-1}	4.27×10^{-12} cm^3 s^{-1}
Geminate recombination rate k/ decay constant τ	7.61×10^8 s^{-1} / 1.31 ns	8.25×10^8 s^{-1} / 1.21 ns
$\mu(\text{h}^+)/\mu(\text{e}^-)$ / cm^2 (Vs)$^{-1}$	$(5.53\text{-}8.6) \times 10^{-4}$ [233]/< 8×10^{-5} [105]	1.2×10^{-3} [205]/ < 8×10^{-5} [105]

5.2.2 Combination with Fullerene Derivatives

The comparison of PBDTTT-C:PC$_{61}$BM devices with the respective p-DTS(FBTTh$_2$)$_2$:PC$_{71}$BM devices showed similar photovoltaic performance. The strongest difference was found for J_{SC} which partly originated from the stronger absorption in the visible part of the spectrum of PC$_{71}$BM compared to PC$_{61}$BM. However, the photophysics exhibited remarkable differences as described in the following paragraphs.

Firstly, PBDTTT-C:PC$_{61}$BM showed ultrafast exciton quenching at the donor-acceptor interface and thus CT states were generated on a sub-ps timescale. In contrast, p-DTS(FBTTh$_2$)$_2$:PC$_{71}$BM blends showed distinct

Table 3. Summary of the figures of merit of PBDTTT-C:PC$_{61}$BM and p-DTS(FBTTh$_2$)$_2$:PC$_{71}$BM solar cells.

Photovoltaic parameters	PBDTTT-C:PC$_{61}$BM	p-DTS(FBTTh$_2$)$_2$:PC$_{71}$BM
V_{OC} / V	0.71	0.72
J_{SC} / mA cm^{-2}	5.70	6.92
FF	0.51	0.57
PCE / %	2.83	3.56

contributions of p-DTS(FBTTh$_2$)$_2$ exciton-induced absorption that decayed with an inverse rate of 27–44 ps depending on the excitation density, in addition to an ultrafast charge generation which accounted for ~25% of the signal. This indicates that the morphology differed for the investigated blends. This is supported by the morphology reported recently in literature. On the one hand, the domain size for p-DTS(FBTTh$_2$)$_2$:PC$_{71}$BM were found to be up to 40 nm.[234] On the other hand, Zusan *et* al. proposed for PBDTTT-C:PC$_{71}$BM blends processed from chlorobenzene without DIO – which is the case in the present investigation – the formation of intermixed donor-acceptor domains alongside pure fullerene domains with diameters between 100 nm and 200 nm.[235] This morphology is in perfect agreement with the exclusively ultrafast charge generation which was observed in spectroscopic experiments in which the polymer was optically excited.

Furthermore, charge recombination differed strongly. p-DTS(FBTTh$_2$)$_2$:PC$_{71}$BM samples recombined *via* bimolecular recombination on a μs timescale with a non-geminate recombination rate of 1.25×10^{-11} cm^3 s^{-1} to the ground state. On the contrary, bimolecular recombination occurred in PBDTTT-C:PC$_{61}$BM blends already on a sub-ns timescale with a non-geminate recombination rate of 2.22×10^{-10} cm^3 s^{-1}. However, charges did not recombine to the ground state but populated the triplet state of the polymer. To allow the $^3\text{CT} \rightarrow T_1$ transition, the CT state energy needs to be higher than the energy of the triplet state of the polymer in order to provide the required driving force. Therefore, the following paragraphs will discuss the differences in the energetic landscape of both blends, namely the energy of the CT state and the triplet state energy.

Firstly, the energy of the CT state is discussed. As shown earlier in Equation 6 (see page 17), E_{CT} correlates with V_{OC} which is reduced by radiative and non-radiative losses. Moreover, V_{OC} and thus also E_{CT} is determined by the HOMO of the donor and the LUMO of the acceptor (see Equation 5). The polymer:fullerene and the small molecule:fullerene sample showed nearly the same V_{OC} value which suggests similar E_{CT} if similar losses are assumed which is in agreement with recent literature.[40, 41, 228] Additionally, PBDTTT-C and p-DTS(FBTTh$_2$)$_2$ possess identical HOMO levels with −5.12 eV determined by CV.[199, 219] PC$_{61}$BM and PC$_{71}$BM exhibit similar LUMO levels with −3.91 eV and −3.85 eV, respectively.[201, 236] These similar energy values are in agreement with the similar V_{OC} and thus also suggest a similar CT state energy. However, reported LUMO values for $PC_{71}BM$ are not very consistent and values are also given as −4.3 eV in literature.[205] Such a low LUMO energy would suggest a lower CT state energy for blends based on $PC_{71}BM$ and thus explain why the driving force for triplet generation is not provided in this blend.

To avoid the uncertainties associated with the differences between the LUMO of $PC_{61}BM$ and $PC_{71}BM$, a blend film of p-DTS(FBTTh$_2$)$_2$ and $PC_{61}BM$ (which was not included in Section 4.4) was investigated with TA spectroscopy. This blend did not exhibit triplet formation in analogy to p-DTS(FBTTh$_2$)$_2$:$PC_{71}BM$ blends which can be seen from the normalized spectra of a respective film shown in Figure 60. This blend film exhibited exclusively contributions of exciton- and charge-induced absorption. Energy levels for p-DTS(FBTTh$_2$)$_2$:$PC_{61}BM$ and PBDTTT-C:$PC_{61}BM$ are nearly identical and consequently the energy of the CT state cannot explain the different behavior of PBDTTT-C and p-DTS(FBTTh$_2$)$_2$.

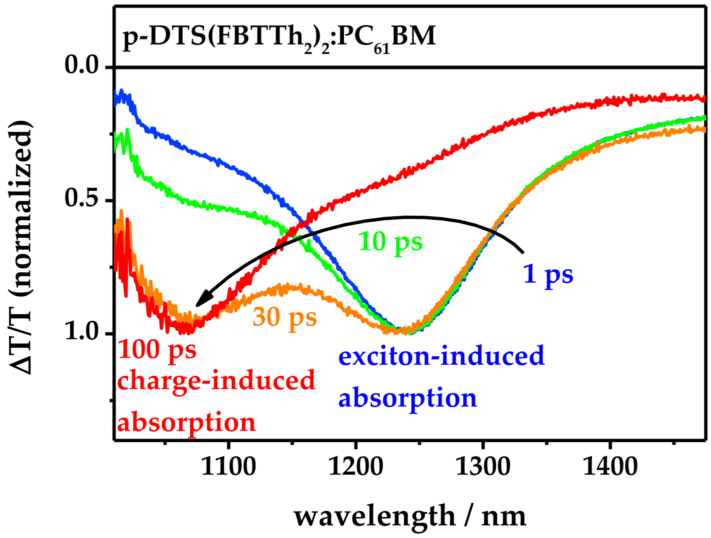

Figure 60. Normalized ps-ns transient spectra at various time delays of a p-DTS(FBTTh$_2$)$_2$:$PC_{61}BM$ blend after excitation with 700 nm. After exciton-quenching and formation of the charges no further evolution of the signal is observed.

Apart from E_{CT}, the energy of the triplet state is important for the determination of the $^3CT \rightarrow T_1$ driving force. Therefore, the energy of the triplet state is discussed in the following paragraph. Density functional theory calculations (DFT, B3LYP) on both donor materials were performed to estimate the energy of the triplet state of the two materials. It should be noted that calculations were done on single molecules in the vacuum and for the polymer with three repeat units. The results of the calculations are shown in Figure 61. The calculations suggest a higher triplet state energy in the PBDTTT-C compared to p-DTS(FBTTh$_2$)$_2$ with values of 1.25 eV and 1.03 eV, respectively. This would imply that triplet formation is more likely in p-DTS(FBTTh$_2$)$_2$ which contradicts the observations in the spectroscopic experiments. Furthermore, the

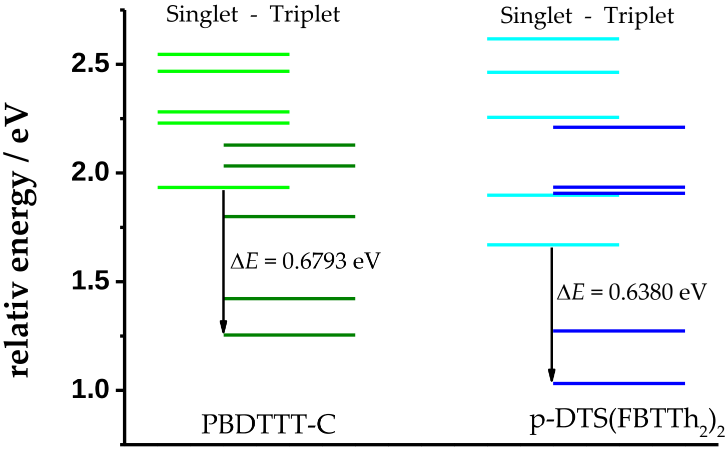

Figure 61. Calculations of the singlet (green and cyan lines) and triplet (olive and blue lines) energy levels of PBDTTT-C (left) and p-DTS(FBTTh$_2$)$_2$ (right).

calculations resulted in a higher energy of the first excited singlet state S_1 for PBDTTT-C with 1.93 eV compared to 1.67 eV for p-DTS(FBTTh$_2$)$_2$. However, this is in contradiction to the virtually identical HOMO–LUMO gaps. Moreover, both materials exhibit a similar onset of absorption with 760 nm/1.63 eV and 745 nm/1.66 eV for PBDTTT-C and p-DTS(FBTTh$_2$)$_2$, respectively. Therefore, the relative singlet–triplet splitting and not the absolute values obtained from calculations are considered for the further argumentation. One can see that PBDTTT-C has a S_1–T_1 splitting which is 41 meV larger than that of p-DTS(FBTTh$_2$)$_2$. Considering the S_1–T_1 splitting and the S_1 energy derived from the onset of absorption, the T_1 energy of PBDTTT-C is ~74 meV smaller than the T_1 energy of p-DTS(FBTTh$_2$)$_2$. This difference might be enough to enable triplet state population in PBDTTT-C but not in the p-DTS(FBBTh$_2$)$_2$.

Furthermore, Dyakonov and co-workers also reported about triplet generation in p-DTS(FBTTh$_2$)$_2$:PC$_{71}$BM blends at conferences.[237, 238] The authors employed spin-sensitive techniques in combination with the detection of photo- and electroluminescence and their experiments suggested a high amount of triplet excitons. The underlying mechanism is postulated to be the electron back transfer of the CT state. However, this work has not been published yet which complicates the comprehensive comparison with our spectroscopic data. Furthermore, the sensitivity of the experiments is very high so that already very low traces of triplets are detectable.

6 Conclusions and Outlook

6.1 Design Principles for Novel Non-fullerene Acceptors

This thesis showed that perylene diimide derivatives are a promising alternative for fullerene derivatives as electron-accepting materials in organic solar cells. However, only non-planar PDI derivatives are amongst the best-performing PDI-based acceptor structures with PCE values in excess of 6%[124, 126] while planar PDI molecules are limited to maximum PCE values of ~3% or even lower.[112, 114, 210] TA spectroscopy revealed that for blends of a planar PDI derivative (see structure **13** in Figure 30 on page 39) with donors based on a small molecule, namely p-DTS(FBTTh$_2$)$_2$, or a low-bandgap polymer, namely PBDTTT-C, the process of charge generation is the bottleneck in the cascade of processes leading to a photocurrent. Independent of the donor structure the charge yield was inferior compared to blends that used an isotropic fullerene derivative as electron acceptor. In the previous Section 5.1.3 the role of interfacial order was discussed and recent progress confirms the superior performance of twisted, non-planar molecular structures compared to planar derivatives not only for PDI-based acceptors but also for electron acceptors based on other aromatic systems.[161, 162] While state-of-the-art fullerene-free OPV often show high current density and open-circuit voltage due to the high spectral coverage and the engineered energy levels, the fill factor is still limited to below 0.57 even for the best devices.[126] On the contrary, state-of-the-art fullerene-based solar cells exhibit FF values of 0.75.[4] Consequently, the performance of non-fullerene based solar cells could be improved by ~30% if the FF was increased *e.g.* by reducing the field-dependence of charge generation and recombination. Very recently, Nuckolls and co-workers presented solar cells based on PTB7 and the PDI derivative **23** (see Figure 31 on page 40) which exceeded PCE values of 9% at the AMN-7 conference in Nelson, New Zealand, in February 2015, showing that non-fullerene structures can compete with the established fullerene derivatives. And still the development of new acceptor-structures is steadily ongoing and new structures – which are not any more included in the background of this thesis – are frequently published.[239] This confirms the trend that 3-D like structures can overcome the drawbacks inherent to planar acceptor structures which have been clarified in this thesis.

6.2 The Role of Triplets in Organic Photovoltaics – Open Questions

In Section 4.2 the population of polymer triplet states *via* non-geminate recombination on a sub-ns timescale was demonstrated for blends of the low bandgap donor polymer PBDTTT-C and PC$_{61}$BM. Very recently, Laquai and co-workers published studies on different donor polymer structures, namely the cyclopentadithiophene-benzothiadiazole copolymers PCPDTBT and PSBTBT[216] as well as the diketopyrrolopyrrole-based donor polymers PTDPP-TT and PFDPP-TT,[218] which also showed triplet formation *via* non-geminate recombination on a sub-ns timescale. Furthermore, a series of various DPP-type polymer structures were investigated during the work on this thesis and also showed similar photophysical behavior. Triplet states are frequently encountered and therefore the clarification of the role of triplets in OPV is still an important task.

However, the precise mechanism of triplet state generation is still under debate and recent studies by Durrant and co-workers suggest also the spin-state mixing of ^{1}CT states as a route to triplet states.[240] For a deeper understanding of the photophysics apart from the mere phenomenological description of triplet state population, a systematic investigation of the energetics in the blends could be beneficial. For example, exact measurements of the CT state energy with electroluminescence and photothermal deflection spectroscopy[96] and a determination of the energy of the triplet state, for instance with time-resolved, pulsed-laser photoacoustic calorimetry as done earlier for C_{60},[241] could be of interest. Moreover, higher demanding theoretical approaches could be applied to backup experimental results and get more precise calculations of the energy levels in the solid state where the packing behavior of the materials is considered which might influence E_{CT} as well as E_T compared to calculations performed in vacuum. These new findings could be used to refine the postulated energetic landscapes in the 'Comprehensive Discussion' of this work and explain the observed differences between PDI and PCBM as well as between PBDTTT-C and p-DTS(FBTTh$_2$)$_2$.

On the experimental side, especially for transient absorption spectroscopy, a higher sensitivity is desirable. The lowest excitation intensity in TA spectroscopy is often dictated by the signal-to-noise ratio which should still allow for meaningful conclusions from the data. However, the excitation intensity is often much higher compared to solar illumination conditions which are relevant for organic solar cells. Yet, high excitation densities will increase the influence of higher-order processes like exciton-exciton annihilation, exciton-charge annihilation, or non-geminate recombination and consequently affect also the formation of triplet states *via* such a pathway. A lower noise level, *e.g.* by the implementation of electronic noise filters like lock-in techniques or more stable supercontinuum generation, would allow for lower excitation intensities which in turn are closer to solar conditions. Thus, TA results could describe the processes in OPV devices better and artifacts associated with the high excitation intensity could be reduced.

Another aspect is that spectroscopic experiments are normally done on thin films without electrodes and therefore without the application of an electric field. TA spectroscopy measurements on devices in reflection could reveal the field dependence of triplet formation and in consequence if triplet formation could be suppressed by an electric field. Furthermore, field-dependent TA measurement could be of potential interest for material systems showing triplet formation.

6.3 Outlook – Further Fields of Research and Emerging Technologies

Besides the development of new acceptor structures, OPV research is still rapidly developing and fields of interest encompass the synthesis of novel donor structures, the optimization of device architectures including sophisticated tandem and triple-junction devices, the use of environmental-friendly, non-chlorinated solvents, and the realization of large-area printing processes.

Each of these research topics offers challenges which have to be addressed. For example, multi-junction solar cells show high V_{OC} values which correspond to the sum of the V_{OC} of the sub cells, however, the current density is limited by the current density of the weakest sub cell and hence current matching is desired. Janssen and coworkers showed a triple-junction solar cell consisting of a sub cell using a wide bandgap donor and two sub cells with an identical low bandgap donor to ensure matched currents with a V_{OC} of 2.33 V.[242] Molecular structures and the device layout with a total number of 9 layers are shown in Figure 62. Such a high V_{OC} enabled water splitting with an efficiency of 3.1%. Yet, a larger number of layers complicates the processing of the devices from solution and the identification of orthogonal solvent, *i.e.* solvents which do not dissolve the previous layer, can be difficult.

Also, the rapid development of lead halide perovskite opens new possibilities for photovoltaic systems which are not based on conventional silicon techniques. Huge scientific effort is invested in the variation of the organic part – typically used molecules are *e.g.* methyl ammonium (MA) and formamidinium (FA) – and

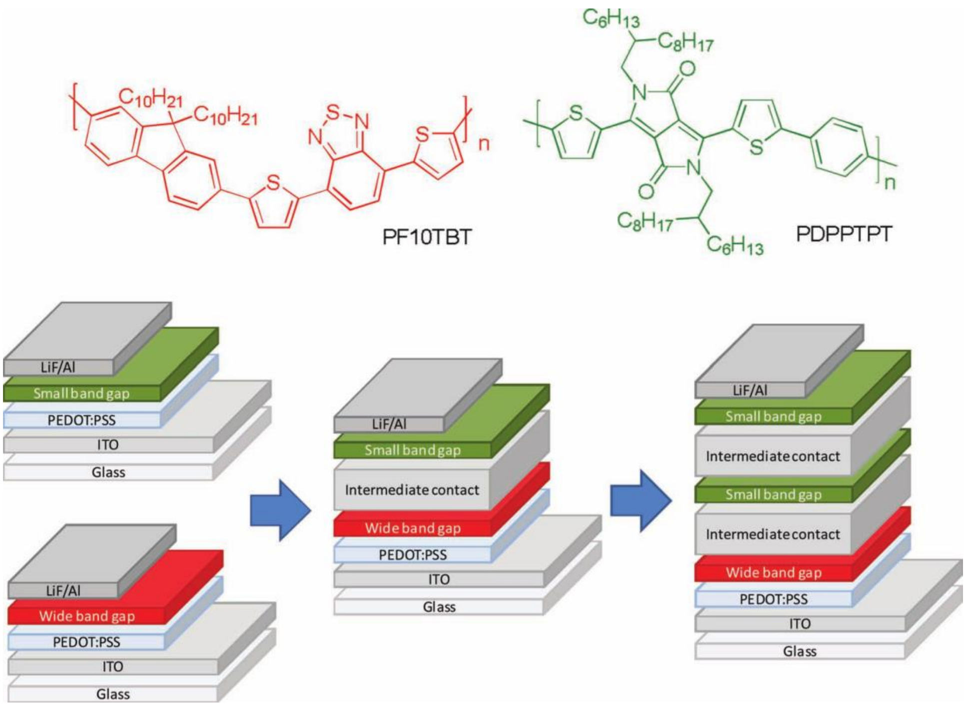

Figure 62. Molecular structures and device architecture as realized by Janssen and co-workers. Reprinted with permission from reference [242]. Copyright (2013) WILEY-VCH Verlag GmbH & Co. KGaA, Weinheim.

the use of different halides. For instance, the fraction of iodine, bromine or chlorine determines the absorption properties of the perovskite.[243] The bandgap of a formamidinium lead trihalide $FAPbI_yBr_{1-y}$ with varying bromine and iodine content can be tuned from 1.48–2.23 eV with a decreasing fraction of iodine.[243] Furthermore, reported diffusion lengths for holes/electrons are 105 nm/129 nm for $MAPbI_3$,[244] 813 nm/177 nm for $FAPbI_3$,[243] and 1213 nm/1069 nm for $MAPbI_{3-x}Cl_x$ which allows for large sample thickness.[244] One of the most important advantages of perovskite-based solar cells is the small exciton binding energy with reported values in the range from 2 meV[245] to 50 meV.[246] Furthermore, different concepts are realized with respect to the use of TiO_2 as electron-selective contact, namely mesoporous TiO_2 nanostructures *versus* compact TiO_2. The use of these nanostructures originates from the routes of perovskite which are found in the field of dye-sensitized solar cells (DSSC). It is highly debated, whether mesoporous structures are necessary at all and efficient perovskite solar cells have been realized which use only compact TiO_2 layers.[247] Moreover, perovskite-based solar cells can be vacuum-processed[247] or fabricated from solution[248] and therefore offer similar methods of production and flexibility compared to classic OPV. Recently, NREL-certified PCE values surpassed 20% showing the huge potential of perovskite-based solar cells to enter market applications.[53] However, a prerequisite for commercial success is to overcome critical points which include long-term stability and the substitution of the toxic lead by less harmful materials like tin. Additionally, *J-V* characteristics of perovskite-based solar cell often exhibit strong hysteresis effects which are still under debate. Concepts to explain the origin of hysteresis include for instance ion migration of excess ions, ferroelectric properties and a large defect density or interface states.[249]

Perovskites have also been in the focus of various spectroscopic studies and the behavior differs fundamentally from organic photovoltaic blends and the measurement.[250-254] For example, Piatkowski *et al.* demonstrated the sub-ps hole and electron injection into TiO_2 and the hole conductor, namely Spiro-MeOTAD.[252] However, the relative large thickness and the scattering associated with the thickness complicates spectroscopic experiments.

List of Abbreviations

A	acceptor
AFM	atomic force microscopy
ALS	alternating least squares
AM	air mass
BHJ	bulk-heterojunction
BS	beam splitter
BT	benzothiadiazole
CB	chlorobenzene
CCD	charge-coupled device
CFW	continuous filter wheel
CN	chloronaphthalene
CT	charge transfer
CuPc	copper phthalocyanine
CW	chopper wheel
D	donor
DFT	density functional theory
DIO	1,8-diiodooctane
DOS	density of states
DPP	diketopyrrolopyrrole
E_{CB}	coulomb binding energy
EFA	evolving factor analysis
E_{CT}	charge-transfer state energy
E_{g}	bandgap energy
$E_{\mathrm{S}}/E_{\mathrm{T}}$	energy of the singlet/triplet state

EQE	external quantum efficieny
F8BT	poly[(9,9-dioctylfluorenyl-2,7-diyl)-*alt*-co-(1,4-benzo-{2,1',3}-thiadiazole)]
FF	fill factor
GDM	gaussian disorder model
GIWAXS	grazing incidence wide-angle x-ray scattering
GS	ground state
GSB	ground state bleach
HOMO	highest occupied molecular orbital
IC	internal conversion
ICBA	indene-C60-bisadducct
IQE	internal quantum efficiency
ISC	intersystem crossing
ITO	indium tin oxide
J_{SC}	short-circuit current density
J-V	current-voltage
KMC	kinetic Monte Carlo
LCAO	linear combination of atomic orbitals
LUMO	lowest unoccupied molecular orbital
MCR	multivariate curve resolution
MEH-PPV	poly[2-methoxy-5-(2-ethylhexyloxy)-1,4-phenylene-vinylene]
MO	molecular orbital
NDI	naphthalene diimide
NIR	near infrared
NMI	naphthalene monoimide
NREL	national renewable energy laboratory
OD	optical density

OFET	organic field effect transistor
OPV	organic photovoltaics
P3HT	poly(3-hexylthiophene)
PBDTBDD	poly(((4,8-bis(5-(2-ethylhexyl)thiophen-2-yl)benzo[1,2-*b*:4,5-*b′*]dithiophene-2,6-diyl) bis(trimethyl))-co-(5,7-bis(2-ethylhexyl)benzo[1,2-*c*:4,5-*c′*]dithiophene-4,8-dione))
PBDTTPD	poly(benzo[1,2-*b*:4,5-*b′*]dithiophene-*alt*-thieno[3,4-*c*]pyrrole-4,6-dione)
PBDTTT-C	poly[(4,8-bis-(2-ethylhexyloxy)-benzo[1,2-*b*:4,5-*b′*]dithiophene)-2,6-diyl-alt-(4-(2-ethylhexanoyl)-thieno[3,4–*b*]thiophene))-2,6-diyl]
PBDTTT-CT	poly(4,8-bis(5-(2-ethylhexyl)-thiophene-2-yl)-benzo[1,2-*b*:4,5-*b′*]dithiophene-*alt* -alkylcarbonyl-thieno[3,4-*b*]thiophene)
PBDTTT-EFT/PTB7-Th/ PBDTT-F-TT/PBDTT-TT-F	poly({4,8-bis[(4-(2-ethylhexyl)thiophen-2-yl)]benzo[1,2-*b*:4,5-*b*']dithiophene-2,6-diyl}{3-fluoro-2-[(2-ethylhexyl)carbonyl]thieno[3,4-*b*]thiophenediyl})
PBDTTT-E-O	poly[4,8-bis-substituted-benzo[1,2-*b*:4,5-*b*']dithiophene-2,6-diyl-*alt*-4-substituted-thieno[3,4-*b*]thiophene-2,6-diyl]
PBDTT-TT	poly[4,8-bis(5-(2-ethylhexyl)thiophen-2-yl)benzo[1,2-*b*;4,5-*b*']dithiophene-2,6-diyl-*alt*-(4-2(2-ethylhexyl)3-fluorothieno[3,4-*b*]thiophene)-2-carboxylate-2,6-diyl]
PBTI3T	poly[*N*-(2-hexyldodecyl)-2,2′-bithiophene-3,3′-dicarboximide-*alt*-5,5-(2,5-bis(3-decylthiophen-2-yl)-thiophene)]
pBTTT	poly[2,5-bis(3-tetradecylthiophen-2-yl)thieno[3,2-*b*]thiophene]
Pc	phthalocyanine
$PC_{61}BM$	[6,6]-phenyl C61 butyric acid methyl ester
$PC_{71}BM$	[6,6]-phenyl C71 butyric acid methyl ester
PCDTBT	poly[*N*-9'-heptadecanyl-2,7-carbazole-*alt*-5,5-(4',7'-di-2-thienyl-2',1',3'-benzothiadiazole)]
PCE	power-conversion efficieny

PCPDTBT	poly[2,6-(4,4-bis-(2-ethylhexyl)-4H-cyclopenta[2,1-*b*:3,4-*b*']dithiophene)-*alt*-4,7(2,1,3-benzothiadiazole)]
PDI	perylene diimide
PDI	polydispersity index
PDPP3T	poly(diketopyrrolopyrrole-terthiophene)
PDS	photothermal deflection spectroscopy
p-DTS(FBTTh$_2$)$_2$	7,7′-(4,4-bis(2-ethylhexyl)-4H-silolo[3,2-*b*:4,5-*b*′]dithiophene-2,6-diyl)bis(6-fluoro-4-(5′-hexyl-[2,2′-bithiophen]-5-yl)benzo[*c*][1,2,5]thiadiazole)
PffBT4T-2DT	poly[(5,6-difluoro-2,1,3-benzothiadiazol-4,7-diyl)-*alt*-(3,3‴-di(2-decyltetradecyl)-2,2′;5′,2″;5″,2‴-quaterthiophen-5,5‴-diyl)]
PIA	photo-induced absorption
PL	photoluminescence
PMI	perylene monoimide
PSBTBT	poly(2,1,3-benzothiadiazole-4,7-diyl[4,4-bis(2-ethylhexyl)-4H-silolo[3,2-*b*:4,5-*b*']dithiophene-2,6-diyl]]
PSEHTT	poly[(4,4′-bis(2-ethylhexyl)dithieno[3,2-*b*:2′,3′-*d*]silole)-2,6-diyl-alt-(2,5-bis(3-(2-ethylhexyl)thiophen-2-yl)thiazolo[5,4-*d*]thiazole)]
PTB7	poly({4,8-bis[(2-ethylhexyl)oxy]benzo[1,2-*b*:4,5-*b*']dithiophene-2,6-diyl}{3-fluoro-2-[(2-ethylhexyl)carbonyl]thieno[3,4-*b*]thiophenediyl})
SCLC	space-charge limited current
SE	stimulated emission
Sn	singlet state
SSC	spatially separated charges
SubPc	subphthalocyanine
SVD	singular value decomposition
TA	transient absorption
TCO	transparent conductive oxide

TDCF	time-delayed collection field
TIPS	triisopropylsilylethynyl
T_n	triplet state
TRPL	time-resolved photoluminescence
TTA	triplet-triplet annihilation
Vis	visible
V_{OC}	open-circuit voltage
VR	vibrational relaxation
WAXS	wide-angle x-ray scattering
WLC	white-light crystal
XRD	x-ray diffraction

List of Scientific Contributions

Publications in Peer-reviewed Journals and Chapters in Edited Books in Descending Order

21) I. Schick, D. Gehrig, M. Montigny, B. Balke, M. Panthöfer, A. Henkel, F. Laquai and W. Tremel, "Effect of Charge Transfer in Magnetic-Plasmonic Au@MOx (M = Mn, Fe) Heterodimers on the Kinetics of Nanocrystal Formation",

Chem. Mater. **2015**, *Article ASAP*; DOI: 10.1021/acs.chemmater.5b01968

20) D. W. Gehrig, I. A. Howard and F. Laquai, "Charge Carrier Generation Followed by Triplet State Formation, Annihilation, and Carrier Recreation in PBDTTT-C:PC60BM Photovoltaic Blends", J. Phys. Chem. C **2015**, *119* (24), pp 13509–13515; DOI: 10.1021/acs.jpcc.5b03467

19) X. Zhuang, D. Gehrig, N. Forler, H. Liang, M. Wagner, M. R. Hansen, F. Laquai, F. Zhang and X. Feng, "Boron/nitrogen co-doped porous carbons derived from conjugated microporous polymers with dimensionality controlled p/n heterostructures for green energy devices", Adv. Mater. **2015**; DOI: 10.1002/adma.201501786

18) D. Xia, D. Gehrig, X. Guo, M. Baumgarten, F. Laquai and K. Müllen, "A spiro-bifluorene based 3D electron acceptor with dicyanovinylene substitution for solution processed non-fullerene organic solar cells",

J. Mater. Chem. A **2015**, *3*, pp 11086–11092; DOI**:** 10.1039/C5TA00108K

17) J.R. Ochsmann, D. Chandran, D.W. Gehrig, H. Anwar, P.K. Madathil, K.-S. Lee and F. Laquai , "Recombination processes in photovoltaic blends of DPP-type copolymers and PC71BM",

Macromol. Rap. Comm. **2015**; DOI: 10.1002/marc.201400714

16) D. W. Gehrig, I. A. Howard, S. Sweetnam, T. M. Burke, M. D. McGehee and F. Laquai, "The Impact of Donor-Acceptor Phase Separation on the Charge Carrier Dynamics in pBTTT:PCBM Photovoltaic Blends",

Macromol. Rapdid Commun. **2015**; DOI: 10.1002/marc.201500112

15) H. Kar, D. W. Gehrig, F. Laquai and S. Ghosh "J-aggregation, impact on excited state dynamics and unique solvent effects on macroscopic assembly of a core-substituted naphthalenediimide"

Nanoscale **2015**, *7*, pp 6729–6736; DOI: 10.1039/C5NR00483G

14) A. K. K. Kyaw, D. Gehrig*, J. Zhang, Y. Huang, G. C. Bazan, F. Laquai and T.-Q. Nguyen "High open-circuit voltage small-molecule p-DTS(FBTTh2)2:ICBA bulk heterojunction solar cells – morphology, excited-state dynamics, and photovoltaic performance"

J. Mater. Chem. A. **2015**, *3*, pp 1530–1539; DOI: 10.1039/C4TA06256F

13) I. Schick, S. Lorenz, D. Gehrig, S. Tenzer, W. Storck, K. Fischer, D. Strand, F. Laquai and W. Tremel "Inorganic Janus particles for biomedical applications"

Beilstein J. Nanotechnol. **2014**, *5*, pp 2346–2362, DOI: 10.3762/bjnano.5.244

12) Z. Jin, D. Gehrig, C. Dyer-Smith, E. J. Heilweil, F. Laquai, M. Bonn and D. Turchinovich "Ultrafast Terahertz Photoconductivity of Photovoltaic Polymer–Fullerene Blends: A Comparative Study Correlated with Photovoltaic Device Performance"

J. Phys. Chem. Lett. **2014**, *5*, pp 3662–3668; DOI: 10.1021/jz501890n

11) D. W. Gehrig, S. Roland, I.A. Howard, V. Kamm, H. Mangold, D. Neher and F. Laquai "Efficiency-Limiting Processes in Low-bandgap Polymer:Perylene Diimide Photovoltaic Blends"

J. Phys. Chem. C **2014**, *118*, pp 20077–20085; DOI: 10.1021/jp503366m

10) A. Sharenko, D. Gehrig*, F. Laquai,T.-Q. Nguyen "The Effect of Solvent Additive on the Charge Generation and Photovoltaic Performance of a Solution-Processed Small Molecule:Perylene Diimide Bulk Heterojunction Solar Cell"

Chem. Mater. **2014**, *26* (14), pp 4109–4118; DOI: 10.1021/cm5010483

9) O. Synooka, F. Kretschmer, M. Hager, M. Himmerlich, S. Krischok, D. Gehrig, F. Laquai, U. Schubert, G. Gobsch, H. Hoppe, "Modification of the Active Layer/PEDOT:PSS Interface by Solvent Additives Resulting in Improvement of Organic Solar Cells Performance"

ACS Appl. Mater. Interfaces **2014**, *6* (14), pp 11068–11081; DOI: 10.1021/am503284b

8) I. Schick, S. Lorenz, D. Gehrig, A.-M. Schilmann, H. Bauer, M. Panthoefer, K. Fischer, D. Strand, F. Laquai, W. Tremel, "Multifunctional Two-Photon Active Silica-Coated Au@MnO Janus Particles for Selective Dual Functionalization and Imaging"

J. Am. Chem. Soc. **2014**, *136* (6), pp 2473–2483; DOI: 10.1021/ja410787u

7) I. A. Howard, H. Mangold, F. Etzold, D. Gehrig, F. Laquai "Transient absorption data analysis by soft-modelling"

Ultrafast Dynamics in Molecules, Nanostructures and Interfaces, Series in Optics and Photonics: Volume 8, World scientific.

6) M. R. Molla, D. Gehrig, L. Roy, V. Kamm, A. Paul, F. Laquai, S. Ghosh, “Self-assembly of carboxylic acid appended naphthalene diimide (NDI) derivatives with tunable luminescent color and electrical conductivity”

Chem. Eur. J. **2014**, *20*, pp 760–771; DOI: 10.1002/chem.201303379

5) W. Zhao, X. Zhuang, D. Wu, F. Zhang, D. Gehrig, F. Laquai, X. Feng, "Boron-π-nitrogen-based conjugated porous polymers with multi-functions"

J. Mater. Chem. A **2013**, *1*, pp 13878–13884; DOI: 10.1039/C3TA13334F

4) D. Gehrig, I. A. Howard, V. Kamm, C. Dyer-Smith, F. Etzold, F. Laquai, "Charge generation in polymer:perylene diimide blends probed by Vis-NIR broadband transient absorption pump-probe spectroscopy"

Proc. SPIE 8811, Physical Chemistry of Interfaces and Nanomaterials XII, **2013**, 88111F; DOI: 10.1117/12.2023757

3) X. Zhuang, F. Zhang, D. Wu, N. Forler, H. Liang, M. Wagner, D. Gehrig, M. R. Hansen, F. Laquai, X. Feng, "Two-Dimensional Sandwich-Type, Graphene-Based Conjugated Microporous Polymers"

Angew. Chem. Int. Ed. **2013**, *52*, pp 9668–9672; DOI: 10.1002/anie.201305982

2) P. Rudolf, F. Kanal, D. Gehrig, J. Niesel, T. Brixner, U. Schatzschneider and P. Nuernberger, "Femtosecond Mid-Infrared Study of the Aqueous Solution Photochemistry of a CO-Releasing Molecule (CORM)"

EPJ Web of Conferences, **2013**, *41*, 05004; DOI: 10.1051/epjconf/20134105004

1) H. Duran, B. Hartmann-Azanza, M. Steinhart, D. Gehrig, F. Laquai, X. Feng, K. Mullen, H.-J. Butt, G. Floudas, "Arrays of Aligned Supramolecular Wires by Macroscopic Orientation of Columnar-Discotic Mesophases"

ACS Nano **2012**, *6* (11), pp 9359–9365; DOI: 10.1021/nn302937t

*co-first author

Conference Contributions

05/2015	Hybrid and Organic Photovoltaics Conference 2015, Rome, Italy. Oral contribution: "The impact of donor-acceptor phase separation on the charge carrier dynamics in pBTTT:PCBM photovoltaic blends"
03/2015	DPG spring meeting, Berlin. Oral contribution: "Efficiency-limiting processes in low-bandgap polymer:perylene diimide photovoltaic blends"
04/2014	MRS spring meeting, San Francisco, CA, USA. Oral contribution: „Positive

	Influence of a Solvent Additive on p-DTS(FBTTh2)2:PDI Organic Solar Cells - A Photophysical Study“
03/2014	CECAM workshop, Bremen: “Charge transport in organic materials”. Poster presentation: “Positive influence of a solvent additive on p-DTS(FBTTh$_2$)$_2$:PDI organic solar cells”
12/2013	MRS fall meeting, Boston, MA, USA. Poster presentation: “Efficiency-limiting processes in polymer:perylene-diimide solar cells”
09/2013	DPG – School on Physics, Bad Honnef: “Innovative Concepts in Photovoltaics”. Poster presentation: “Efficiency-limiting processes in polymer:perylene-diimide solar cells”
07/2013	Symposium of the “Nanosystems Initiative Munich” and the project „Solar Technologies Go Hybrid“, Munich: „Nanosystems for Solar Energy Conversion“. Poster presentation: “Photophysical processes in polymer:PDI solar cells”
05/2013	Hybrid and Organic Photovoltaics Conference 2013, Sevilla, Spain. Poster presentation: “Photophysical processes in polymer:PDI solar cells”
03/2013	Spring school in the framework of the priority program 1355 of the Deutsche Forschungsgemeinschaft (DFG). “Elementary processes of Organic Photovoltaics“. Poster presentation: “Photophysical processes in polymer:PDI solar cells”
03/2013	Spring meeting of the German Physical Society, Regensburg. Poster presentation: “Photophysical processes in polymer:PDI solar cells”

Curriculum Vitae

Name	Dominik Werner Gehrig
Date of birth	October 24th, 1986
Place of birth	Karlstadt am Main

Education

05/2012 – present	PhD thesis at the Max Planck Institute for Polymer Research, Mainz. Supervised

	by Assoc. Prof. Dr. Frédéric Laquai
10/2010 – 03/2012	M.Sc. in Chemistry with distinction (grade 1.0), University of Würzburg Master thesis in the group of Prof. Dr. F. Würthner, Institute for Organic Chemistry: „Synthesis of a perylene bisimide and its application in organic electronics“
10/2007 – 09/2010	B.Sc. in Chemistry with distinction (grade 1.1), University of Würzburg Bachelor thesis in the group of Prof. Dr. C. Lambert, Institute for Organic Chemistry: „Synthesis and photophysical investigation of a donor-acceptor-substituted Iridium(III) triad“
06/2006	General qualification for university entrance (Abitur, grade 1.2), Johann-Schöner-Gymnasium Karlstadt

Scholarships

11/2012 – 10/2015	Kekulé scholarship of the Fonds der Chemischen Industrie (FCI)
10/2009 – 03/2012	Scholarship of the “Max Weber-Programm des Freistaates Bayern zur Hochbegabtenförderung nach dem Bayerischen Eliteförderungsgesetz”

References

[1] F. C. Krebs, N. Espinosa, M. Hösel, R. R. Søndergaard, M. Jørgensen, *Adv. Mater.* **2014**, *26*, 29.

[2] http://www.munichre.com/de/media-relations/publications/press-releases/2015/2015-01-07-press-release/index.html, accessed 07/05/2015.

[3] C. J. Mulligan, C. Bilen, X. Zhou, W. J. Belcher, P. C. Dastoor, *Sol. Energy Mater. Sol. Cells* **2015**, *133*, 26.

[4] Y. Liu, J. Zhao, Z. Li, C. Mu, W. Ma, H. Hu, K. Jiang, H. Lin, H. Ade, H. Yan, *Nat. Commun.* **2014**, *5*, 5293.

[5] Y. Liu, C.-C. Chen, Z. Hong, J. Gao, Y. Yang, H. Zhou, L. Dou, G. Li, *Sci. Rep.* **2013**, *3*, 3356.

[6] N. O. Lipari, C. B. Duke, *J. Chem. Phys.* **1975**, *63*, 1768.

[7] G. D. Scholes, G. Rumbles, *Nat. Mater.* **2006**, *5*, 683.

[8] J. Gierschner, H.-G. Mack, L. Lüer, D. Oelkrug, *J. Chem. Phys.* **2002**, *116*, 8596.

[9] R. B. Woodward, *J. Am. Chem. Soc.* **1941**, *63*, 1123.

[10] R. E. Peierls, *Quantum Theory of Solids*, Clarendon Press, Oxford, **1955**.

[11] W. P. Su, J. R. Schrieffer, A. J. Heeger, *Phys. Rev. B* **1980**, *22*, 2099.

[12] M. Pope, C. E. Swenberg, Oxford University Press, New York, **1999**.

[13] A. Jablonski, *Nature* **1933**, *131*, 839.

[14] J. Franck, E. G. Dymond, *Trans. Faraday Soc.* **1926**, *21*, 536.

[15] E. Condon, *Phys. Rev.* **1926**, *28*, 1182.

[16] M. Born, R. Oppenheimer, *Ann. Phys.* **1927**, *389*, 457.

[17] M. Kasha, *Farad. Discuss.* **1950**, *9*, 14.

[18] R. C. Dhingra, J. A. Poole, *Chem. Phys. Lett.* **1968**, *2*, 108.

[19] S. Singh, W. J. Jones, W. Siebrand, B. P. Stoicheff, W. G. Schneider, *J. Chem. Phys.* **1965**, *42*, 330.

[20] R. E. Merrifield, P. Avakian, R. P. Groff, *Chem. Phys. Lett.* **1969**, *3*, 386.

[21] C. Jundt, G. Klein, B. Sipp, J. Le Moigne, M. Joucla, A. A. Villaeys, *Chem. Phys. Lett.* **1995**, *241*, 84.

[22] P. M. Zimmerman, Z. Zhang, C. B. Musgrave, *Nat. Chem.* **2010**, *2*, 648.

[23] D. N. Congreve, J. Lee, N. J. Thompson, E. Hontz, S. R. Yost, P. D. Reusswig, M. E. Bahlke, S. Reineke, T. Van Voorhis, M. A. Baldo, *Science* **2013**, *340*, 334.

[24] H. Sternlicht, G. C. Nieman, G. W. Robinson, *J. Chem. Phys.* **1963**, *38*, 1326.

[25] T. N. Singh-Rachford, F. N. Castellano, *Coord. Chem. Rev.* **2010**, *254*, 2560.

[26] J.-H. Lambert, *Photometria*, Sumptibus Viduae Eberhardi Klett, **1760**.

[27] Beer, *Ann. Phys.* **1852**, *161*, 67.

[28] M. Ravi, A. Samanta, T. P. Radhakrishnan, *J. Phys. Chem.* **1994**, *98*, 9133.

[29] F. Würthner, T. E. Kaiser, C. R. Saha-Möller, *Angew. Chem. Int. Ed.* **2011**, *50*, 3376.

[30] H. Hoppe, N. S. Sariciftci, *J. Mater. Res.* **2004**, *19*, 1924.

[31] S. Günes, H. Neugebauer, N. S. Sariciftci, *Chem. Rev.* **2007**, *107*, 1324.

[32] T. M. Clarke, J. R. Durrant, *Chem. Rev.* **2010**, *110*, 6736.

[33] M. C. Scharber, N. S. Sariciftci, *Prog. Polym. Sci.* **2013**, *38*, 1929.

[34] J. D. Servaites, M. A. Ratner, T. J. Marks, *Energy Environ. Sci.* **2011**, *4*, 4410.

[35] C. Tanase, E. J. Meijer, P. W. M. Blom, D. M. de Leeuw, *Phys. Rev. Lett.* **2003**, *91*, 216601.

[36] V. D. Mihailetchi, H. X. Xie, B. de Boer, L. J. A. Koster, P. W. M. Blom, *Adv. Funct. Mater.* **2006**, *16*, 699.

[37] M. Lenes, M. Morana, C. J. Brabec, P. W. M. Blom, *Adv. Funct. Mater.* **2009**, *19*, 1106.

[38] C. J. Brabec, A. Cravino, D. Meissner, N. S. Sariciftci, T. Fromherz, M. T. Rispens, L. Sanchez, J. C. Hummelen, *Adv. Funct. Mater.* **2001**, *11*, 374.

[39] M. C. Scharber, D. Mühlbacher, M. Koppe, P. Denk, C. Waldauf, A. J. Heeger, C. J. Brabec, *Adv. Mater.* **2006**, *18*, 789.

[40] K. Vandewal, K. Tvingstedt, A. Gadisa, O. Inganas, J. V. Manca, *Nat. Mater.* **2009**, *8*, 904.

[41] K. Vandewal, K. Tvingstedt, A. Gadisa, O. Inganäs, J. V. Manca, *Phys. Rev. B* **2010**, *81*, 125204.

[42] T. M. Burke, S. Sweetnam, K. Vandewal, M. D. McGehee, *Adv. Energy Mater.* **2015**, DOI: 10.1002/aenm.201500123.

[43] J. C. Blakesley, D. Neher, *Phys. Rev. B* **2011**, *84*, 075210.

[44] G. F. Burkhard, E. T. Hoke, M. D. McGehee, *Adv. Mater.* **2010**, *22*, 3293.

[45] C. W. Tang, *Appl. Phys. Lett.* **1986**, *48*, 183.

[46] N. S. Sariciftci, D. Braun, C. Zhang, V. I. Srdanov, A. J. Heeger, G. Stucky, F. Wudl, *Appl. Phys. Lett.* **1993**, *62*, 585.

[47] G. Yu, J. Gao, J. C. Hummelen, F. Wudl, A. J. Heeger, *Science* **1995**, *270*, 1789.

[48] J. J. M. Halls, C. A. Walsh, N. C. Greenham, E. A. Marseglia, R. H. Friend, S. C. Moratti, A. B. Holmes, *Nature* **1995**, *376*, 498.

[49] J. C. Hummelen, B. W. Knight, F. LePeq, F. Wudl, J. Yao, C. L. Wilkins, *J. Org. Chem.* **1995**, *60*, 532.

[50] S. E. Shaheen, C. J. Brabec, N. S. Sariciftci, F. Padinger, T. Fromherz, J. C. Hummelen, *Appl. Phys. Lett.* **2001**, *78*, 841.

[51] S. H. Park, A. Roy, S. Beaupre, S. Cho, N. Coates, J. S. Moon, D. Moses, M. Leclerc, K. Lee, A. J. Heeger, *Nat. Photon.* **2009**, *3*, 297.

[52] Y. Liang, Z. Xu, J. Xia, S.-T. Tsai, Y. Wu, G. Li, C. Ray, L. Yu, *Adv. Mater.* **2010**, *22*, E135.

[53] NREL, http://rredc.nrel.gov/solar/spectra/am1.5/, accessed 06/30/2015.

[54] L. Lüer, H. J. Egelhaaf, D. Oelkrug, G. Cerullo, G. Lanzani, B. H. Huisman, D. de Leeuw, *Org. Electron.* **2004**, *5*, 83.

[55] J. E. Kroeze, T. J. Savenije, M. J. W. Vermeulen, J. M. Warman, *J. Phys. Chem. B* **2003**, *107*, 7696.

[56] P. E. Shaw, A. Ruseckas, I. D. W. Samuel, *Adv. Mater.* **2008**, *20*, 3516.

[57] I. A. Howard, R. Mauer, M. Meister, F. Laquai, *J. Am. Chem. Soc.* **2010**, *132*, 14866.

[58] A. Foertig, A. Baumann, D. Rauh, V. Dyakonov, C. Deibel, *Appl. Phys. Lett.* **2009**, *95*, 052104.

[59] D. Rauh, C. Deibel, V. Dyakonov, *Adv. Funct. Mater.* **2012**, *22*, 3371.

[60] T. Kirchartz, B. E. Pieters, J. Kirkpatrick, U. Rau, J. Nelson, *Phys. Rev. B* **2011**, *83*, 115209.

[61] R. A. Marcus, *J. Chem. Phys.* **1956**, *24*, 966.

[62] A. J. Ward, A. Ruseckas, M. M. Kareem, B. Ebenhoch, L. A. Serrano, M. Al-Eid, B. Fitzpatrick, V. M. Rotello, G. Cooke, I. D. W. Samuel, *Adv. Mater.* **2015**, DOI: 10.1002/adma.201405623.

[63] C. L. Braun, *J. Chem. Phys.* **1984**, *80*, 4157.

[64] L. Onsager, *Phys. Rev.* **1938**, *54*, 554.

[65] J.-L. Brédas, J. E. Norton, J. Cornil, V. Coropceanu, *Acc. Chem. Res.* **2009**, *42*, 1691.

[66] P. Peumans, S. R. Forrest, *Chem. Phys. Lett.* **2004**, *398*, 27.

[67] C. Schwarz, H. Bässler, I. Bauer, J.-M. Koenen, E. Preis, U. Scherf, A. Köhler, *Adv. Mater.* **2012**, *24*, 922.

[68] F. C. Jamieson, E. B. Domingo, T. McCarthy-Ward, M. Heeney, N. Stingelin, J. R. Durrant, *Chem. Sci.* **2012**, *3*, 485.

[69] L. G. Kaake, D. Moses, A. J. Heeger, *J. Phys. Chem. Lett.* **2013**, *4*, 2264.

[70] A. G. Gagorik, J. W. Mohin, T. Kowalewski, G. R. Hutchison, *Adv. Funct. Mater.* **2014**, *25*, 1996.

[71] S. M. Falke, C. A. Rozzi, D. Brida, M. Maiuri, M. Amato, E. Sommer, A. De Sio, A. Rubio, G. Cerullo, E. Molinari, C. Lienau, *Science* **2014**, *344*, 1001.

[72] H. Bässler, *Phys. Status Solidi B* **1993**, *175*, 15.

[73] A. Miller, E. Abrahams, *Phys. Rev.* **1960**, *120*, 745.

[74] P. G. Le Comber, W. E. Spear, *Phys. Rev. Lett.* **1970**, *25*, 509.

[75] G. Horowitz, R. Hajlaoui, P. Delannoy, *J. Phys. III France* **1995**, *5*, 355.

[76] T. M. Burke, M. D. McGehee, *Adv. Mater.* **2014**, *26*, 1923.

[77] N. Vukmirović, C. S. Ponseca, H. Němec, A. Yartsev, V. Sundström, *J. Phys. Chem. C.* **2012**, *116*, 19665.

[78] T. M. Clarke, A. M. Ballantyne, J. Nelson, D. D. C. Bradley, J. R. Durrant, *Adv. Funct. Mater.* **2008**, *18*, 4029.

[79] D. P. McMahon, D. L. Cheung, A. Troisi, *J. Phys. Chem. Lett.* **2011**, *2*, 2737.

[80] S. Sweetnam, K. R. Graham, G. O. Ngongang Ndjawa, T. Heumüller, J. A. Bartelt, T. M. Burke, W. Li, W. You, A. Amassian, M. D. McGehee, *J. Am. Chem. Soc.* **2014**, *136*, 14078.

[81] W. C. Tsoi, S. J. Spencer, L. Yang, A. M. Ballantyne, P. G. Nicholson, A. Turnbull, A. G. Shard, C. E. Murphy, D. D. C. Bradley, J. Nelson, J.-S. Kim, *Macromolecules* **2011**, *44*, 2944.

[82] P. Westacott, J. R. Tumbleston, S. Shoaee, S. Fearn, J. H. Bannock, J. B. Gilchrist, S. Heutz, J. deMello, M. Heeney, H. Ade, J. Durrant, D. S. McPhail, N. Stingelin, *Energy Environ. Sci.* **2013**, *6*, 2756.

[83] C. Groves, *Energy Environ. Sci.* **2013**, *6*, 1546.

[84] A. Zusan, K. Vandewal, B. Allendorf, N. H. Hansen, J. Pflaum, A. Salleo, V. Dyakonov, C. Deibel, *Adv. Energy Mater.* **2014**, *4*, 1400922.

[85] I.-W. Hwang, J. Young Kim, S. Cho, J. Yuen, N. Coates, K. Lee, M. Heeney, I. McCulloch, D. Moses, A. J. Heeger, *J. Phys. Chem. C.* **2008**, *112*, 7853.

[86] M. Scarongella, A. A. Paraecattil, E. Buchaca-Domingo, J. D. Douglas, S. Beaupre, T. McCarthy-Ward, M. Heeney, J. E. Moser, M. Leclerc, J. M. J. Frechet, N. Stingelin, N. Banerji, *J. Mater. Chem. A* **2014**, *2*, 6218.

[87] A. C. Mayer, M. F. Toney, S. R. Scully, J. Rivnay, C. J. Brabec, M. Scharber, M. Koppe, M. Heeney, I. McCulloch, M. D. McGehee, *Adv. Funct. Mater.* **2009**, *19*, 1173.

[88] R. J. Kline, D. M. DeLongchamp, D. A. Fischer, E. K. Lin, L. J. Richter, M. L. Chabinyc, M. F. Toney, M. Heeney, I. McCulloch, *Macromolecules* **2007**, *40*, 7960.

[89] N. C. Cates, R. Gysel, Z. Beiley, C. E. Miller, M. F. Toney, M. Heeney, I. McCulloch, M. D. McGehee, *Nano Lett.* **2009**, *9*, 4153.

[90] N. C. Miller, S. Sweetnam, E. T. Hoke, R. Gysel, C. E. Miller, J. A. Bartelt, X. Xie, M. F. Toney, M. D. McGehee, *Nano Lett.* **2012**, *12*, 1566.

[91] M. Scarongella, J. De Jonghe-Risse, E. Buchaca-Domingo, M. Causa’, Z. Fei, M. Heeney, J.-E. Moser, N. Stingelin, N. Banerji, *J. Am. Chem. Soc.* **2015**, *137*, 2908.

[92] E. Buchaca-Domingo, A. J. Ferguson, F. C. Jamieson, T. McCarthy-Ward, S. Shoaee, J. R. Tumbleston, O. G. Reid, L. Yu, M. B. Madec, M. Pfannmoller, F. Hermerschmidt, R. R. Schroder, S. E. Watkins, N. Kopidakis, G. Portale, A. Amassian, M. Heeney, H. Ade, G. Rumbles, J. R. Durrant, N. Stingelin, *Mater. Horizon.* **2014**, *1*, 270.

[93] A. A. Bakulin, A. Rao, V. G. Pavelyev, P. H. M. van Loosdrecht, M. S. Pshenichnikov, D. Niedzialek, J. Cornil, D. Beljonne, R. H. Friend, *Science* **2012**, *335*, 1340.

[94] G. Grancini, M. Maiuri, D. Fazzi, A. Petrozza, H. J. Egelhaaf, D. Brida, G. Cerullo, G. Lanzani, *Nat. Mater.* **2013**, *12*, 29.

[95] M. Scharber, *Nat. Mater.* **2013**, *12*, 594.

[96] K. Vandewal, S. Albrecht, E. T. Hoke, K. R. Graham, J. Widmer, J. D. Douglas, M. Schubert, W. R. Mateker, J. T. Bloking, G. F. Burkhard, A. Sellinger, J. M. J. Fréchet, A. Amassian, M. K. Riede, M. D. McGehee, D. Neher, A. Salleo, *Nat. Mater.* **2014**, *13*, 63.

[97] W. Shockley, H. J. Queisser, *J. Appl. Phys.* **1961**, *32*, 510.

[98] T. Liu, A. Troisi, *Adv. Mater.* **2013**, *25*, 1038.

[99] X. Corp., JP 03024059 A2, **1991**.

[100] BASF, DE-OS 21 39 688, **1973**.

[101] G. Seybold, G. Wagenblast, *Dyes Pigm.* **1989**, *11*, 303.

[102] BASF, DE-OS 34 34 059, **1985**.

[103] Z. Chen, M. G. Debije, T. Debaerdemaeker, P. Osswald, F. Würthner, *ChemPhysChem* **2004**, *5*, 137.

[104] H. Langhals, *Heterocycles* **1995**, *40*, 477.

[105] I. A. Howard, F. Laquai, P. E. Keivanidis, R. H. Friend, N. C. Greenham, *J. Phys. Chem. C.* **2009**, *113*, 21225.

[106] M. Hiramoto, H. Fujiwara, M. Yokoyama, *J. Appl. Phys.* **1992**, *72*, 3781.

[107] J. B. Whitlock, P. Panayotatos, G. Sharma, M. D. Cox, R. R. Sauers, G. R. Bird, *Opt. Eng.* **1993**, *32*, 1921.

[108] P. Peumans, V. Bulović, S. R. Forrest, *Appl. Phys. Lett.* **2000**, *76*, 2650.

[109] J.-i. Nakamura, C. Yokoe, K. Murata, K. Takahashi, *J. Appl. Phys.* **2004**, *96*, 6878.

[110] A. K. Pandey, S. Dabos-Seignon, J.-M. Nunzi, *Appl. Phys. Lett.* **2006**, *89*, 113506.

[111] K. N. N. Unni, A. K. Pandey, S. Alem, J.-M. Nunzi, *Chem. Phys. Lett.* **2006**, *421*, 554.

[112] V. Kamm, G. Battagliarin, I. A. Howard, W. Pisula, A. Mavrinskiy, C. Li, K. Müllen, F. Laquai, *Adv. Energy Mater.* **2011**, *1*, 297.

[113] T. Ye, R. Singh, H.-J. Butt, G. Floudas, P. E. Keivanidis, *ACS Appl. Mater. Interfaces* **2013**, *5*, 11844.

[114] A. Sharenko, C. M. Proctor, T. S. van der Poll, Z. B. Henson, T.-Q. Nguyen, G. C. Bazan, *Adv. Mater.* **2013**, *25*, 4403.

[115] A. Sharenko, D. Gehrig, F. Laquai, T.-Q. Nguyen, *Chem. Mater.* **2014**, *26*, 4109.

[116] S. Rajaram, R. Shivanna, S. K. Kandappa, K. S. Narayan, *J. Phys. Chem. Lett.* **2012**, *3*, 2405.

[117] R. Shivanna, S. Shoaee, S. Dimitrov, S. K. Kandappa, S. Rajaram, J. R. Durrant, K. S. Narayan, *Energy Environ. Sci.* **2014**, *7*, 435.

[118] X. Zhang, Z. Lu, L. Ye, C. Zhan, J. Hou, S. Zhang, B. Jiang, Y. Zhao, J. Huang, S. Zhang, Y. Liu, Q. Shi, Y. Liu, J. Yao, *Adv. Mater.* **2013**, *25*, 5791.

[119] L. Ye, W. Jiang, W. Zhao, S. Zhang, D. Qian, Z. Wang, J. Hou, *Small* **2014**, *10*, 4658.

[120] W. Jiang, L. Ye, X. Li, C. Xiao, F. Tan, W. Zhao, J. Hou, Z. Wang, *Chem. Commun.* **2014**, *50*, 1024.

[121] L. Ye, W. Jiang, W. Zhao, S. Zhang, Y. Cui, Z. Wang, J. Hou, *Org. Electron.* **2015**, *17*, 295.

[122] Y. Zhang, L. Chen, K. Zhang, H. Wang, Y. Xiao, *Chem. Eur. J.* **2014**, *20*, 10170.

[123] Y. Lin, Y. Wang, J. Wang, J. Hou, Y. Li, D. Zhu, X. Zhan, *Adv. Mater.* **2014**, *26*, 5224.

[124] Y. Zhong, M. T. Trinh, R. Chen, W. Wang, P. P. Khlyabich, B. Kumar, Q. Xu, C.-Y. Nam, M. Y. Sfeir, C. Black, M. L. Steigerwald, Y.-L. Loo, S. Xiao, F. Ng, X. Y. Zhu, C. Nuckolls, *J. Am. Chem. Soc.* **2014**, *136*, 15215.

[125] Y. Zhong, B. Kumar, S. Oh, M. T. Trinh, Y. Wu, K. Elbert, P. Li, X. Zhu, S. Xiao, F. Ng, M. L. Steigerwald, C. Nuckolls, *J. Am. Chem. Soc.* **2014**, *136*, 8122.

[126] J. Zhao, Y. Li, H. Lin, Y. Liu, K. Jiang, C. Mu, T. Ma, J. Y. L. Lai, H. Yan, *Energy Environ. Sci.* **2015**, *8*, 520.

[127] Y. Liu, C. Mu, K. Jiang, J. Zhao, Y. Li, L. Zhang, Z. Li, J. Y. L. Lai, H. Hu, T. Ma, R. Hu, D. Yu, X. Huang, B. Z. Tang, H. Yan, *Adv. Mater.* **2015**, *27*, 1015.

[128] P. E. Hartnett, A. Timalsina, H. S. S. R. Matte, N. Zhou, X. Guo, W. Zhao, A. Facchetti, R. P. H. Chang, M. C. Hersam, M. R. Wasielewski, T. J. Marks, *J. Am. Chem. Soc.* **2014**, *136*, 16345.

[129] Y. Zhang, Y. Xiao, Y. Xie, L. Zhu, D. Shi, C. Cheng, *Org. Electron.* **2015**, *21*, 184.

[130] w. Chen, X. Yang, g. long, X. Wan, Y. Chen, q. Zhang, *J. Mater. Chem. C* **2015**, *3*, 4698.

[131] Y. Cai, L. Huo, X. Sun, D. Wei, M. Tang, Y. Sun, *Adv. Energy Mater.* **2015**, DOI: 10.1002/aenm.201500032.

[132] S. M. Lindner, S. Hüttner, A. Chiche, M. Thelakkat, G. Krausch, *Angew. Chem. Int. Ed.* **2006**, *45*, 3364.

[133] M. Sommer, S. M. Lindner, M. Thelakkat, *Adv. Funct. Mater.* **2007**, *17*, 1493.

[134] M. Sommer, S. Hüttner, U. Steiner, M. Thelakkat, *Appl. Phys. Lett.* **2009**, *95*, 183308.

[135] P. Cheng, X. Zhao, W. Zhou, J. Hou, Y. Li, X. Zhan, *Org. Electron.* **2014**, *15*, 2270.

[136] Y.-J. Hwang, T. Earmme, B. A. E. Courtright, F. N. Eberle, S. A. Jenekhe, *J. Am. Chem. Soc.* **2015**, *137*, 4424.

[137] F. G. Brunetti, X. Gong, M. Tong, A. J. Heeger, F. Wudl, *Angew. Chem. Int. Ed.* **2010**, *49*, 532.

[138] D. H. Wang, A. K. K. Kyaw, J.-R. Pouliot, M. Leclerc, A. J. Heeger, *Adv. Energy Mater.* **2013**, 1300835.

[139] V. S. Gevaerts, A. Furlan, M. M. Wienk, M. Turbiez, R. A. J. Janssen, *Adv. Mater.* **2012**, *24*, 2130.

[140] S. Kouijzer, S. Esiner, C. H. Frijters, M. Turbiez, M. M. Wienk, R. A. J. Janssen, *Adv. Energy Mater.* **2012**, *2*, 945.

[141] K. H. Hendriks, G. H. L. Heintges, V. S. Gevaerts, M. M. Wienk, R. A. J. Janssen, *Angew. Chem. Int. Ed.* **2013**, *52*, 8341.

[142] W. Li, A. Furlan, K. H. Hendriks, M. M. Wienk, R. A. J. Janssen, *J. Am. Chem. Soc.* **2013**, *135*, 5529.

[143] W. Li, K. H. Hendriks, A. Furlan, W. S. C. Roelofs, M. M. Wienk, R. A. J. Janssen, *J. Am. Chem. Soc.* **2013**, *135*, 18942.

[144] W. Li, K. H. Hendriks, W. S. C. Roelofs, Y. Kim, M. M. Wienk, R. A. J. Janssen, *Adv. Mater.* **2013**, *25*, 3182.

[145] W. Li, K. H. Hendriks, A. Furlan, W. S. C. Roelofs, S. C. J. Meskers, M. M. Wienk, R. A. J. Janssen, *Adv. Mater.* **2014**, *26*, 1565.

[146] D. Chandran, K.-S. Lee, *Macromol. Res.* **2013**, *21*, 272.

[147] G. Zhang, Y. Fu, Z. Xie, Q. Zhang, *Sol. Energy Mater. Sol. Cells* **2011**, *95*, 1168.

[148] P. Sonar, G.-M. Ng, T. T. Lin, A. Dodabalapur, Z.-K. Chen, *J. Mater. Chem.* **2010**, *20*, 3626.

[149] P. E. Schwenn, K. Gui, A. M. Nardes, K. B. Krueger, K. H. Lee, K. Mutkins, H. Rubinstein-Dunlop, P. E. Shaw, N. Kopidakis, P. L. Burn, P. Meredith, *Adv. Energy Mater.* **2011**, *1*, 73.

[150] Y. Fang, A. K. Pandey, A. M. Nardes, N. Kopidakis, P. L. Burn, P. Meredith, *Adv. Energy Mater.* **2013**, *3*, 54.

[151] M. Morana, H. Azimi, G. Dennler, H.-J. Egelhaaf, M. Scharber, K. Forberich, J. Hauch, R. Gaudiana, D. Waller, Z. Zhu, K. Hingerl, S. S. van Bavel, J. Loos, C. J. Brabec, *Adv. Funct. Mater.* **2010**, *20*, 1180.

[152] Y. Fang, A. K. Pandey, D. M. Lyons, P. E. Shaw, S. E. Watkins, P. L. Burn, S.-C. Lo, P. Meredith, *ChemPhysChem* **2014**, 1295.

[153] J. T. Bloking, X. Han, A. T. Higgs, J. P. Kastrop, L. Pandey, J. E. Norton, C. Risko, C. E. Chen, J.-L. Brédas, M. D. McGehee, A. Sellinger, *Chem. Mater.* **2011**, *23*, 5484.

[154] J. T. Bloking, T. Giovenzana, A. T. Higgs, A. J. Ponec, E. T. Hoke, K. Vandewal, S. Ko, Z. Bao, A. Sellinger, M. D. McGehee, *Adv. Energy Mater.* **2014**, *4*, 1301426.

[155] Y. Shu, Y.-F. Lim, Z. Li, B. Purushothaman, R. Hallani, J. E. Kim, S. R. Parkin, G. G. Malliaras, J. E. Anthony, *Chem. Sci.* **2011**, *2*, 363.

[156] E. Ahmed, G. Ren, F. S. Kim, E. C. Hollenbeck, S. A. Jenekhe, *Chem. Mater.* **2011**, *23*, 4563.

[157] Y. Liu, L. Zhang, H. Lee, H.-W. Wang, A. Santala, F. Liu, Y. Diao, A. L. Briseno, T. P. Russell, *Adv. Energy Mater.* **2015**, DOI: 10.1002/aenm.201500195.

[158] Y. Zhou, L. Ding, K. Shi, Y.-Z. Dai, N. Ai, J. Wang, J. Pei, *Adv. Mater.* **2012**, *24*, 957.

[159] T. V. Pho, F. M. Toma, M. L. Chabinyc, F. Wudl, *Angew. Chem. Int. Ed.* **2013**, *52*, 1446.

[160] R.-Q. Lu, Y.-Q. Zheng, Y.-N. Zhou, X.-Y. Yan, T. Lei, K. Shi, Y. Zhou, J. Pei, L. Zoppi, K. K. Baldridge, J. S. Siegel, X.-Y. Cao, *J. Mater. Chem. A* **2014**, *2*, 20515.

[161] H. Li, T. Earmme, S. Subramaniyan, S. A. Jenekhe, *Adv. Energy Mater.* **2015**, DOI: 10.1002/aenm.201402041.

[162] H. Li, Y.-J. Hwang, B. A. E. Courtright, F. N. Eberle, S. Subramaniyan, S. A. Jenekhe, *Adv. Mater.* **2015**, DOI: 10.1002/adma.201500577.

[163] O. K. Kwon, J.-H. Park, D. W. Kim, S. K. Park, S. Y. Park, *Adv. Mater.* **2015**, DOI: 10.1002/adma.201405429.

[164] H. Yan, Z. Chen, Y. Zheng, C. Newman, J. R. Quinn, F. Dotz, M. Kastler, A. Facchetti, *Nature* **2009**, *457*, 679.

[165] M. Schubert, B. A. Collins, H. Mangold, I. A. Howard, W. Schindler, K. Vandewal, S. Roland, J. Behrends, F. Kraffert, R. Steyrleuthner, Z. Chen, K. Fostiropoulos, R. Bittl, A. Salleo, A. Facchetti, F. Laquai, H. W. Ade, D. Neher, *Adv. Funct. Mater.* **2014**, *24*, 4068.

[166] C. Lee, H. Kang, W. Lee, T. Kim, K.-H. Kim, H. Y. Woo, C. Wang, B. J. Kim, *Adv. Mater.* **2015**, DOI: 10.1002/adma.201405226.

[167] J. W. Jung, J. W. Jo, C.-C. Chueh, F. Liu, W. H. Jo, T. P. Russell, A. K. Y. Jen, *Adv. Mater.* **2015**, DOI: 10.1002/adma.201501214.

[168] Z. Tang, B. Liu, A. Melianas, J. Bergqvist, W. Tress, Q. Bao, D. Qian, O. Inganäs, F. Zhang, *Adv. Mater.* **2015**, *27*, 1900.

[169] D. Xia, D. Gehrig, X. Guo, M. Baumgarten, F. Laquai, K. Muellen, *J. Mater. Chem. A* **2015**, *3*, 11086.

[170] T. Zhou, T. Jia, B. Kang, F. Li, M. Fahlman, Y. Wang, *Adv. Energy Mater.* **2011**, *1*, 431.

[171] K. N. Winzenberg, P. Kemppinen, F. H. Scholes, G. E. Collis, Y. Shu, T. Birendra Singh, A. Bilic, C. M. Forsyth, S. E. Watkins, *Chem. Commun.* **2013**, *49*, 6307.

[172] Y. Yang, G. Zhang, C. Yu, C. He, J. Wang, X. Chen, J. Yao, Z. Liu, D. Zhang, *Chem. Commun.* **2014**, *50*, 9939.

[173] Z. Mao, W. Senevirathna, J.-Y. Liao, J. Gu, S. V. Kesava, C. Guo, E. D. Gomez, G. Sauvé, *Adv. Mater.* **2014**, *26*, 6290.

[174] H. Bai, Y. Wang, P. Cheng, J. Wang, Y. Wu, J. Hou, X. Zhan, *J. Mater. Chem. A* **2015**, *3*, 1910.

[175] Y. Lin, Z.-G. Zhang, H. Bai, J. Wang, Y. Yao, Y. Li, D. Zhu, X. Zhan, *Energy Environ. Sci.* **2015**, *8*, 610.

[176] Y. Lin, J. Wang, Z.-G. Zhang, H. Bai, Y. Li, D. Zhu, X. Zhan, *Adv. Mater.* **2015**, *27*, 1170.

[177] B. Verreet, B. P. Rand, D. Cheyns, A. Hadipour, T. Aernouts, P. Heremans, A. Medina, C. G. Claessens, T. Torres, *Adv. Energy Mater.* **2011**, *1*, 565.

[178] P. Sullivan, A. Duraud, l. Hancox, N. Beaumont, G. Mirri, J. H. R. Tucker, R. A. Hatton, M. Shipman, T. S. Jones, *Adv. Energy Mater.* **2011**, *1*, 352.

[179] N. Beaumont, S. W. Cho, P. Sullivan, D. Newby, K. E. Smith, T. S. Jones, *Adv. Funct. Mater.* **2012**, *22*, 561.

[180] B. Ebenhoch, N. B. A. Prasetya, V. M. Rotello, G. Cooke, I. D. W. Samuel, *J. Mater. Chem. A* **2015**, *3*, 7345.

[181] K. Cnops, B. P. Rand, D. Cheyns, B. Verreet, M. A. Empl, P. Heremans, *Nat. Commun.* **2014**, *5*, 3406.

[182] F. Wudl, M. Kobayashi, A. J. Heeger, *J. Org. Chem.* **1984**, *49*, 3382.

[183] Y. Ikenoue, F. Wudl, A. J. Heeger, *Synth. Met.* **1991**, *40*, 1.

[184] J. L. Brédas, *Synth. Met.* **1987**, *17*, 115.

[185] E. E. Havinga, W. ten Hoeve, H. Wynberg, *Synth. Met.* **1993**, *55*, 299.

[186] G. Brocks, A. Tol, *J. Phys. Chem.* **1996**, *100*, 1838.

[187] Z. G. Zhang, J. Wang, *J. Mater. Chem.* **2012**, *22*, 4178.

[188] W. Li, K. Hendriks, A. Furlan, A. Zhang, M. M. Wienk, R. A. J. Janssen, *Chem. Commun.* **2015**, *51*, 4290.

[189] H. Bürckstümmer, N. M. Kronenberg, M. Gsänger, M. Stolte, K. Meerholz, F. Würthner, *J. Mater. Chem.* **2010**, *20*, 240.

[190] N. M. Kronenberg, V. Steinmann, H. Bürckstümmer, J. Hwang, D. Hertel, F. Würthner, K. Meerholz, *Adv. Mater.* **2010**, *22*, 4193.

[191] C. D. Wessendorf, G. L. Schulz, A. Mishra, P. Kar, I. Ata, M. Weidelener, M. Urdanpilleta, J. Hanisch, E. Mena-Osteritz, M. Lindén, E. Ahlswede, P. Bäuerle, *Adv. Energy Mater.* **2014**, *4*, 1400266.

[192] A. Mishra, C. Uhrich, E. Reinold, M. Pfeiffer, P. Bäuerle, *Adv. Energy Mater.* **2011**, *1*, 265.

[193] R. Fitzner, E. Reinold, A. Mishra, E. Mena-Osteritz, H. Ziehlke, C. Körner, K. Leo, M. Riede, M. Weil, O. Tsaryova, A. Weiß, C. Uhrich, M. Pfeiffer, P. Bäuerle, *Adv. Funct. Mater.* **2011**, *21*, 897.

[194] M. K. R. Fischer, S. Wenger, M. Wang, A. Mishra, S. M. Zakeeruddin, M. Grätzel, P. Bäuerle, *Chem. Mater.* **2010**, *22*, 1836.

[195] C.-Q. Ma, M. Fonrodona, M. C. Schikora, M. M. Wienk, R. A. J. Janssen, P. Bäuerle, *Adv. Funct. Mater.* **2008**, *18*, 3323.

[196] C. Uhrich, R. Schüppel, A. Petrich, M. Pfeiffer, K. Leo, E. Brier, P. Kilickiran, P. Bäuerle, *Adv. Funct. Mater.* **2007**, *17*, 2991.

[197] K. Schulze, C. Uhrich, R. Schüppel, K. Leo, M. Pfeiffer, E. Brier, E. Reinold, P. Bäuerle, *Adv. Mater.* **2006**, *18*, 2872.

[198] Q. Zhang, B. Kan, F. Liu, G. Long, X. Wan, X. Chen, Y. Zuo, W. Ni, H. Zhang, M. Li, Z. Hu, F. Huang, Y. Cao, Z. Liang, M. Zhang, T. P. Russell, Y. Chen, *Nat. Photon.* **2015**, *9*, 35.

[199] T. S. van der Poll, J. A. Love, T.-Q. Nguyen, G. C. Bazan, *Adv. Mater.* **2012**, *24*, 3646.

[200] C. M. Proctor, S. Albrecht, M. Kuik, D. Neher, T.-Q. Nguyen, *Adv. Energy Mater.* **2014**, *4*, 1400230.

[201] A. K. K. Kyaw, D. H. Wang, V. Gupta, W. L. Leong, L. Ke, G. C. Bazan, A. J. Heeger, *ACS Nano* **2013**, *7*, 4569.

[202] C. M. Proctor, J. A. Love, T.-Q. Nguyen, *Adv. Mater.* **2014**, *26*, 5957.

[203] L. A. Perez, K. W. Chou, J. A. Love, T. S. van der Poll, D.-M. Smilgies, T.-Q. Nguyen, E. J. Kramer, A. Amassian, G. C. Bazan, *Adv. Mater.* **2013**, *25*, 6380.

[204] S. Gélinas, A. Rao, A. Kumar, S. L. Smith, A. W. Chin, J. Clark, T. S. van der Poll, G. C. Bazan, R. H. Friend, *Science* **2013**, *343*, 512.

[205] A. K. K. Kyaw, D. Gehrig, J. Zhang, Y. Huang, G. C. Bazan, F. Laquai, T.-Q. Nguyen, *J. Mater. Chem. A* **2015**, *3*, 1530.

[206] A. Sharenko, N. D. Treat, J. A. Love, M. F. Toney, N. Stingelin, T.-Q. Nguyen, *J. Mater. Chem. A* **2014**, *2*, 15717.

[207] W. Ni, X. Wan, M. Li, Y. Wang, Y. Chen, *Chem. Commun.* **2015**, *51*, 4936.

[208] C. A. Gueymard, D. Myers, K. Emery, *Solar Energy* **2002**, *73*, 443.

[209] V. B. Kamm, Dissertation thesis, Johannes Gutenberg-Universität Mainz (Mainz), **2013**.

[210] D. W. Gehrig, S. Roland, I. A. Howard, V. Kamm, H. Mangold, D. Neher, F. Laquai, *J. Phys. Chem. C.* **2014**, *118*, 20077.

[211] A. De Juan, R. Tauler, *Anal. Chim. Acta* **2003**, *500*, 195.

[212] A. de Juan, R. Tauler, *Crit. Rev. Anal. Chem.* **2006**, *36*, 163.

[213] J. Jaumot, R. Tauler, *Chemom. Intell. Lab. Syst.* **2010**, *103*, 96.

[214] I. A. Howard, H. Mangold, F. Etzold, D. Gehrig, F. Laquai, *Ultrafast Dynamics in Molecules, Nanostructures and Interfaces* **2014**, *Volume 8, World Scientific*.

[215] D. Gehrig, I. A. Howard, V. Kamm, C. Dyer-Smith, F. Etzold, F. Laquai, *Proc. SPIE* **2013**, *8811*, 88111F.

[216] F. Etzold, I. A. Howard, N. Forler, A. Melnyk, D. Andrienko, M. R. Hansen, F. Laquai, *Energy Environ. Sci.* **2015**, *8*, 1511.

[217] D. W. Gehrig, I. A. Howard, F. Laquai, *J. Phys. Chem. C.* **2015**, DOI: 10.1021/acs.jpcc.5b03467.

[218] J. R. Ochsmann, D. Chandran, D. W. Gehrig, H. Anwar, P. K. Madathil, K.-S. Lee, F. Laquai, *Macromol. Rapid Commun.* **2015**, DOI: 10.1002/marc.201400714.

[219] H.-Y. Chen, J. Hou, S. Zhang, Y. Liang, G. Yang, Y. Yang, L. Yu, Y. Wu, G. Li, *Nat. Photon.* **2009**, *3*, 649.

[220] Y. Li, *Acc. Chem. Res.* **2012**, *45*, 723.

[221] Y. He, H.-Y. Chen, J. Hou, Y. Li, *J. Am. Chem. Soc.* **2010**, *132*, 1377.

[222] D. W. Gehrig, I. A. Howard, S. Sweetnam, T. M. Burke, M. D. McGehee, F. Laquai, *Macromol. Rapid Commun.* **2015**, DOI: 10.1002/marc.201500112.

[223] F. Etzold, Dissertation thesis, Johannes Gutenberg-Universität Mainz (Mainz), **2014**.

[224] E. J. Meijer, D. M. de Leeuw, S. Setayesh, E. van Veenendaal, B. H. Huisman, P. W. M. Blom, J. C. Hummelen, U. Scherf, T. M. Klapwijk, *Nat. Mater.* **2003**, *2*, 678.

[225] J. Li, F. Dierschke, J. Wu, A. C. Grimsdale, K. Mullen, *J. Mater. Chem.* **2006**, *16*, 96.

[226] C. Arantes, M. Scholz, R. Schmidt, V. Dehm, M. L. M. Rocco, A. Schöll, F. Reinert, F. Würthner, *Applied Physics A* **2012**, *108*, 629.

[227] J. H. Oh, S. Liu, Z. Bao, R. Schmidt, F. Würthner, *Appl. Phys. Lett.* **2007**, *91*, 212107.

[228] D. Veldman, S. C. J. Meskers, R. A. J. Janssen, *Adv. Funct. Mater.* **2009**, *19*, 1939.

[229] Y. He, G. Zhao, B. Peng, Y. Li, *Adv. Funct. Mater.* **2010**, *20*, 3383.

[230] E. H. A. Beckers, S. C. J. Meskers, A. P. H. J. Schenning, Z. Chen, F. Würthner, P. Marsal, D. Beljonne, J. Cornil, R. A. J. Janssen, *J. Am. Chem. Soc.* **2005**, *128*, 649.

[231] M. Aghamohammadi, A. Fernández, M. Schmidt, A. Pérez-Rodríguez, A. R. Goñi, J. Fraxedas, G. Sauthier, M. Paradinas, C. Ocal, E. Barrena, *J. Phys. Chem. C.* **2014**, *118*, 14833.

[232] L. J. A. Koster, V. D. Mihailetchi, P. W. M. Blom, *Appl. Phys. Lett.* **2006**, *88*, 052104.

[233] L. Huo, S. Zhang, X. Guo, F. Xu, Y. Li, J. Hou, *Angew. Chem.* **2011**, *123*, 9871.

[234] J. A. Love, C. M. Proctor, J. Liu, C. J. Takacs, A. Sharenko, T. S. van der Poll, A. J. Heeger, G. C. Bazan, T.-Q. Nguyen, *Adv. Funct. Mater.* **2013**, *23*, 5019.

[235] A. Zusan, B. Gieseking, M. Zerson, V. Dyakonov, R. Magerle, C. Deibel, *Sci. Rep.* **2015**, *5*, 8286.

[236] Z.-G. Zhang, H. Li, B. Qi, D. Chi, Z. Jin, Z. Qi, J. Hou, Y. Li, J. Wang, *J. Mater. Chem. A* **2013**, *1*, 9624.

[237] S. Väth, H. Kraus, A. Baumann, K. Tvingstedt, A. Sperlich, V. Dyakonov, J. Love, T.-Q. Nguyen, in *DGP Frühjahrstagung*, Berlin, **2015**.

[238] H. Kraus, K. Tvingstedt, A. Baumann, A. Sperlich, V. Dyakonov, J. Love, T.-Q. Nguyen, in *MRS Spring Meeting & Exhibit*, San Francisco, CA, **2015**.

[239] J. Wang, Y. Yao, S. Dai, X. Zhang, W. Wang, Q. He, L. Han, Y. Lin, X. Zhan, *J. Mater. Chem. A* **2015**, na.

[240] S. D. Dimitrov, S. Wheeler, D. Niedzialek, B. C. Schroeder, H. Utzat, J. M. Frost, J. Yao, A. Gillett, P. S. Tuladhar, I. McCulloch, J. Nelson, J. R. Durrant, *Nat. Commun.* **2015**, *6*, 6501.

[241] R. R. Hung, J. J. Grabowski, *J. Phys. Chem.* **1991**, *95*, 6073.

[242] S. Esiner, H. van Eersel, M. M. Wienk, R. A. J. Janssen, *Adv. Mater.* **2013**, *25*, 2932.

[243] G. E. Eperon, S. D. Stranks, C. Menelaou, M. B. Johnston, L. M. Herz, H. J. Snaith, *Energy Environ. Sci.* **2014**, *7*, 982.

[244] S. D. Stranks, G. E. Eperon, G. Grancini, C. Menelaou, M. J. P. Alcocer, T. Leijtens, L. M. Herz, A. Petrozza, H. J. Snaith, *Science* **2013**, *342*, 341.

[245] Q. Lin, A. Armin, R. C. R. Nagiri, P. L. Burn, P. Meredith, *Nat. Photon.* **2015**, *9*, 106.

[246] V. D'Innocenzo, G. Grancini, M. J. P. Alcocer, A. R. S. Kandada, S. D. Stranks, M. M. Lee, G. Lanzani, H. J. Snaith, A. Petrozza, *Nat Commun* **2014**, *5*.

[247] M. Liu, M. B. Johnston, H. J. Snaith, *Nature* **2013**, *501*, 395.

[248] M. M. Lee, J. Teuscher, T. Miyasaka, T. N. Murakami, H. J. Snaith, *Science* **2012**, *338*, 643.

[249] H. J. Snaith, A. Abate, J. M. Ball, G. E. Eperon, T. Leijtens, N. K. Noel, S. D. Stranks, J. T.-W. Wang, K. Wojciechowski, W. Zhang, *J. Phys. Chem. Lett.* **2014**, *5*, 1511.

[250] K.-C. Wang, J.-Y. Jeng, P.-S. Shen, Y.-C. Chang, E. W.-G. Diau, C.-H. Tsai, T.-Y. Chao, H.-C. Hsu, P.-Y. Lin, P. Chen, T.-F. Guo, T.-C. Wen, *Sci. Rep.* **2014**, *4*, 4756.

[251] L. Wang, C. McCleese, A. Kovalsky, Y. Zhao, C. Burda, *J. Am. Chem. Soc.* **2014**, *136*, 12205.

[252] P. Piatkowski, B. Cohen, F. Javier Ramos, M. Di Nunzio, M. K. Nazeeruddin, M. Gratzel, S. Ahmad, A. Douhal, *Phys. Chem. Chem. Phys.* **2015**, *17*, 14674.

[253] T. Leijtens, G. E. Eperon, S. Pathak, A. Abate, M. M. Lee, H. J. Snaith, *Nat Commun* **2013**, *4*, 2885.

[254] Q. Shen, Y. Ogomi, J. Chang, T. Toyoda, K. Fujiwara, K. Yoshino, K. Sato, K. Yamazaki, M. Akimoto, Y. Kuga, K. Katayama, S. Hayase, *J. Mater. Chem. A* **2015**, *3*, 9308.